Universitat d'Alacant
Universidad de Alicante

Fundamental properties of High-Mass X-ray Binaries

Ana González-Galán

PhD Thesis

June 2014

El Dr IGNACIO NEGUERUELA DÍEZ, profesor titular de la Universidad de Alicante, del Departamento de Física, Ingeniería de Sistemas y Teoría de la Señal,

CERTIFICA:

Que la presente memoria se ha llevado a cabo bajo su dirección, por ANA GONZÁLEZ GALÁN, y constituye su Tesis Doctoral para optar al Grado de Doctor.

Para que conste y en cumplimiento de la legislación vigente, firma el presente certificado el Dr IGNACIO NEGUERUELA DÍEZ, an Alicante a ? de Junio de 2014.

Abstract

The aim of this thesis is to characterise a sample of High Mass X-ray Binaries (HMXBs) formed by: IGR J00370+6122, XTE J1855-026, AX J1841.0-0535 and AX J1845.0-0433. These objects are composed by pulsars (rotating neutron stars) accreting material from the wind of their supergiant companions. The X-rays are produced in the interaction of the accreted material with the strong gravitational field of the neutron star that accelerates this material and heats it up to $\sim 10^7$ K.

The study of HMXBs has strong implications in several areas of Physics and Astrophysics. They contain neutron stars which study is essential to constrain the equation of state of nuclear dense matter, and provides insights on the astrophysical models of core collapse and Supernovae explosions. HMXBs considered as a population give information on the properties of the galaxy. In addition they are excellent test-beds to study accretion physics and outflows.

The X-ray behaviour of these systems determines the class of system (classical HMXBs, Supergiant Fast X-ray Transients, Be/X-ray Binaries). The differences in the X-ray emission are supposed to be due to the different properties of the binary systems, such as the orbital properties, the magnetic field of the neutron star or the spectral type of the donor star. HMXBs in this thesis are wind-fed systems, therefore, the properties of the wind (which depend on the spectral type) and the interaction of this wind with the gravitational field of the compact object are key elements to understand the X-ray emission.

Therefore, in this thesis an orbital solution for each target of study has been determined using optical spectra of the donor star. Moreover, to check if wind variability is related to the orbit of the binary system, analysis of $\mathrm{H}\alpha$ variations have been carried out. Furthermore, in the case of IGR J00370+6122 and

XTE J1855-026 we have obtained an atmosphere model for each of the donor stars allowing us to characterise the atmospheres of these stars, and consequently to determine physical parameters such as the $T_{\rm eff}$ or the $\log g$. Finally publicly X-ray light curves have been analysed to study the X-ray emission of the different sources against their orbital periods. As a general conclusion, it seems there is a continuum of properties of these systems more than a strict classification. A combination of factors, of which some of them could be unknown, might be the cause of their different X-ray flux behaviours.

The outline of this thesis is as follows: the scientific context is given in Chapter 1; an overview of the analysis performed for each of the sources of study is presented in Chapter 2; Chapter 3 is dedicated to the description of a pipeline optimised for the reduction of FRODOSpec spectra of obscured red sources (donor stars of the targets of study); Chapters (4, 5 and 6) present the characterisation of the four sources in this thesis, which are different kind of wind-fed systems; and finally general conclusions and future work are given in Chapter 7.

Contents

CHAPTER 1

High Mass X-ray Binaries

The discovery of the first extra-solar X-ray source [Sco X-1; Giacconi et al., 1962] constituted the beginning of X-ray astronomy. Since then, the interest and discoveries related to X/γ-ray astronomy has grown thanks to the ability to send X-ray space missions above the Earth's atmosphere with more than half a million X-ray sources detected up to date.

X-ray binaries (XRBs) are point-like X-ray sources. These systems consist of a compact object – a neutron star (NS) or a black hole (BH) – orbiting a companion, or donor, star from which there is an accretion of material. Following the canonical model, first proposed by Shklovskii [1967], this material is accelerated in the strong gravitational field of the compact star and heated up to $\sim 10^7$ K before being accreted, giving as a result the observed X-ray radiation. The basic division of XRBs into the high-mass (HMXBs) and low-mass (LMXBs) systems refers to the mass of the donor star. The donor star of LMXBs is a low-mass star, with a typical mass of $\lesssim 1\,\mathrm{M}_\odot$, and a spectral type later than B. While the masses of donor stars in HMXBs are normally taken to be $\gtrsim 10\,\mathrm{M}_\odot$, they are hot luminous OB supergiants. There have been detected ~ 300 high energy binary systems in the Milky Way of which $\sim 60\%$ are LMXBs and $\sim 40\%$ are HMXBs [Chaty, 2013].

Most of the compact objects hosting HMXBs [$\gtrsim 60\%$; in't Zand et al., 2007] are known to be pulsars, i.e. rotating NSs (see Fig. 1.1 for an scheme of this kind of system). These pulsars have strong magnetic fields ($\sim 10^{12}$ G) of which magnetic axis is not aligned with its rotational axis (see Fig. 1.2). Therefore, the X-ray radiation coming from the material accreted on to the pulsar is mod-

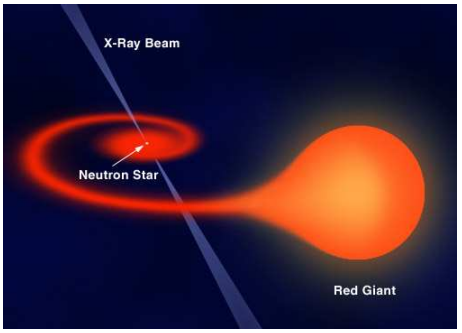

Figure 1.1: Scheme of a HMXB with an rotating NS (© HKU@LCSD).

ulated by the stellar rotation of the pulsar. For a review of this subject, see e.g., Nagase [1989].

This thesis consists of the study of a sample of HMXBs hosting rotating NSs with supergiant companions. The study of these systems has a profound impact in several areas of Physics and Astrophysics:

- NSs are collapsed objects with the highest densities known in the observable Universe. Therefore, measuring their masses is essential to constrain the equation of state (EOS) of nuclear dense matter [e.g., Timmes et al., 1996, Lattimer, 2012, Kiziltan et al., 2013].
- NSs are the final stage of massive stars after their explosion as a Supernovae (SN). Measurements of minimum masses give insights into massive star evolutionary models and on the astrophysical models of core collapse and SN explosions [e.g., Clark et al., 2002, Haensel et al., 2007].
- HMXBs are young systems, so they may act as tracers of star formation [e.g., Grimm et al., 2003, Lutovinov et al., 2005].
- HMXBs are formed and evolve as binary systems. Consequently, their study gives insights into the evolutionary models of binary systems, as well as into the different evolutionary paths of isolated stars compared to those forming part of a binary system [e.g., Langer, 2012, van den Heuvel, 2012].
- When considered as a population, they can provide information on properties of galaxies [e.g., Gilfanov et al., 2004].

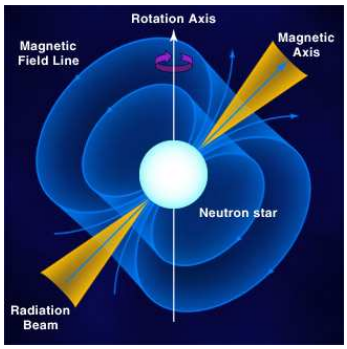

Figure 1.2: Scheme of a pulsar (© HKU@LCSD).

- They are excellent testbeds to study accretion physics and outflows [e.g., Mirabel and Rodríguez, 1999].
- They provide some of the few astrophysical environments for the acceleration of particles and production of very high energy radiation [Aharonian et al., 2005].

Along this Chapter of the thesis I am going to give a description of the donor stars of HMXBs (Sec. 1.1) as well as the compact objects constituting these binary systems (Sec. 1.2), followed by a summary of the interactions between both stars (Sec. 1.3.2). The different types of HMXBs are described in Sec. 1.4 along with the possible explanations for their differences in behaviour, while Sec. 1.5 gives a general outlook of their formation and evolution.

1.1 About the donor star: OB supergiants

A star is born when a cloud of gas and dust collapses to the point when the material in the center of the clump is so dense and hot that the nuclear fusion of H nuclei into He nuclei can occur. The outflow of energy released by these reactions provides the pressure necessary to halt the collapse. The evolutionary phase called main-sequence (MS) can last for billions of years; a star spends most of its life on this phase. During the MS, in the core of the star is taking

place the fusion of H into He. When the H in the core of the star runs out, the energy flow from the core of the star stops. Then the central regions of the star will slowly collapse and heat up. Nuclear reactions in a shell of gas outside the core will provide a new source of energy, and cause the star to expand outward in the "red giant" phase. The most important factor that influences the life of a star on the MS is its own mass. More massive stars have higher temperatures, greater initial luminosities and more energy generation in their cores to provide radiation pressure enough to support their own gravity. To balance their excesses in luminosity and energy generation, the lifetimes of massive stars are shortened significantly compared to solar and lower mass stars.

The difference in colours of the stars corresponds to different surface temperatures. This connection comes from the fact that stellar spectra can be approximated by black-body radiation where the temperature defines the wavelength peak emission (i.e., the colour) according to Wien's Displacement Law

$$\lambda_{\max} = \frac{b}{T}, \tag{1.1}$$

where $b \sim 2.898$ mm K denotes Wien's displacement constant. These temperatures describe a black-body of the same energy output as the observed star [Karttunen et al., 2007], and are called effective temperatures (T_{eff}).

The Harvard Spectral Classification sorts the spectra into different categories according to their T_{eff}, labeled with letters. Ordering them from high to low temperature the sequence reads as:

O–B–A–F–G–K–M–L–T–(Y)[1]

Starting with spectral type O with temperatures between $15000 - 35000$ K and shining bright blue, the sequence goes over yellow G stars, similar to the Sun, with temperatures of ~ 5500 K to the colder reddish M type stars with temperatures around 3000 K [Karttunen et al., 2007].

Additionally, the Yerkes Spectral Classification added luminosity classes to take into account surface gravities, denoted by roman numerals. Six luminosity

[1] Types L and T were added after the discovery of very cold brown dwarfs in the 80s and 90s [e.g., Kirkpatrick, 2005]. While the spectral class Y was proposed by Kirkpatrick et al. [1999], if objects beyond T type stars should be discovered. These Y objects, as predicted by Kirkpatrick et al. [1999], have recently been discovered [see e.g., Cushing et al., 2011, Kirkpatrick et al., 2012].

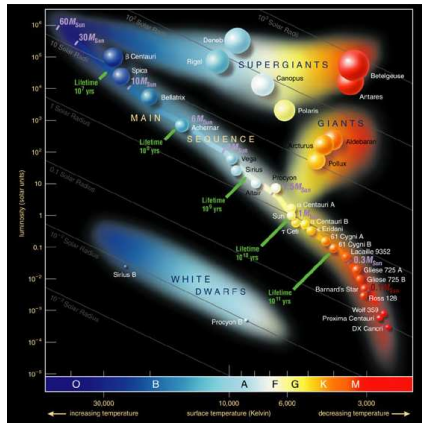

Figure 1.3: HR diagram (© Pearson Education, publishing as Addison Wesley).

classes are defined from Ia, the most luminous supergiants, with the lowest surface gravities, to V, the main sequence of dwarf stars, less luminous and with higher gravity values [Karttunen et al., 2007].

According to these spectral types and luminosities, corresponding to different temperatures and surface gravities that give rise to different spectral features due to the differences in physical environments of the photospheres, stars can be placed on the so-called Hertzsprung–Russell (HR) diagram (Fig. 1.3). This name comes from the combination of the names of their developers: Ejnar Hertszprung and Henry Norris Russell. Since this diagram was built up (1911), it has been used as a classification system to explain stellar types and evolution.

Donor stars in HMXBs are, in most cases, hot luminous OB supergiants, except for the special case of Be X-ray binaries where the donor star is a Be star.

Be stars are non-supergiant fast-rotating B-type and luminosity class III-V stars which at some point of their lives have shown spectral lines in emission, hence the qualifier "*e*" in their spectral types [e.g., Porter and Rivinius, 2003]. They also show an amount of infrared (IR) radiation that is larger than that expected from an absorption-line B star of the same spectral type, an effect known as IR-excess. Both the emission lines and the characteristic strong IR-excess are

attributed to the presence of circumstellar material in a disc-like geometry. The causes that give rise to the disc are not well understood [e.g., Riquelme et al., 2012].

From this point forward I am going to focus on OB supergiant stars, also known as "early-type" supergiants, the donor stars hosting the HMXBs in this thesis. These massive stars have high luminosities. They are hot stars for most of their evolution being powerful cosmic engines.

1.1.1 The life of OB Supergiants

Supergiants are defined as stars of luminosity class I [e.g., Morgan and Keenan, 1973]. This luminosity class indicate the weakest gravities (i.e., largest radii, at a given mass) from gravity-sensitive spectroscopic absorption lines at a given spectral type [e.g., Kudritzki et al., 2008].

During the MS phase, massive stars ($M \gtrsim 8\,M_{\odot}$) the precursors of OB supergiant stars, generate most of their energy in their cores not through the common branch of the *pp* chain[2], but through the CNO cycle, of which most common branch is:

$$
\begin{aligned}
^{12}\mathrm{C} + ^{1}\mathrm{H} &\rightarrow ^{13}\mathrm{N} + \gamma \\
^{13}\mathrm{N} &\rightarrow ^{13}\mathrm{C} + \mathrm{e}^{+} + \nu \\
^{13}\mathrm{C} + ^{1}\mathrm{H} &\rightarrow ^{14}\mathrm{N} + \gamma \\
^{14}\mathrm{N} + ^{1}\mathrm{H} &\rightarrow ^{15}\mathrm{O} + \gamma \\
^{15}\mathrm{O} &\rightarrow ^{15}\mathrm{N} + \mathrm{e}^{+} + \nu \\
^{15}\mathrm{N} + ^{1}\mathrm{H} &\rightarrow ^{12}\mathrm{C} + ^{4}\mathrm{He}
\end{aligned}
$$

The slowest reaction in this cycle is the combination of $^{14}\mathrm{N}$ with $^{1}\mathrm{H}$, reason why N tends to accumulate in the core, and observed in the surface of the star when any mechanism has dredged up the internal, nuclear processed layers: i.e., convection during the red-giant or later phases of evolution, rotational mixing if a star is a rapid rotator, or a heavy mass transfer in a binary system [McSwain, 2004]. Indeed, following the work of Crowther et al. [2006], galactic early B supergiants have on average, [N/C] and [N/O] increased relative to Solar abundances $+1.1$ dex[3] and $+0.8$ dex.

[2] $^{1}\mathrm{H} + ^{1}\mathrm{H} \rightarrow ^{2}\mathrm{H} + \mathrm{e}^{+} + \nu$; $^{2}\mathrm{H} + ^{1}\mathrm{H} \rightarrow ^{3}\mathrm{He} + \gamma$; $^{3}\mathrm{He} + ^{3}\mathrm{He} \rightarrow ^{4}\mathrm{He} + 2\,^{1}\mathrm{H}$.

[3] The name "dex" is a contraction of "decimal exponent". It is a logarithmic unit used in astronomy. One dex equals a factor of 10.

As the massive star evolves, the conversion of H into He increases the molecular weight. This fact rises the interior temperature leading to the enhancement of the star luminosity throughout its MS lifetime [McSwain, 2004].

For the case of fast-rotating stars the support of gas pressure is less important. They begin their MS phase at lower luminosities and $T_{\rm eff}$ compared to those non-rotating stars of the same mass. In these stars, rotational mixing takes place enriching the He and N abundance in the envelope, decreasing its opacity, and thus, they are over-luminous for their masses [e.g., Heger and Langer, 2000, Maeder, 2009, Langer, 2012].

At near solar metallicity, most current massive star evolution models predict that after core H exhaustion, stars below the LBV limit[4] expand all the way, leave the MS phase and, reach the red supergiant stage (RSG) with a cooler temperature [Brott et al., 2011].

During this process, the core suffers a contraction and the central temperature rises giving way to He burning that stops this core contraction. This He burning takes place through the 3α process:

$$^{4}\mathrm{He}+^{4}\mathrm{He}\leftrightharpoons{}^{8}\mathrm{Be}$$
$$^{8}\mathrm{Be}+^{4}\mathrm{He}\rightarrow{}^{12}\mathrm{C}+\gamma$$

And, as the abundance of ^{12}C grows in the core, the reaction

$$^{12}\mathrm{C}+^{4}\mathrm{He}\rightarrow{}^{16}\mathrm{O}+\gamma$$

takes over and both ^{4}He and ^{12}C became depleted. The reaction

$$^{16}\mathrm{O}+^{4}\mathrm{He}\rightarrow{}^{20}\mathrm{Ne}+\gamma$$

then begins, but further reactions beyond ^{20}Ne are rare in the core.

As the energy released per unit of mass in these reactions is ~ 10 less than in the CNO cycle, He burning occurs at a faster rate to maintain the higher luminosity of the star [McSwain, 2004].

He core burning ends when all of the He has been processed, but it continues in a shell surrounding the core. Similar to the end of the MS, the He burning

[4] LBV≡Luminous Blue Variables, luminous, hot, unstable supergiants associated with stars near their Eddington limit that suffer irregular eruptions [e.g., Nota and Lamers, 1997].

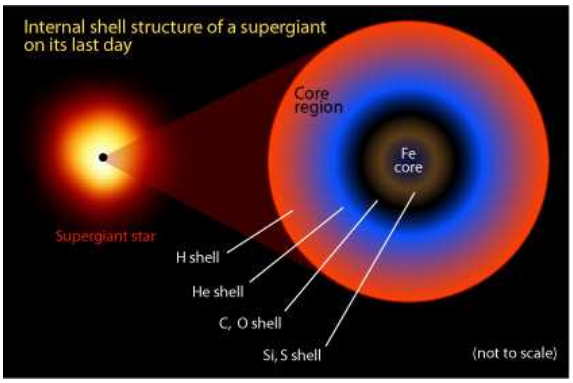

Figure 1.4: Internal shell structure of a supergiant star on its last day. Successive internal layers have different temperatures, with the inner layers being hotter than the outer ones. Different layers contain different elements produced by fusion, with a dense core of iron at the centre. (© Australia Telescope Outreach and Education).

shell increases the mass of the core. The core then contracts, and the star luminosity increases, taking it up the HR diagram in the so-called asymptotic giant branch [Ostlie and Carroll, 1996]. The outer envelope of the supergiant now reaches deeper and both CNO and 3α processed material appear at the stellar surface.

The stars will continue with faster and faster cycles of core burning followed by contractions with concentric shells of lower mass elements burning above the core in an "onion skin model" (Fig. 1.4). Fusion can not progress beyond Fe in the cores of stars because the binding energy released by further fusion is negative, so these reactions would deplete the energy of the star rather than generating energy.

Therefore, after having finished burning its nuclear fuel, the star undergoes a SN explosion through an iron-core collapse, one of the most violent releases of energy in the Universe. During this phenomena, the core of the star is compressed to very high densities, resulting in a NS, the most compact star in the observable Universe (Sec. 1.2). While the outer layers, or external shells, produce a final splash of photons, kinetic energy, and newly synthesized chemical elements to the surrounding medium giving rise to the so-called SN Remmants. This process is a key agent in stimulating the interstellar medium of

star-forming galaxies, driving their evolution throughout the history of the Universe [Mac Low et al., 2005].

The process described above occurs for massive stars with $M \lesssim 25\,\mathrm{M}_\odot$, it means the $\sim 80\%$ of massive stars. At solar-metallicities, stars between ~ 30 and $\sim 40\,\mathrm{M}_\odot$ suffer a mass loss during the RSG that might be sufficient to strip the external layers deeply enough to become a Wolf-Rayet (WR[5]) star [e.g., Ekström et al., 2013]. Stars with masses between 30 an $40\,\mathrm{M}_\odot$ can possibly (but not necessarily) go through RSG, LBV and WR; and stars above $40\,\mathrm{M}_\odot$ go through LBV and WR phase [e.g., Meynet et al., 2011]. Supernovae collapse occurs at the end of all of them independently of their initial masses. However this collapse is different [see Sec. 1.2, and Smartt, 2009] depending on their evolutionary path.

The post-MS evolution of massive single stars is little understood. Not only their mass and metallicity, but also its rotation is an important ingredient in their evolution [e.g., Maeder, 2009, Meynet et al., 2011, Ekström et al., 2013].

1.1.2 Stellar winds of Supergiants

These luminous red supergiant stars have low surface gravities, and are known to suffer great mass loss in the form of a radiation-driven stellar wind [see Kudritzki and Puls, 2000, for a review]. Material is accelerated outwards from the stellar atmosphere to a final velocity v_∞ according to a law that may be approximated as

$$v_w = v_\infty \left(1 - \frac{R_*}{r}\right)^\beta \tag{1.2}$$

where R_* is the radius of the star and β is a factor generally lying in the interval $\sim 0.8 - 1.2$.

Under these circumstances, high wind velocities (supersonic) are reached at a moderate height above the surface of the star (for example, for $\beta = 1.0$, $v_w(2R_*) = 0.2v_\infty$, i.e., $1000\,\mathrm{km\,s^{-1}}$). These strong stellar winds plow supersonically through

[5] WR stars are named after Wolf and Rayet [1867] who identified three stars in Cygnus with strong broad emission lines instead of narrow absorption lines. These stars typically have wind densities an order of magnitude higher than massive O stars. They show at their surfaces the products of H-burning and the 3α process. For a review of this kind of stars see Crowther [2007].

the surrounding medium, and may be enhanced by pulsations or eruptions during advanced evolutionary stages, when the wind may also become enriched in elements synthesized in the stellar interior.

These winds are highly structured with the presence of large-scale (quasi)-cyclical structures that may be induced by instabilities generated by the star itself [see e.g., Kaper and Fullerton, 1998]. Theory also predicts the existence of smaller-scale stochastic structure, caused by the appearance of shocks in the wind flow directly related to its intrinsic instability. These structures caused by shocks decelerate and compress rarefied gas, collecting most of the mass into a sequence of dense clumps bounded by shocks dominating the wind structure beyond $r \gtrsim 3R_*$ [e.g., Runacres and Owocki, 2002] and perhaps much closer to the stellar surface [Puls et al., 2006]. The observed stochastic variability on short time scales of $\mathrm{H}\alpha$ profiles in O-type stars is consistent with the predictions of wind models with cumpling [Markova et al., 2005]. Thus, the approximation of a smooth wind of constant density must be considered unrealistic.

1.2 About the compact object: Neutron stars

All the compact components of the sources of study in this thesis are NSs, the most compact stars in the observable Universe. The phrase "neutron star" appeared in the literature for the first time in Baade and Zwicky [1934].

NSs were given this name because their interior is largely composed of neutrons. They have a typical mass of $M \sim 1-2\,\mathrm{M}_\odot$, and a radius ranging between ~ 10 and 14 km. Therefore, the mass density ρ, in such a star is $\sim 10^{15}$ g cm^{-3}, which is 3 times normal nuclear density[6]. Such matter cannot be obtained under laboratory conditions, and its properties and even composition remain to be clarified. [e.g., Lattimer and Prakash, 2004, Potekhin, 2010, Lattimer, 2012].

An upper mass limit for NSs of $\sim 3.4\,\mathrm{M}_\odot$ was predicted by Tolman [1939] and Oppenheimer and Volkoff [1939] following the work of Chandrasekhar [1931]. Since then, continuing discussion on the mass range a NS can attain has spawned a vast literature [e.g., Thorsett and Chakrabarty, 1999, Baumgarte et al., 2000, Schwab et al., 2010, Lattimer, 2012, Kiziltan et al., 2013] due to its implications in Physics and Astrophysics.

[6] The typical density of a heavy atomic nucleus is $\rho \sim 2.7 \times 10^{14}$ g cm^{-3}.

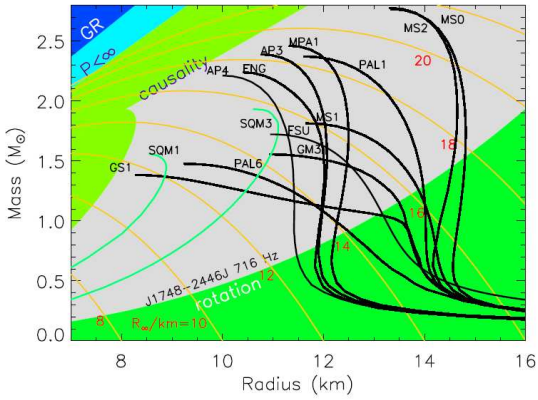

Figure 1.5: Figure 2 of Lattimer [2012] representing mass to radius diagram showing the predictions of different EOS. The different models are labeled according to Lattimer [2012], who states in his original caption: "Typical $M - R$ curves for hadronic EOS (*black curves*) and strange quark matter (SQM) EOS (*green curves*). The EOS names are given in Lattimer and Prakash [2001]. Regions of the $M - R$ plane excluded by General Relativity (GR), finite pressure, and causality are indicated. The orange curves show contours of $R_\infty = R/\sqrt{1 - 2GM/Rc^2}$. The region marked rotation is bounded by the realistic mass-shedding limit for the highest-known pulsar frequency, 716 Hz, for PSR J1748–2446 [Hessels et al., 2006]".

A NS is a possible end product of the death of a heavy star (Sec. 1.1 and Fig. 1.6) with $M \gtrsim 8\,\mathrm{M}_\odot$. After the SN explosion the core of the star is compressed gravitationally to very high densities giving as a result the "core-collapse SN", forming a NS in the Central SN Remnant, or a BH in the case of the core having a mass above the maximum limit [$\sim 3\,\mathrm{M}_\odot$, Oppenheimer and Volkoff, 1939] where the compression cannot be stopped. Therefore, masses at birth of NSs are tuned by the intricate details of the astrophysical processes that drive massive stellar evolution, core collapse and SN explosions [e.g., Timmes et al., 1996, Haensel et al., 2007, Schwab et al., 2010, Potekhin, 2010].

NS masses lower than $1.2\,\mathrm{M}_\odot$ would challenge the paradigm of gravitational-collapse NS formation. Iron cores of $8 - 10\,\mathrm{M}_\odot$ progenitors stars have $M \sim 1.25\,\mathrm{M}_\odot$, and the lowest mass NS may form from such progenitor. While accord-

ing to thermodynamics NS have a minimum gravitational mass $\sim 0.9 - 1.2\,M_\odot$ since masses smaller than this minimum are dynamically unstable and cannot lead to NS [Lattimer, 2012]. There are two interesting candidates of low mass NSs below the limit of $1.2\,M_\odot$, SMC X–1 and 4U 1538–52, both of them XRBs with $1-\sigma$ upper limits to mass of $1.122\,M_\odot$ and $1.1\,M_\odot$ respectively [Rawls et al., 2011].

The maximum mass of a NS delineates the low mass limit of stellar mass BHs, and combined with measurements of NS radii, it also provides a distinctive insight into the structure of matter at supranuclear densities. Different assumptions on the behaviour of matter under these extrem conditions have been put forward resulting in different EOS (see Fig. 1.5) [e.g., Lattimer and Prakash, 2001, 2004, Lattimer, 2007, 2012]. Observations can help distinguish between different models.

The largest NS mass measured up to date corresponds to the value of $2.4\,M_\odot$. Two XRBs have NSs with this mass value, 4U 1700–377 [Clark et al., 2002] and PSR B1954+20 [van Kerkwijk et al., 2011], although the large systematic errors of these values claim caution. According to modern theory the maximum value for a NS mass is $\sim 2.5\,M_\odot$, which is compatible with the observational results (this maximum value depends on the EOS used [see Fig. 1.5, Potekhin, 2010, Lattimer, 2012].

Only 33 relatively precise NS masses are available with a total of 65 measurements, while ~ 2000 objects have been detected as pulsars (`http://www.atnf.csiro.au/people/pulsar/psrcat/`). This small number of measurements is due to the difficulties in determining the masses in an independent way. XRBs provide one of the few possible ways of such measurements through the mass function of the optical component of the binary system. Indeed, 23% of the 65 values come from XRBs [Lattimer, 2012].

Most NS masses lie close to 1.3 to $1.4\,M_\odot$. In particular, the XRBs NS mass distribution peaks at $\sim 1.4\,M_\odot$, which is considered as a canonical mass. The available data suggest that these NSs have radii near 10 km. An important fact is that the estimates of the EOS from astrophysical observations are converging with those from laboratory studies [Lattimer, 2012].

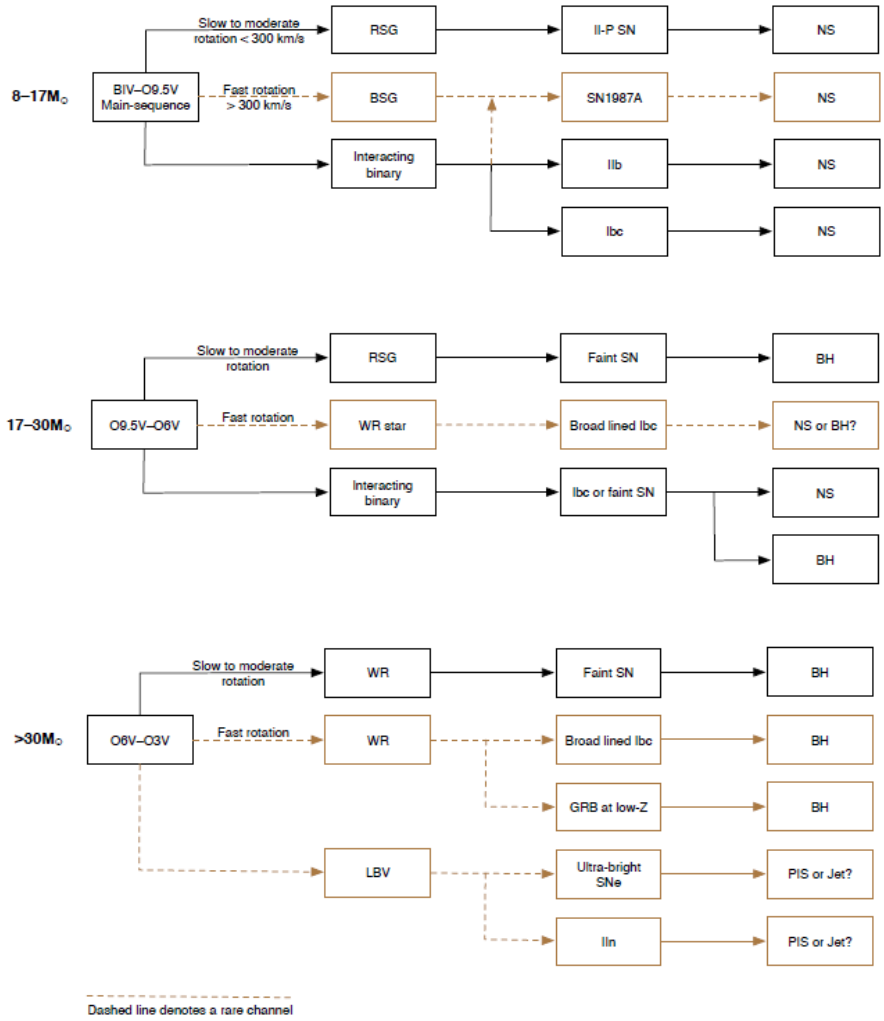

Figure 1.6: A summary diagram of the likely evolutionary scenarios and end states of massive stars [Fig. 12 of Smartt, 2009]. Different types of Supernovae are classified by the appearance of their optical spectra.

1.3 Interaction mechanisms

The interactions between the stars in a binary system influence the evolution of the system as a whole in addition to the evolution of the individual components. This interaction consists basically of the tidal effects and the mass transfer. The X-ray radiation observed is a consequence of this interaction added to the extreme gravitational effect of the NS.

1.3.1 Tidal effects: Orbital circularisation

Tidal forces are supposed to cause the rotational velocity of the stars to match the orbital angular velocity of the system, in other words, synchronous rotation. In addition, the eccentricity will decrease, causing their elliptical orbit to circularise. According to Hilditch [2001], the time scales for the synchronization and circularisation processes are:

$$t_{\rm sync} \simeq 10^4 \frac{1+q}{2q} P_{\rm orb}^4 \text{ years, and} \tag{1.3}$$

$$t_{\rm circ} \simeq \frac{10^6}{q} \left[\frac{1+q}{2}\right]^{5/3} P_{\rm orb}^{16/3} \text{ years,} \tag{1.4}$$

where P is the orbital period in days and the mass ratio of the system is

$$q = \frac{M_A}{M_B} \leq 1. \tag{1.5}$$

Consequently, the initial orbital period of the binary is critical to understand the interaction between both stars and thus their evolution.

1.3.2 Mass transfer: Accretion

The accretion process is a transfer of mass from the donor star (supergiant) to the compact object (NS). The kind of process taking place in each system depends basically on the spetral type, the mass of the donor star and the orbital separation of the binary system. The gravitational energy is the driving force for accretion in all of them. Therefore, the shape and structure of the gravitational potential in a binary system have to be taken into account.

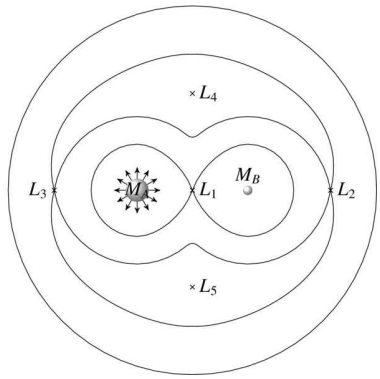

Figure 1.7: Figure 2 of de Val-Borro et al. [2009] representing the Roche potential on the orbital plane showing the location of the Lagrangian points for a mass ratio $q = 1$.

Gravitational potential in a binary system: Roche-lobe

The theoretical description of the gravitational potential in a binary system is found in the studies of the French mathematician Eduard Albert Roche (1820–1883). The gravitational potential, known as Roche potential, of two point masses M_A and M_B in a circular Keplerian orbit around their center of mass, takes the following form in the corotating frame of reference [Frank et al., 2002]:

$$\Phi(r) = -\frac{GM_A}{|\vec{r} - \vec{r_A}|} - \frac{GM_B}{|\vec{r} - \vec{r_B}|} - \frac{1}{2}(\vec{\omega} \times \vec{r})^2, \tag{1.6}$$

where $\vec{r_A}$ and $\vec{r_B}$ are the position vectors of the center of the two stars, and $\vec{\omega}$ is the angular velocity of the binary system. The first two terms in the equation represent the gravitational potential of each component and the last term the influence of the centrifugal force.

Fig. 1.7 shows the equipotential surfaces of the Roche potential in the binary orbital plane for a binary system with a mass ratio $q = M_A/M_B = 1$. The Roche-lobe is defined as the volume surrounding an object within which material is gravitationally bound to this object. In a binary system each of the stars has its own Roche-lobe, and the two Roche-lobes together are the equipotential surfaces forming the inner-most "eight-like" solid line of Fig. 1.7. The shape of this combination of both Roche-lobes depends on the orbital separation and its size is given by the mass ratio q ($q = 1$ in this case). The equilibrium points, where

the total gravitational force vanishes, are called Lagrange points ($L_1 - L_5$). If material from the donor star reaches the saddle point L_1 having momentum in the outward direction, it can enter the Roche-lobe of the compact object. A similar mass transfer can happen for matter crossing the L_2 point inwards.

Binaries are classified into three categories depending of their size with respect to their Roche-lobe:

- *Detached systems:* The radii of both stars are well within their Roche-lobes.
- *Semi-detached systems:* One of the stars fills its Roche-lobe.
- *Contact systems:* Both stars are filling their Roche-lobes and possibly sharing a common envelope.

Accretion mechanisms in HMXBs

There are three mechanisms known by which mass transfer can proceed in a HMXB:

- **Roche-lobe overflow:**
  It occurs when the donor star reaches or exceeds its Roche-lobe and, so, starts an overflow of matter through the inner L_1 point to the compact object (it is a *semi-detached* system). The accretion of material in this kind of systems is such that it is accumulated in a disc surrounding the NS that is so-called *accretion disc*. This kind of interaction occurs mainly in LMXBs, although it also appears in persistent HMXBs [e.g., Negueruela, 2010]. When the *accretion disc* is surrounding the NS, there is a transfer of angular momentum from the disc to the NS that produces changes in its spin period [see e.g., González-Galán et al., 2012].

- **Be emission mechanism:**
  It is a special case for Be X-ray Binaries. The donor star in these systems is a Be star (for details see Sec. 1.1) with a circumstellar disc. In the simplest picture when the NS passes through this circumstellar disc, the mass is transferred from the donor star to the NS [see e.g., Okazaki and Negueruela, 2001, Negueruela et al., 2001, Reig, 2011, for a detailed explanation].

– **Stellar wind accretion:**
  There is a mass ejection in the form of a wind from the donor star that reaches the Roche-lobe of the compact object. This mass transfer can either be directly via L_1, or the stellar wind may loose its kinetic and angular momentum in the neighbourhood of L_2.

The HMXBs in this thesis do not fill their Roche-lobe, but host luminous OB stars that have powerful winds. Consequently, their accretion is through stellar wind accretion (for more details on stellar wind accretion see Sec. 1.3.4).

1.3.3 X-ray production and Eddington limit

The first who suggested that accretion of matter towards a NS in a binary system could produce an X-ray source were Zel'dovich and Novikov [1964]. The potential energy of the accreted material falling down the deep gravitational field of the NS is transformed into kinetic energy and heated up to $\sim 10^7$ K due to collisions before reaching the surface of the compact object, thus producing the X-ray radiation observed [e.g., Shklovskii, 1967]. Consequently:

$$L_{\rm X} \propto \zeta \frac{dM}{dt}, \tag{1.7}$$

where $\frac{dM}{dt} = \dot{M}$ is the accretion rate, and ζ is the efficiency factor for converting potential energy into radiation.

There is a limit to the accretion rate ($\dot{M}$), as soon as the radiative pressure on the material exceeds the gravitational force. Assuming spherical symmetric accretion of a fully ionized H plasma, the main radiative pressure will be exerted on the material via Thomson scattering of the photons by the electrons, of which scattering cross-section $\sigma_{\rm T}$ is a factor of $\sim 10^8$ larger than for protons [Frank et al., 2002]. The main gravitational force is exerted on the more massive protons with mass $m_{\rm p}$. Through electromagnetic coupling, electrons and protons appear as closely connected pairs, so that the Eddington luminosity is reached at equilibrium between the radiative pressure on the electrons and the gravitational force on the protons [Frank et al., 2002]:

$$\frac{L\sigma_{\rm T}}{4\pi r^2 m_{\rm p} c} = \frac{GM_{\rm X}}{r^2}, \tag{1.8}$$

where $M_{\rm X}$ is the mass of the NS, and r is the distance to the center of the star.

Therefore, the Eddington luminosity can be written as:

$$L_{\rm Edd} = \frac{4\pi G M_{\rm X} m_{\rm p} c}{\sigma_{\rm T}} \simeq 1.3 \times 10^{38} \left(\frac{M}{M_\odot}\right) {\rm ergs}^{-1}, \tag{1.9}$$

which is about an order of magnitude higher than observed in flares from HMXBs.

Following this reasoning, for $L_{\rm X} \gtrsim L_{\rm Edd}$, the outward pressure of radiation would exceed the inward gravitational attraction and the accretion would be halted. However, as NSs are highly magnetised and the accreted material is ionised, accretion does not happen in a spherically symmetric way, it is collimated onto the magnetic poles of the NS. Therefore, finding sources with luminosities above the Eddington limit is not in contradiction with the theory as long as this value is only valid for spherical symmetric accretion.

1.3.4 The theory of wind accretion

The classical Bondi-Hoyle-Lyttleton accretion [see Edgar, 2004, for a review] represents an approximation of the accretion process when the wind velocity (v_w) of the donor star[7] is much higher than the orbital velocity ($v_{\rm orb}$) of the NS[8]. In this approximation, the accretion rate ($\dot{M}$) of a NS immersed in a fast wind is governed by its accretion radius [9] given by

$$r_{\rm acc} \propto \frac{2GM_{\rm X}}{v_{\rm rel}^2}, \tag{1.10}$$

where the relative velocity of the accreted material with respect to the NS is $v_{\rm rel}^2 = v_w^2 + v_{\rm orb}^2$. For typical values of the wind velocity, $r_{\rm acc} \sim 10^8$ m, decreasing by a factor of a few from $r = 2R_*$ to $r = 10R_*$.

The accretion rate is then:

$$\dot{M} = 4\pi \left(GM_{\rm X}\right)^2 \frac{v_w\left(r\right)\rho\left(r\right)}{v_{\rm rel}^2}, \tag{1.11}$$

[7] For early supergiant stars it can reach supersonic values $v_w(2R_*) \sim 1000\,{\rm km\,s^{-1}}$ (see Sec. 1.1.2).

[8] In these systems: $v_{\rm orb}(2R_*) \sim 200\,{\rm km\,s^{-1}}$.

[9] Accretion radius of a NS≡The maximum distance at which the gravitational potential of the NS well can deflect the stellar wind and focus the out-flowing material towards itself.

where $\rho(r)$ is the wind density. If we assume a certain efficiency factor in the transformation of gravitational energy into X-ray luminosity, the X-ray luminosity will be proportional to

$$L_{\mathrm{X}} \propto \dot{M} \sim \frac{\rho(r)\, v_w(r)}{v_{\mathrm{rel}}^4}. \tag{1.12}$$

This dependency means that, in this approximation, the X-ray luminosity of a NS in a circular orbit is constant. In an eccentric orbit, the luminosity varies with orbital phase. Different systems differ in their orbital parameters and wind properties leading to different X-ray light curve behaviours (persistent, transient, etc.).

The overall behaviour of persistent X-ray source is well reproduced by this simple model [Negueruela, 2010]. However, detailed analysis of the X-ray light curves of HMXBs, the highly structured wind of the donor stars, the impact of the X-ray radiation on the wind, etc., provide strong evidence for a much more complex physical situation.

Moreover, NSs in these systems have strong magnetic fields ($\sim 10^{12}$ G). Thus, as material approaches the NS, it is captured by the magnetic field and deflected along the magnetic field lines. In addition, this magnetic field has an effect on the accretion of material in the form of a balance between the strength of the magnetic field itself and the ram pressure of the incoming material [e.g., Bozzo et al., 2008]. This incoming material could be stopped at the magnetosphere if the ram pressure is low (compared to the magnetic field), and the NS may be then in the propeller regime [Illarionov and Sunyaev, 1975] and the accretion centrifugally inhibited.

One of the latest models related to the wind accretion mechanisms is the quasi-spherical accretion proposed by Shakura et al. [2012]. This model accepts the classical Bondi-Hoyle-Lyttleton accretion for supersonic winds, and explains accretion from subsonic winds by a quasi-static shell that forms above the magnetosphere from which the NS can accrete via instabilities [e.g., Shakura et al., 2012, 2013, 2014].

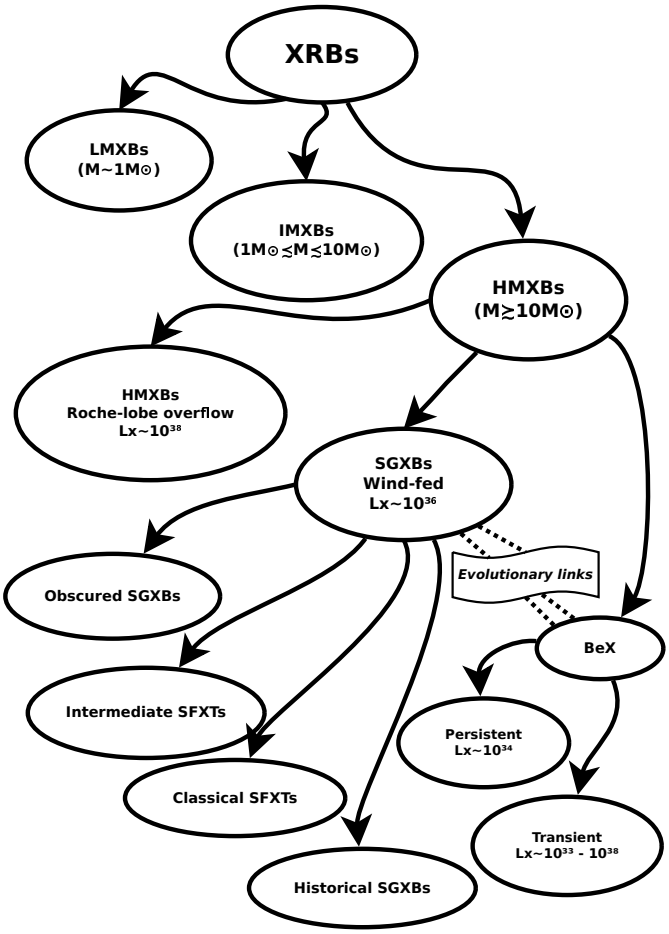

Figure 1.8: Current classification of X-ray binaries.

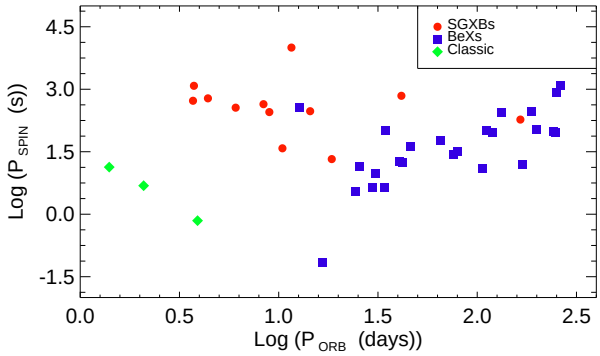

Figure 1.9: The $P_{\rm spin}/P_{\rm orb}$ (Corbet's) diagram for a large sample of HMXBs. "Classical" HMXBs are fed through localised Roche-lobe overflow and have very short spin periods. Be/X-ray binaries show a moderately strong correlation between their orbital and spin periods [Corbet, 1984]. Wind-fed systems have long spin periods, uncorrelated to their orbital period.

1.4 Classification of HMXBs

Based on the type of the optical star, the accretion mechanisms taking place, and their X-ray behaviour, HMXBs are further classified into several subgroups (see Fig. 1.8 for a detailed scheme of the classification).

Corbet [1986] found that the position of an object in the spin period vs. orbital period ($P_{\rm spin}/P_{\rm orb}$) diagram (see Fig. 1.9) correlates with other physical properties, allowing the definition of meaningful three subgroups that have been divided in sub-subgroups along time with the discovery of new sources. These sub and sub-subgroups are described throughout this section.

1.4.1 Roche-lobe overflow HMXBs

A few objects with very close orbits and short spin periods are observed as very bright ($L_{\rm X} \sim 10^{38}\,{\rm erg\,s}{-1}$) persistent X-ray sources, with clear evidence for an accretion disc. Their NSs are spinning up most of the time, because angular momentum is transferred with the accreted material [Negueruela, 2010].

1.4.2 Be X-ray Binaries

Be X-ray binaries (BeXBs) are systems with a Be star counterpart (see Sec. 1.1 for details of a Be star). In these systems, material from a circumstellar disc is accreted onto the compact object.

Most BeXBs have relatively wide orbits ($P_{\rm orb} \gtrsim 20$ d), with moderate to large eccentricities [$e \gtrsim 0.3$; Reig, 2011], and the compact companion spends most of its time far away from the disc surrounding the Be star [van den Heuvel and Rappaport, 1987]. In consequence, they are transient sources, that show very low X-ray fluxes in quiescence [$L_{\rm X} \lesssim 10^{33}$ erg s^{-1}; e.g., Campana et al., 2002], with the outbursts ,reaching X-ray luminosities close to the Eddington limit for a NS ($L_{\rm X} \sim 10^{38}$ erg s^{-1}), often occurring at regular intervals, separated by the orbital period, and generally close to periastron [e.g., Okazaki and Negueruela, 2001, Negueruela et al., 2001].

Persistent BeXBs also exist [Reig and Roche, 1999]. These persistent systems show much less X-ray variability and lower luminosities [$L_{\rm X} \lesssim 10^{35}$ erg s^{-1}; Reig, 2011].

BeXBs populate a rather narrow region of the $P_{\rm spin}/P_{\rm orb}$ diagram (see Fig. 1.9). This correlation between $P_{\rm spin}$ and $P_{\rm orb}$ [found for the first time by Corbet, 1984] is believed to be connected to some physical equilibrium between the spin down of the NSs when they are not accreting and their spin up during outbursts, indicative of the formation of transitory accretion discs [e.g., Wilson et al., 2008].

1.4.3 Supergiant X-ray Binaries

Wind-fed HMXBs are systems mostly composed of an OB supergiant donor star and a long-$P_{\rm spin}$ NS, known as Supergiant X-ray Binaries (SGXBs).

In SGXBs, the compact star interacts with the strong stellar wind of the supergiant producing the persistent X-rays observed in these systems [with typically $L_{\rm X} \sim 10^{36}$ erg s^{-1}; Nagase, 1989] with occasional flaring variability on short time scales (seconds), but rather stable in the long run. Almost all these systems are X-ray pulsars, and orbital solutions exist for most of them. They have orbital periods ranging from $\gtrsim 3$ d to ~ 15 d and present circular or low-eccentricity orbits [e.g. Negueruela et al., 2008c], with the single exception of

GX 301−2, powered by a B1.5 Ia$^+$ hypergiant. Many of them display eclipses of the X-ray source.

Over the last years there has been a huge increase in the number of HMXBs known of which properties differ from the "historical" SGXBs. While the number of sources increases it becomes clearer that the separation among them is not well defined, there is a kind of continuum in properties along the different types of SGXBs [e.g., Walter and Zurita Heras, 2007, Negueruela et al., 2008c]. Hereafter I give an overview of these "new" systems and possible explanations to their different behaviour.

Obscured SGXBs

An example of obscured or absorbed SGXB is IGR J16318/-4848 discovered by Courvoisier et al. [2003] exhibiting an unusually high level of absorption in X-rays and a strong intrinsic absorption in the optical [Chaty, 2013]. This led Filliatre and Chaty [2004] to suggest that the material absorbing in X-rays was concentrated around the compact object, while the one absorbing in optical/infrared was surrounding the whole system.

Further mid-infrared (MID) observations also suggest that there is a dense and absorbing circumstellar material envelope surrounding the whole binary system like a cocoon of dust, creating a persistent and luminous X-ray emission together with a high absorption in the optical and a MID excess [Chaty, 2013].

Classical Supergiant Fast X-ray Transients

One relatively recent discovery in this field is the existence of systems having X-ray fast transient phenomena, generally with a steeper rise and a slower decay of the X-ray flux of several orders of magnitude, and lasting from minutes up to a few hours [Sguera et al., 2006]. Fast transients have always been identified with supergiant companions [e.g. in't Zand, 2005, Negueruela et al., 2006a, Blay et al., 2012], leading to the definition of the Supergiant Fast X-ray Transients [SFXTs, Negueruela et al., 2006b] as a sub-class of SGXBs. SFXTs spend most of their time at X-ray luminosities between $L_{\rm X} \sim 10^{32}$ to 10^{34} erg s^{-1}, well below the "normal" X-ray luminosity of SGXBs, with very brief excursions to outburst luminosities of up to a few times 10^{36} erg s^{-1} [e.g. Rampy et al., 2009, Sidoli et al., 2009, Sidoli, 2012]. The typical X-ray variability factor is $\lesssim 20$ in

SGXBs while it is $\gtrsim 100$ in SFXTs [Walter and Zurita Heras, 2007]. The underlying mechanism that produces the fast X-ray outburst in SFXTs is still not well understood.

A number of hypothesis have been put forward to explain the different behaviour in SFXTs from "normal" SGXBs. Some of the models proposed invoke the structure in the wind of the supergiant companion that could produce sudden episodes of accretion onto the compact component. This structure could be either in the form of clumping in a spherically symmetric outflow from the supergiant donor [in't Zand, 2005, Walter and Zurita Heras, 2007, Negueruela et al., 2008c, Zurita Heras and Walter, 2009, Blay et al., 2012], or in the form of an equatorial density enhancement in the wind from the supergiant, inclined at some angle to the orbit of the NS [Romano et al., 2007, Sidoli et al., 2007]. Another possible explanation is the existence of an eccentric orbit which could lead the NS to cross zones of large and variable absorption [Negueruela et al., 2008c, Blay et al., 2012]. Of course, a clumpy spherical wind can exist together with an eccentric orbit [Blay et al., 2012]; this scenario would also explain the quasi-stable X-ray luminosity of SGXBs, since they have circular orbits. Furthermore, Bozzo et al. [2008] proposed a model that makes use of transitions between accretion gating mechanisms, such as centrifugal and magnetic barriers, brought about by variations in the stellar wind, to explain the large dynamic range in flux observed in this systems. Ducci et al. [2010] have proposed a scenario that links all these mechanisms.

Recent theoretical considerations [e.g. Oskinova et al., 2012] and observations [e.g. Sidoli et al., 2013] strongly suggest that wind clumpiness is not the only explanation for the flaring behaviour, leading to the widespread idea that some "gating" mechanism mediates the accretion onto the NS. Proposed mechanisms include a magnetic barrier that prevents direct accretion [subsonic propeller regime; Doroshenko et al., 2011] and a switch in the polar beam configuration due to a variation in the optical depth of the accretion column [Shakura et al., 2013]. The recently proposed "accumulation mechanism" [Drave et al., 2014], which may be a natural consequence of quasi-spherical accretion and the changes in accretion configuration described by Shakura et al. [2013], seems to be an excellent candidate for this gating process, as it removes the need for the accreting objects in all SFXTs to be magnetars [e.g., Bozzo et al., 2008, Grunhut et al., 2014].

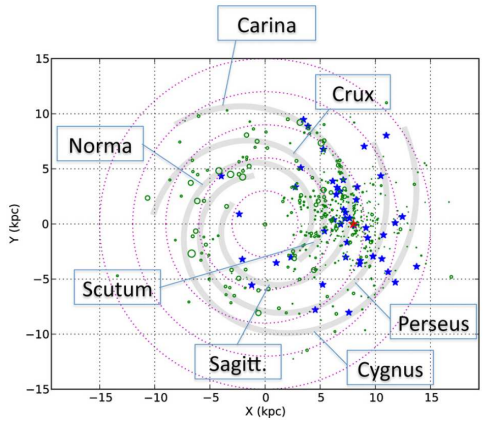

Figure 1.10: Figure from [Coleiro and Chaty, 2013], who state in their original caption: "Distribution of HMXBs (blue stars) and distribution of star formation complexes (green circles). The circle radius represent the different excitation parameter value. The spiral model from Russeil [2003] is also plotted and the red star represents the Sun position at 8 kpc from the Galactic center."

Intermediate Supergiant Fast X-ray Transients

Intermediate SFXTs exhibit a higher X-ray luminosity and a lower variability factor with longer flares than classical SFXTs [Smith et al., 2012]. These sources represent a link between SFXTs where the X-ray emission is completely dominated by flaring, and the persistent and brighter canonical SGXBs.

1.5 Formation and evolution of HMXBs

According to statistical analysis of the Galactic distribution of XRBs, the stellar birth place is very important in their formation [e.g., Koyama et al., 1990, Lutovinov et al., 2005, Dean et al., 2005, Bodaghee et al., 2012]. These works show that LMXBs are concentrated within the galactic bulge, while HMXBs, under-abundant in the central kpc, are spread over the whole Galactic plane, confined in a disc, exhibiting an uneven distribution, preferentially towards the tangential directions of the spiral arms (see Fig. 1.10). This spatial distribution was expected, because LMXBs are constituted of companion stars belonging to old stellar population, while HMXBs containing young companion stars, re-

main close to their stellar birth-site, and hence should theoretically follow the passage of the wave density associated with the rotation of the spiral arms [Lin et al., 1969], inducing a burst of stellar formation.

1.5.1 Overview of the formation picture

HMXBs exist due to the large-scale mass transfer that occurs during the evolution of a close binary system prior to the SN explosion in which the compact star was formed [e.g., van den Heuvel and Heise, 1972, Tutukov and Yungelson, 1973]. Thanks to this mass transfer the more evolved component –which initially was the more massive one– will transfer its H-rich envelope to its companion before it explodes as a SN, becoming the less massive component of the system ("Algol paradox"[10]). Simple celestial mechanics shows that the explosive mass ejection from the less massive component of a binary does not disrupt the system [Blaauw, 1961], but imparts it with a runaway velocity as well as with a high eccentricity.

During the close binary phase, the more massive star –the one that ends up first as a SN– transfers material to the less massive star. Therefore, the less massive may appear as an enriched star for its mass. Consequently, higher abundances could appear for supergiants in HMXBs than for isolated ones.

Figure 1.11 shows a rough outline of the evolution of a massive binary with initial components of $20M_{\odot}$ and $8M_{\odot}$ up to the X-ray binary phase taken from van den Heuvel [1976]. In this scheme conservation of mass and orbital angular momentum during mass transfer phases is assumed, which is, of course, a rather crude assumption. The conservation of these parameters depends on the binary configuration and the evolutionary status of the donor star. Some authors, such as Wellstein et al. [2001] or Petrovic et al. [2005] have developed studies about non-conservative evolutionary models.

After the first phase of mass transfer the system consists of an He star –which is the residual core of the previous massive star– and a massive MS star –the original secondary that received the H-rich envelope of its companion–. Massive He stars are identified with the WR, which in many cases are members of close binaries that are direct progenitors of the HMXBs [e.g., van den Heuvel,

[10] The "Algol paradox" is a reversal of the mass ratio of the binary system, in which the more massive star in a binary appears less evolved than its companion [Hilditch, 2001].

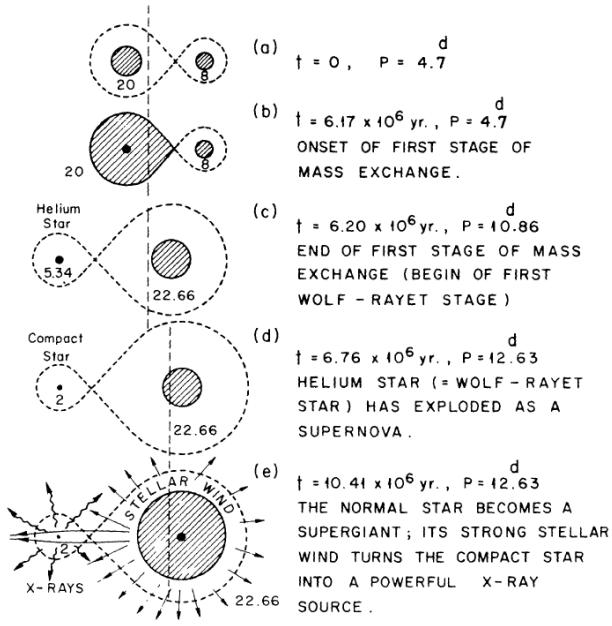

Figure 1.11: Outline of the evolution of a massive close binary into a HMXB [van den Heuvel, 1976]. Numbers near the stars indicate masses in solar masses.

1973]. Due to the sudden explosive mass loss, the center of mass is accelerated and the system becomes a runaway star. After this, it takes a very long time before the companion star leaves the main sequence and becomes a supergiant with a strong stellar wind.

1.5.2 Evolution during the HMXB phase

A priori, HMXBs should have high eccentricities at birth due to the SN explosion, and the variety of parameters suggest that the birth of NSs results in a measurable eccentricity in (almost) all systems, but tidal circularisation reduces it in systems with small orbits, which is in concordance with theory (see Sec. 1.3.1).

SGXBs with orbital periods smaller than 8 days have negligible eccentricities. Vela X-1, with $P_{\rm orb} = 8.9$ d and B0.5 Iab companion, has a low eccentricity $e = 0.09$, but 4U 1907+09, with $P_{\rm orb} = 8.4$ d and a late-O supergiant companion has $e = 0.28^{+0.10}_{-0.14}$ [in 't Zand et al., 1998]. EXO 1722−363, with an early B companion and $P_{\rm orb} = 9.7$ d has an eccentricity smaller than $e = 0.2$ and perhaps negligible [Thompson et al., 2007]. This variety suggests that the birth of neutron stars results in a measurable eccentricity in (almost) all systems, but tidal circularisation reduces it in systems with small orbits.

Pfahl et al. [2002] suggested that HMXBs could be roughly divided into three groups according to their orbits:

- Moderately wide ($P_{\rm orb} \sim 20 - 100$ d) binaries with a significant ($e > 0.3$) eccentricity caused by a "kick" at the formation of the NS.
- Short-period ($P_{\rm orb} \lesssim 10$ d) systems in which tidal circularisation has resulted in low-eccentricities.
- Wide ($P_{\rm orb} \gtrsim 30$ d) binaries with low ($e < 0.2$) eccentricities, resulting from weaker kicks, perhaps related to electron-capture SN stars with an outer radiation zone.

Observational data suggest that a binary containing stars with an outer radiation zone will suffer substantial tidal effects when the ratio between the semi-major axis and the stellar radius is smaller than ~ 4 [North and Zahn, 2003]. For typical values of mass and radius for an OB star orbited by a NS, this corresponds to orbital periods smaller than ~ 10 d.

Liu et al. [2011] propose an scenario where some SGXBs could have evolved from BeXBs. The Be stars will eventually evolve to supergiants, and some will become SGXBs when accretion restarts. These authors give two possible examples for this evolutionary channel: IGR J11215-5952 and IGR J18483-0311.

1.5.3 The "Common Envelope Phase"

The "common envelope phase" is a key in the evolution of close binary systems. This phase starts when the massive star begins to overflow its Roche-lobe and, in consequence, the compact object enters inside the envelope of its companion, in an orbit which is rapidly decreasing due to a large loss of orbital angular momentum. This phase has been invoked by Paczyński [1967] to explain how

high energy binary systems with very short $P_{\rm orb}$ can be formed, while both components of these systems –large stars at their formation– would not have been able to fit inside a binary system with such a small orbital separation. This phase of inward spiralling, currently taken into account in population synthesis models, but never observed yet, probably because it is short [models predict a maximum duration of only ~ 1000 years; Meurs and van den Heuvel, 1989] compared to the lifetime of a massive star ($\sim 10^{6-7}$ years), is an ingredient of prime importance for understanding the evolution of high energy binary systems [Tauris and van den Heuvel, 2006]. A possible proof of this phase could be the new subclass of HMXBs so-called obscured HMXBs.

1.5.4 Final evolution of HMXBs

The HMXB could finally evolve in different ways depending on the limits of their orbits:

Wide HMXBs

During the common envelope phase the massive star ejects its $\rm H$-rich envelope, and only its core (consisting of $\rm He$ and heavier elements) remains together with the compact star in a very narrow orbit. There is an example of such a system in our Galaxy [Cygnus X-3; van Kerkwijk et al., 1992], and several more in other galaxies, e.g.: IC10 X-1 and NGC300 X-1 [van den Heuvel, 2012].

When the $\rm He$ star in such a system explodes as a SN, and the system is not disrupted, an eccentric close binary results consisting of two compact stars. The nine double NS that are presently known, and which all have eccentric orbits, might be the result of such an evolutionary history [e.g., Flannery and van den Heuvel, 1975, van den Heuvel, 2007, 2009]. Their progenitors will in most cases have been BeXs, since in these systems the compact stars are NSs, and the Be stars are mostly less massive than $20\,\rm M_\odot$ their final remnants will also be NSs. While the remnants of systems like IC10 X-1 and NGC300 X-1 will most probably be double black holes binaries [e.g., Tauris and van den Heuvel, 2006, van den Heuvel, 2009].

Close HMXBs

The drop in orbital binding energy during spiral in in close HMXBs is not enough to expell the $\rm H$-rich envelope of the massive star before the compact object en-

ters the core. As a result the compact object spirals in completely and ends up in the center of the masive star. When the compact object is a NS, the resulting star is called a Thorne-Zytkow Object (TZO): a massive star with a NS in its center; the envelope of this star is very extended giving it the outside appearance of a red supergiant [Thorne and Zytkow, 1975, 1977]. These TZOs are exotic theoretical objects of which energy comes either from accretion onto the NS, for those with envelope mass $< 8M_{\odot}$, or via the exotic rapid proton process in the more massive ones [e.g., Podsiadlowski, 1996]. The formation rate of this exotic objects is equal to the formation rate of close HMXBs [van den Heuvel, 2012], and Podsiadlowski [1996] suggested that they could be the precursors of LMXBs with black hole companions.

CHAPTER 2

Characterisation of HMXBs:

Observations & Data Analysis

The aim of this thesis is to characterise a sample of HMXBs. To achieve this purpose the procedure shown in Fig. 2.1 has been followed for every HMXB of study.

The observational data set obtained consists of series of optical spectra, mainly for radial velocity determinations (see Secs. 2.2.3 and 2.2.4). Therefore, most of the observations have been taken in *Service Time* due to the need of having temporary series separated by different gaps to determine the orbital solution of the targets of study. Consequently, the data obtained for this objective comes from instruments where the *Service Time* mode is available.

For two of the sources it has also been possible to fit a FASTWIND stellar atmosphere model using high quality spectra. This fit, together with the radial velocity determinations, gives an almost complete set of the physical parameters of the binary systems.

Periodicity searches within available X-ray light curves, and the analysis of the X-ray flux behaviour of these light curves along the orbital period complements this study.

This Chapter consists of two main Sections:

1. Instruments used for the observations.
2. Steps followed during the reduction of the data.

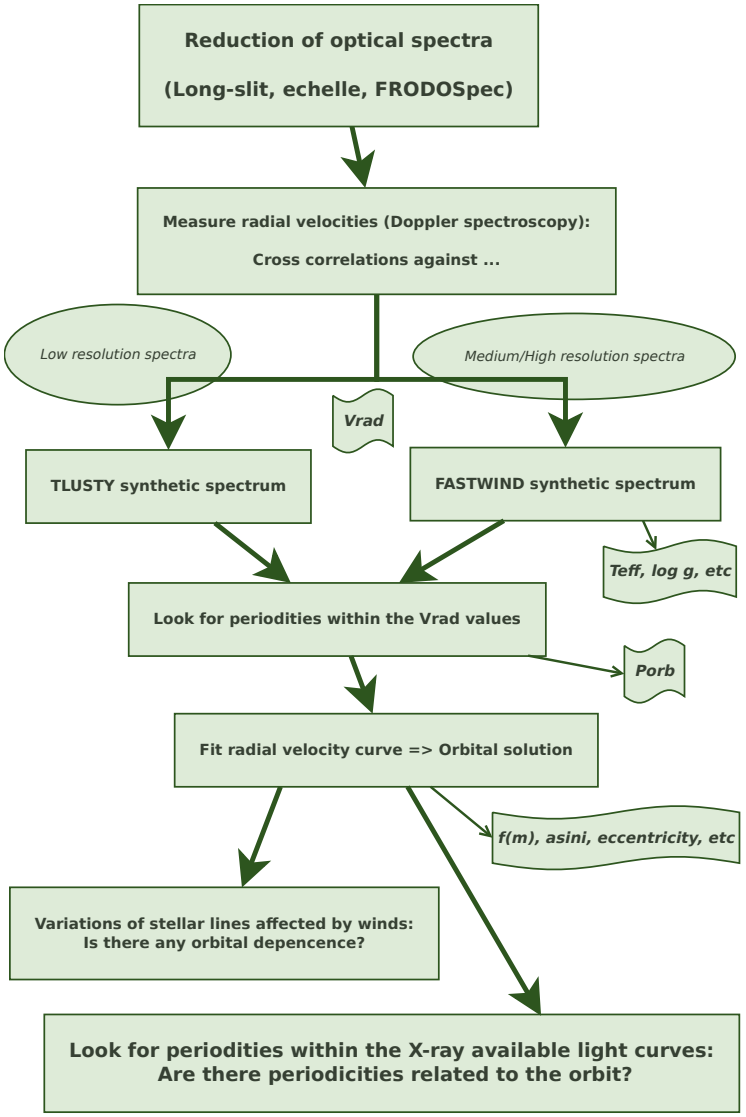

Figure 2.1: Scheme of the data analysis.

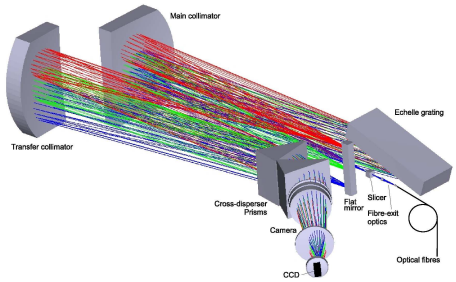

Figure 2.2: HERMES optical layout [Raskin et al., 2011].

2.1 Observations

The observation logs for every source can be found in the corresponding chapter (see Tables 4.1, 4.2,5.1, 5.2, 5.3, 5.4, 6.2, 6.1, 6.3, 6.4 and 6.5). Hereafter I present an overview of every instrument used to obtain these datasets.

2.1.1 Optical spectra

FRODOSpec@LT

For details of this instrument read Chapter 3.

HERMES@Mercator

The High Efficiency and Resolution Mercator Echelle Spectrograph [HERMES, Fig. 2.2; Raskin et al., 2011, and `http://www.mercator.iac.es/instruments/hermes/`] is mounted on Mercator Telescope. The Mercator Telescope is a 1.2 m semi-robotic telescope at the Observatorio del Roque de los Muchachos on La Palma, Spain.

HERMES is an echelle (see Sec. 2.2.1) fibre-fed prism-cross-dispersed spectrograph with two observing modes:

- The high resolution mode (HRF): $R \sim 85000$.
- The simultaneous wavelength reference mode (LRF): $R \sim 63000$.

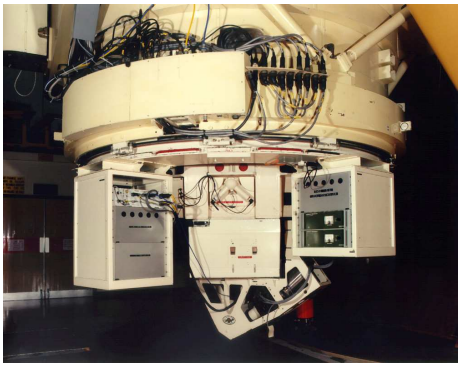

Figure 2.3: IDS@INT 2.5 m Telescope (©B. W. Hadley).

The spectral coverage of this echelle spectrograph goes from 377 to 900 nm making it an ideal instrument for building up time series of high-quality data of variable stellar phenomena [Raskin et al., 2011].

IDS@INT

The Intermediate Dispersion Spectrograph (IDS, Fig. 2.3) is a long-slit spectrograph (see Sec. 2.2.1) which sits at the Cassegrain Focal station of the 2.5 m Isaac Newton Telescope and is equipped with a 235−mm focal length camera (`http://www.ing.iac.es/astronomy/instruments/ids/`).

IDS is offered with a set of 16 gratings, and with two CCDs: the blue-sensitive EEV10 CCD (4096×2048 pixels), and the new RED+2 detector (4096×2048 pixels), more sensitive in the red and with much reduced *fringing*[1], which is offered since semester 11A.

FIES@NOT

The high-resolution FIbre-fed Echelle Spectrograph [FIES, Fig. 2.4; Frandsen and Lindberg, 1999, Telting et al., 2014, and `http://www.not.iac.es/instruments/fies/`] is located at the Nordic Optical Telescope (NOT). The NOT is a 2.5 m telescope,

[1] *Fringing* is an interference effect of red and IR light in the thinned substrate of back-illuminated CCDs, which become transparent to these wavelengths.

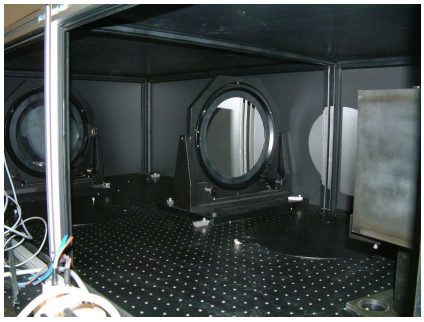

Figure 2.4: FIES@NOT (©IAC).(I dont like this pic

it is placed at the Observatorio del Roque de los Muchachos on La Palma, Spain [Ardeberg, 1989].

FIES is a cross-dispersed echelle spectrograph with three different observing modes:

- High resolution mode: $R \sim 67000$
- Medium resolution mode: $R \sim 46000$
- Low resolution mode: $R \sim 25000$

The entire spectral range $370-730$ nm is covered without gaps in a single, fixed setting [Frandsen and Lindberg, 1999, Telting et al., 2014].

ISIS@WHT

The Intermediate dispersion Spectrograph and Imaging System (ISIS, Fig. 2.5) is mounted at the Cassegrain focus of the 4.2 m William Herschel Telescope (WHT) at the Observatorio del Roque de los Muchachos on La Palama, Spain (`http://www.ing.iac.es/PR/wht_info/whtisis.html`, `http://www.ing.iac.es/Astronomy/instruments/isis/index.html`).

ISIS is a high-efficiency, double-armed, medium-resolution ($8-120$ Å/mm) spectrograph, capable of long-slit work up to ~ 4' slit length and ~ 22" slit width. Use of dichroic slides permits simultaneous observing in both blue and red arms, which are optimised for their respective wavelength ranges.

Figure 2.5: ISIS spectrograph off the telescope (© Javier Méndez).

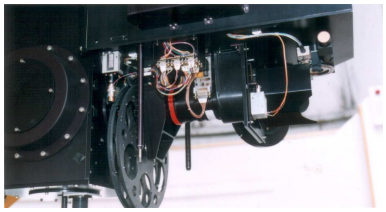

Figure 2.6: Side view of the long-slit spectrograph mounted on the 1.3 m Skinakas Telescope (© Skinakas Observatory).

Skinakas

A Focal Reducer is mounted on the 1.3 m Telescope located at the Skinakas Observatory, on top of the Ida mountain in Central Crete (`http://skinakas.physics.uoc.gr/en/`). In the spectroscopy mode, of this Focal Reducer, a reflection grating is introduced in the collimator path. Using different gratings, resolutions ranging from 0.57 Å/pixel to 4 Å/pixel are achievable with a 15 μm pixel CCD camera. A Slit Wheel offering 6 positions with slit widths: 80 μm, 160 μm, 320 μm and 640 μm is part of this configuration. A 2 k×0.8 k CCD camera is attached to the slit spectrograph.

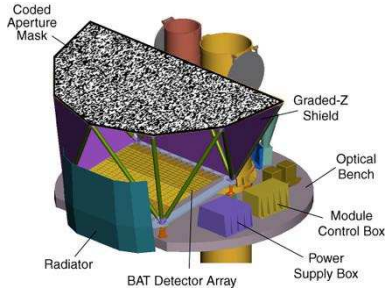

Figure 2.7: Schematic view of BAT with its coded mask (©NASA).

2.1.2 X-ray light curves

BAT@Swift

The Burst Alert Telescope [BAT, Fig. 2.7; Barthelmy et al., 2005, Krimm et al., 2013, and `http://swift.gsfc.nasa.gov/about_swift/bat_desc.html`] on-board Swift, a NASA mission that was launched on November 2004 [Gehrels, 2004], is a coded-aperture imager with a very wide field of view of about 2 steradians, which operates in the 15–150 keV band. The BAT angular resolution is 22' (FWHM).

The BAT continually monitors the sky with more than about 70% of the sky observed on a daily basis. Results from this survey are publicly available (`http://swift.gsfc.nasa.gov/docs/swift/results/transients/index.html`) in the form of light curves covering the 15–50 keV energy band on two time scales: a single Swift pointing (~20 min) and the weighted average for each day.

ASM@RXTE

The Rossi X-ray Timing Explorer (RXTE; a NASA mission that was launched on December 1995; `http://heasarc.gsfc.nasa.gov/docs/xte/learning_center/what_is_RXTE.html`) had three instruments on board:

– The Proportional Counter Array (PCA), sensible to the X-ray range 2 – 60 keV.

Figure 2.8: The All Sky Monitor of RXTE (©NASA).

- The High Energy X-ray Timing Expermient (HEXTE), which extends the X-ray sensitivity of RXTE up to 200 keV.
- The All Sky Monitor (ASM) that rotated in such a way as to scan most of the sky every 1.5 hours at $2 - 10$ keV giving observers an opportunity to spot any new phenomenon quickly.

The All Sky Monitor [ASM, Fig. 2.8; Levine et al., 1996] onboard the RXTE; a NASA consists of three Scanning Shadow Cameras (SSCs) mounted on a motorized rotation drive. Each SSC contains a position-sensitive proportional counter (PSPC) that views the sky through a slit mask covering a field of fiew (FOV) of 6° by 90° FWHM. Each SSC is sensitive in the energy range of approximately $1.5 - 12$ keV, with on-axis effective areas of $\sim 10\,\mathrm{cm}^2$, $\sim 30\,\mathrm{cm}^2$ and ~ 23 cm^2 at 2, 5, and 10 keV, respectively.

The ASM monitored the sky from January 1996 until December 2011, when the satellite operations were terminated. The ASM light curves are publicly available (`http://xte.mit.edu/ASM_lc.html`) in the form of light curves covering the $1.5 - 12$ keV energy band on two time-scales: a series of 90 s exposures known as dwells, and the 'one-day average' light curves, where each data point represents the one-day average of the fitted source count rates from a number (typically $5 - 10$) of individual ASM dwells.

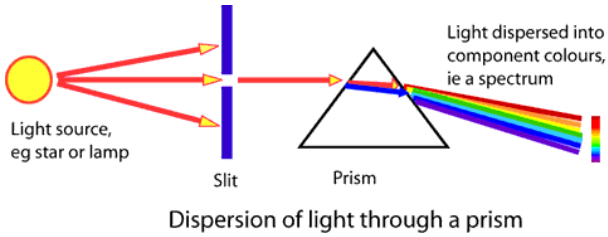

Figure 2.9: This is a simplistic scheme of a long-slit spectrometer. The slit limits the light entering the spectrometer so that it acts as a point source of light from a larger image. Then, the light goes through the dispersive element (in this case it is a prism, but in real modern spectrometers it is a diffraction grating to avoid the loss of light). And finally, there would be a detector to save the image of the dispersed light (©ATNF).

2.2 Data analysis

During this Section I am going to follow the process described in Fig. 2.1 outlining the different stages of the procedure.

2.2.1 Reduction of optical spectra

There are optical spectra from different instruments, consequently they are different kind of spectra:

- Long-slit spectra: IDS@INT, ISIS@WHT, Slit-spectrograph of Skinakas.
- Echelle spectra: HERMES@MERCATOR, FIES@NOT.
- FRODOSpec spectra: FRODOSpec@LT[2].

The optical spectrum is, up to date, the most useful observational data for an astronomer. Therefore, spectroscopy is one of the fundamental tools of the astronomer. There are several programs dedicated to the reduction of this kind of data, such as *Starlink* (`http://starlink.jach.hawaii.edu/starlink`) or IRAF [*Image Reduction Analysis Facility*; National Optical Astronomy Observatories, 1999].

[2]The Chapter 3 is related to the reduction of this kind of spectra.

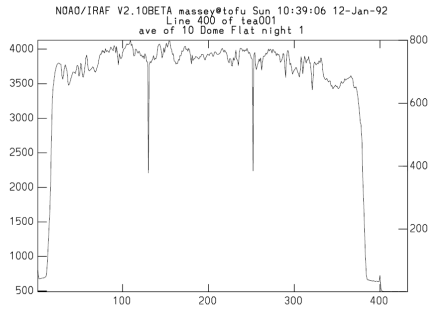

Figure 2.10: Example of a line cut through a FLAT that shows the region containing good data. The intensity drops down in the few first and last rows indicating the bad quality of that rows [Massey et al., 1992].

Reduction of long-slit spectra

Long-slit spectroscopy involves observing a celestial object through an elongated slit aperture, and refracting this light with a prism or diffraction grating (see Fig. 2.9).

Apart from the observation of the scientific object, some other calibration images should be taken during the night: BIAS, FLATS and *arc calibration lamps*. In this Section I am going to give an overview of how to reduce a long-slit spectrum with IRAF [Massey, 1997, Massey et al., 1992, for a detailed description].

Pre-Extraction Reduction:

– **BIAS subtraction:**
  First of all, the BIAS should be subtracted from all the frames to remove pre-flash illumination or any residual structure in the CCD. The IRAF task *zerocombine* is used to combine all the BIAS frames to reduce the noise with respect to an individual BIAS frame. Then, this combined BIAS is subtracted from the rest of frames by the task *imcombine*.

– **FLAT-field correction:**
  FLAT calibration images are useful to remove variations in the pixel-to-pixel sensitivity of the detector and/or by distortions in the optical path. The steps to remove these effects are:

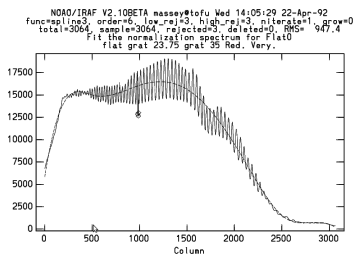

(a) Example of FLAT response being fitted to an order 6 function.

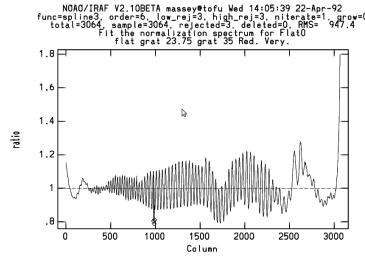

(b) Ratio of the data of the FLAT to the fit shown in Fig.2.11a.

Figure 2.11: Example of FLAT normalisation by fitting a function with the task *response* [Massey, 1997].

- Examine FLAT exposures (if there are several) and check that all of them have the same size, slit and binning (through the HEADER keywords), as well as discard those saturated FLAT images if there is any, together with those with a median number of counts above the rest (a list of the statistics of the image can be obtained using *imstat*).
- Combine all the FLAT images through a median after rejecting the pixels with maximum and minimum values. This step can be performed with *imcombine* selecting the appropriate options of the task.
- Examine and determine the area of the combined FLAT image that contains good data by plotting the image with the task *implot*. Fig. 2.10 shows an example where, by eye, one can distinguish the area of the CCD that has a good response from that area that has no response to the incoming light. Select the reliable area of the CCD with the task *imcopy*, creating a new FLAT image with just the desirable area and apply the same operation to the rest of the frames (arc calibration lamps and science frames).
- Remove the structure of the FLAT along the dispersion axis by fitting a function interactively with the task *response* (Fig. 2.11). This process gives as a result a normalised FLAT image.
- Divide all the frames (science and arc calibration lamps) by the normalised FLAT image with the task *imarith*.

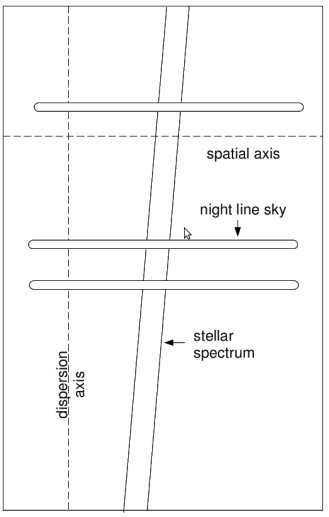

Figure 2.12: Scheme of a perfect stellar long-slit spectrum taken from Massey et al. [1992].

Extraction and wavelength calibration:

A schematic view of a long-slit spectrum is given in Fig. 2.12 where the dispersion axis is along columns, and the spatial axis is along rows. The steps to follow after the BIAS subtraction and FLAT-field correction have been performed are:

–**Find the spectrum**
This may be done manually by examining a cut along the spatial axis (Fig. 2.13) and indicating the appropriate peak with a cursor, or it can be done automatically if the appropriate spectrum is the strongest peak present.

–**Define the extraction and the background windows**
In practice this is done by specifying the size of the extraction window in terms of the number of pixels to the left of the center of the spatial profile, and the number of pixels to the right of the center of the profile. Similarly the background region is defined in terms of a region to the left and right of the center of the profile. One can then examine these regions displayed upon a cut along the spatial axis, and alter them if needed.

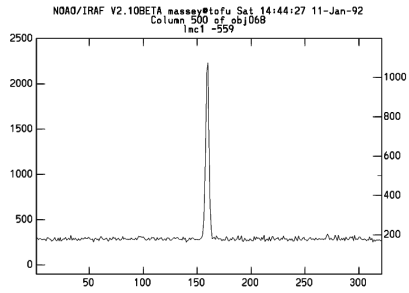

Figure 2.13: A cut perpendicular to the dispersion axis shows the location and width of the spatial profile where the spectrum is located [Massey et al., 1992].

– **Trace the center of the spatial profile as a function of the dispersion axis**
Even though we assume that the spatial axis is exactly along a row or column, the spectrum will not be exactly perpendicular to the spatial axis (see Fig. 2.12). Instead, the exact center of the spatial profile will shift slightly with location along the dispersion axis (this may be because of differential atmospheric refraction, distortions introduced by the camera optics, etc.).

– **Add the spectrum within the extraction window, subtracting sky**
At each point along the dispersion axis, the data within the extraction aperture is added, and the sky background is subtracted.

– **Wavelength calibration**
It consists of a change from pixel scale to wavelength scale by making use of the appropriate comparison exposure or arc calibration lamp.

  - Extract the one-dimension spectrum from the appropriate comparison exposure using the identical aperture and trace used for the object spectrum that is going to be calibrated.
  - Determine the dispersion solution for this comparison spectrum. This can be done interactively the first time, and the solution used as starting point to determine the dispersion solution for other comparison exposures.
  - If a second comparison exposure will be used for providing the wavelength calibration for the object spectrum (such as interpolating in

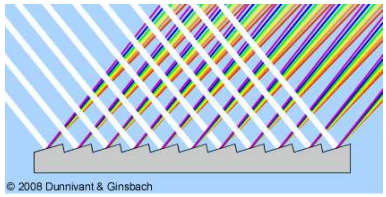

Figure 2.14: Illustration of a high angle coarsely ruled grating used in *echelle* spectrometers. It looks like a kind of ladder or stairs, the meaning of *échelle* in french. This concept of a coarsely-ruled grating used at grazing angles was discovered by Michelson [1898] where he referred to it as an "echelon".

time between two comparison exposures, or using the average solution of comparison exposures that were taken immediately before and after the object exposure), repeat the previous steps for the second exposure.

– Using the dispersion solution(s), put the object spectrum on a linear wavelength scale by interpolating to a constant $\Delta\lambda/pixel$.

All these steps can be performed by the IRAF routine *doslit* in just one step but with interaction, or using different routines such as *apall*, *identify*, etc..

After all this process has been finished, the spectrum has been extracted and wavelength calibrated. Another optional step is the normalisation of the continuum. It just consists of the fit of the continuum of the spectrum to a function avoiding the spectral lines, and dividing the spectrum by this function. It can be done by the IRAF task *continuum*.

Reduction of *echelle* spectra

The name *echelle* comes from the french word *échelle*, meaning stairs or ladder. *Echelle* spectra are generated by the use of a high angle coarsely ruled diffraction grating (Fig. 2.14) usually cross-dispersed by a low diffraction grating, grism or prism (see Fig. 2.15 for an scheme), configuration discovered by Nagaoka and Mishima [1923]. The resulting spectrum is a high resolution, closely spaced array of side-by-side orders of large spectral coverage (Fig. 2.16).

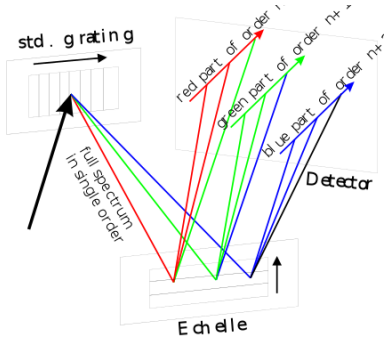

Figure 2.15: This figure shows the layout of an *echelle* spectrometer. The first standard grating is optimised for a single lower order, while multiple higher orders of the *echelle* diffraction grating (see Fig. 2.14 for an illustration of this kind of grating) have an optimised output intensity. Both diffractive elements are mounted orthogonally in such a way that the highly illuminated orders of the *echelle* are transversally separated. Since only parts of the full spectrum of each individual order lie in the illuminated region, only portions of the different orders overlap spectrally (©Wikipedia).

Figure 2.16: Echelle output spectrum (©ANDOR).

The *echelle* spectra in this thesis come from two instruments which have official pipelines for their reduction. The details of these pipelines can be found at `http://www.mercator.iac.es/instruments/hermes/hermesdrs.php` and `http://www.not.iac.es/instruments/fies/fiestool/FIEStool.html`.

2.2.2 Stellar atmosphere models: Synthetic spectra

A model atmosphere comprises a complete description of the depth-behaviour of a set of variables that characterise the system: temperature, pressure, density of ions and electrons, velocity fields and chemical composition. By reproducing the emergent energy distribution (the spectrum) it is possible to assign values to the fundamental stellar properties.

A model atmosphere consists in solving a series of equations related to the atmospheric structure (radiative transfer equation, statistical equilibrium equation, energy balance equation, motion equation and continuity equation) through an iterative procedure [Urbaneja, 2004]. From the mathematical point of view the problem is tractable but it is not possible to solve the equations in a practical amount of time. Therefore, with the objective of reducing the complexity of the system, a series of simplifications are assumed. Here I lay-out the two classical simplifications of model atmospheres:

- **Local Thermodynamic Equilibrium (LTE)**
  Assuming LTE is a very good approximation for a photosphere of a solar-like star, but completely wrong with strong winds that imply more radiative processes than collisional ones [Urbaneja, 2004].

- **Plane-parallel model**
  The plane-parallel model treats the star as a set of plane-parallel layers. This approximation is a good one for stars with low density winds where the extension of the atmosphere is negligible and the continuum of the spectrum is formed below the sonic point[3] in a quasi-hydrostatic photosphere. But, in the case of supergiants with dense winds and no hydrostatic equilibrium, the photosphere moves beyond the sonic point, generating the formation of the lines and the continuum through the mass outflow, this approximation does not work properly [Urbaneja, 2004].

[3] The sonic point is the point where the stellar wind makes a transition from subsonic to supersonic flow.

The main purpose is to obtain a good enough synthetic spectrum to be able to do an accurate cross-correlation for $V_{\rm rad}$ determinations (see Sec. 2.2.3). But if there is a good enough observed spectrum it is possible to measure the fundamental physical parameters ($T_{\rm eff}$, $\log\ g$, etc.) providing an almost complete picture of the star.

Stellar model atmospheres, hence synthetic spectra, have been obtained by two different methods depending on the data available.

TLUSTY atmosphere models grid

The TLUSTY atmosphere models grid [Lanz and Hubeny, 2003, 2007] gives a comprehensive grid of 680 and 1540 metal *line–blanketed*[4], non-LTE, plane-parallel, hydrostatic model atmospheres for the basic parameters appropriate to O-type stars and early B-type stars respectively. As the targets of study are this kind of stars, by generating several synthetic spectra with different parameters and comparing the results with the observed spectra it is possible to choose and obtain a good synthetic spectrum that reproduces qualitatively the properties observed in the empirical spectra. Therefore, using this grid of models would be enough for $V_{\rm rad}$ determinations.

FASTWIND code

For two of the targets of study, we have good quality spectra opening the possibility of modelling a much better stellar atmosphere, and consequently, determine physical parameters such as the $T_{\rm eff}$, $\log g$, or the chemical abundances. This analysis has been performed by using the FASTWIND (Fast Analysis of STellar atmospheres with Winds) code developed by Santolaya-Rey et al. [1997], Puls et al. [2005].

This part of the analysis has been performed by the collaborators Dr. Artemio Herrero, Dr. Norberto Castro and Dr. Sergio Simón-Díaz. For this reason, I am just going to give a brief explanation of the performed diagnostic for the main physical parameters. For additional details on the analysis see Castro et al. [2012].

[4] *Line-blanketing* is an effect caused by metallic spectral absorption lines that absorb a fraction of the radiant energy of the star, a phenomenon so-called *blocking effect*, and then re-emit it at a lower frequency as part of the *backwarming effect*.

This model atmosphere has some simplifications but it is better for the sources of study than other atmosphere models (i.e. TLUSTY) for stars with winds because it is a non-LTE model atmosphere code with mass loss, *line-blanketing* and assumes spherical symmetry instead of being plane-parallel.

The rotational velocity of the star ($v_{\rm rot}$) is an input parameter for this model. This $v_{\rm rot}$ produces a broadening of the spectral lines due to the Doppler effect. This effect is determined by performing a Fourier transform of the O or Si lines as explained in Simón-Díaz and Herrero [2007].

Once the $v_{\rm rot}$ is used as an input for the model, an iterative procedure starts where the rest of the parameters of the star are determined by visual fitting of hydrogen Balmer, He and Si II/IV lines.

Effective Temperature

The $T_{\rm eff}$ is the parameter that determines the spectral type of the star (see Chapter 1, Sec. 1.1 and Fig. 1.3). This parameter is usually determined using the ionization balance method. The principle relies on the computation of synthetic spectra from atmosphere models at different temperatures. Depending on the temperature, the ionization of the elements present in the atmosphere is different, therefore, the lines of ions of the same element but of different ionization states are also sensitive to the $T_{\rm eff}$. Comparing the relative strength of lines from successive ions of the same elements in the synthetic spectra and the observed spectra yields the $T_{\rm eff}$ of the star [e.g., Herrero et al., 1992, Puls et al., 1996, Martins et al., 2002]. The most reliable indicators for O and early-B stars are He I and He II, with He I λ4471 and He II λ4542 being the classical diagnostics lines [Martins, 2011].

However, in supergiant stars, He II lines are contaminated by the wind. This contamination affects the $T_{\rm eff}$ determination giving as a result a lower value due to the emission component of the wind added to the absorption "original" line. This effect affects even more in HMXBs where this wind is interacting with gravitational effects and X-ray radiation coming from the compact object. Consequently, the classical comparison of He II to He I line strengths cannot be used in this case.

The strength of Si and other metallic lines is dependent on the microturbulent velocity ($v_{\rm turb}$). This $v_{\rm turb}$ causes a broadening of the spectral lines due to the

Doppler effect occasioned by the convection of the gas in the interior of the star. Although the strengths of Si lines are affected by $v_{\rm turb}$, the ratios of the EW of Si IV to Si III are almost insensitive to this effect [Urbaneja, 2004]. Therefore, the silicon ionization balance has been used as indicator of the $T_{\rm eff}$.

Surface gravity

The surface gravity is given by fits of the hydrogen Balmer [e.g., Martins, 2011] lines which are less affected by the $v_{\rm turb}$ and dominated by the Stark effect [Urbaneja, 2004]. This effect consists on the splitting of atomic spectral lines as a result of an externally applied electric field. The resulting broadening of the wings of the spectral lines is proportional to the ion and electron density in a plasma and is therefore a good indicator of pressure in a stellar atmosphere and hence of the luminosity of the star.

With values of the $T_{\rm eff}$ and $\log\ g$ it is possible to estimate mass and spectroscopic radius through the HR diagram (Fig. 1.3).

Mass loss rate

The main diagnostic of the mass loss rate ($\dot{M}$) in an optical spectrum is the Hα line [e.g., Puls et al., 1996]. If the density is enough, hydrogen recombination leads to Hα wind emission which adds to the underlying photospheric absorption. For strong winds, the emission completely dominates the line profile. The high variability of this line in our spectra (see Figs. 4.9, 5.12, 6.7 and 6.8) makes it not possible to determine $\dot{M}$ with accuracy.

2.2.3 Measuring radial velocities

Measuring Doppler shifts

The "*true motion*" of the stars can be decomposed into two components (see Fig. 2.17):

- "*Proper motion*": Velocity projected on the celestial sphere, perpendicular to the line of sight.
- "*Radial velocity*" ($V_{\rm rad}$): Velocity through the line of sight.

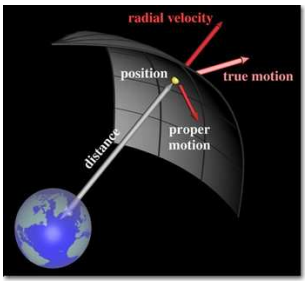

Figure 2.17: Scheme of the movement of a star across the sky (©RAVE@AIP). True motion is decomposed into two components, the "proper motion" and the radial velocity.

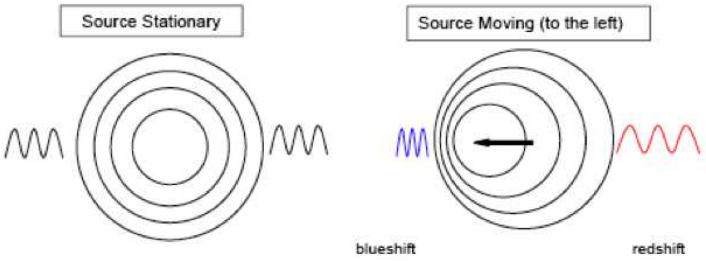

Figure 2.18: Scheme of the Doppler effect (©University of Chicago). The diagram illustrates how our perception of light changes depending on whether the source of the light is stationary, moving towards us, or moving away from us.

Therefore, as stars are electromagnetic-wave emitters, and they are not stationary, their waves arrive to our telescopes affected by the Doppler effect (see Fig. 2.18). So, measuring Doppler shifts on their spectra we are measuring their velocity along the line of sight or $V_{\rm rad}$:

$$\frac{\lambda_{\rm obs}-\lambda_{\rm emit}}{\lambda_{\rm emit}}=\frac{\Delta\lambda}{\lambda_{\rm emit}}=\frac{V_{\rm rad}}{c}\Rightarrow\begin{cases}\text{Approaching the observer}\Rightarrow V_{\rm rad}>0\Rightarrow\Delta\lambda>0\\ \text{Recening from the observer}\Rightarrow V_{\rm rad}<0\Rightarrow\Delta\lambda<0\end{cases}\tag{2.1}$$

The targets of this study are binary stars. Consequently, apart from their natural movement across the sky, they are moving in an orbit about a common center of masses (see Fig. 2.19). Therefore, the velocity of the star through the line of sight or $V_{\rm rad}$ has two components:

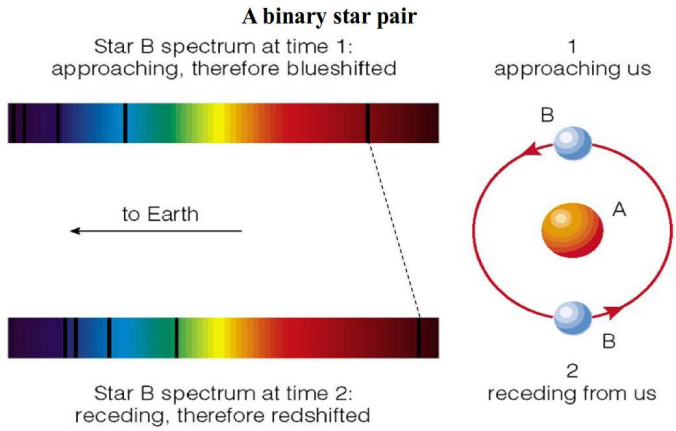

Figure 2.19: Scheme of how the orbital motion causes Doppler shifts in the spectrum of a star of a binary system (©NASA).

- The $V_{\rm rad}$ component due to the true motion (see Fig. 2.17), also denoted as γ and called systemic velocity.
- The $V_{\rm rad}$ due to the movement of the stars about the common center of masses (see Fig. 2.19), also called orbital velocity ($v_{\rm orb}$).

Summarising, it is possible to measure $V_{\rm rad}$ values of the optical component of the HMXB through the Doppler shifts on the optical spectra.

LSR velocity correction

To compare $V_{\rm rad}$ values observed when the Earth is at different positions in its orbit, the LSR velocity correction is applied. This correction consists of correcting the wavelength scale for the motion of the Earth with respect to the Local Standard of Rest (LSR).

This is basically a Doppler correction of the shifts of the wavelength caused by the rotation of the Earth, the motion of the Earth about the Earth-Moon barycentre, the orbit of this barycentre about the Sun, and finally, by the solar motion with respect to the LSR.

The IRAF task *rvcorrect* is used to apply this correction using the following parameters:

- The position of the observed source in the sky (right ascension (RA) and declination (Dec)).
- The Universal Time at the beginning of the observation.
- The length of time that the source has been exposed.
- The location of the observatory where the observation has been done.
- $v_\odot = 20$ km s^{-1} → Velocity of the Sun relative to the LSR.
- $RA(v_\odot) = 18:00:00 \rightarrow RA$ in hours of the solar motion relative to the LSR.
- $Dec(v_\odot) = 30:00:00 \rightarrow DEC$ in degrees of the solar motion relative to the LSR.
- $EPOCH(v_\odot) = 1900 \rightarrow$ Epoch in years for the solar motion components.

Cross-correlation methods to obtain $V_{\rm rad}$ values

Summarising, once the LSR velocity correction is applied to the spectra, it is possible to measure the $V_{\rm rad}$ values through the Doppler shifts of the spectral lines . These Doppler shifts are measured using cross-correlations.

The cross-correlation is a measure of similarity of two waveforms as a function of a lag (time-lag, wavelength-lag, etc.) or a shift applied to one of them (see Fig. 2.20). Making use of the shift ($\Delta\lambda$) measured with the cross-correlation and Eq. 2.1, the $V_{\rm rad}$ values are obtained:

$$V_{\rm rad} = c\frac{\Delta\lambda}{\lambda_{\rm emit}} \tag{2.2}$$

These cross-correlations can be performed against:

- Gaussians located at the corresponding wavelength at rest.
- Template spectrum. (← *This is the method used in this thesis.*)

Creating or fitting a Gaussian, a Lorentzian or a Voigt profile with the amplitude of the lines of the observed spectra but in rest, and cross-correlating this line against the observed one is a straightforward and easy method to measure the Doppler shift, therefore the $V_{\rm rad}$ [Parimucha and Škoda, 2007]. But with this

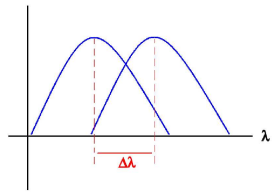

Figure 2.20: In this scheme the same function is plotted with a lag in the x axis that, in this case, corresponds to the wavelength (λ). A cross-correlation measures this lag or shift (in this case $\Delta\lambda$).

method we are assuming a symmetry in the spectral line profile that in the case of the targets of study in this thesis is not true.

Cross-correlating the observed spectra against a template spectrum, which could be a synthetic spectrum generated using a stellar atmosphere model (see Sec. 2.2.2), gives better results in the case of the sources of study in this thesis. If the template is not reproducing the properties of the observed spectrum it will give even worst measurements of $V_{\rm rad}$ than the previous method. But if the template is a good template, i.e. a synthetic spectrum that reproduces the properties of every line in the spectrum corresponding to its spectral type, the similarity between this template and the observed spectrum will be better than in the case of fitting a Gaussian, and, consequently, the cross-correlation function will be better [Parimucha and Škoda, 2007].

Therefore, I am using synthetic spectra and cross-correlating these spectra at rest against the observed spectra.

Spectral lines for the cross-correlation

Absorption lines of metallic elements coming from deep layers of the stellar atmosphere are best suited to determine $V_{\rm rad}$ measurements. Lines coming from the outer layers, specially Balmer lines [Barziv et al., 2001], are more affected by winds causing emission features (e.g., *P-Cygni* profiles[5]) that complicates the determination of the central peak of the lines. This phenomenon occurs

[5]The *P-Cygni* profile is characterised by broad and strong emission lines red-shifted with corresponding blue-shifted and narrower absorption lines. This shape is generally caused by large-scale motion of material. In this case it could be the consequence of the out-flowing wind from the star. For more details and information see Robinson [2007].

especially in HMXBs where the optical component, whose $V_{\rm rad}$ determination is the objective, has strong winds plus an interaction of these winds with the gravitational effects of its compact companion as well as with the X-ray radiation [e.g., Reynolds et al., 1993, van der Meer et al., 2007].

The optical components, or donor stars, of HMXBs are obscured stars with very low signal at blue wavelengths where these metallic lines are observed. It means that obtaining blue spectra is not easy. Although we have blue spectra for some of the sources of study most of the spectra in this thesis are red spectra. Therefore choosing a spectral wavelength range for the cross-correlation is not an easy task.

Using *fxcor* IRAF task for the cross-correlations

The *fxcor* task of IRAF computes radial velocities via Fourier cross-correlations [Alpaslan, 2009].

Using this task it is possible to select the zones of the template (synthetic spectrum) and the empirical spectrum to be cross-correlated. It re-bins both spectra to the same dispersion to have a better cross-correlation.

Determining the center of the cross-correlation peak is the key step in measuring a relative shift or velocity between the object and the template. This task provides a variety of methods finding the "gaussian", "lorentzian" or "parabola" function that fits best the data sets in this thesis. These methods use weights that vary continuously from one at the estimated center to zero at the endpoints of the fitting region. The functional form of the weights is a power law with specified exponent. A value of one (the default) produces linearly decreasing weights.

Errors in the pixel shift are computed from the center parameter of the fitting function. Velocity errors are computed based on the fitted peak height and the antisymmetric noise as described in Tonry and Davis [1979]. Dispersion/pixel-width errors are not computed in this release but are planned for a future release.

2.2.4 Orbital solutions

The *real* or *absolute* orbit is the orbit of both stars about the common center of masses. Assuming one of the objects in the binary system is much more massive than the other, it is possible to consider the most massive object as fixed in one of the foci of the ellipse. This approximation is known as the *relative* or *true* orbit, and this orbit is the one where Kepler's equations can be applied[6]. But, what we observe from our telescopes is the *apparent* orbit, that is the *relative* orbit projected along the line of sight.

The fundamental elements that characterise an orbit are (see Fig. 2.21):

- $P_{\rm orb}$ ≡Orbital period. It is the time taken to make one complete orbit.
- i ≡Inclination angle between the orbital plane and the line of sight.
- a ≡Semi-major axis, half the major axis of an orbit's ellipse.
- $e = \sqrt{1 - \frac{b^2}{a^2}}$ ≡Eccentricity. In the equation a and b are the semi-major and semi-minor axes of the orbit's ellipse.
- γ ≡Systemic velocity, the velocity of the center of masses of the binary system.
- $r_{\rm per}$ ≡Pericenter, also known as periapsis or periastron, it is the point of closest approach and corresponds to the maximum speed, $r_{\rm per} = (1-e)a$.
- $r_{\rm ap}$ ≡Apocenter, also known as apoapsis or apastron, it is the maximum distance and corresponds to the minimum velocity, $r_{\rm ap} = (1+e)a$.
- Ω ≡Longitude of the ascending node, angle between line of nodes and the zero point of longitude in the reference plane.
- ω ≡Argument of pericenter, it is the angle from the ascending node to the body in the orbital plane (denoted Θ_0 when measured from any point in the orbital plane).
- $\varpi \equiv$ Longitude of pericenter, a broken angle, measured in the reference plane from the zero point to the ascending node and then around the orbit, $\varpi \equiv \omega + \Omega$.
- T ≡Time of pericenter passage, it is the time at which the body passes through pericenter.

[6] Kepler's 1st law: *"The orbit of every object in a binary system is an ellipse with the most massive object at one of the two foci"*.

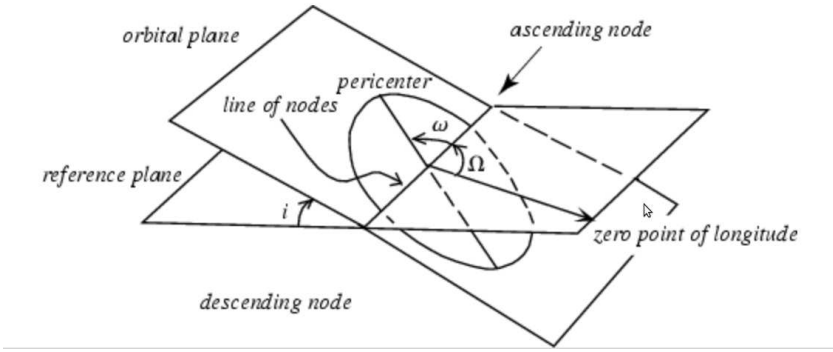

Figure 2.21: Scheme of the *relative* orbit projected over the reference plane (line of sight) giving the *apparent* orbit (© Eric W. Weisstein (Wolfram Research)). Some of the fundamental elements for the characterization of the orbit such as the line of nodes, the pericenter, i (inclination), Ω (longitude of the ascending node), or ω (argument of the pericenter) are indicated.

There are several spectra for the same source (optical component of the HMXB) taken at different stages in the orbit. Therefore, all the spectra are shifted due to the proper motion of the binary system in the same direction (see Fig. 2.17), but some of the spectra are "blue-shifted" and some others are "red-shifted" due to the orbital movement (Fig. 2.19). Therefore, the equation describing $V_{\rm rad}$ values obtained by cross-correlating the empirical spectra with the synthetic spectra using *fxcor* is:

$$V_{\rm rad} = \gamma + v_{\rm orb}, \tag{2.3}$$

where γ is the velocity of the center of masses or the projection along the line of sight of the proper motion, also known as systemic velocity with the same contribution to $V_{\rm rad}$ for all the observations of one source. And $v_{\rm orb}$ is the radial component of the orbital velocity of the binary system.

Making use of the Kepler's 2nd law[7], the equation of movement of one object about the other is:

$$\frac{1}{2}r^2\frac{d\theta}{dt} = \text{constant} = \frac{\text{ellipse area}}{P_{ORB}} \Rightarrow r^2\frac{d\theta}{dt} = \frac{2\pi a^2\sqrt{1-e^2}}{P_{\rm orb}}, \tag{2.4}$$

[7] Kepler's 2nd law: *"A line joining two bodies sweeps out equal areas during equal intervals of time"*. It is a consequence of the conservation of angular momentum.

where r is the distance between the focus of the ellipse and the position of the the object in the orbit

$$r = \frac{a(1-e^2)}{1+e\cos\theta}, \tag{2.5}$$

it just follows the equation of an ellipse, and θ is the angle formed by the semi-major axis a and r.

The projection of the movement along the line of sight is:

$$V_{\rm rad} = \gamma + v_{\rm orb} = \gamma + \frac{d}{dt}\left(r\sin(\theta+\omega)\sin i\right) \tag{2.6}$$

Building up these equations:

$$v_{\rm orb} = K\left(\cos(\theta+\omega) + e\cos\omega\right) \ , \tag{2.7}$$

where

$$K = \frac{2\pi a}{P_{\rm orb}\sqrt{1-e^2}}\sin i, \tag{2.8}$$

is the semi-amplitude of the radial velocity curve (see Fig. 2.22).

Looking for periodicities within $V_{\rm rad}$

I search for periodicities within the $V_{\rm rad}$ data set of each HMXB using different algorithms available in the *Starlink* package PERIOD [Dhillon et al., 2001].

For this kind of data sets the most useful algorithm is SCARGLE, which consists on redefining the classical periodogram, so-called Discrete Fourier Periodogram[8], in such a manner as to make it invariant to a shift of the origin of time. Lomb [1976] and Scargle [1982] developed a novel type of periodogram analysis, quite powerful at finding and testing the significance of weak periodic signals in otherwise random, unevenly sampled data. Horne and Baliunas [1986] have elaborated on the method, and Press and Rybicki [1989] present a fast implementation of the algorithm, a modified version of which is used by

[8]The Discrete Fourier Periodogram is defined as $I\left(\omega_j\right) = |d\left(\omega_j\right)|^2 = d_c\left(\omega_j\right)^2 + d_s\left(\omega_j\right)^2, j = 0,1,...,n-1$, where $d\left(\omega_j\right)$ is the Discrete Fourier Transform (DFT;$d\left(\omega_j\right) = \sum_{t=1}^{n} x_t e^{-2\pi i\omega_j t}/\sqrt{n} = \sum_{t=1}^{n}\cos\left(2\pi\omega_j t\right)/\sqrt{n} - i\times\sum_{t=1}^{n}\sin\left(2\pi\omega_j t\right)/\sqrt{n} = d_c\left(\omega_j\right) - i\times d_s\left(\omega_j\right), j = 0,1,...,n-1$) for a data series $x_1,...,x_n$, and $\omega_j = j/n$ is one of the Fourier frequencies.

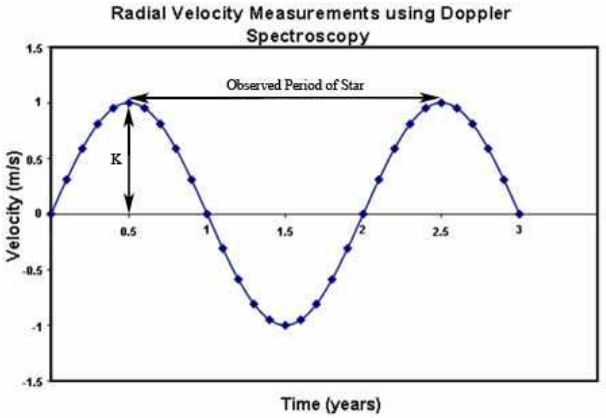

Figure 2.22: Radial velocity theoretical curve (© Wikimedia Commons). In this curve the γ value has already been removed from the $V_{\rm rad}$ points (notice the *y* axis is centred at 0 m s^{-1}). It is a theoretical curve, but in the real ones we do not have such a sample of data points and we fold all the $V_{\rm rad}$ values over the $P_{\rm orb}$ to obtain this curve. The values of $P_{\rm orb}$ and K are indicated.

PERIOD. This implementation uses Fast Fourier Transforms (FFTs) to increase the speed of computation.

With this method a preliminary value of $P_{\rm orb}$ is obtained from the $V_{\rm vrad}$ data set.

Fitting the radial velocity curve with SBOP

Fitting the radial velocity consists of fitting the empirical $V_{\rm rad}$ values to a smooth curve like the one shown in Fig. 2.22 and consequently, obtaining those parameters defining this curve:

- $P_{\rm orb} \equiv$ Orbital period.
- $T \equiv$ Time of pericenter passage.
- $e \equiv$ Eccentricity.
- $\omega \equiv$ Argument of pericenter.
- $\gamma \equiv$ Systemic velocity.
- $K \equiv$ Semi-amplitude of the radial velocity curve.

SBOP is the *Spectroscopic Binary Orbit Program*, an adaptation of the FORTRAN II computer program given in Wolfe et al. [1967] developed by Dr. Paul B. Etzel to solve spectroscopic binary systems.

The fit of the $V_{\rm rad}$ values to obtain the radial velocity curve is achieved by performing several iterations that refine a set of preliminary elements by a differential correction procedure. The initial elements of the orbit could be either supplied by the user, or derived using the Russell-Wilsing method [Wilsing, 1893, Russell, 1902, Binnendijk, 1960], which is an approximation method based on a Fourier curve-fitting procedure where the only parameter that must be known is the orbital period. The differential-correction procedure can be accomplished either with the method of Lehmann-Filhés [1894] re-discussed by Underhill [1966], or with the method of Sterne [1941] re-discussed by Hiltner [1962].

I fix the period to the value obtained from the periodicity analysis, and give a set of initial parameters as variables for a first iteration, assigning different weights (depending on the uncertainties) to the different radial velocity points. Using the solution of this first iteration, I then use Lehmann-Filhés [1894] method implemented in SBOP for single-lined systems. After several iterations, the convergence for most orbital parameters is obtained, and then I set free the period while fixing other parameters and repeat the procedure. Once an accurate value for the orbital period is obtained, I fix it to that value, set free the other parameters and repeat again until all parameters converge.

Physical values from the radial velocity curve

Notice that there are two stars in the binary system and we only have values of $V_{\rm rad}$ for one of them (the optical component of the HMXB). The ideal situation would be having two radial velocity curves, one for each of the objects of the binary system, giving a complete solution for each binary system.

From the fit of the radial velocity curve the values of the projected semi-major axis and the mass function (a minimum mass value for the object located at the focus of the ellipse) are obtained:

- **Projected semi-major axis:**

$$K_0 = \frac{2\pi a_0}{P_{\rm orb}\sqrt{1-e^2}}\sin i \Rightarrow a_0 \sin i = K_0 \frac{P_{\rm orb}\sqrt{1-e^2}}{2\pi} \tag{2.9}$$

- **Mass function:**
  - Following Kepler's *"harmonic"* or 3rd law[9]:

$$P_{\rm orb}^2 M = \frac{4\pi^2}{G} a^3 \Rightarrow P_{\rm orb}^2 \left(M_0 + M_{\rm X}\right) = \frac{4\pi^2}{G} \left(a_0 + a_{\rm X}\right)^3 \tag{2.10}$$

  - Making use of the Theorem of the Center of Masses:

$$\frac{M_{\rm X}}{M_0} = \frac{a_0}{a_{\rm X}} = \frac{K_0}{K_{\rm X}} = q \Rightarrow P_{\rm orb}^2 \left(M_0 + M_{\rm X}\right) = a_0^3 \frac{4\pi^2}{G} \frac{\left(M_{\rm X} + M_0\right)^3}{M_{\rm X}^3} \tag{2.11}$$

  - Projecting along the line of sight:

$$\frac{a_0^3 \sin^3 i}{P_{\rm orb}^2} \frac{4\pi^2}{G} = \frac{\left(M_{\rm X} \sin i\right)^3}{\left(M_0 + M_{\rm X}\right)^2} = f(M_{\rm X}) \Rightarrow M_{\rm X} = \frac{K_0^3 P_{\rm orb} \left(1 - e^2\right)^{3/2}}{2\pi G \sin^3 i} \left(1 + \frac{1}{q}\right)^2 \tag{2.12}$$

Masses calculated this way are called "*dynamical masses*", and are usually different from masses calculated from $T_{\rm eff}$ and $\log g$ values, that are called "*spectroscopic masses*". These differences are not dramatical and are due, mainly, to the different evolutionary paths followed by isolated and binary stars, as well as the effects caused by the X-ray radiation and random winds on the spectral lines used for the radial velocity determinations. A mass in between the spectroscopic and dynamical mass would be a good value for the mass of the star, but we should take into account that it is only possible to obtain a dynamical mass when the binary system is an eclipsing one and there are orbital solutions for both components.

After all these calculations the main physical parameters of the binary system have been obtained.

2.2.5 Hα variations: *Variations of stellar winds along the orbit*

The purpose is to be able to distinguish if there are variations of the wind related to the orbit. Balmer H lines, mainly Hα, are strongly affected by stellar winds, being one of the main indicators of mass-loss [e.g., Klein and Castor, 1978,

[9] Kepler's 3rd law:*"The square of the orbital period is directly proportional to the cube of the semi-major axis of its orbit"*. It is a consequence of the conservation of energy.

Leitherer, 1988, Puls et al., 1996, 2008]. Consequently, measuring variations in the Hα profile along the observations would give an idea of the changes in the wind and mass loss along the orbit.

Variations of spectral lines can be observed as changes in the EW. This parameter can be measured with IRAF by fitting the line to a Gaussian or a Voigt profile, or by another IRAF task that subtracts the linear continuum and sums up the pixels.

In the case of the targets of study, it has been observed that this line changes dramatically from one observation to another (see e.g., Figs 4.9, 5.12, 5.13, 6.7 and 6.8). Consequently, in some cases it has not been possible to measure the EW. Therefore, these changes are just observed visually by plotting the Hα line (after optimising the normalisation for this line and smoothing the profile by making a gaussian or a median filter) ordered by date and ordered by the orbital phase.

2.2.6 X-ray flux behaviour along the orbit

Searches of long-term periodicities along the orbit together with bibliographic searches of X-ray luminosities and outbursts previously reported complements this study as the X-ray behaviour is the key to set the HMXB in any of the established subgroups (see Sec. 1.4 of Chapter 1).

Moreover, if the orbital period is also found in the X-ray light curve, apart from giving strength to the orbital period found in the $V_{\rm rad}$ data set, it may be an indicator of eccentricity, or, of an eclipse in the binary system. In addition, foldings (see Fig. 2.23 for an example) of the X-ray light curves over the orbital period give an idea of the range of the X-ray flux changes along the orbit.

Periodicity searches within the X-ray publicly curves have been performed using different algorithms available in the *Starlink* package PERIOD [Dhillon et al., 2001].

In this case, the SCARGLE method is also useful, but as the data sets are more extended in time and the number of data points are much larger than in the case of $V_{\rm rad}$ values, it is also possible to use the CLEAN algorithm. This algorithm is an adapted version of the Roberts et al. [1987] code, and it is partic-

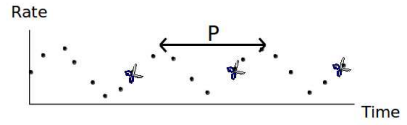

(a) Ideal light curve where the period can be seen by eye.

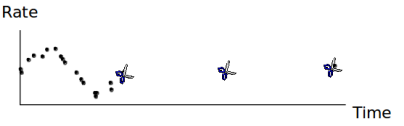

(b) Same ideal light curve as in Fig. 2.23a cut in segments equal to the period and put on top of each other.

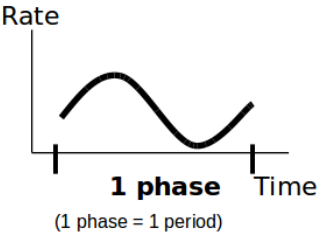

(c) Folding of the ideal light curve of Fig 2.23a after doing the averages of the superimposed points shown in Fig. 2.23b.

Figure 2.23: Example of an ideal folded light curve.

ularly useful for unequeally spaced data. The algorithm basically deconvolves the spectral window from the discrete Fourier Power Spectrum. This produces a CLEAN spectrum, which is largely free of the many effects of spectral leakage.

Foldings (see Fig. 2.23) have also been performed with the *Starlink* package PERIOD by the task FOLD. This task folds the data on a given period and zero point transforming the data onto a phase scale, where one phase unit is equal to one period and phase zero is defined by the zero point. This folding has a number of bins selected by the user, and the task averages all the data points falling into each bin giving different weights depending of the uncertainties in the data points. If the zero point is not known, the data can be folded by taking the first data point as the zero point.

CHAPTER 3

FRODOSpec integral field spectrograph data reduction pipeline

The Fibre-fed RObotic Dual-beam Optical Spectrograph (FRODOSpec, see Fig. 3.1), is an integral field spectrograph [Morales-Rueda et al., 2004, and `http://telescope.livjm.ac.uk/Info/TelInst/Inst/FRODOspec/`] located at the Liverpool Telescope (LT, see Fig. 3.2). The LT is a 2.0 metre fully robotic Cassegrain telescope that is operating unattended at the Observatorio del Roque de los Muchachos on La Palma, Spain [Steele, 2004, and `http://telescope.livjm.ac.uk/index.php`].

FRODOSpec is a bench mounted spectrograph with two optical paths, known as arms, that are utilised by separating the incident light around $5750\,\text{Å}$ into two bandwidths using a dichroic beam-splitter. The light down each arm is collimated, dispersed and focused onto CCDs, with the elements of each optical chain separately optimised for blue and red light. An optical scheme is shown in Fig. 3.3.

Two dispersive elements are available for each arm: a conventional diffraction grating and a higher resolution Volume Phase Holographic (VPH) grating. Resolving power and wavelength ranges for each arm and dispersive element are shown in Table 3.1.

Light is transmitted from the focal plane of the telescope to the spectrograph by a bundle of 144 optical fibres. At the telescope focal plane, the fibres are arranged in a regular pattern to form a 12×12 integral field unit (IFU), with each

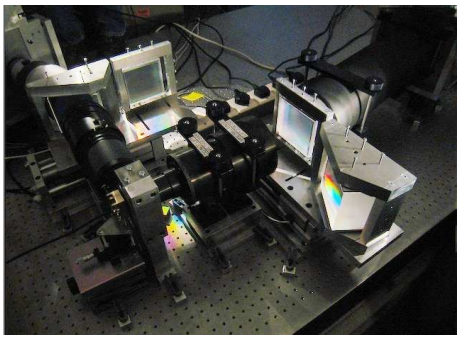

Figure 3.1: Part of FRODOSpec on an optical bench before shipping to site (© 2007 A. Scott.)

Figure 3.2: The Liverpool Telescope (© 2005 R. Smith).

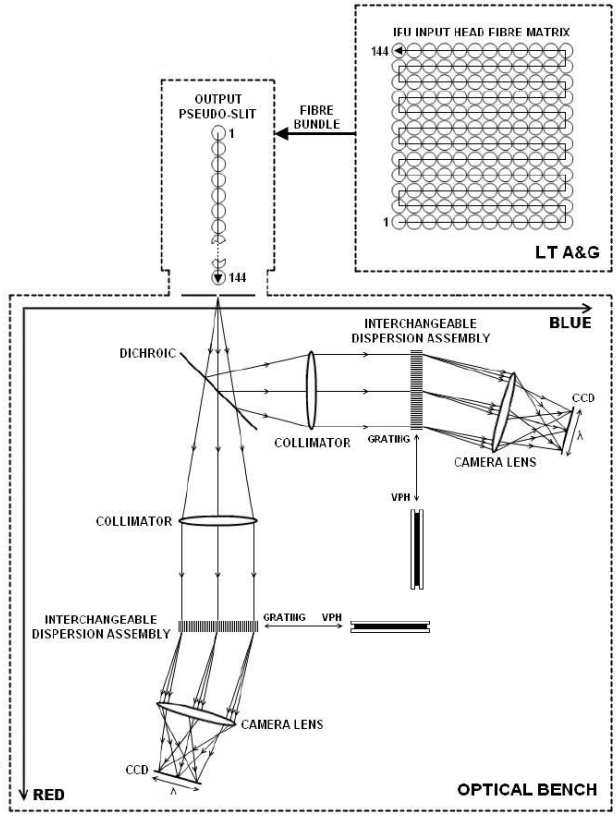

Figure 3.3: FRODOSpec optical scheme from Barnsley et al. [2012].

Table 3.1: Wavelength ranges, resolving powers and dispersions for the different FRODOSpec arms/dispersive elements [Barnsley et al., 2012].

Arm/Disp. Elem.	Start (Å)	End (Å)	R	Disp. (Å/px)
Red Grating	5800	9400	2200	1.6
Red VPH	5900	8000	5300	0.8
Blue Grating	3900	5700	2600	0.8
Blue VPH	3900	5100	5500	0.35

fibre coupled to a microlens to minimise light losses. Each fibre/microlense covers a field of view on sky of $\sim 0.83'' \times \sim 0.83''$, corresponding to a total field of view of $10'' \times 10''$. At the input of the spectrograph, the fibres are rearranged to form a pseudo-slit which acts as the entrance aperture.

Data taken by FRODOSpec is oficially reduced by two sequentially invoked pipelines. The first pipeline, known as the L1, is a CCD processing pipeline which performs BIAS subtraction, overscan trimming and CCD flat fielding. The second pipeline, known as the L2, performs the processes unique to integral field spectra reduction. The L2 became operational on 9th July 2010, with the second version released in May 2011. Full details of this pipeline may be found in Barnsley et al. [2012].

The reduction of the pipeline present in this work starts when the L1 official pipeline finishes. Therefore, the final products of the L1 official pipeline are the input of this pipeline. I started to reduce spectra before the L2 pipeline was developed, and once L2 final products became available, I realised that my reduced spectra had better signal to noise than those obtained with the official LT pipeline. Moreover, the official L2 pipeline does not remove cosmic rays and does not handle about the *fringing* (see Sec. 3.3.4) introduced in the red arm (see Fig. 3.9), while my pipeline does remove almost all the cosmic rays and reduces *fringing* to a very low level.

Notice that my pipeline has been developed and optimised mainly to reduce red spectra although the reduction of blue spectra is also implemented.

In this Chapter I give an overview of my pipeline (Sec. 3.1) including a flow chart of how it works (Fig. 3.4), followed by a summary about how to use it (Sec. 3.2). After these two Sections I give a description of each one of the modules (Sec. 3.3), and finally there is a comparison of my results with the results of the official pipeline (Sec. 3.4).

3.1 Overview

My pipeline reduces semi-automatically several observation nights at the same time. It consists of a main script which calls different modules dedicated to different steps of the reduction process as shown in Fig. 3.4.

I have developed this pipeline mainly to reduce the spectra of the red arm because the sources of study have basically no signal in the blue arm due to a very low efficiency (see Fig. 3.5). These sources are very obscured and the instrument does not work properly in the blue arm (the sources must have at least a $B \leq 12$ to have any signal). The blue arm reduction has been developed but not optimised.

3.1.1 Input data

The input data is the output data of the official L1 pipeline reduction, so the BIAS subtraction, overscan trimming and CCD flat fielding have already been done.

The output of the official L1 pipeline comes in the form of a *tgz* file. This *tgz* file contains all the files which appear in the observation log of that night (see Table 3.2 for an example). It means that there are arcs, flats, and science spectra taken with both arms of FRODOSpec, and RATCam (LT optical CCD camera) images. Those files whose name starts with 'b' are from the blue arm, and those starting with 'r' are from the red arm. It is possible to distinguish between the different kinds of frames through the headers of the fits files.

All the science fits files from July 2010 onwards have 8 extensions as shown in Table 3.3. For the reduction that is performed with my pipeline we just need the [0] extension of the fits file which is the L1 data product of the science frame.

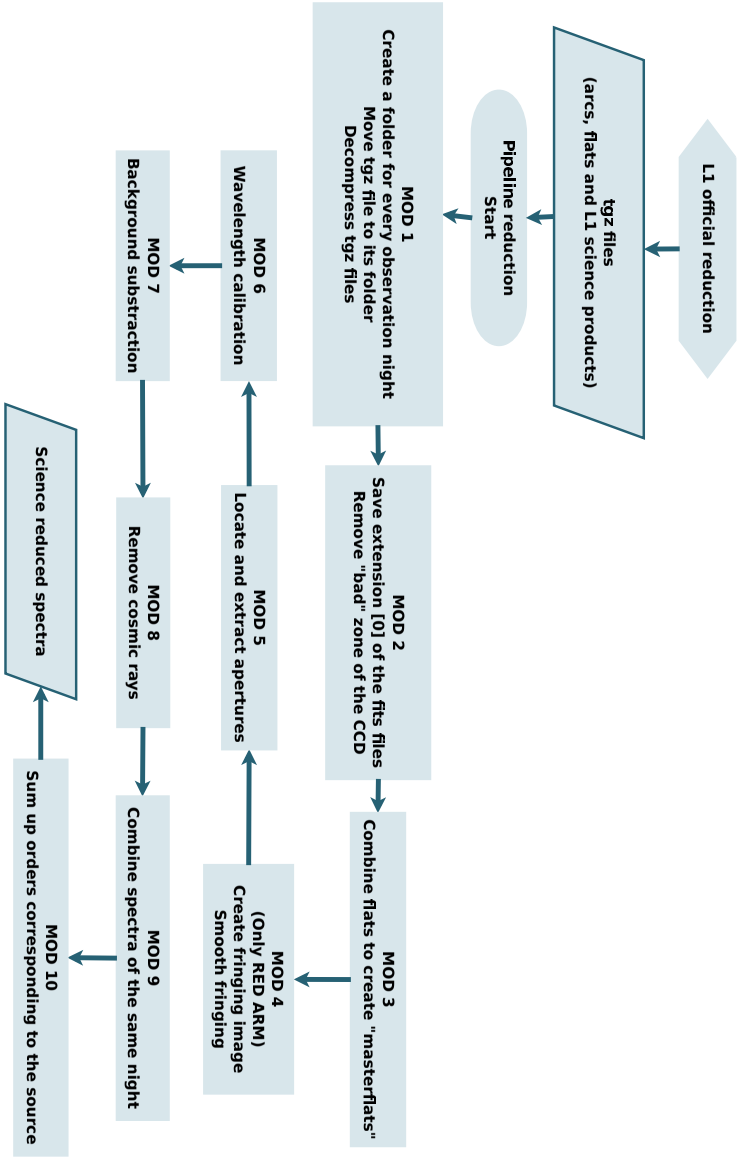

Figure 3.4: Flow chart of the developed pipeline.

Table 3.2: Observation log of the FRODOSpec observation night corresponding to 18th of June 2012.

OBJECT	PROPID	RA	dec	UT START	AIRM	INST	FILTERS	BIN	GRATING	EXP	SEING	EXT	SKY	FILENAME
AXJ1841	CL12A07	18:41:02	-5:35:23	00:43:41.1	1.290	RATCam	SDSS-R clear	2	NA	10.0	0.8	-999.0	99.9	c_q_20120618_72_1_1_1 0
AXJ1841	CL12A07	18:41:00	-5:34:56	00:44:19.1	1.289	RATCam	SDSS-R clear	2	NA	10.0	0.8	-999.0	99.9	c_q_20120618_72_2_1_1 0
AXJ1841	CL12A07	18:41:00	-5:34:55	00:44:57.4	1.287	RATCam	SDSS-R clear	2	NA	10.0	1.0	-999.0	99.9	c_q_20120618_72_3_1_1 0
AXJ1841	CL12A07	18:41:00	-5:35:46	00:46:27.8	1.284	FrodoSpec	NONE NONE	1	Red-High	1.0	0.0	-999.0	99.9	r_a_20120618_3_1_1_1 0
AXJ1841	CL12A07	18:41:00	-5:35:46	00:46:30.7	1.284	FrodoSpec	NONE NONE	1	Blue-High	60.0	0.0	-999.0	99.9	b_a_20120618_3_1_1_1 0
AXJ1841	CL12A07	18:41:00	-5:35:46	00:48:10.4	1.281	FrodoSpec	NONE NONE	1	Red-High	60.0	0.0	-999.0	99.9	r_a_20120618_4_1_1_1 0
AXJ1841	CL12A07	18:41:00	-5:35:46	00:48:13.3	1.281	FrodoSpec	NONE NONE	1	Blue-High	60.0	0.0	-999.0	99.9	b_a_20120618_4_1_1_1 0
AXJ1841	CL12A07	18:41:00	-5:35:46	00:50:09.2	1.277	FrodoSpec	NONE NONE	1	Red-High	1200.0	0.0	-999.0	99.9	r_e_20120618_5_1_1_2 0
AXJ1841	CL12A07	18:41:00	-5:35:46	00:50:12.0	1.277	FrodoSpec	NONE NONE	1	Blue-High	1200.0	0.0	-999.0	99.9	b_e_20120618_5_1_1_2 0
AXJ1841	CL12A07	18:41:00	-5:35:46	01:10:48.8	1.243	FrodoSpec	NONE NONE	1	Red-High	1200.0	0.0	-999.0	99.9	r_e_20120618_5_2_1_2 0
AXJ1841	CL12A07	18:41:00	-5:35:46	01:10:51.6	1.243	FrodoSpec	NONE NONE	1	Blue-High	1200.0	0.0	-999.0	99.9	b_e_20120618_5_2_1_2 0
AXJ1841	CL12A07	18:41:00	-5:35:46	01:31:20.9	1.222	FrodoSpec	NONE NONE	1	Red-High	1200.0	0.0	-999.0	99.9	r_e_20120618_5_3_1_2 0
AXJ1841	CL12A07	18:41:00	-5:35:46	01:31:23.7	1.222	FrodoSpec	NONE tNONE	1	Blue-High	1200.0	0.0	-999.0	99.9	b_e_20120618_5_3_1_2 0
AXJ1841	CL12A07	18:41:00	-5:35:46	01:52:02.9	1.211	FrodoSpec	NONE NONE	1	Red-High	60.0	0.0	-999.0	99.9	r_a_20120618_6_1_1_1 0
AXJ1841	CL12A07	18:41:00	-5:35:46	01:52:05.7	1.211	FrodoSpec	NONE NONE	1	Blue-High	60.0	0.0	-999.0	99.9	b_a_20120618_6_1_1_1 0
AXJ1845	CL12A07	18:45:02	-4:34:02	02:57:52.2	1.228	RATCam	SDSS-R clear	2	NA	10.0	0.9	-999.0	99.9	c_q_20120618_121_1_1_1 0
AXJ1845	CL12A07	18:45:01	-4:33:04	02:58:30.2	1.228	RATCam	SDSS-R clear	2	NA	10.0	0.9	-999.0	99.9	c_q_20120618_121_2_1_1 0
AXJ1845	CL12A07	18:45:01	-4:33:55	02:59:55.3	1.230	FrodoSpec	NONE NONE	1	Red-High	1.0	0.0	-999.0	99.9	r_a_20120618_7_1_1_1 0
AXJ1845	CL12A07	18:45:01	-4:33:55	02:59:58.2	1.230	FrodoSpec	NONE NONE	1	Blue-High	60.0	0.0	-999.0	99.9	b_a_20120618_7_1_1_1 0
AXJ1845	CL12A07	18:45:01	-4:33:55	03:01:39.1	1.233	FrodoSpec	NONE NONE	1	Red-High	60.0	0.0	-999.0	99.9	r_a_20120618_8_1_1_1 0
AXJ1845	CL12A07	18:45:01	-4:33:55	03:01:42.0	1.233	FrodoSpec	NONE NONE	1	Blue-High	60.0	0.0	-999.0	99.9	b_a_20120618_8_1_1_1 0
AXJ1845	CL12A07	18:45:01	-4:33:55	03:03:29.7	1.235	FrodoSpec	NONE NONE	1	Red-High	1200.0	0.0	-999.0	99.9	r_e_20120618_9_1_1_2 0
AXJ1845	CL12A07	18:45:01	-4:33:55	03:03:35.5	1.235	FrodoSpec	NONE NONE	1	Blue-High	1200.0	0.0	-999.0	99.9	b_e_20120618_9_1_1_2 0
AXJ1845	CL12A07	18:45:01	-4:33:55	03:24:02.0	1.271	FrodoSpec	NONE NONE	1	Red-High	1200.0	0.0	-999.0	99.9	r_e_20120618_9_2_1_2 0
AXJ1845	CL12A07	18:45:01	-4:33:55	03:24:05.6	1.271	FrodoSpec	NONE NONE	1	Blue-High	1200.0	0.0	-999.0	99.9	b_e_20120618_9_2_1_2 0
AXJ1845	CL12A07	18:45:01	-4:33:55	03:44:33.9	1.320	FrodoSpec	NONE NONE	1	Red-High	1200.0	0.0	-999.0	99.9	r_e_20120618_9_3_1_2 0
AXJ1845	CL12A07	18:45:01	-4:33:55	03:44:36.7	1.320	FrodoSpec	NONE NONE	1	Blue-High	1200.0	0.0	-999.0	99.9	b_e_20120618_9_3_1_2 0
AXJ1845	CL12A07	18:45:01	-4:33:55	04:05:28.8	1.387	FrodoSpec	NONE NONE	1	Red-High	60.0	0.0	-999.0	99.9	r_a_20120618_10_1_1_1 0
AXJ1845	CL12A07	18:45:01	-4:33:55	04:05:31.6	1.387	FrodoSpec	NONE NONE	1	Blue-High	60.0	0.0	-999.0	99.9	b_a_20120618_10_1_1_1 0

Table 3.3: L2 data products are eight part multi-extension fits files with each extension containing a snapshot of the data taken at key stages of the reduction process. The lowest tier of reduction product available to the user is the L1 image.

HDU Index	EXTNAME	Details
0	L1_IMAGE	L1 image
1	RSS_NONSS	Non sky subtracted row stacked spectra
2	CUBE_NONSS	Non sky subtracted datacube
3	RSS_SS	Sky subtracted row stacked spectra
4	CUBE_SS	Sky subtracted datacube
5	SPEC_NONSS	Non sky subtracted 1D spectrum
6	SPEC_SS	Sky subtracted 1D spectrum
7	COLCUBE_NONSS	Non sky subtracted collapsed datacube image

Each of these science frames (data products of L1) consists of 144 fibre spectra located in a CCD image (see Fig. 3.5), and it presents some differences with respect of a traditional long-slit such as the flux propagates spatially as a function of fibre profile.

In addition to the science frames, flats are needed for the aperture extraction, and arcs for the wavelength calibration. Consequently, the input data involves:

- Science frames (extension [0] of the L1 data products, 144 fibre spectra in a CCD image, Fig. 3.5).
- Flat images (Fig. 3.7).
- Arc images (Fig. 3.10).

3.1.2 Reduction process

The 144 fibre spectra of the science frames have the same wavelength range, although there are small shifts in position along the dispersion axis (Fig. 3.10 shows an example of a blue and a red arc lamp comparison image). Therefore, the treatment of the data is as if it were a *echelle* spectrum once the *fringing* effect (see Fig. 3.9) has been corrected in the case of the data of the red arm.

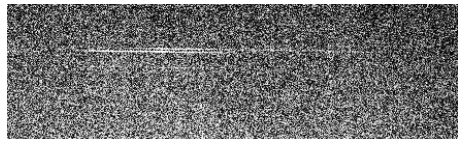

(a) FRODOSpec blue arm AX J1841.0-0535 (18th June 2012) science frame (L1 official pipeline data product). B=15.9

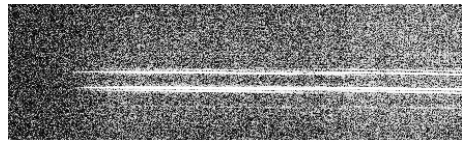

(b) FRODOSpec red arm AX J1841.0-0535 (18th June 2012) science frame (L1 official pipeline data product). I=10.9

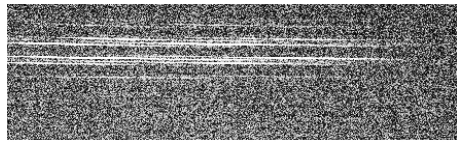

(c) FRODOSpec blue arm LS III +46°11 (17th Dec 2011) science frame (L1 official pipeline data product). B=12.3

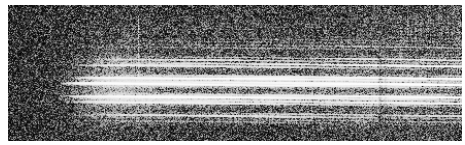

(d) FRODOSpec red arm LS III +46°11 (17th Dec 2011) science frame (L1 official pipeline data product). I=**?**

Figure 3.5: Examples of science input spectra (L1 official pipeline science products) of two different sources in both arms. The blue arm has almost no signal in both sources. Some of the fibres come from the background and some come from the object itself, but they are not the same in all frames.

After the extraction of the 144 spectra has been done, we assume there are 144 individual spectra. Some of these 144 spectra correspond to background and some of them correspond to the science spectrum itself, but the columns which correspond to the science spectrum and to the background are not the same in every observation. The selection of the background and the source itself is done by the median of counts of each spectrum. After the selection has been performed, the background subtraction is done, most of the cosmic rays are removed through a median filter and all the fibres which correspond to the science spectrum are summed up.

For a schematic view of the reduction process see Fig. 3.4, and for a more detailed explanation see Sec. 3.3.

3.1.3 Ouput data products

The main output data are the individual science spectra (see Fig. 3.6), but during the process some other products are saved in different subfolders (see Sec. 3.2), such as the background spectrum, the science spectra before removal of the cosmic rays, or the *fringing* image.

3.1.4 Coding platform

The pipeline has been developed in the interactive, object-oriented, extensible programming language *Python*. Basically, it is an *ipython* script that uses IRAF tasks. To be able to call these IRAF tasks it uses the *PyRAF* environment. Together with the IRAF tasks (or routines), my pipeline makes use of some of the functions of the *Python* libraries *numpy* and *pyfits*.

3.2 How to use the pipeline

The developed pipeline consists of a main script that calls the different modules (see Fig. 3.4). These modules are independent of each other, which means that can be used separately, but in this Section I am just going to give an explanation of how to use the complete pipeline. To use the modules separately it is important to read Sec. 3.3.

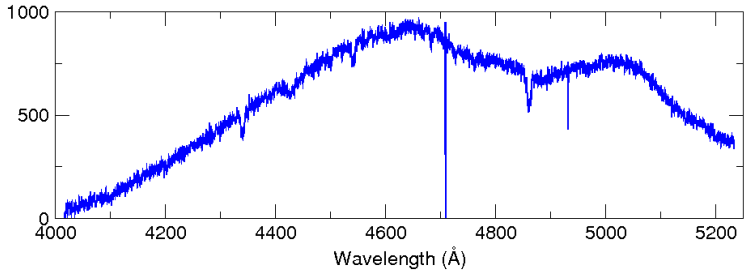

(a) FRODOSpec blue arm LS III +46°11 science reduced spectrum of 17th of December 2011.

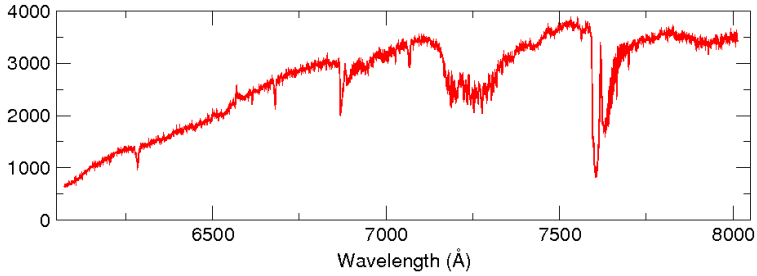

(b) FRODOSpec red arm AX J1841.0-0535 science reduced spectrum of 18th of June 2012.

Figure 3.6: Examples of science reduced spectra with my pipeline.

Notice there are some programs which have to be installed in the computer as it was explained in Sec. 3.1.4 (*Python*, *ipython*, IRAF, *PyRAF*, and the libraries *pyfits* and *numpy* of *Python*).

My pipeline reduces semi-automatically several observation nights at the same time. The *'semi'* comes because the user has to identify one arc spectrum every time the pipeline is run to be able to have a wavelength calibration good enough to use the final spectra to obtain radial velocities. Indeed it is possible to reduce all nights corresponding to an observation period in just one run of this pipeline, although it is not recommended, as the *fringing* is more or less stable but not completely. So it is better to reduce just 3 consecutive nights in each run. It is also not recommended to reduce just one night because the extraction of the science spectra is done using as reference 'masterflats' which have better statistics if there are more than just one night.

This pipeline is given as a *.tar* file which contains:

- *Redude_FRODOLT.py* : Main script of the pipeline.
- *Modules* : Folder with the different modules of the pipeline.
- *CalFiles folder* : Folder with the calibration files (*blue_ltxenon.dat* and *red_ltxenon.dat*, lists of the lines of the Xenon arc comparison lamps).
- *login.cl* : File required to use IRAF.

To use the pipeline copy this *.tar* file inside the folder where the reduction is going to be performed and also include in this folder all the observation nights, or the *tgz* data products that are going to be reduced. Decompress the pipeline, type *ipython* and then 'run Reduce_FRODOLT'. The screen will show the steps followed by the pipeline and at some point it will appear a screen to identify one red arc and one blue arc[1]. Once the arcs are identified, no more interaction is required and the pipeline will finish the process showing in the screen "********THE END**********".

The generated products are saved into different subfolders inside a folder called *'YourResults'* located inside the folder where the reduction has been done:

- *red_fring.fits* : The red *fringing* image obtained (see Fig. 3.9).
- *database* : The IRAF database generated during the reduction process.

[1] The arc identification is done like in IRAF, but for details on how to do it read Sec. 3.3.6

- *MasterFlats* : This folder contains the 'masterflats' of both arms.
- *Arcs* : This folder contains the wavelength calibrated arcs.
- *WlCal_Spec* : This folder contains the wavelength calibrated science spectra before the background subtraction (still in the form of 144 spectra per frame).
- *Background* : This folder contains the background spectra.
- *BackSub_Spec* : This folder contains the science spectra after background subtraction (still in the form of 144 spectra per every fits file).
- *No_CR* : This folder contains the science spectra after background subtraction and cosmic rays removal (still in the form of 144 spectra per frame).
- *Comb_Spec* : This folder contains the science spectra of the same night combined in case of several spectra of the same source at the same night after background subtraction and cosmic rays removal (still in the form of 144 spectra per frame).
- ***Reduced_Spec*** : This folder contains the main final product, **the reduced final science spectra**.

3.3 Step by step of my pipeline

This section describes all the steps of the developed pipeline. Therefore, every subsection corresponds to a module of the pipeline. In each subsection an explanation of the importance of that module is given, as well as how to use that module independently (it is important to notice that some knowledge of *ipython* and IRAF is required), and the inputs and outputs of each of them.

Most of these modules call to different IRAF functions whose parameters are optimised in the case of the red arm, and almost optimised in the case of the blue arm. It is possible to go into any of them and change the parameters with a bit of knowledge of *python* and IRAF.

The reduction of the blue and the red arm spectra of FRODOSpec is done concurrently. All the steps to follow are exactly the same, but the signal of the blue spectra is much lower, for this reason some of the reduction parameters are different.

Table 3.4: Overview of the inputs and the products obtained of each module of my pipeline.

MOD	Input	Products
1	Path (data reduction here) Path of the *tgz* files	Path of the observation folders
2	Path (data reduction here) Path of the observation folders	Red & blue fits files cut
3	Path (data reduction here) Path of the red fits files cut Path of the blue fits files cut	Red & blue 'masterflats'
4	Path (data reduction here) Path of the observation folders Path of the red 'masterflat' Path of the red fits files cut	*Fringing* image. Red science spectra , arcs & 'masterflat' corrected of the *fringing* effect
5	Path (data reduction here) Path of the blue 'masterflat' Path of the *fringing* corrected red 'masterflat' Path of the blue cut images Path of the red images with the *fringing* corrected	Extracted red & blue science spectra & arcs
6	Path (data reduction here) Path of the extracted arcs Path of the extracted science spectra	Science spectra wavelenght calibrated
7	Path (data reduction here) Path of the science spectra wavelenght calibrated	Science spectra background substracted
8	Path (data reduction here) Path of the science spectra background substracted	Science spectra without cosmic rays
9	Path (data reduction here) Path of the science spectra after removing cosmic rays	Science combined spectra taken at the same night
10	Path (data reduction here) Path of the science combined spectra	**Final science reduced spectra**

To have a schematic view take a look to the flow chart shown in Fig. 3.4 and also to the Table 3.4 which gives an overview of the inputs and products of each module which can be used individually. To use the whole pipeline in just one step see Sec. 3.2.

The input products of the pipeline are directly the *tgz* files downloaded (see Sec. 3.1.1 for details). The first thing that the main script of the pipeline does is to save the current location in a *Python* object called *path*, which is going to be an input for every module. Then, it looks for the files required for the reduction such as the *tgz* files with the frames done during the observation nights, the *login.cl* of IRAF and the red and blue arc lists. Once it is done, it starts calling the different modules as follows.

3.3.1 MODULE 1: *Locate files*

In Sec. 3.2 it has been explained that it is better to reduce more than one observation night each time. Assuming it is the case, and there are more than one *tgz* file in the folder where the reduction is going to be performed, this module is useful because it creates automatically an individual folder for every observation night where the corresponding *tgz* is decompressed.

Input

- Path (data reduction here).
- Path of the *tgz* files.

Output

- Path of the observation folders. *(Input of MODULES 2 & 4)*

Independent use

Since this is the first module a more detailed explanation of how to use it independently is going to be given.

Type *ipython* on the terminal, and then:

- *import os as os* : Import the *Python* library *os*.

- *import sys as sys* : Import the *Python* library *sys*.
- *import glob as glob* : Import the *Python* library *glob*.
- *path=os.getcwd()* : Save the current location in the object *path*. **It is an input of every module.**
- *sys.path.append(path+'/Modules')* : Add the location of the different modules to the *path*.
- *tar=glob.glob(path+"/*_1.tgz")* : Save *tgz* files in a *Python* list.
- *import Module1 as module1* : Import MODULE 1.
- *obs_folders = module1.folders_tar(path = path, tar = tar)* : Call MODULE 1 and save the result in the *Python* list *obs_folders*.

Process

- Create a folder for each observation night.
- Move *tgz* files into the corresponding folder.
- Decompress *tgz* files.
- Save the location of the observation folders in a *Python* list which is called *obs_folders*.

3.3.2 MODULE 2: *Prepare frames*

Every science fits file has several extensions (see Table 3.3), but only the extension [0], which is the one corresponding to the output image of L1 official pipeline, is required for the reduction. It is known that IRAF tasks give some troubles when the input fits file has several extensions, so this module creates a new fits file with just the extension required for the reduction process.

Moreover there is a 'bad zone' of the CCD (see Fig. 3.7) which has no signal. Therefore, to optimise the reduction, this module removes this zone of the CCD taking into account that this 'bad zone' is different in the red and in the blue frames.

Input

- Path (data reduction here).
- Path of the observation folders. *(Output of MODULE 1)*

(a) FRODOSpec blue arm flat field image (17th of December 2011).

(b) FRODOSpec red arm flat field image (18th of June 2012).

Figure 3.7: Examples of FRODOSpec flat field images. There is a zone of the CCD where there is no signal, and this zone is different in both arms.

Output

- Path of the red fits files cut. *(Input of MODULES 3 & 4)*
- Path of the blue fits files cut. *(Input of MODULES 3 & 5)*

Independent use

The first thing to do is to go into *ipython*. Then, create the inputs and follow these steps:

- *import sys as sys* : Import the *Python* library *sys*.
- *sys.path.append(path+'/Modules')* : Add the location of the different modules to the *path*.
- *import Module2 as module2* : Import MODULE 2.
- *red_cut, blue_cut = module2.preparefits (path = path, obs_folders = obs_folders)* : Call MODULE 2 and save the path of the results in two *Python* lists (*red_cut* and *blue_cut*).

Process

- Look for blue and red frames inside the observation folders and create independent lists.
- Save extension [0] of every frame in a new fits file.
- Cut the bad zone of every frame.
- Save the location of the red cut frames and blue cut frames.

3.3.3 MODULE 3: *Create 'masterflats'*

All science frames consist of 144 fibre individual spectra whose extraction is done through the IRAF routine *apall* of the *echelle* package (see Sec. 3.3.5). This routine needs a reference image to locate the different fibres or apertures of the spectra because the true cross-dispersion axis and the dispersion axis are just approximately aligned with the corresponding pixel axis of the CCD.

The *apall* task of the *echelle* package looks for the maximums of the cross-dispersion axes in a reference image. This reference could be a flat image (Fig. 3.7), but for a better location of the apertures all the blue flats and red flats are summed up to distinguish better the position of the fibres (see Fig. 3.8).

Input

- Path (data reduction here).
- Path of the red fits files cut. *(Output of MODULE 2)*
- Path of the blue fits files cut. *(Output of MODULE 2)*

Output

- Path of the red 'masterflat'. *(Input of MODULE 4)*
- Path of the blue 'masterflat'. *(Input of MODULE 5)*

Independent use

Go into *ipython*, create the inputs, and follow these steps (notice the only thing that is changing in each module is how to call the *Python* module):

- *import sys as sys* : Import the *Python* library *sys*.

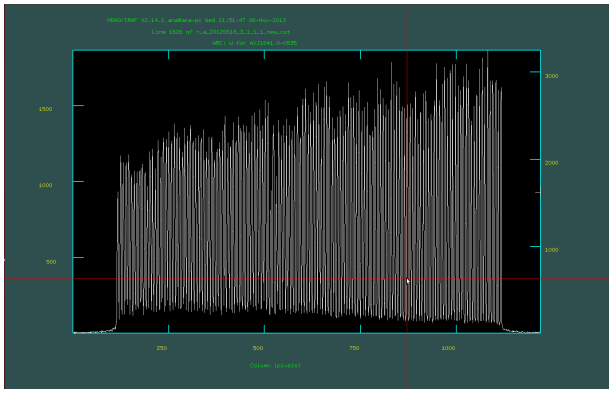

(a) Cross-dispersion axes signal of the red flat shown in Fig. 3.7b corresponding to the observing night of 18th of June 2012.

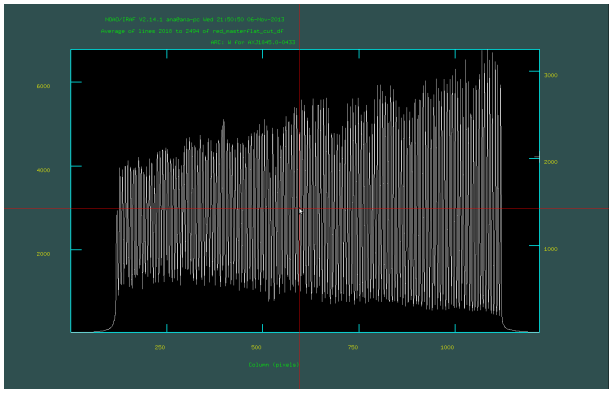

(b) Cross-dispersion axes signal of the red masterflat shown in Fig. **??** corresponding to the observing nights of 16th, 17th and 18th of June 2012.

Figure 3.8: Cross-dispersion axes flats signals. Notice that in the individual flat (Fig. 3.8a) the difference between the minimum and the maximum is much lower than in the 'masterflat' image (Fig. 3.8b)

- *sys.path.append(path+'/Modules')* : Add the location of the different modules to the *path*.
- *import Module3 as module3* : Import MODULE 3.
- *red_masterflat_cut, blue_masterflat_cut = module3.combflats(path = path, red_cut = red_cut, blue_cut = blue_cut)* : Call MODULE 3 and save the path of the results in two *Python* objects (*red_masterflat_cut* and *blue_masterflat_cut*).

Process

- Look for red and blue flats independently through the headers of the different frames.
- Save red and blue flats in independent *Python* lists.
- Sum up all red flats and all blue flats creating 'masterflats' using the IRAF routine *imcombine*.
- Save the location of these 'masterflats'.

3.3.4 MODULE 4: *Correct the **fringing** of the RED ARM*

Fringing is an interference effect of red and infrared light in the thinned substrate of back-illuminated CCDs, which become transparent to these wavelengths. In general, it looks like a wavy pattern as shown in Fig. 3.9 which affects all red frames. It is easier to detect it in the 'masterflat' than in any of the other possible frames. In this module a normalised *fringing* image is extracted from the red 'masterflat' using the IRAF routine *apflatten* which removes overall profile shapes from flat fields. All red frames are divided by this image to correct this effect.

Input

- Path (data reduction here).
- Path of the observation folders. *(Output of MODULE 1)*
- Path of the red 'masterflat'. *(Output of MODULE 3)*
- Path of the red fits files cut. *(Output of MODULE 2)*

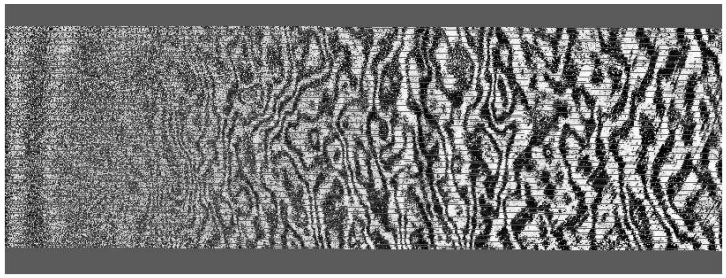

Figure 3.9: This wavy pattern corresponds to a FRODOSpec *fringing* image that has been extracted from the red 'masterflat' using the IRAF routine *apflatten*. Notice that the waves are more intense in the right part, it is because the *fringing* effect is more intense at longer wavelengths.

Output

- Path of the red images with the *fringing* corrected (science spectra and arcs). *(Input of MODULE 5)*
- Path of the red 'masterflat' with the fringing corrected. *(Input of MODULE 5)*

Independent use

Go into *ipython*, create the inputs, import the *sys* package of *Python*, add the location of the different modules to the path, import the module and call it as follows:

red_df, red_masterflat_cut_df = module4.defring(path = path, obs_folders = obs_folders, red_masterflat_cut = red_masterflat_cut, red_cut = red_cut)

Process

- Look for the arcs and science spectra within the list of red frames.
- Create the *fringing* image using the red 'masterflat' and the function *apflatten* of IRAF.
- Divide arcs, science spectra and red 'masterflat' by the *fringing* image.
- Save the location of the frames where the *fringing* effect has been corrected.

3.3.5 MODULE 5: *Locate and extract apertures*

Science and arcs frames consist of 144 fibre individual spectra. This module extracts the individual 144 spectra with the *apall* routine of the *echelle* package of IRAF. For this extraction a reference image is needed as the true cross-dispersion axis and the dispersion axis are not exactly aligned with the corresponding pixel axes of the CCD.

My pipeline uses as reference the 'masterflats', the one without *fringing* in the case of the red frames. It is important to remove the *fringing* before this step because it could affect to the location and profile fitting of the fibres.

The IRAF task *apall* looks for the maximums along the cross-dispersion axes about the middle of the dispersion axis and fits a function for each maximum along the dispersion axis (each maximum corresponds to a fibre).

Input

- Path (data reduction here).
- Path of the blue 'masterflat'. *(Output of MODULE 3)*
- Path of the red 'masterflat' without *fringing*. *(Output of MODULE 4)*
- Path of the blue cut images. *(Output of MODULE 2)*
- Path of the red images withouth *fringing*. *(Output of MODULE 4)*

Output

- Path of the extracted science spectra. *(Input of MODULE 6)*
- Path of the extrated arcs. *(Input of MODULE 6)*

Independent use

Go into *ipython*, create the inputs, import the *sys* package of *Python*, add the location of the different modules to the path, import the module and call it as follows:

red_ap_sci, blue_ap_sci, red_ap_arc, blue_ap_arc = module5.traceapall (path = path, red_masterflat_cut_df = red_masterflat_cut_df, blue_masterflat_cut = blue_masterflat_cut, blue_cut = blue_cut, red_df = red_df)

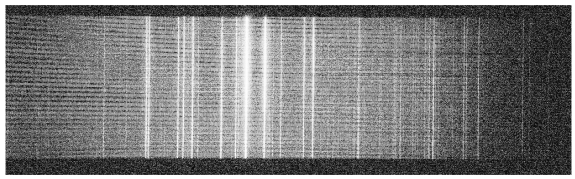

(a) FRODOSpec Xenon blue arc comparison image taken the 17th of December 2011.

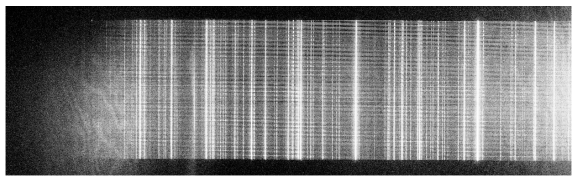

(b) FRODOSpec Xenon red arc comparison image taken the 18th of June 2012.

Figure 3.10: FRODOSpec Xenon arcs comparison images

Process

- Locate the apertures of the 'masterflats' using the *apall* routine of the *echelle* package of IRAF.
- Distinguish between science and arc frames going through the headers of the frames to create two different *Python* lists.
- Extract apertures of science and arc frames using as reference the apertures found in the 'masterflats'.
- Save the location of the arcs and science spectra extracted.

3.3.6 MODULE 6: *Wavelength calibration (interactive)*

In an *echelle* standard spectrum every fibre has a different wavelength range, however in FRODOSpec spectra all the fibres have the same wavelength range although there are small shifts in position along the dispersion axis (see Fig. 3.10). This module carries out the wavelength calibration of the science spectra by performing an interpolation of the arcs taken on the same night as the science

spectrum to have an accurate enough calibration to use the final science spectrum for radial velocity determinations.

One of the arcs is manually calibrated through the IRAF routine *ecidentify* which requires an interaction that consists on the calibration of this arc using the *PyRAF* interface shown in Fig. 3.11a. Within the files given in my pipeline there are two files (*blue_ltxenon.dat* and *red_ltxenon.dat*) with the location of the wavelength of the emission lines of both Xenon arc lamps (see Fig. 3.12). The key step is to identify a few lines in each order near the first, middle, and last apertures. In other words, there is no need to identify lines in all the apertures, but at least three apertures should have identifications. With the help of the atlas of the comparisons lamps given in Fig. 3.12 that have been directly downloaded from the official web page[2], set the cursor on a known line, type **m** and type in the wavelength. Mark several lines across the order and then move to a new aperture with the **j**, **k** or **o** key. As all the orders have the same wavelength range, knowing the wavelength of one order will enable one to predict the wavelengths in the rest of the orders. After three or more apertures have had lines marked type **f** to fit the wavelength vs the pixel position. Now a plot of deviations of the fit vs pixel number is displayed (Fig. 3.11b) and interactive fitting may be done. But first, using the initial fit, one could go back to the line identification mode by typing **q** and mark all the possible lines in agreement with the fitting typing **l**. Then type **f** again to do a new fit this time with more lines and now interact with this fitting until you are satisfied with the result.

To interact it might be useful to change from wavelength vs pixel, to wavelength vs residuals, which is done through typing **x** (to change the magnitude of the *x* axis) and **r** (to give it the value 'residuals'), although there are several options this is the one I use. It is possible to change the kind of the function fitted typing **xorder** and **yorder**, but every time a parameter of the fitting function changes you must type **f** again. Once you are satisfied with the fitting just type **q** to go out of the interactive fitting, and **q** again to go out of the line identification interface. Once the calibration of this arc is performed, the rest of the reduction process is automatic.

Additional arcs are calibrated based upon this first solution using the routine *ecreidentify* of the package *echelle* of IRAF. This task attempts to center all the lines using the line centers of the first arc as the starting point.

[2](http://telescope.livjm.ac.uk/Info/TelInst/Inst/FRODOspec/)

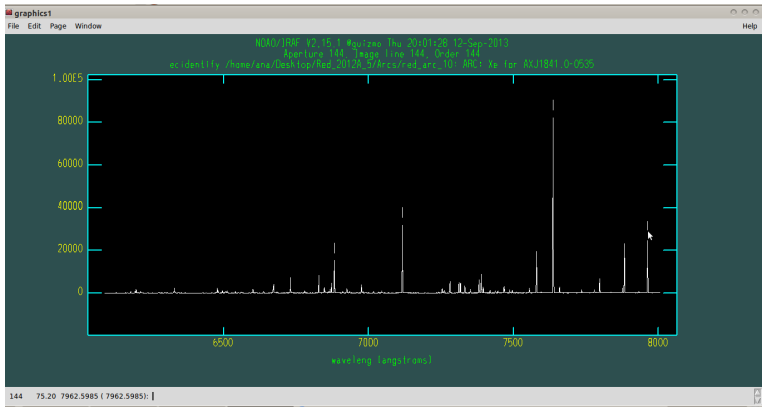

(a) Line identification *pyraf* interface of *ecidentify*.

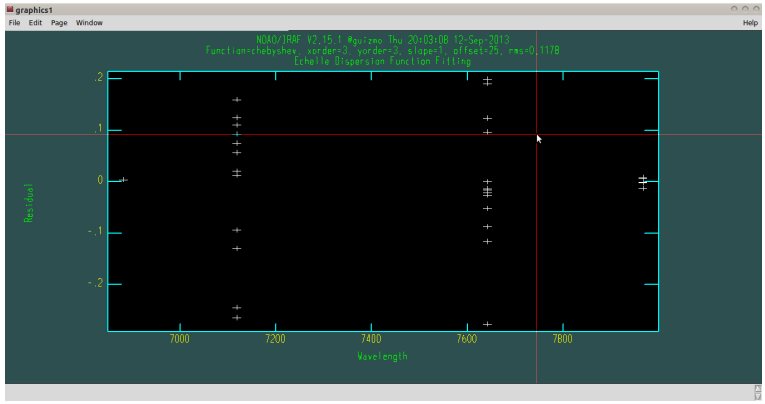

(b) Interactive fitting *pyraf* interface of *ecidentify*

Figure 3.11: *Pyraf* interactive interface of *ecidentify*

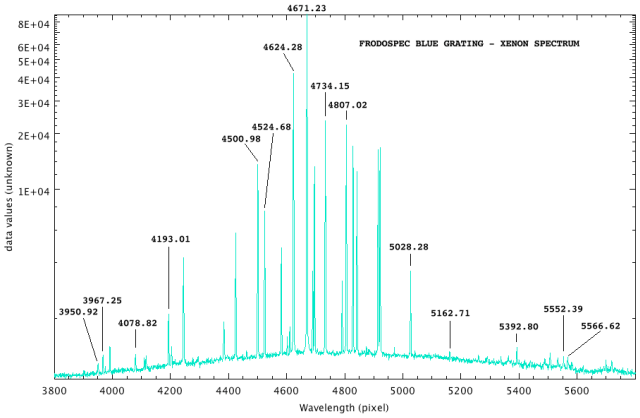

(a) Xenon arc in FRODOSpec blue grating (downloaded from `http://telescope.livjm.ac.uk/Info/TelInst/Inst/FRODOspec/`).

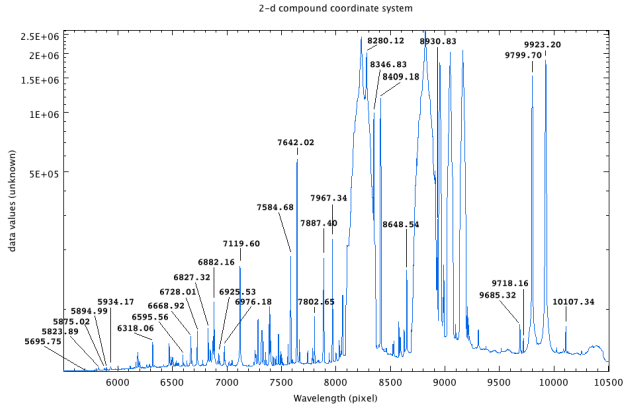

(b) Xenon arc in FRODOSpec red grating (downloaded from `http://telescope.livjm.ac.uk/Info/TelInst/Inst/FRODOspec/`).

Figure 3.12: Xenon arcs of FRODOSpec

Then, using the IRAF routine *refspectra* the arcs of the same night as one science spectrum are assigned to that science spectrum. And finally, the dispersion solution is applied to the science spectrum by interpolating within all the arcs assigned to the science spectrum through the IRAF routine *dispcor*.

Input

- Path (data reduction here).
- Path of the extracted arcs. *(Output of MODULE 5)*
- Path of the extracted science spectra. *(Output of MODULE 5)*

Output

- Path of the science spectra wavelength calibrated. *(Input of MODULE 7)*

Independent use

Go into *ipython*, create the inputs, import the *sys* package of *Python*, add the location of the different modules to the path, import the module and call it as it follows:

red_sci_cal, blue_sci_cal = module6.lambdacal(path = path, red_ap_arc = red_ap_arc, blue_ap_arc = blue_ap_arc, red_ap_sci = red_ap_sci, blue_ap_sci = blue_ap_sci)

Process

- Calibrate manually one arc with the IRAF routine *ecidentify* of the *echelle* package using the *pyraf* interface shown in Fig. 3.11.
- Identify the rest of the arcs using the IRAF routine *ecreidentify* of the *echelle* package.
- All the arcs taken on the same night of each science spectrum are assigned to that science spectrum making use of the task *refspec* of IRAF.
- Interpolate the arcs corresponding to the science spectrum to obtain the wavelength solution of every science spectrum by using the routine *dispcor* of IRAF.
- Save the location of the resulting wavelength calibrated science spectra.

3.3.7 MODULE 7: *Background subtraction*

The background subtraction, which is performed within this module of my pipeline, is an important step of the reduction process of a science spectrum.

The selection of the fibres corresponding to background is done through the median of counts of every fibre which is obtained by using the routine *imstat* of IRAF. This selection does not follow the same procedure in the red and in the blue arm due to the lower signal of the blue arm. Indeed, I have not been able to perform a good enough background subtraction of the blue arm for any of the spectra we have.

A histogram of the median values is done to select the fibres as shown in Fig. 3.13. Most of the fibres have a median counts value lower than 100 (see Fig.3.13a) as expected looking at the science input images shown in Fig. 3.5. Those fibres with higher values are the ones which are pointing to the scientific object (see Sec. 3.3.10), and those ones with the highest values could even be fibres affected by cosmic rays.

My pipeline looks for the maximum of this histogram. It considers as background those fibres corresponding to this maximum plus half of the fibres before this maximum together with those fibres belonging to the bin of the histogram after this maximum (see Fig. 3.13b). Those fibres with the lowest values are considered just noise and consequently, not taken into account.

After the selection of background fibres is performed, all these fibres are combined with the routine *scombine* of IRAF giving a median background spectrum (see Fig. 3.14). Then, the *sarith* task of IRAF is used to subtract this background spectrum to each of the 144 fibre spectra.

Input

- Path (data reduction here)
- Path of the wavelength calibrated spectra. *(Ouput of MODULE 6)*

Output

- Path of the background subtracted science spectra. *(Input of MODULE 8)*

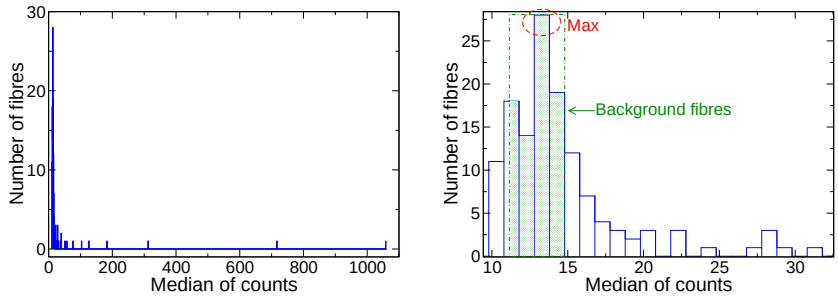

(a) Histogram of the median of counts.

(b) Zoom of Fig. 3.13a.

Figure 3.13: Examples of histograms of the median counts of the fibres of the red FRODOSpec spectrum of AX J1841.0-0535 of 18th of June 2012. Fig. 3.13a shows the complete histogram while Fig. 3.13b shows a zoom of the zone where the background fibres are selected.

Independent use

Go into *ipython*, create the inputs, import the *sys* package of *Python*, add the location of the different modules to the path, import the module and call it as follows:

red_sci_backsub, blue_sci_backsub = module7.backsub(path = path, red_sci_cal = red_sci_cal, blue_sci_cal = blue_sci_cal)

Process

- Calculate the median number of counts of every fibre.
- Select fibres of the science frames corresponding to background by the median number of counts (see Fig. 3.13b).
- Combine the fibres corresponding to background to create a background spectrum (see Fig. 3.14).
- Remove the background from all 144 fibres of the science frame.
- Save the location of the background subtracted frame.

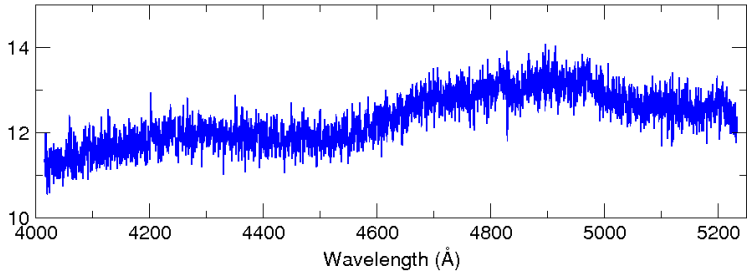

(a) FRODOSpec blue arm median background spectrum of 17th of December 2011.

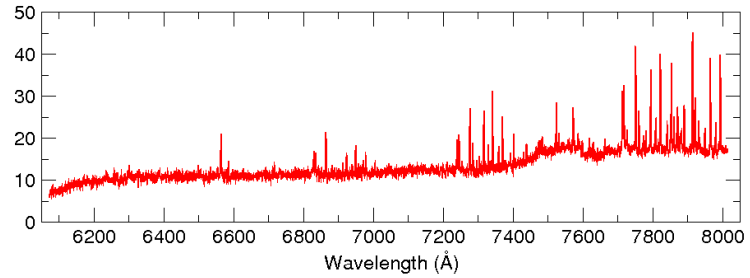

(b) FRODOSpec red arm median background spectrum of 18th of June 2012.

Figure 3.14: Examples of background spectra.

3.3.8 MODULE 8: *Remove cosmic rays*

Cosmic rays are present in several of the 144 fibre spectra affecting the final spectrum if they are not removed.

The selection of fibres which correspond to the object is done through the median number of counts of each fibre as explained in Sec.3.3.10. A cosmic ray in a fibre might change its value of median counts. Consequently it is important to remove cosmic rays before selecting the fibres which correspond to the scientific object.

This module is able to remove most of these cosmic rays applying a median filter to each of the 144 fibres by making use of the Median Absolute Deviation (MAD). MAD is a robust measure of the variability of a univariate sample of quantitative data. The expectation of $\sim 1.48MAD$ for large samples of normally distributed values is approximately equal to the population standard deviation but a more robust measure. The median filter of my pipeline removes the pixels whose number of counts is $\gtrsim 12\times 1.48MAD$ taking 7 pixels to calculate the MAD value, because we have found that this is the optimum range to remove cosmic rays in this kind of data.

Input

- Path (data reduction here)
- Path of the science spectra background subtracted. *(Output of MODULE 7)*

Output

- Path of the science spectra after cosmic rays removal. *(Input of MODULE 9)*

Independent use

Go into *ipython*, create the inputs, import the *sys* package of *Python*, add the location of the different modules to the path, import the module and call it as follows:

red_NCR, blue_NCR = module8.cosmic(path = path, red_sci_backsub = red_sci_backsub, blue_sci_backsub = blue_sci_backsub)

Process

- Calculate the MAD value for each 7 pixels of every 144 spectra.
- Mask bad pixels: Remove those pixels whose number of counts is $\gtrsim 12\times 1.48MAD$.
- Save the location of the new frame.

3.3.9 MODULE 9: *Combine science spectra*

Doing an average of the science spectra of the same night for a given object (if there are more than one) results in a better signal to noise. This average is performed using the IRAF task *scombine*. This routine performs the average correctly but it writes the parameters of one of the input frames at random in the header of the resulting fits file. Therefore, my pipeline modifies the header keywords related to time parameters written by IRAF putting down the correct ones.

If we have two or three spectra per night, the total exposure time will be the sum of the exposures of the individual spectra. This total exposure time is saved in the header of the fits file as EXPTIME1. But, for radial velocity determinations the quantity of time from the beginning of the first exposure to the end of the last exposure is needed, and it is not the same value as EXPTIME1. This quantity is calculated by my pipeline and saved in the header as EXPTIME2.

Input

- Path (data reduction here).
- Path of the science spectra after cosmic rays removal. *(Output of MOD 8)*

Output

- Path of the science combined spectra. *(Input of MODULE 10)*

Independent use

Go into *ipython*, create the inputs, import the *sys* package of *Python*, add the location of the different modules to the path, import the module and call it as follows:

red_sci_comb, blue_sci_comb = module9.combine(path = path, red_NCR = red_NCR, blue_NCR = blue_NCR)

Process

- Go through the headers of the fits files to by object and night.
- If there is more than one frame per object and night: average the frames of the same night and object.
- Modify the header keywords referring to time of the averaged frames:
  - DATE-OBS = DATE-OBS of the first frame.
  - UTSTART = UTSTART of the first frame.
  - MJD = MJD of the first frame.
  - EXPTIME1 = Sum of the exposure times of the averaged frames.
  - EXPTIME2 = Total time in seconds since the first exposure starts until the last exposure finishes.
  - UTMIDDLE = Date in days of the middle of the 'total' observation.
- Save the location of the combined spectra.

3.3.10 MODULE 10: *Select science object fibres*

This is the last step of my pipeline. This module selects those fibres corresponding to the science spectrum through the median counts of every fibre which is obtained using the IRAF task *imstat*.

Those fibres that were considered background in Sec. 3.3.7, now are considered noise (notice the median of counts values of Fig. 3.15 are lower than those in Fig. 3.13). All those fibres with a value of median counts well above the average value of the noise $+15\sigma$ are considered object, but setting up a minimum value of 20 counts to consider the fibre as object (see Fig. 3.15b).

Once this selection has been done, by the IRAF routine *scombine* all these fibres are summed up giving as a result the final science spectrum (Fig. 3.6).

Input

- Path (data reduction here).
- Path of the science combined spectra. (*Output of MODULE 9)*

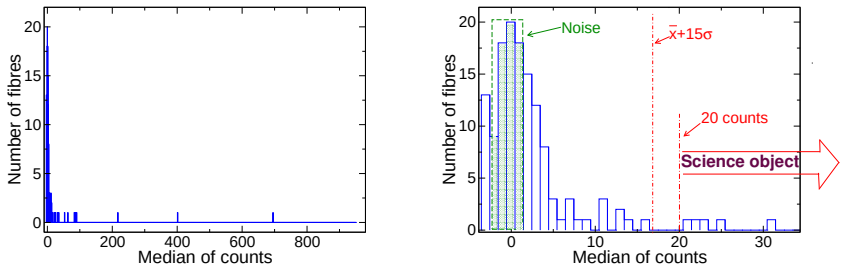

(a) Histogram of the median of counts.

(b) Zoom of Fig. 3.15a.

Figure 3.15: Examples of histograms of the median counts of the fibres of the red FRODOSpec spectrum of AX J1841.0-0535 of 18th of June 2012 after removing the background. Fig. 3.15a shows the complete histogram while Fig. 3.15b shows a zoom of the zone where the noise fibres are, and the limits for the selection of the science object fibres.

Output

- Path of the reduced science spectra. ***(Final result of the pipeline)***

Independent use

Go into *ipython*, create the inputs, import the *sys* package of *Python*, add the location of the different modules to the path, import the module and call it as follows:

red_final, blue_final = module10.final(path = path, red_sci_comb = red_sci_comb, blue_sci_comb = blue_sci_comb)

Process

- Calculate the median number of counts of every fibre.
- Select fibres of the science frames corresponding to the science spectrum through the median of counts of each of the 144 fibre spectra.
- Sum up the fibres corresponding to the science spectrum.
- Save the location of the final reduced science spectrum.

3.4 My results *vs* Official results

For the comparison of the results of my pipeline with those obtained with the official one I am going to show some examples of spectra reduced with both pipelines (see Figs. 3.16, 3.17 and 3.18).

First of all, I would like to remind that my pipeline has mainly been developed and optimised for the reduction of the red arm of FRODOSpec data, due to the low statistics of our blue spectra (see Fig. 3.5a). The blue arm reduction process is exactly the same except for the low signal or 'bad zone' of the CCD (Fig. 3.7) and the *fringing* effect (Fig. 3.9) that only affects the red spectra.

Fig. 3.16 shows an example of comparison of the reduction of both pipelines in the red arm. The top panel of this figure shows the reduction performed with my pipeline, while the other panels correspond to the results of the official L2 FRODOSpec pipeline. That observing night three spectra of the source were taken, so my pipeline averaged these three spectra (see Sec. 3.3.9) giving as a result an averaged spectrum. This averaged spectrum should have about the same counts level as the L2 official data product, but the signal of the spectrum obtained with my pipeline is moderately higher. The spectra of the official pipeline do have cosmic rays while the spectrum of mine does not have any of them. Another important thing to take into account here is the *fringing*, which is $\sim 15\%$ in the right part of the official data products whereas it is $\lesssim 1\%$ in the resulting spectrum of my pipeline. This higher level of signal, absence of cosmic rays and much lower level of *fringing* makes my result better than the official one.

To better compare the results I show in Fig. 3.17 an example of an observing night where only one spectrum of the source was obtained. Notice again the absence of cosmic rays of my spectrum, its higher signal, and the difference of the *fringing* in the right side of both spectra.

Fig. 3.18 shows an example of comparison of the reduction of both pipelines in the blue arm analogous to Fig. 3.16. Three spectra of the source were taken that night, consequently my pipeline averaged these three spectra giving as a result an averaged spectrum that should have about the same number of counts as the three individual results of L2 official pipeline. However, it has a higher signal. There are a couple of absorption lines that should not be there

(~ 4700Å and ~ 4930Å), but it does not have cosmic rays while the official results do have.

Barnsley et al. [2012] consider that the methods to remove cosmic rays are unrealistic, because those cosmic rays lying close to strong emission lines are particularly hard to distinguish. For the sources of study of my thesis, where there are no intense emission lines, and the emission lines that appear are clearly broad lines (i.e. $\mathrm{H}\alpha$, see Figs. 5.12, 6.7 and 6.8) compared to cosmic rays, it has been possible to develop and implement a method that gives quite good results as can be appreciated in Figs. 3.16, 3.17 and 3.18.

Moreover the aperture location in the official L2 FRODOSpec pipeline is done by using a flat reference image where the maximums are located along the cross-dispersion axes and a function is fitted to the fibre profile. Therefore, the process is almost the same as the one followed my pipeline. The difference is that my pipeline performs this step after the correction of the *fringing*, this is probably one of the reasons why my results have a better signal.

Finally for the selection of the background and science object fibres, the official pipeline, instead of doing it by using the median value of counts, sums up all the counts contained in each of the individual fibres smoothing the spectra before the selection to reduce the effect of the cosmic rays. The methods are similar and should give similar results, but with my pipeline the selection of the fibres corresponding to the object is performed after removing cosmic rays. Consequently, the effect of cosmic rays in my pipeline is completely removed and not only smoothed, which makes a difference.

In conclusion, for the kind of objects of my thesis my pipeline gives better quality results than the official one in terms of cosmic rays, *fringing* and signal to noise ratio. This better quality is observed not only when an averaged spectrum is obtained (Fig. 3.16), but also in a single night spectrum as it is shown in Fig. 3.17. Regarding to the blue arm case, it would be useful to obtain good quality spectra to optimise the reduction process.

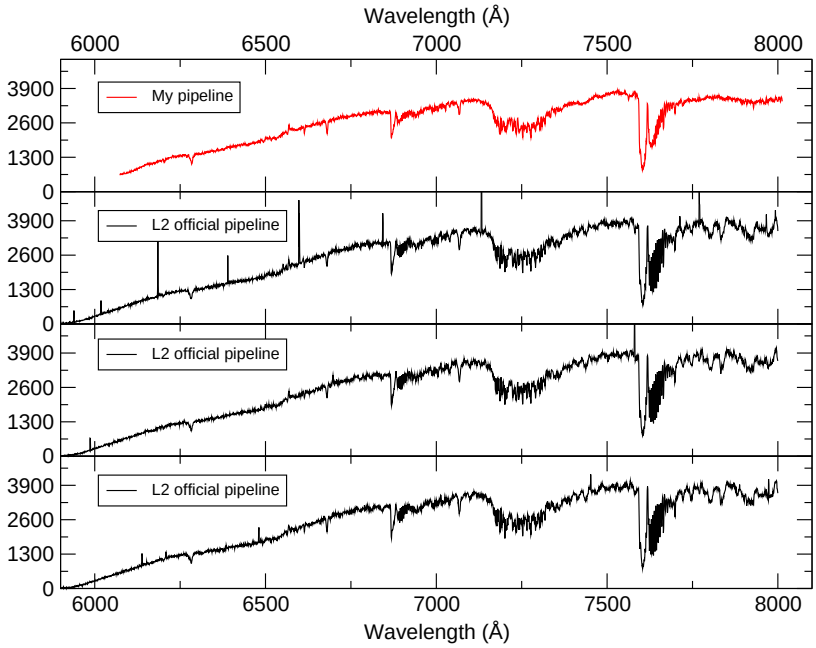

Figure 3.16: AX J1841.0-0535 reduced spectrum with my pipeline, and the L2 official data products (18th of June 2012). That night three spectra of the source where taken, consequently my pipeline averaged these three spectra (as explained in Sec. 3.3.9). Notice the *fringing* on the right part of the spectra, it is $\sim 15\%$ in the official results while in my results it goes down to a $\lesssim 1\%$.

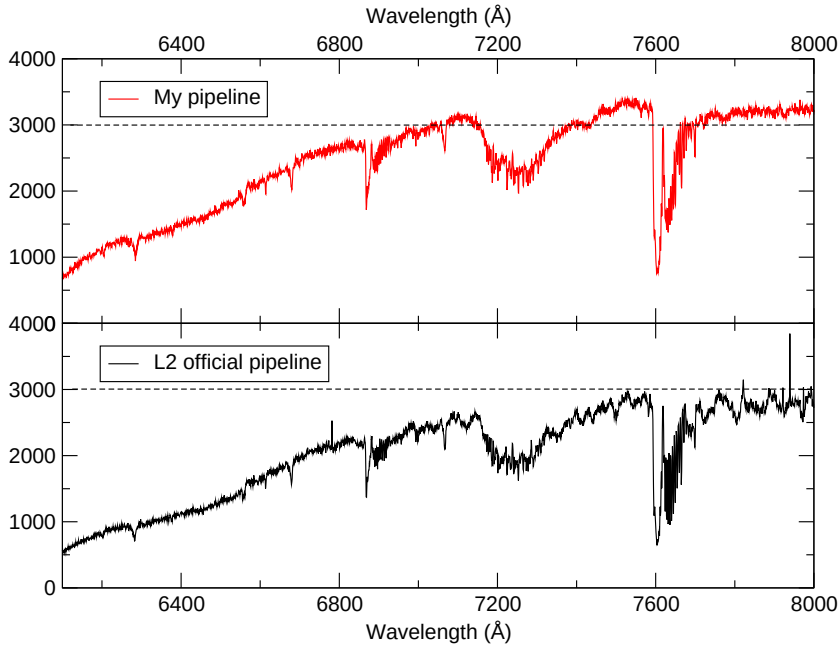

Figure 3.17: AX J1841.0-0535 reduced spectrum with my pipeline, and the L2 official data product (16th of June 2012). Notice the *fringing* on the right part of the spectra, it is $\sim 15\%$ in the official results while in my results it goes down to a $\lesssim 1\%$, the absence of cosmic rays and the higher signal in the result of my pipeline.

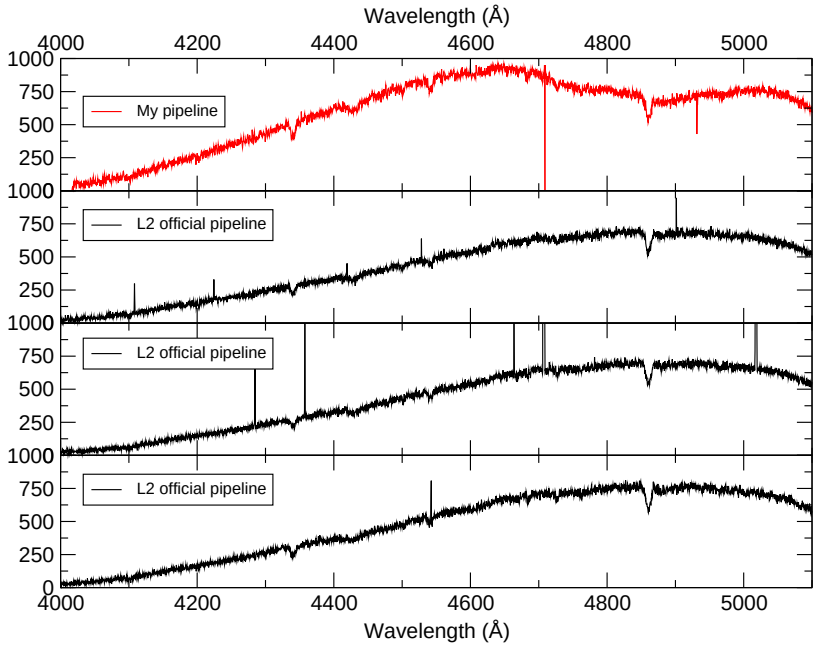

Figure 3.18: Comparison of spectra of LSIII +46°11 reduced with my pipeline and with the L2 official pipeline (17th of December 2011). That night three spectra of the source where taken, consequently my pipeline averaged these three spectra (as explained in Sec. 3.3.9).

CHAPTER 4

IGR J00370+6122[1]

IGR J00370+6122 is a HMXB discovered in December 2003 during a 1.2 Ms INTErnational Gamma Ray Astrophysics Laboratory (INTEGRAL) observation [den Hartog et al., 2004, 2006]. The error circle of this detection included the ROentgen SATellite (ROSAT) source 1RXS J00709.6+612131, which had been identified with the OB star BD $+60°$ 73 = LS I $+61°$161 [Rutledge et al., 2000, Rutledge, 2004]. This source was originally classified as a B1 Ib star by Morgan et al. [1955]. Based on an intermediate-resolution spectrum, Reig et al. [2005] classified BD $+60°$ 73 as a BN0.5 II–III star, without any evidence for a circumstellar disc. This spectral type would place IGR J00370+6122 outside the two main divisions of HMXBs (it is neither a Be star nor a supergiant).

Using data from the ASM, den Hartog et al. [2004] found that the X-ray flux from IGR J00370+6122 is very strongly modulated at 15.665 ± 0.006 days. in't Zand et al. [2007] interpreted its behaviour as a series of outbursts separated by the orbital period. The X-ray light curve is dominated by fast flaring and the absorption column is much higher than the interstellar value, leading to the suggestion that the system is powered by wind accretion in a very eccentric orbit [in't Zand et al., 2007]. Pointed Proportional Counter Array (PCA) on board RXTE observations detected a very likely modulation at 346 ± 6 seconds during a bright X-ray flare, which was interpreted as the detection of the pulsar period from a neutron star [in't Zand et al., 2007]. Grunhut et al. [2014] have recently published an orbital solution that confirms the high eccentricity expected for the system, and suggests a high inclination of the orbit.

[1] This Chapter is an adaptation of the accepted paper for publication in A&A González-Galán et al. [2014].

4.1 Observations

Optical spectra of BD $+60^\circ$ 73 were taken during different observing campaigns between 2009 and 2013 (Table 4.1). The observations were obtained with HERMES and FIES and are composed of 22 high-quality spectra obtained at different epochs spanning more than 3 years of observations.

ASM X-ray light curve is covering more than 15 years of observations, while the BAT light curve covers a total of 9 years (Table 4.2).

4.2 Data analysis & Results

One of the best-quality spectra of BD $+60^\circ$ 73 is shown in Fig. 4.1, where line identifications are also provided. The spectrum was artificially degraded to a resolving power of $R = 4\,000$ for spectral classification. A large number of MK standards, observed with the same instrumentation and subjected to the same procedure, were used for comparison. The spectrum, of much better quality than those used in Reig et al. [2005], indicates a slightly later spectral type $\mathrm{B0.7}$ (based on the ratio of $\mathrm{Si\ III}$ and $\mathrm{Si\ IV}$ lines, the main spectral type indicator) and somewhat higher luminosity. The best spectral type from direct comparison would be $\mathrm{B0.7\ Ib–II}$, with evidence of strong N over-abundance. However, we note that the star is a very fast rotator ($v \sin i \approx 135\,\mathrm{km\,s^{-1}}$; see Sec. 4.2.2), and this is known to generally lead to the assignment of lower luminosity, as the standards rotate more slowly[2]. In view of this, we take $\mathrm{BN0.7\ Ib}$.

4.2.1 Distance

Traditionally, BD $+60^\circ$ 73 has been considered a member of the Cas OB4 association [Humphreys, 1978]. For this association Humphreys [1978] gives a distance modulus $DM = 12.3$, while Garmany and Stencel [1992] give $DM = 12.2$. Photoelectric UBV photometry for BD $+60^\circ$ 73 is provided by Hiltner [1956] and Haug [1970], who give essentially identical values, suggesting no variability ($V = 9.65$). Therefore we can combine the optical photometry of Haug

[2] The number of Galactic early-B supergiants with projected rotational velocities above $80\,\mathrm{km\,s^{-1}}$ is marginal; most of them concentrate around $40 - 80\,\mathrm{km\,s^{-1}}$ [see Fig. 14 in Simón-Díaz and Herrero, 2014].

Table 4.1: Log of high-resolution optical spectra of BD $+60^\circ$ 73.

#	Date	MJD	$T_{\rm exp}$ (s)	Instrument
1	30/10/2009 00:02:06	55135.08	5400	HERMES
2	30/10/2009 23:06:02	55136.04	5400	HERMES
3	31/10/2009 22:27:40	55137.02	5400	HERMES
4	01/11/2009 21:40:26	55137.98	7200	HERMES
5	02/11/2009 22:15:30	55139.01	5400	HERMES
6	03/11/2009 23:11:47	55140.05	5400	HERMES
7	04/11/2009 21:43:40	55140.99	5400	HERMES
8	06/11/2009 23:34:06	55143.06	5400	HERMES
9	09/11/2009 01:09:17	55145.13	5400	HERMES
10	14/06/2011 04:46:43	55726.70	1200	HERMES
11	17/06/2011 04:45:41	55729.70	1200	HERMES
12	19/06/2011 05:11:19	55731.72	1200	HERMES
13	20/06/2011 04:06:44	55732.67	1200	HERMES
14	11/09/2011 01:14:42	55815.56	1200	FIES
15	12/09/2011 01:42:40	55816.58	1200	FIES
16	08/11/2011 22:55:49	55874.46	900	HERMES
17	26/10/2012 00:15:58	56226.52	1200	HERMES
18	26/10/2012 23:13:34	56227.47	1200	HERMES
19	28/01/2013 19:55:47	56321.33	1200	FIES
20	29/01/2013 20:08:48	56322.34	900	FIES
21	30/01/2013 19:45:34	56323.32	900	FIES
22	05/02/2013 20:40:58	56329.36	1300	FIES

Table 4.2: Observation log of X-ray data of IGR J00370+6122.

Date	MJD	Data points	Instrument	Energy range
05/01/1996–31/12/2011	50087–55927	82105 (dwells)	ASM@RXTE	1.5–12.2 keV
05/01/1996–31/12/2011	50087–55927	5407 (daily)	ASM@RXTE	1.5–12.2 keV
15/02/2005–02/06/2014	53416–56445	2690	BAT@Swift	15–50 keV

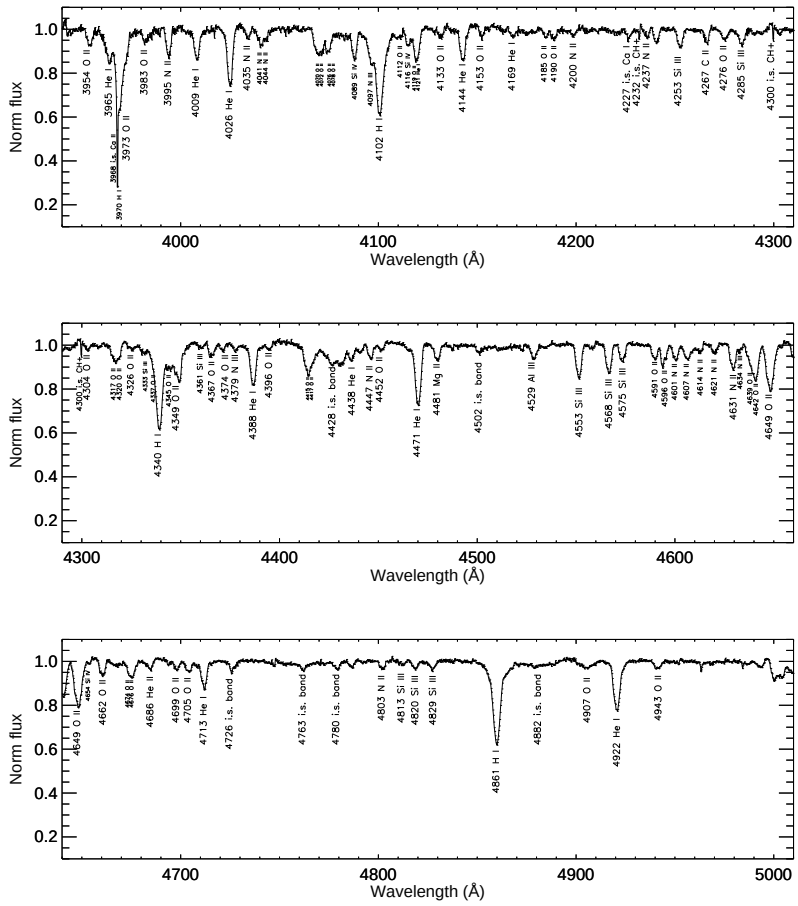

Figure 4.1: Spectrum of BD $+60^{\circ}$ 73 over the classification region, obtained with the FIES spectrograph on September 2011, 11.

[1970] with the near-infrared photometry from 2MASS [Skrutskie et al., 2006]. By using these data as input for the χ^2 code for parametrised modelling and characterisation of photometry and spectroscopy CHORIZOS implemented by Maíz-Apellániz [2004], we found that the extinction to the source can be well reproduced by a standard law with $R = 3.1$.

If we assume an intrinsic colour $(B-V)_0$=-0.20, [interpolating in the calibration of Fitzgerald, 1970], we obtain $E(B-V) = 0.77$. The synthetic spectrum has the same intrinsic $(B-V)_0 = -0.20$. For a standard extinction law, $A_{\rm V} = 2.39$, and then $m_{\rm V} = 7.26$. For a distance of $DM = 12.3$, this leads to an absolute magnitude of $M_{\rm V} = -5.0$ mag. This is a rather low value for a supergiant, though marginally consistent with the spectral type. Absolute magnitude calibrations for a B0.7 Ib star would support a value close to $M_{\rm V} = -5.7$ mag [e.g. Turner, 1980, Humphreys and McElroy, 1984]. However, this luminosity would place BD $+60^\circ$ 73, at a distance of ~ 4 kpc, far away from any spiral arm in this direction [e.g. Negueruela and Marco, 2003].

Another way of estimating the distance to BD $+60^\circ$ 73 is by making use of the interstellar lines in its spectrum to study the radial velocity distribution of interstellar material along its line of sight. We calculate the velocity scale with respect to the LSR by assuming that the motion of the Sun with respect to the LSR corresponds to $+16.6\,{\rm km\,s^{-1}}$ towards Galactic coordinates $l = 53^\circ$; $b = +25^\circ$. In Fig. 4.2, we show the interstellar Na I D lines; both present identical morphologies, with two well-separated components. The Ca II K line is also shown, displaying a very similar morphology.

In the Na I D lines, one of the components is centred on $-4\,{\rm km\,s^{-1}}$, extending from low positive values to $\approx -12\,{\rm km\,s^{-1}}$. The second component is centred on $-24\,{\rm km\,s^{-1}}$, and has a shoulder extending to $\approx -35\,{\rm km\,s^{-1}}$. The K I 7699Å line, which is not saturated, has two narrow components, centred on $-8\,{\rm km\,s^{-1}}$ and $-21\,{\rm km\,s^{-1}}$. These two components are readily identified with absorbing clouds located in the Local arm and the Perseus arm.

In Fig. 4.3, we show the dependence of radial velocity with distance in the direction to BD $+60^\circ$ 73 ($l = 121\overset{\circ}{.}2$, $b = -01\overset{\circ}{.}5$) according to two widely used Galactic rotation curves. One is computed assuming circular galactic rotation and adopting the rotation curve of Brand and Blitz [1993], with a circular rotation velocity at the position of the Sun ($d_{\rm GC} = 8.5\,{\rm kpc}$) of $220\,{\rm km\,s^{-1}}$. The other one follows the rotation curve of Reid et al. [2009]. Along this line of sight, all

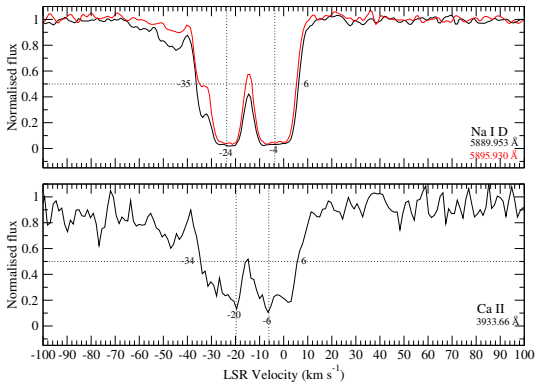

Figure 4.2: *Top:* Interstellar Na I D doublet (5890Å full line, 5896Å dashed line) in the spectrum of BD +60° 73. *Bottom:* The Ca II K line at 3934Å displaying a similar morphology, but rather lower SNR.

LSR velocities should be negative and increase with distance. Absorption at positive velocities must be therefore caused by clouds in the immediate vicinity of the Sun. The nearby ($l = 120.^{\circ}8$, $b = +0.^{\circ}1$) B1 Ia supergiant κ Cas, located at a distance $d \sim 1$ kpc [Humphreys, 1978], only shows the low-velocity component. Its lines have exactly the same profile on the positive side, though they are broader on the negative side and more saturated, as this object is closer to the Galactic Plane.

The core of the high velocity component is located around $v_{\rm LSR} = -24\,{\rm km\,s^{-1}}$. This velocity corresponds to a distance $d \approx 2.5$ kpc according to the rotation curve of Brand and Blitz [1993] and ≈ 1.8 kpc according to the rotation curve of Reid et al. [2009]. Both distances indicate that this component arises from material in the Perseus arm. There are very large deviations from circular motion in the Perseus arm [Reid et al., 2009], but we can use objects with independent distance determinations to constrain the distance to the absorbing material. The nearby H II region Sh2-177 ($l = 120.^{\circ}6$, $b = -0.^{\circ}1$) has a $v_{\rm LSR} = -34\,{\rm km\,s^{-1}}$, while Sh2-173 ($l = 119.^{\circ}4$, $b = -0.^{\circ}8$) has $v_{\rm LSR} = -35\,{\rm km\,s^{-1}}$ [in both cases, undisturbed gas velocities; Fich and Blitz, 1984]. Both H II regions have published distances compatible with the estimates for Cas OB4.

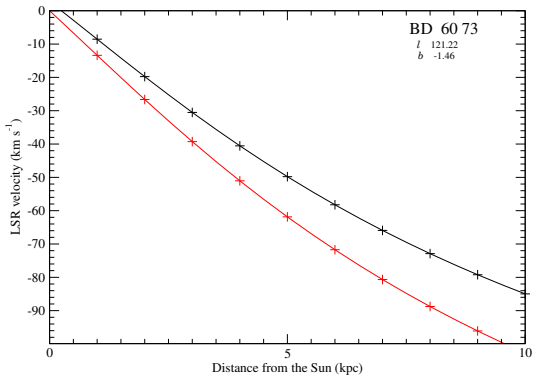

Figure 4.3: Radial velocity with respect to the local standard of rest (LSR) due to galactic rotation as a function of distance, using the rotation curve of Brand and Blitz [1993, black curve] and that of Reid et al. [2009, red curve].

More recently, Russeil et al. [2007] has estimated a distance $d = 3.1$ kpc for Sh2-173 ($DM = 12.5$), which they assume also valid for Sh2-172 and Sh2-177. We can assume that the material producing absorption the feature centred on $\approx -33\,\mathrm{km\,s^{-1}}$ must be at the same distance. In view of this, BD $+60°$ 73 must be at least at the same distance, and likely not much further away.

There is some indication in all the interstellar lines of a weak component at $v_{\mathrm{LSR}} \approx -45\,\mathrm{km\,s^{-1}}$. However, the existence of this component would not necessarily imply a higher distance. Along this line of sight, there are very large deviations from circular motion, and the nearby H II region Sh2-175 ($l = 120.^{\circ}4$, $b = +2.^{\circ}0$), with a distance estimate of 1.7 kpc, has a velocity $v_{\mathrm{LSR}} = -50\,\mathrm{km\,s^{-1}}$ [Fich and Blitz, 1984]. Therefore, if this weak component at high velocities is real, it is likely to arise from foreground material associated to this H II region. In view of this, we accept a distance of 3.1 kpc for BD $+60°$ 73. This implies an absolute magnitude $M_{\mathrm{V}} = -5.2$ mag.

4.2.2 FASTWIND model fit

We first applied the IACOB-BROAD IDL (Interactive Data Language) tool described in Simón-Díaz and Herrero [2014] to estimate the projected rotational velocity ($v \sin i$) of the star and the amount of macroturbulent broadening ($\Theta_{\rm RT}$) affecting the line-profiles. The analysis of the Si III 4553Å line resulted in the combination ($v \sin i$, $\Theta_{\rm RT} = (135, 67)$ km s^{-1} providing the best fitting solution. While such a large macroturbulent broadening contribution is commonly found in early B supergiants, the projected rotational speed of this star is very high compared to objects of similar spectral type [e.g. Markova et al., 2014, Simón-Díaz and Herrero, 2014, and references therein].

A quantitative spectroscopic analysis was subsequently performed by means of FASTWIND (see Sec. 2.2.2 of Chapter 2). An initial analysis was done following the strategy described in Castro et al. [2012], based on an automatised χ^2 fitting of synthetic FASTWIND spectra including lines from H, He I-II, Si II-IV, Mg II, C II, N II-III, and O II to the global spectrum between 3900 and 5100Å. The parameters and abundances derived were then carefully revised by using a more refined grid of FASTWIND models specifically constructed for this study and a *by eye* comparison of the observed and synthetic spectra for individual diagnostic lines of interest (see Table 4.3). In both cases the value of the wind-strength Q-parameter was fixed to a value $\log Q = -13.0$, because Hα shows weak and variable emission (see Fig. 4.9), rendering the determination of wind properties rather uncertain. The line-broadening $v \sin i$ and $\Theta_{\rm RT}$ parameters were fixed to the values indicated above during the analysis process.

The parameters obtained are summarized in Table 4.4. We found very good agreement (within the uncertainties) between the global-χ^2 and the individual-line *by eye* solutions. The best fit is obtained for $T_{\rm eff} = 24\,000$ K and $\log g = 2.90$. The temperature value is typical for the spectral type. The low effective gravity fully supports the supergiant classification. Because of the high rotational velocity, the effective gravity has an important centrifugal contribution. When corrected for this effect, the actual gravity becomes $\log g_{\rm c} = 3.00$ [Repolust et al., 2004].

The He relative abundance ($Y_{\rm He} = N({\rm He})/N({\rm H})$) is very poorly constrained. Depending on the diagnostic line considered and the value of the microturbulence, the derived abundance ranges from 0.15 to 0.30. Globally, the best fitting solution is obtained for $Y_{\rm He} = 0.25$. This high He abundance is indicative of a

Table 4.3: Diagnostic lines considered in the *by eye* individual-line analysis (see text for explanation).

Hβ, Hγ, Hδ
He I 4471, 4387, 5875, 6678
Si III 4552, 4567, 4574, Si IV 4116
O II 4661, Mg II 4481, C II 4267, N II 3995

Table 4.4: Stellar parameters derived from the spectroscopic analysis (upper panel), and calculated using the photometry of Haug [1970] and assuming $d = 3.1$ kpc (lower panel).

$v \sin i$ (km s^{-1})	135 ± 7
$\Theta_{\rm RT}$ (km s^{-1})	67 ± 7
$T_{\rm eff}$ (K)	$24\,000 \pm 1\,500$
$\log g$	2.9 ± 0.2
$\xi_{\rm t}$ (km s^{-1})	15 ± 5
$Y_{\rm He}$	0.25 ± 0.10
$\log Q$	-13.0 (assumed)
d(kpc)	3.1 ± 0.3
$M_{\rm V}$	-5.2 ± 0.3
R_* ($R_\odot$)	16.5 ± 2.3
$\log(L_*/L_\odot)$	4.91 ± 0.16
$M_*/M_\odot$	10 ± 5

Table 4.5: Chemical abundances in $\log\left(\frac{N(\mathrm{X})}{N(\mathrm{H})}\right) + 12$ resulting from the FASTWIND spectroscopic analysis of BD $+60^\circ$ 73. We also include for comparison the set of chemical abundances derived by Nieva and Przybilla [2012] for B-type stars in the Solar neighbourhood, and the solar abundances from Asplund et al. [2009].

Species	BD $+60^\circ$ 73	B-type stars	Sun
Si	7.55 ± 0.15	7.50 ± 0.05	7.51 ± 0.03
Mg	7.55 ± 0.15	7.56 ± 0.05	7.60 ± 0.04
C	7.75 ± 0.15	8.33 ± 0.04	8.43 ± 0.05
N	8.40 ± 0.15	7.79 ± 0.04	7.83 ± 0.05
O	8.75 ± 0.15	8.76 ± 0.05	8.69 ± 0.05

high degree of chemical evolution. The other abundances derived (C, N, O, Si, Mg) are summarised in Table 4.5. We also include for comparison the set of chemical abundances for B-type stars in the Solar neighbourhood derived by Nieva and Przybilla [2012], and the solar abundances from Asplund et al. [2009]. While Si, Mg and O abundances are compatible with the Solar ones and those proposed by Nieva and Przybilla [2012] as cosmic abundance standard, the star appears N-enhanced, and C-depleted, suggesting a fair degree of chemical evolution, in agreement with the He abundance. The values are similar to those of very luminous (class Ia) early-B supergiants [Crowther et al., 2006].

Stellar parameters can be derived by scaling the absolute magnitude of the synthetic spectrum to the observed M_{V}. With this method, and using the values found above for the effective temperature and the effective gravity corrected for rotation, we calculate the parameters listed in the bottom panel of Table 4.4. Alternatively, the mass can be estimated by placing the star on evolutionary tracks. In Fig. 4.4, we compare the position of BD $+60^\circ$ 73 with the evolutionary tracks of Brott et al. [2011] for the assumed distance $d = 3.1$ kpc. We show tracks with both zero and high initial rotational velocity. The position of BD $+60^\circ$ 73 is compatible with the tracks for an initial mass M_* in the $17 - 18\,\mathrm{M}_\odot$ range close to the end of hydrogen core burning. Mass loss until this point is not very important, and so the present-day mass should be only a fraction of a solar mass lower. When the error bars are taken into account, we come to an evolutionary present-day mass of $17 \pm 2\,\mathrm{M}_\odot$.

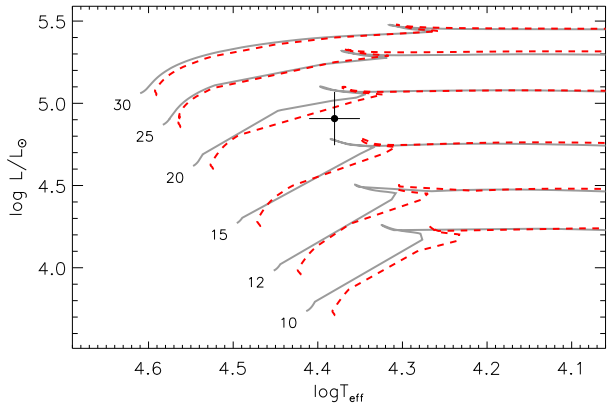

Figure 4.4: Evolutionary tracks and the position of BD $+60°$ 73 in the Hertzsprung-Russell diagram. The evolutionary tracks are from Brott et al. [2011], for initial $v_{\rm rot} = 0$ (grey, continuous) and $v_{\rm rot} = 377\,{\rm km\,s^{-1}}$ (red, dashed).

4.2.3 Orbital solution

The radial velocity points have been obtained by cross-correlating the observed spectra with a FASTWIND synthetic spectrum corresponding to the parameters and abundances indicated in Tables 4.4 and 4.5. The IRAF routine *fxcor* was used to this aim. For the cross-correlation H and He lines, which may be contaminated by residual wind emission in an early-type supergiant [e.g. van der Meer et al., 2007], have been avoided, and only the region of the spectrum between 4540Å and 4660Å has been used. This region contains no He I or H I lines, but numerous metallic lines (mostly Si III, O II and N II), which are more suitable for radial velocity determinations, because they arise in deep photospheric layers. The individual radial velocity measurements are listed in Table 4.6.

We searched for periodicities within the $V_{\rm rad}$ points using different algorithms available in the *Starlink* package PERIOD [Dhillon et al., 2001]. All of them resulted in a highest peak at values compatible within their errors, and also compatible with the periodicity found in the X-ray light curve [den Hartog et al., 2004]. Figure 4.5 shows the result obtained with the algorithm CLEAN (implemented in PERIOD), which is particularly useful for unequally spaced data. This

Table 4.6: Radial velocities of BD $+60^{\circ}$ 73 sorted by phase. The first column of this table is the number of the observation from Table 4.1. The second column is the phase of the observation, according to the orbital solution described in Table 4.7 (measurements have been sorted using this parameter). The third column is the radial velocity. The last column shows the residuals from the radial velocity curve calculated (see Fig. 4.6) and the observational points.

#	Phase	$V_{\rm rad}$ (km s^{-1})	O-C (km s^{-1})
10	0.0055	-102.1 ± 5.5	3.9
20	0.0390	-98.8 ± 6.4	-3.5
21	0.1018	-81.7 ± 7.5	-2.2
11	0.1970	-67.1 ± 1.6	4.3
1	0.2290	-73.5 ± 0.8	-3.2
2	0.2938	-72.2 ± 0.7	-3.2
12	0.3259	-68.4 ± 2.1	0.2
3	0.3525	-68.0 ± 0.7	0.4
13	0.3869	-69.3 ± 1.9	-0.9
4	0.4143	-66.2 ± 0.8	2.3
16	0.4404	-65.7 ± 1.2	2.3
5	0.4797	-62.7 ± 0.8	6.1
22	0.4875	-73.7 ± 0.7	-4.8
6	0.5460	-72.2 ± 0.8	-2.7
7	0.6060	-75.2 ± 0.8	-4.6
14	0.6793	-70.3 ± 0.8	2.1
8	0.7358	-72.0 ± 0.7	2.6
15	0.7444	-79.9 ± 0.6	-5.0
9	0.8705	-84.4 ± 0.9	0.3
17	0.9204	-92.3 ± 1.3	0.8
19	0.9747	-107.1 ± 1.1	-1.1
18	0.9815	-106.0 ± 1.2	1.0

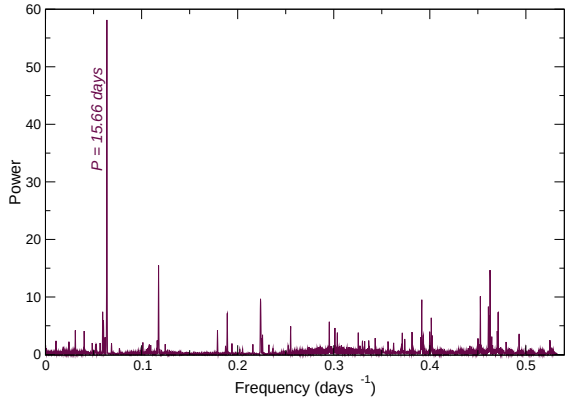

Figure 4.5: "Clean" periodogram of the radial velocity points obtained with the PERIOD package within the *Starlink* environment.

algorithm basically deconvolves the spectral window from the discrete Fourier power spectrum producing a *"clean"* power spectrum. A significance calculation of the value obtained was performed using the SIG routine of PERIOD, applying 1000 Monte Carlo simulations. The result of this significance calculation, representing the probability that the period is not actually equal to the value quoted, is $FAP2 \sim 0.7\%$. Therefore we can assume that the period of 15.66 days, which is found both from the X-ray observations [den Hartog et al., 2004], and from the radial velocity of the optical component, is the orbital period of the binary system.

A radial velocity curve was obtained by fitting the $V_{\rm rad}$ points using SBOP as described in Sec. 2.2.4 of Chapter 2. This curve is shown in Fig. 4.6, where the residuals from the observed data points to the theoretical curve are also shown. The parameters of this best-fit curve are shown in Table 4.7. The orbital period, $P_{\rm orb} = 15.6610 \pm 0.0017$ d, is identical within the errors to the 15.665 ± 0.006 d periodicity found in the X-ray light curve by in't Zand et al. [2007], but slightly smaller and more precise. All parameters are well determined with the exception of the mass function, which has an error $\approx 30\%$.

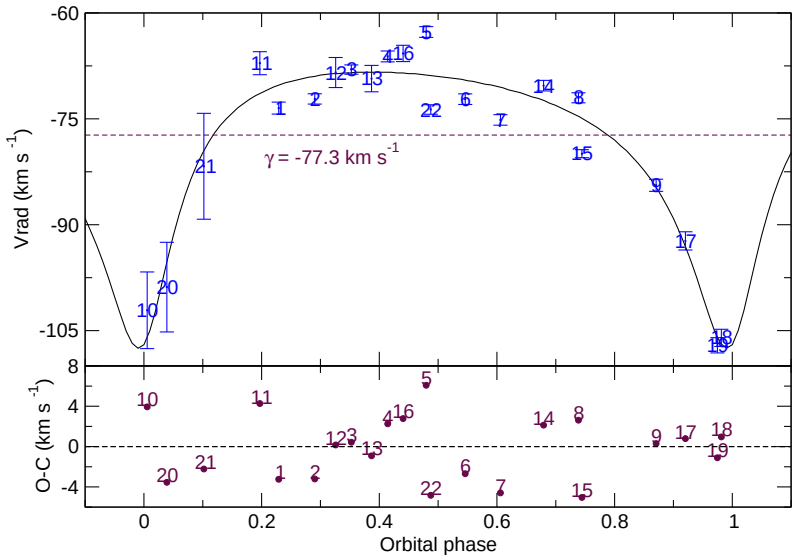

Figure 4.6: *Top:* Best-fit radial velocity curve and real data folded on the 15.661 d period derived from our data analysis. Phase 0 corresponds to periastron. *Bottom:* Residuals from the observed radial velocity points to best-fit radial velocity curve.

Table 4.7: Orbital parameters obtained by fitting the radial velocity points using Lehmann-Filhès method implemented in SBOP.

T_0(HJD-2450000)	5084.52 ± 0.37
$P_{\rm orb}$ (days)	15.6610 ± 0.0017
e	0.56 ± 0.07
γ (km s^{-1})	−77.3 ± 1.4
K_0 (km s^{-1})	19.6 ± 1.9
ω (degrees)	194 ± 9
$a_0 \sin i$ (km)	(3.5 ± 0.4) 10^6
$f(M)$ ($M_\odot$)	0.0069 ± 0.0023

The relatively large uncertainty of the mass function is connected to the moderately large residuals in the orbital fit. In other HMXBs, such as Vela X-1, large residuals are also seen, showing a modulation at multiples of the orbital frequency [Quaintrell et al., 2003]. This modulation led to the suggestion that the oscillations were tidally induced by the companion. Strong radial velocity excursions are also seen in the peculiar transient IGR J11215−5952 [Lorenzo et al., 2014] and in the HMXB GX 301−2 [Kaper et al., 2006], both of which have very massive and luminous counterparts. Since macroturbulence is relatively large in BD $+60°73$, and a connection has been claimed between pulsations and macroturbulence broadening [e.g. Simón-Díaz et al., 2010], it is tempting to suspect that the large residuals in the fit to the radial velocity curve may be connected to pulsations. We have searched for periodicities within these residuals, finding no obvious results, though the number of measurements is probably too small to rule out completely the possibility of tidally induced pulsations in BD $+60°73$.

4.2.4 X-ray light curves

The X-ray light curves from the ASM and BAT have been searched for periodicities between 3 and 300 days, using different algorithms available within the *Starlink* package PERIOD, and also using an epoch folding analysis implemented in the software DES7 [see Larsson, 1996, for details on the method implemented on this software]. Analyses of the ASM dwell-by-dwell and daily-average light curves and the BAT light curve give consistent results, finding values for the period (see Fig. 4.7) that are compatible among themselves within their respective error bars, compatible with the period found from the radial velocity points, and also with the X-ray period published in in't Zand et al. [2007] or in den Hartog et al. [2004].

We have performed the folding of these light curves on all the periods that we have found, and also on the value of $P = 15.6627 \pm 0.0042$ days published by in't Zand et al. [2007]. All the foldings are similar to each other in shape; the count rate has a clear maximum around $\phi = 0.2$ (using the ephemeris from the radial velocity curve solution) and presents a broad flat minimum around apastron. All the foldings present some evidence of a flux drop just before the maximum, close to periastron. The highest peak is found for the folding on the orbital period derived from the radial velocity curve (which also has the smallest formal error). Therefore we interpret this as the most accurate $P_{\rm orb}$.

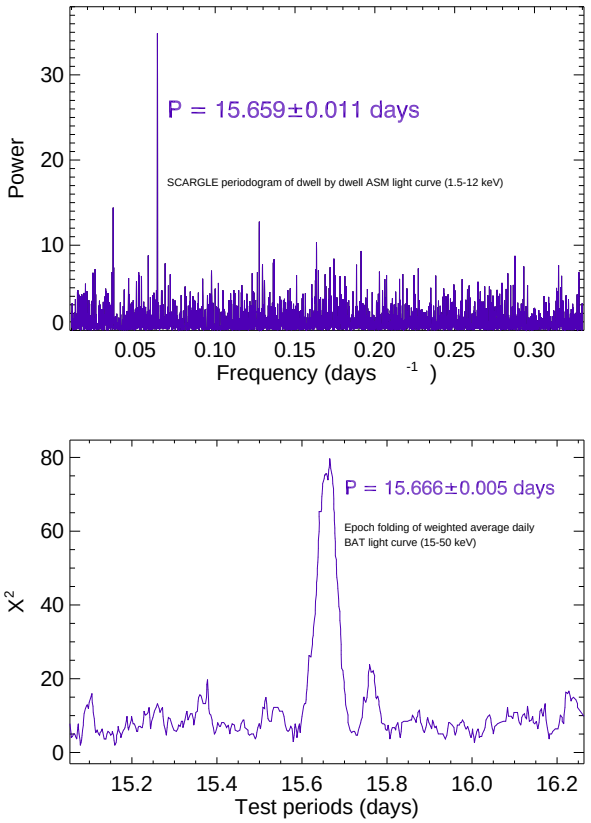

Figure 4.7: Examples of the period searching within the ASM and BAT X-ray light curves of IGR J00370+6122. *Top panel:* SCARGLE periodogram obtained with PERIOD for the 'raw' (dwell by dwell) ASM light curve. *Bottom panel:* Epoch folding of the weighted-average daily BAT light curve.

Fig. 4.8 shows the folding of the daily average ASM light curve (top panel) and the folding of the BAT daily light curve (bottom panel) over this period. In both cases, the folding has been performed with DES7, and the individual points have been weighted according to their errors. Phase zero of these foldings corresponds to the periastron passage, while the red dashed lines indicate the time of eclipse according to the SBOP orbital solution.

The maximum of the folded ASM light curve is around orbital phase $\phi = 0.25$ (~ 4 days after periastron). The shape of the light curve is very similar to that shown in in't Zand et al. [2007] for data taken until November 2006, in spite of the slightly different folding periods. The maximum of the BAT folded light curve is reached slightly before $\phi = 0.2$, which means less than 3 days after periastron passage. This suggests that the maximum luminosity in the hard X-rays (energy range $15 - 50$ keV) may occur some time before the maximum in the softer band (energy range $1.5 - 12$ keV). The BAT light curve is very similar in shape to the ASM light curve, and also quite similar to the *INTEGRAL*/ISGRI light curve in the $20 - 45$ keV range shown by in't Zand et al. [2007], who also found some difference in shape between the soft and hard X-ray folded light curves, along with a delay between the maximum flux of the ISGRI and ASM folded light curves, with the ISGRI maximum taking place before the ASM one, which is also in accordance with our results.

The minimum of the ASM light curve is at around 0.12 cts/s. According to Remillard and Levine [1997], the ASM has a bias of $+1$ mCrab and systematics make difficult detections below 5 mCrab (corresponding to ~ 0.08 cts/s). Therefore the source is very likely detected outside the outbursts, at a level ~ 10 times lower than the peak luminosity, as anticipated by in't Zand et al. [2007]. This seems to be borne out by the BAT light curve. In any case, the pointed observations with the PCA reported by in't Zand et al. [2007] show that these integrated fluxes represent the average of many flares superimposed on a quiescence flux at least ~ 50 times lower. Therefore, the folded light curves merely represent the average behaviour, in the sense that the peaks of some flares have much higher values than the peak of the folded light curves.

Given the spectral parameters determined by in't Zand et al. [2007] and our value of the distance (3.1 kpc), we can make an estimation of the X-ray luminosity in both energy ranges. Assuming a power law spectrum with an absorption column $N_{\rm H}$=7×10^{22} cm^{-2}, a photon index $\Gamma = 2.3$ for the ASM energy

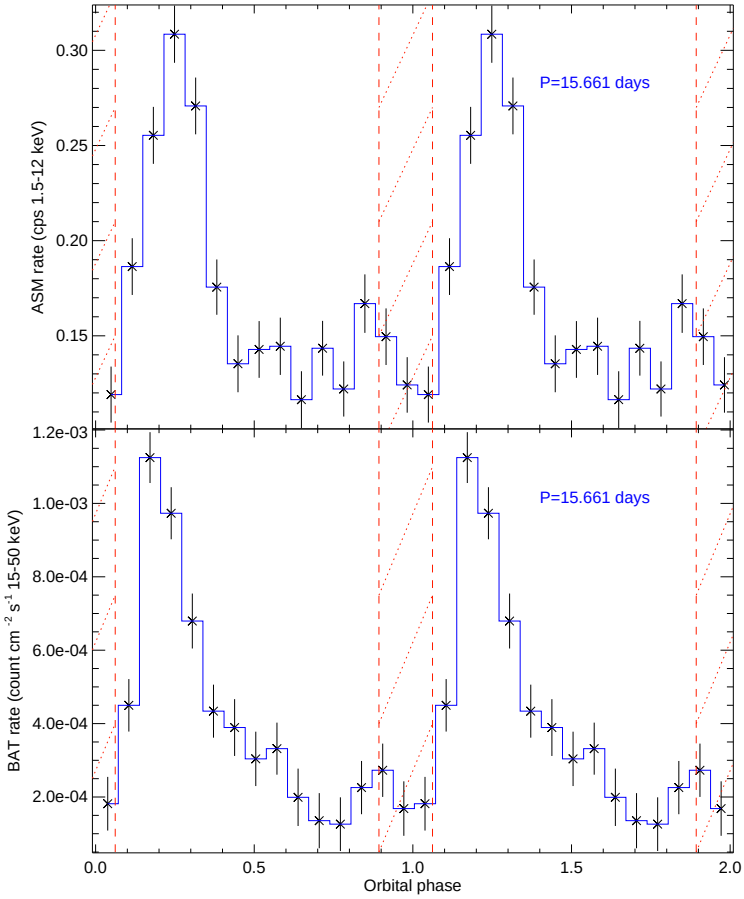

Figure 4.8: Average folded light curves in two energy ranges over the orbital period ($P_{\rm orb}$ = 15.6610 ± 0.0017 days). Phase zero corresponds to the periastron passage in the SBOP orbital solution. Red dashed lines indicate the time of possible eclipse according to this solution ($\phi \epsilon [0.86 - 1.06]$). *Top panel:* Weighted folded ASM light curve (from daily average datapoints). *Bottom panel:* Weighted folded BAT light curve (from daily average datapoints).

range $(1.5 - 12\,\mathrm{keV})$, and a $\Gamma = 1.84$ for the BAT energy range $(15 - 50\,\mathrm{keV})$, we determine the maximum and minimum luminosities of the average foldings as $L^{\mathrm{MIN}}_{1.5-12\ \mathrm{keV}} \sim 9.7 \times 10^{34}\ \mathrm{erg\,s^{-1}}$, $L^{\mathrm{MAX}}_{1.5-12\ \mathrm{keV}} \approx 2.5 \times 10^{35}\ \mathrm{erg\,s^{-1}}$, $L^{MIN}_{15-50\ \mathrm{keV}} \sim 8.5 \times 10^{34}\ \mathrm{erg\,s^{-1}}$, and $L^{\mathrm{MAX}}_{15-50\ \mathrm{keV}} \approx 4.7 \times 10^{35}\ \mathrm{erg\,s^{-1}}$.

4.2.5 Evolution of Hα

The X-ray behaviour of IGR J00370+6122 seems typical of wind-fed accreting sources. The shape of Hα (Fig. 4.9), on the other hand, is reminiscent of a Keplerian geometry, and similar to those seen in shell Be stars with very small or incipient discs [e.g. o And; Clark et al., 2003]. This kind of line profiles, however, is also seen in OB supergiants [e.g. HD 47240; Morel et al., 2004]. Since the neutron star must come quite close to the stellar surface at periastron, given the high eccentricity, the presence of weak emission components could be the result of mass being lost from the B supergiant and settling into some kind of disc configuration.

To explore this possibility, Fig. 4.9 shows the evolution of Hα ordered by orbital phase. Very similar profiles are seen at different phases, while relatively different profiles are seen at almost the same phase. This suggests that the shape of Hα is not driven by orbital effects. To quantify this assertion, we measured the FWHM of the absorption trough by fitting a Gaussian profile to the region between 6555 and 6570Å. The range was the same in all spectra for consistency. Figure 4.10 shows the evolution of the $FWHM$ with time and with orbital phase. The changes in the line shape seem to occur on a time-scale of several days, and not to depend on the orbital phase. Therefore we conclude that the variability in Hα is mostly due to the stellar wind, and does not reflect episodic mass loss locked to the orbital period.

4.3 Discussion

We have determined the astrophysical parameters of BD $+60^{\circ}$ 73 and obtained an orbital solution for the IGR J00370+6122 binary system. To understand its implications for the physics of wind-accreting HMXBs we must estimate the range of parameters allowed by our solution.

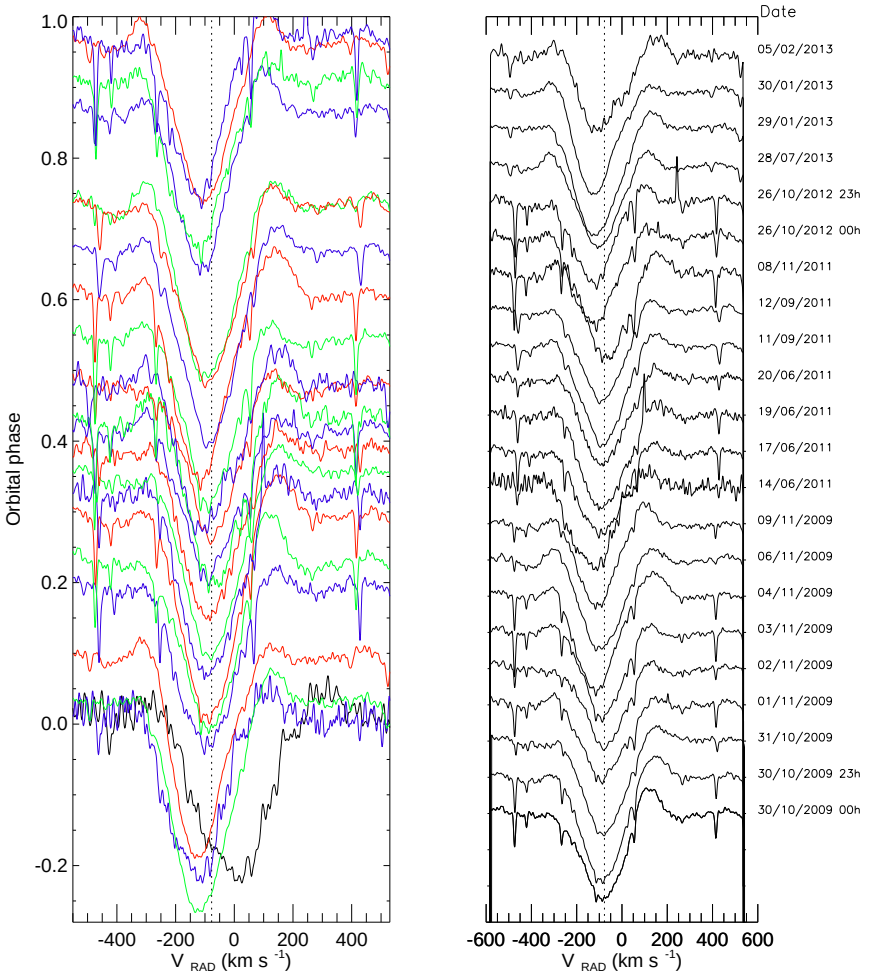

Figure 4.9: Temporal evolution of the normalised Hα profile, sorted by orbital phase (*left*) or in time sequence, with the date indicated (*right*).

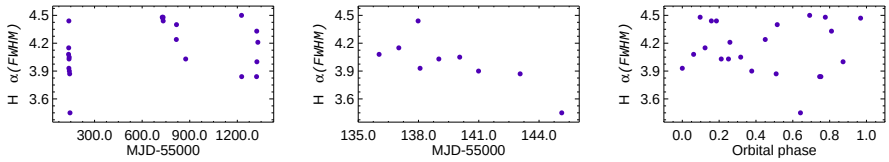

Figure 4.10: Full-width half-maximum ($FWHM$; in Å) of the Hα line. *Left:* Evolution with time for our whole data set. *Middle:* Evolution with time in the 2009 campaign with HERMES. *Right:* Evolution with the orbital phase of the binary system.

4.3.1 Orbital parameters

The mass of the optical companion may be determined from the atmosphere parameters. In many cases, supergiants show a discrepancy between spectroscopic and evolutionary masses [Herrero et al., 1992, Herrero, 2007]. In the case of BD $+60°$ 73, the discrepancy is moderate. With a spectroscopic mass $M_* = 10 \pm 5\,\mathrm{M}_\odot$, and an evolutionary mass $M_* = 17 \pm 2\,\mathrm{M}_\odot$, the values are compatible at slightly above $1\,\sigma$. As the spectroscopic value has a very strong dependence on the value of $\log g$, we favour a mass $\sim 15\,\mathrm{M}_\odot$, fully within typical values for a low-luminosity supergiant [e.g. Markova and Puls, 2008]. This mass is lower than those typically found in calibrations for the spectral type [e.g. $22\,\mathrm{M}_\odot$ as assumed by Grunhut et al., 2014] owing to its relatively low luminosity. The stellar radius, $16.5\,\mathrm{R}_\odot$, is again smaller than typical for the spectral type due to the same reason (relatively low luminosity).

Unfortunately, we cannot constrain the mass of the NS, as a pulse phase analysis does not exist. Masses of NSs in HMXBs range from $1.1\,\mathrm{M}_\odot$ in SMC X-1 [van der Meer et al., 2007] to $1.9\,\mathrm{M}_\odot$ in Vela X-1 [Quaintrell et al., 2003]. Since the mass function has a large relative uncertainty, we cannot impose strong constraints. Figure 4.11 shows the range of possible masses for the neutron star, as a function of the mass of the companion and the inclination. A companion mass $\sim 15\,\mathrm{M}_\odot$ rules out inclinations $\leq 45°$ (which would require NS masses $M_\mathrm{X} \sim 2\,\mathrm{M}_\odot$), and indicates an inclination not very far from $i \approx 60°$ for a canonical $M_\mathrm{X} = 1.44\,\mathrm{M}_\odot$. As an illustration, Fig. 4.12 shows the range of possible mass values allowed by the uncertainty in $f(M)$ when we fix $i = 60°$. We see that for a given value of the companion mass, for instance $M_* = 15\,\mathrm{M}_\odot$, a wide range of values is allowed for the neutron star mass $M_\mathrm{X} = 1.3 - 1.6$. In view of this, for the rest of the discussion, we will assume a nominal value of $M_\mathrm{X} = 1.44\,\mathrm{M}_\odot$.

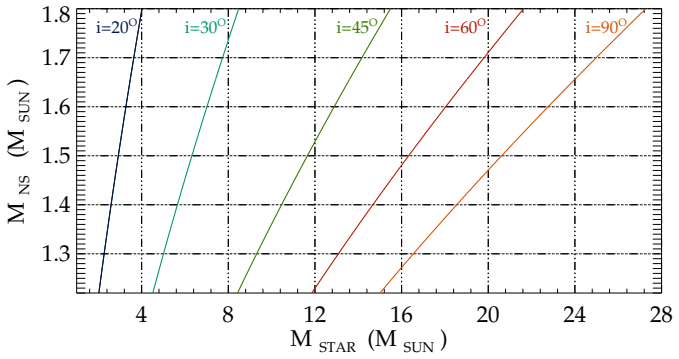

Figure 4.11: Relations between the supergiant mass and neutron star mass. Lines of constant orbital inclination constructed from the mass function are labelled.

A more stringent constraint on the inclination may be obtained from the likely presence of an eclipse in the folded X-ray light curves. Even though, given the very low out-of-peak fluxes, the detection cannot be statistically significant, all soft and hard X-ray light curves show evidence for a drop in flux just before the main peak. As shown in Fig. 4.8, this drop coincides with the time of possible eclipse according to our orbital solution. Therefore we consider the existence of an eclipse likely. If this is actually the case, the inclination of the system must be $\geq 60°$. In particular, for the canonical $M_{\rm X} = 1.44\,{\rm M}_{\odot}$, and our values of $M_* = 15\,{\rm M}_{\odot}$ and $R_* = 17\,{\rm R}_{\odot}$, the inclination must be $i \geq 71°$. This inclination value agrees with $i \sim 72°$ proposed by Grunhut et al. [2014], even though they assume a much larger radius ($R_* = 35\,{\rm R}_{\odot}$) than we derive ($R_* = 16.5\,{\rm R}_{\odot}$). As we cannot constrain the duration of the eclipse, we cannot constrain any further the inclination, but values as high as $i = 75°$ are easily compatible with the masses discussed here (see Fig. 4.11). With these masses and the eccentricity found in Sec 4.2.3, the periastron distance is $r = 36\,{\rm R}_{\odot}$, i.e. $2.1\,{\rm R}_*$. The orbit corresponding to these parameters is displayed in Fig. 4.13.

Comparing our orbital solution with the solution found by Grunhut et al. [2014], all the parameters are compatible with each other within errors (mass function, systemic velocity, semi-amplitude, etc) except for the time of periastron

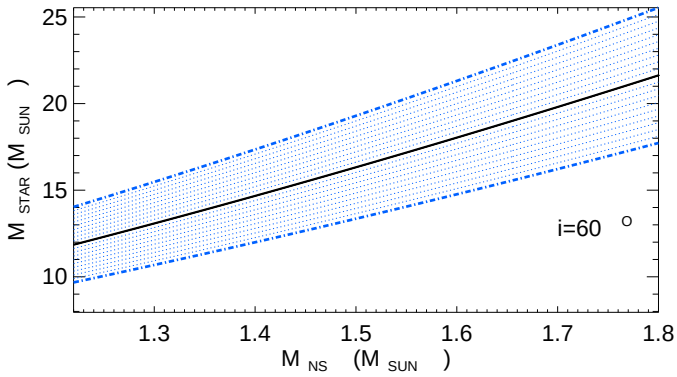

Figure 4.12: Relation between the supergiant mass and the neutron star mass for $i = 60°$. The shaded area represents the range of values allowed within one standard deviation for our value of $f(M)$.

passage. Time of periastron passage in Grunhut et al. [2014] differs by ~ 0.1 phases (according to our ephemeris) from our value. The two values, however, are consistent within errors at the $2 - \sigma$ level, which represents a good agreement if we take into account the ~ 133 orbital cicles between the two dates. The values of the eccentricity are compatible with each other, confirming the high eccentricity. Grunhut et al. [2014] have fixed the orbital period value to that of in't Zand et al. [2007], while we have calculated an orbital period through a periodogram of the radial velocity measurements and the X-ray light curves, and refined the value via the fitting of the orbital solution with SBOP. Therefore we expect our value of the orbital period to be more accurate than that of in't Zand et al. [2007]. In conclusion, Grunhut et al. [2014] find a totally compatible orbital solution using a completely independent data set. We can thus consider the orbital parameters of this HMXB firmly determined.

4.3.2 Evolutionary context

The stellar properties of BD $+60°$ 73, and in particular its high level of chemical evolution, are rather unusual. The star displays a very high $v \sin i$ for a supergiant. In addition, both the He abundance and the $\mathrm{N/C}$ ratio are typical of stars displaying a high degree of processing, such as $\mathrm{B\,Ia}$ supergiants

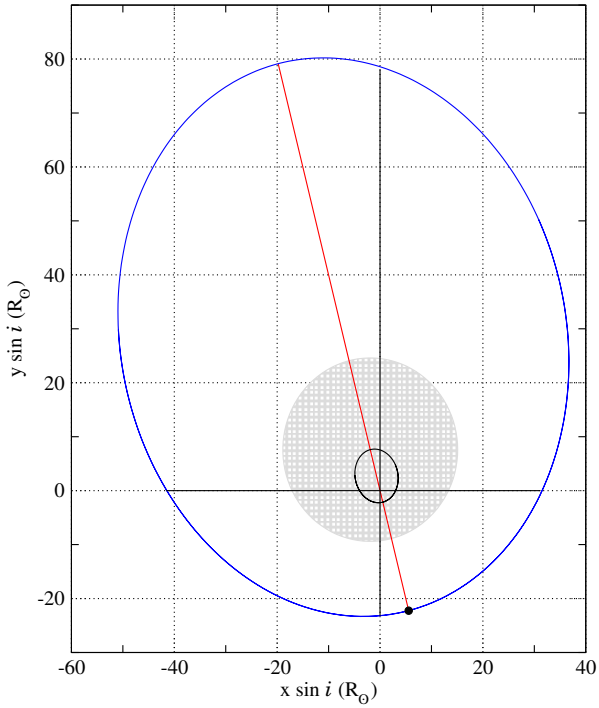

Figure 4.13: Relative orbit of the compact object around the optical star in IGR J00370+6122 as seen from above the orbital plane. The position of periastron is indicated and joined to the apastron by the straight line depicting the major axis of the orbit. The shaded area signals the approximate size of the supergiant, and the small ellipse inside it represents its orbital motion around the centre of mass. The coordinates are in solar radii and represent projected distances.

[e.g. Crowther et al., 2006]. It is possible to relate the high level of chemical evolution to the high rotational velocity, assuming that it is the result of mass transfer from the progenitor of the neutron star prior to its supernova explosion. In classical models for the formation of SGXBs, the original primary transfers mass to the secondary, leading to its "rejuvenation" [Podsiadlowski et al., 1992, Wellstein et al., 2001, Langer, 2012]. If mass transfer is conservative, the mass of the original secondary can grow until it becomes rather more massive than the primary initially was [e.g. Wellstein and Langer, 1999]. After the primary explodes as a supernova, the original secondary evolves to the supergiant phase, perhaps over-luminous for its mass [Dray and Tout, 2007], developing a strong wind that feeds the neutron star.

For a limited range of initial parameters, Pols [1994] found that mass transfer could lead to a reversal of the supernova order. The original secondary would receive the whole H-rich envelope of the primary, becoming much more massive, and then fill its Roche lobe, leading to reverse mass transfer and probably a common-envelope phase. The explosion of the original secondary would occur while the original primary is still some sort of He star. The observational characteristics of such a He star are not known.

As explained in Sect. 4.2.2, the He abundance of BD $+60^\circ$ 73 is not well constrained, but is high. The most likely value is $Y_{\mathrm{He}} = 0.25$, with a permitted range between 0.15 and ~ 0.3. The He abundances of B supergiants are generally assumed to be close to the Solar value, $Y_{\mathrm{He}} = 0.10$ [e.g. Markova and Puls, 2008]. For very luminous (luminosity class Ia) supergiants, Crowther et al. [2006] assumed $Y_{\mathrm{He}} = 0.20$, indicative of some chemical evolution, since they found N/C ratios similar to that found for BD $+60^\circ$ 73. For the blue hypergiants ζ^1 Sco and HD 190603, which are expected to be in a more advanced stage of evolution, Clark et al. [2012] found $Y_{\mathrm{He}} = 0.20$, while Kaper et al. [2006] found $Y_{\mathrm{He}} = 0.29$ for the B1 Ia$^+$ donor in the SGXB GX 301−2.

Therefore BD $+60^\circ$ 73 may be the B supergiant with the second highest He abundance measured. Together with its relatively high N/C ratio, very high rotational velocity and perhaps mild under-luminosity (see Sect. 4.2.1), this evidence of chemical evolution may be indicating a non-standard evolutionary channel for IGR J00370+6122. However, given the lack of a theoretical evolutionary model that can reproduce these characteristics, we will not try to infer the formation history of the system and stick to the standard scenario.

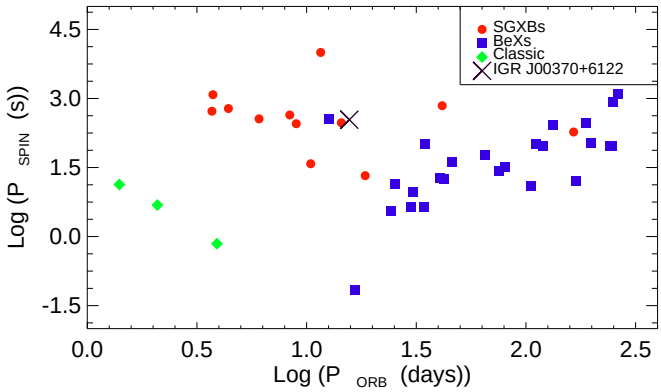

Figure 4.14: The $P_{\rm spin}/P_{\rm orb}$ (Corbet's) diagram for a large sample of HMXBs (see Fig. 1.9 of Chapter 1). The position of IGR J00370+6122 is marked by a cross.

Within this evolutionary scenario, a major observational constraint is given by the pulse period of the neutron star. in't Zand et al. [2007] observed IGR J00370+6122 on four occasions with the PCA, always close to the predicted time of maximum X-ray flux, according to the ASM light curve. The X-ray flux detected was very variable, with evidence for strong flaring, leading in't Zand et al. [2007] to conclude that the ASM folded light curves simply represent averages of many flares. During the strongest of these flares, which took place on MJD 53566, reaching a $L_{3-60\,\rm keV} \sim 3.2 \times 10^{36}\,\rm erg\,s^{-1}$ [in't Zand et al., 2007, ; value scaled to our distance], the flux was strongly modulated. Timing analysis revealed a very probable pulsation at $P_{\rm spin} = 346 \pm 6\,\rm s$ that cannot be considered certain due to the brevity of the flare [in't Zand et al., 2007]. The combination of flaring behaviour and long spin period is typical of a wind-accreting system, as expected for a supergiant companion. Fig. 4.14 shows the $P_{\rm spin}/P_{\rm orb}$ diagram, where different kinds of HMXBs occupy different positions according to its accretion behaviour [Corbet, 1986].

The position of IGR J00370+6122 in Fig. 4.14 is typical of wind-fed supergiant systems, giving further support to the putative spin period. According to the classical interpretation [e.g. Corbet, 1984, Waters and van Kerkwijk, 1989], the spin periods of Be/X-ray binaries are equilibrium periods for the magnetized

neutron stars. The equilibrium is as a consequence of spin-up episodes during accretion and spin-down episodes when accretion is inhibited by centrifugal effects [see also Stella et al., 1986]. In the case of wind-fed systems, the observed spin periods are believed to be the equilibrium values reached when the donor was still on the main sequence, as there is no effective way for a new equilibrium to be achieved when the source is a supergiant [Waters and van Kerkwijk, 1989, Liu et al., 2011]. In this scenario, the detection of a pulse period typical of wind accretors in IGR J00370+6122 has two immediate consequences:

- IGR J00370+6122 is not a young system. The supernova explosion of the progenitor to the neutron star took place when BD $+60^\circ$ 73 was still close to the main sequence, as the pulsar had time to slow down from its presumably very short initial spin period to its current value.
- In spite of the fast rotation measured in BD $+60^\circ$ 73, the system did not go through a Be/X-ray binary phase before becoming a supergiant X-ray binary. Liu et al. [2011] have described scenarios in which a Be/X-ray binary may turn into an SFXT as the donor star evolves off the main sequence, but the spin period of the neutron star is not expected to slow down again. The SFXT IGR J18483−0311, with a putative $P_{\rm spin} = 21$ s, was considered to be the best candidate to have followed this evolutionary path, but this spin period has recently been called into question [Ducci et al., 2013]. We note that no Be/X-rays binaries are known with an orbital period as short as IGR J00370+6122. Only the peculiar LMC transient A 0538−66 has a similar $P_{\rm orb} = 16.7$ d, but this object does not seem to behave as a classical Be/X-ray binary and the putative $P_{\rm spin} = 0.069$ s, detected only once, sets it apart from all Be/X-ray binaries.

The fact that IGR J00370+6122 is not a young system indicates that it might have had time to circularise (see Sec. 1.5.2). Observational data suggest that a binary containing stars with an outer radiation zone will suffer substantial tidal effects when the ratio between the semi-major axis and the stellar radius is smaller than ~ 4 [North and Zahn, 2003]. For typical values of mass and radius for an OB star orbited by a neutron star, this corresponds to orbital periods smaller than ~ 10 d. Three SGXBs with orbital periods longer than 10 d show measurable, but moderate eccentricity. OAO 1657−415, with $P_{\rm orb} = 10.4$ d, has $e = 0.11$ [Barnstedt et al., 2008]. 2S 0114+650, with $P_{\rm orb} = 11.6$ d, has $e = 0.18 \pm 0.05$ [Grundstrom et al., 2007]. Finally, 1E 1145.1−6141, with an orbital period $P_{\rm orb} = 14.4$ d, has $e = 0.20 \pm 0.03$ [Ray and Chakrabarty, 2002]. The fact that IGR J00370+6122, with a slightly longer orbital period, has a much

larger eccentricity, $e = 0.56 \pm 0.07$, supports the idea that the system will not have time to circularise during the lifetime of the optical companion. The wide-orbit SGXB GX 301−2, with a B1 Ia$^+$ donor and a $P_{\rm orb} = 46.5$ d, has a slightly smaller eccentricity, $e = 0.46$ [Kaper et al., 2006]. Only the peculiar system IGR J11215−5952, with a $P_{\rm orb} = 164.6$ d, is likely to have a higher eccentricity [Lorenzo et al., 2014].

The systemic velocity of BD $+60°$ 73 is $v_{\rm hel} = -77\,{\rm km\,s^{-1}}$, corresponding to $v_{\rm LSR} \approx -70{\rm km\,s^{-1}}$. This systemic velocity is perfectly compatible with the $-81 \pm 3\,{\rm km\,s^{-1}}$ addopted by Grunhut et al. [2014], who obtained different values of this parameter for their four different data sets. Our value is indeed equal to their γ_3 value [see Table 3 of Grunhut et al., 2014]. The few members of Cas OB4 with published velocities seem to cluster around $v_{\rm hel} \approx -50{\rm km\,s^{-1}}$ [Humphreys, 1978]. Therefore the recoil velocity of the system after the supernova explosion was $\approx -25\,{\rm km\,s^{-1}}$ in the radial direction. The tangential component was not very important either, as it has no significant proper motions [$-1.66 \pm 1.04\,{\rm mas\,yr^{-1}}$; $0.51 \pm 1.05\,{\rm mas\,yr^{-1}}$; van Leeuwen, 2007]. These values are in agreement with the average of other members of Cas OB4 (e.g. HD 1544 with $-1.68 \pm 0.82\,{\rm mas\,yr^{-1}}$; $-1.3 \pm 0.6\,{\rm mas\,yr^{-1}}$ or BD $+63°70$ with $-2.26 \pm 0.93\,{\rm mas\,yr^{-1}}$; $-0.9 \pm 0.74\,{\rm mas\,yr^{-1}}$, which have the smaller formal errors in the *Hipparchos* catalogue; van Leeuwen 2007). Therefore the supernova explosion that imparted a rather high eccentricity to the system does not seem to have given it a very high recoil velocity. With this peculiar radial velocity, BD $+60°$ 73 may have travelled 2.5 pc in 1 Myr, and therefore cannot be very far away from its natal location.

4.3.3 The zoo of wind-fed X-ray binaries

The spectral classification of BD $+60°$ 73, at the very limit of the Ib luminosity class, and its low absolute magnitude suggest that it is the less luminous of all mass donors in well-studied wind-fed supergiant binaries, either SGXBs or SFXTs. The relatively weak wind, combined with the rather wide orbit, results in a low X-ray luminosity, with an average peak luminosity $L_{\rm X} \sim 10^{35}\,{\rm erg^{o},s^{-1}}$, below the average X-ray luminosity of persistent SGXBs, but above the average X-luminosity of SFXTs in quiescence. Its flaring behaviour, with most of the X-ray luminosity being released in a small fraction of time, is reminiscent of SFXTs, and indeed could be considered similar to those of intermediate SFXTs with long orbital periods, such as SAX J1818.6−1703 [Zurita Heras and Chaty,

2009]. IGR J18483−0311, which has a similar orbital period $P_{\rm orb} = 18.5$ d, displays an *INTEGRAL*/ISGRI $20 - 40$ keV light curve [Sguera et al., 2007b] very similar in shape to that of IGR J00370+6122 [in't Zand et al., 2007], even if the peak luminosity is much higher, at least 5 times brighter for a source at approximately the same distance [Rahoui and Chaty, 2008]. The maximum X-ray luminosity reported up to date is that of the flare detected by in't Zand et al. [2007] with the PCA in MJD 53566, reaching $L_{3-60\,\rm keV} \sim 3.2 \times 10^{36}\,\rm erg\,s^{-1}$ [in't Zand et al., 2007, ; value scaled to our distance]. Comparing this value to the minimum X-ray luminosity of the folded X-ray light curves (Fig. 4.8), we find a dynamical range for the X-ray luminosity of IGR J00370+6122 of $\sim 10^2$, which is below the canonical value to define a SFXT [$> 10^3$; e.g., Walter and Zurita Heras, 2007]. Therefore although the X-ray light curve of IGR J00370+6122 is dominated by a flaring behaviour (contrary to the behaviour of persistent SGXBs) this flaring does not achieve the dynamical range of SFXTs.

This "intermediate" systems are supposed to represent a link between sources where the X-ray emission is completely dominated by flaring (the SFXTs) and the persistent (and brighter) canonical wind-fed SGXBs. Monitoring of IGR J18483−0311 with *Swift* over a whole orbital period revealed a dynamical range $> 1\,200$ [Romano et al., 2010], well above the threshold used by Walter and Zurita Heras [2007] to classify an object as an SFXT. Romano et al. [2010] suggested that the X-ray light curve of IGR J18483−0311 could be explained by an eccentricity ~ 0.4. Our orbital solution for IGR J00370+6122, together with the orbital solution of Grunhut et al. [2014] that supports ours, reveals very similar orbital parameters for this system.

We know that the SFXT behaviour cannot be primarily related to the orbital size or eccentricity. SFXTs with small orbits are known, such as IGR J16479−4514 [Jain et al., 2009] or IGR 17544−2619 [Clark et al., 2009], both with periods < 5 d. On the other hand, IGR J16465−4507 has a long orbital period, $P_{\rm orb} = 30.2$ d, and a moderate dynamical range that make it more similar to canonical SGXBs [La Parola et al., 2010, Clark et al., 2010]. Given the high eccentricity of IGR J00370+6122, the neutron star must come as close to the donor star at periastron as in a persistent system like 1E 1145.1−6141, which is much brighter in the X-rays. The SFXT behaviour is also unlikely to be primarily related to the spin period of the neutron star, as SFXTs and SGXBs seem to have similar spin periods. However, we note that the published spin periods for IGR J18483−0311 and IGR 17544−2619 have been recently called

into question [Ducci et al., 2013, Drave et al., 2014]. As the spin period of IGR J00370+6122 cannot be considered completely certain, the only SFXT left with an observed spin period is the intermediate system IGR J16465−4507, with $P_{\rm spin} = 227$ s [Walter and Zurita Heras, 2007].

In addition, recent observations of high variability and off states in the canonical SGXBs 4U 1907+09 [Şahiner et al., 2012, Doroshenko et al., 2012] and IGR J16418−4532 [Drave et al., 2013] help to blur the difference between persistent and transient wind-accreting X-ray binaries. The properties of IGR J00370+6122, make it intermediate between classical persistent SGXBs and "intermediate" SFXTs, adding one more point to this continuum. Moreover, as the donor star in IGR J00370+6122 evolves, it will increase its luminosity, turning into a later-type, more luminous supergiant, similar to the counterparts of 2S 0114+65 or 1E 1145.1−6141. We can therefore expect IGR J00370+6122 to evolve into a typical, persistent SGXB, showing that a given source may move across the parameter space and pass through both the SFXT and SGXB phases.

4.4 Conclusions

We have presented a detailed spectral analysis of BD $+60°\,73$, the optical counterpart to IGR J00370+6122, derived its astrophysical parameters and described its orbital motion. We classify BD $+60°\,73$ as a $\mathrm{BN0.7\,Ib}$ star just at the lower limit in luminosity for a supergiant, and find $T_{\rm eff} = 24\,000$ K and $\log g = 2.90$. At a distance of 3.1 kpc, the star may be slightly under-luminous for the spectral type and effective gravity found. However, the absolute magnitude derived, $M_{\rm V} = -5.2$, is within the margins allowed by the error bars in $\log g$ and the uncertainty in spectral type allowed by the very fast rotational velocity of the star, $v \sin i \approx 135\,\mathrm{km\,s^{-1}}$. The spectroscopic mass $M_* = 10 \pm 5\,\mathrm{M}_\odot$ is compatible with the evolutionary mass $M_* = 17 \pm 2\,\mathrm{M}_\odot$, leading to an assumed value of $M_* = 15\,\mathrm{M}_\odot$.

Abundance analysis reveals a high degree of chemical processing, with a $\mathrm{N/C}$ ratio and a He abundance typical of highly evolved stars, such as blue hypergiants. Together with the high rotational velocity, this level of chemical evolution may be an indication of a non-standard evolutionary channel, or perhaps substantial accretion of processed material from the progenitor of the neutron star.

The orbital solution reveals a high eccentricity ($e = 0.56 \pm 0.07$) and suggests a periastron distance $r \approx 2\,\mathrm{R}_*$. The X-ray emission is strongly peaked around orbital phase $\phi = 0.2$, though the observations are consistent with some level of X-ray activity happening at all orbital phases.

With this parameters, IGR J00370+6122 is the most eccentric HMXB with a supergiant donor up to date. Its X-ray light curve has a very similar shape to that of the "intermediate" SFXT IGR J18483−0311, but rather lower average luminosity. Though its whole X-ray flux apparently consists of flares, with a very low quiescence level, the integrated flux over many orbits seems to show only a moderate contrast between the peak, centred at orbital phase $\phi = 0.2$, and other phases. In this sense, its behaviour could also be interpreted as a more extreme version of the light curves of persistent SGXBs. The relatively wide orbit, high eccentricity and low luminosity of the companion (implying only a moderate mass loss) contribute to explain this low X-ray flux. The future evolution of the mass donor, which must expand and become more luminous (thus sporting a higher mass-loss rate), will very likely turn IGR J00370+6122 into a persistent SGXB.

The low average X-ray luminosity, together with the flaring nature of the high-energy emission, prevents confirmation of a possible eclipse, for which we find hints in all long-term folded light curves slightly before periastron (located at $\phi = 0$). The possibility of the eclipse is reinforced by the fact that the mass function suggests a high inclination $i \geq 60^\circ$. Observations with high-sensitivity missions are needed to confirm or reject this hypothesis, which would imply an inclination $i \sim 70^\circ$.

Aside from the inclination angle, the astrophysical parameters of IGR J00370+6122 are well constrained. Its properties support the idea that the difference between persistent SGXBs and SFXTs are unlikely to be explained by a single, simple factor, such as higher eccentricity or wind clumping, or even a combination of both, and, together with other recent findings, strongly point towards the existence of some gating mechanism, controlling the accretion flow on to the neutron stars in wind-fed X-ray systems.

CHAPTER 5

XTE J1855-026

The X-ray source XTE J1855-026 is a HMXB firstly identified during RXTE scans along the Galactic plane in 1998 by Corbet et al. [1998]. The X-ray source showed pulsations at a period of 361 seconds, and also a modulation at a period of 6.067 ± 0.004 days, which was interpreted as the orbital period of the system. The location of the source in the orbital period/spin period diagram [Corbet, 1986] was interpreted as an indication that XTE J1855-026 was likely to consist of a NS accreting from the wind of an early spectral type (O or B) supergiant primary [Corbet et al., 1999].

Corbet et al. [1999] measured the location of the source for the first time as $RA = 18^h55^m30^s$ and $Dec. = -02°34'52''$ with an estimated uncertainty at the 90% confidence level of $2'$ including systematic effects using 11 PCA on board RXTE scanning observations of the Scutum region. An improved location of $RA = 18^h55^m31^s.3$ and $Dec. = -02°36'24''.0$ (J2000.0) with a systematic uncertainty of less than $12''$ was obtained by Corbet and Mukai [2002] with data from the imaging detectors on board the Advanced Satellite for Cosmology and Astrophysics (ASCA).

Corbet and Mukai [2002] present a more detailed and precise analysis of this source. With the improved (due to the more accurate determination of the position) and extended [6 years of observations -more than 3 years since the results presented in Corbet et al., 1999] ASM@RXTE light curve, the orbital period was refined to be 6.0724 ± 0.0009 days. The ASM light curve folded over this period is shown in Fig. 5.1. The PCA light curve, which covers the course of one complete orbital cicle, (Fig. 5.2) shows a near total eclipse where pulsa-

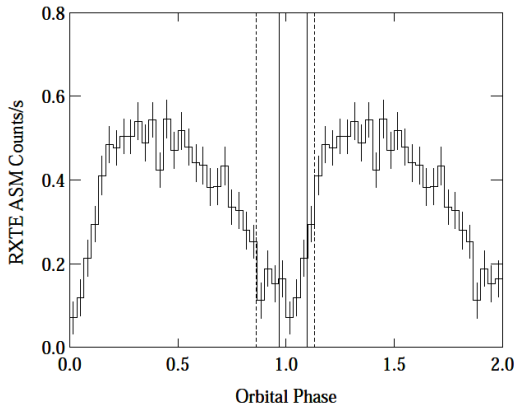

Figure 5.1: Fig. 1 of Corbet and Mukai [2002]. ASM@RXTE ($1.5 - 12.2$ keV) light curve of XTE J1855-026 folded on the orbital period of 6.0724 ± 0.0009 days obtained from fitting a sine wave to the orbital modulation. The solid and dashed vertical lines indicate the lower and upper limits on the eclipse duration, respectively, as derived from the PCA and ASCA observations.

tions, -present during all the rest of the light curve-, are not present. The resulting pulse period from the analysis of this light curve is 360.741 ± 0.002 seconds, which is consistent with the value of 361.1 ± 0.4 seconds found in Corbet et al. [1999]. This eclipse can also be seen in Fig. 5.1 where there is a systematic offset of ~ 0.15 ASM counts s^{-1}. A pulse-timing orbit obtained with PCA observations is shown in Fig. 5.3 together with a circular orbit fit and the table of the orbital parameters of the different orbital fits obtained by Corbet and Mukai [2002]. This orbital solution shows that the eccentricity is found to be very low with a best-fit of 0.04 ± 0.02. Assuming that the eclipse is symmetric around phase 0 for the circular orbit fit, the total phase duration would be in the range of $0.198 - 0.262$. The lower limit on the eclipse duration implies a minimum radius of the mass donating star of approximately $20\,R_{\odot}$, consistent with that of a B0I star, comparable with the primaries in other wind-accretion driven HMXBs. The orbital period and pulse period are also comparable with parameters measured for similar systems. A less likely interpretation could be that XTE J1855-026 is instead a Be/NS binary, in which case it would have an unusually short orbital period for such a system.

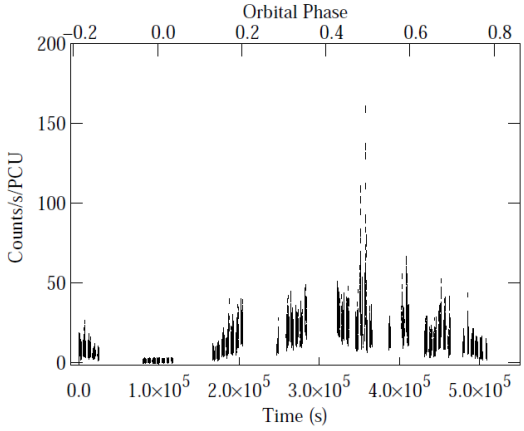

Figure 5.2: Fig. 2 of Corbet and Mukai [2002]. Background-subtracted light curve of XTE J1855-026 obtained with the PCA@RXTE ($2 - 60$ keV). Time is relative to the start of the observation at MJD 51488.066.

The optical counterpart was firstly identified by Verrecchia et al. [2002] as a relatively bright star right on the edge of the $12''$ ASCA error circle [given by Corbet and Mukai, 2002] with coordinates $RA = 18^h55^m30^s.5$ and $Dec. = -02°36'21''$. This object was identified in 1999 observations taken at the Loiano Observatory (Bologna, Italia) as the only Hα emission line object inside the $2'$ error circle of XTE J1855-026. Low-resolution spectroscopy ($4800 - 7000$Å) taken on Septemeber 1999 with the European Southern Observatory (ESO) 3.6 m telescope at La Silla shows Hα emission ($EW = -6$Å) and He I absorption lines on a very steep continuum ($B = 16.1$, $I = 11.5$), indicating a very reddened early-type star. Likely emission-infilling in Hβ and shallow weak He II at 4512 Å suggested that the object was likely not a supergiant. A red intermediate resolution spectrum taken on July 2000 with the Observatoire de Haute-Provence (OHP) 1.93 m telescope shows double-peaked (with much stronger red peak) Hα emission with an $EW = -5.5$Å and apparent weak *P-Cygni* profiles in the He I lines, which, if real, should indicate mass loss. This observed asymmetric emission line profiles may be interpreted as those of a Be star with a Global One-Armed Oscillation in its circumstellar disc [see e.g., Okazaki,

1991, 1996, Negueruela et al., 1998]. However, as this object was likely to be the counterpart of XTE J1855-026 (therefore have a NS orbiting in a ~ 6 days orbit) the interpretation of the *P-Cygni* profiles is more likely to be an extended mass loss.

The position of the source was refined by Romano et al. [2008] with observations of the X-Ray Telescope (XRT) on board the Swift satellite to a value of $RA = 18^h55^m30^s.44$ and $Dec. = -02°36'18''.6$ (J2000.0) with an uncertainty of $1.9''$ at a confidence level of 90%, confirming the identification with the optical counterpart proposed by Verrecchia et al. [2002]. High-quality spectra taken in August 2003 with the 4.2 m WHT at La Palma (Spain) by Negueruela et al. [2008a] show this counterpart to be a B0 Iaep luminous supergiant.

The X-ray luminosity of the source cannot be determined as the distance is unknown, but Corbet et al. [1999] gave a value for the X-ray flux based on a fit of a combined PCA/HEXTE (both on board RXTE) spectrum. This fit consists of the standard pulsar model [White et al., 1983] of an absorbed power law with a high-energy cutoff plus a Gaussian line appearing near 6.4 keV, giving a value of $F_{2-10keV} \sim 1.1 \times 10^{-10}$ erg cm^{-2} s^{-1}. Since the identification of the source, three bright flares have been reported:

- During the observation of the inner Galactic disc (PI Georg Weidenspointner) that were performed between 2010-03-12 and 2010-03-14 23:04 (UTC), the Integral Burst Alert System [IBAS; Mereghetti et al., 2003] detected a bright flare from the source that was firstly interpreted as a Gamma Ray Burst (GRB) by the automatic IBAS pipeline and later retracted by Mereghetti et al. [2010]. Off-line analysis showed the presence of three different flares separated by one spin period (~ 360 seconds). The duration of the first flare is the largest one with ~ 130 seconds, the second in time is the shortest one with ~ 55 seconds, and the third flare is in between with ~ 80 seconds. The average $20 - 40$ keV flux of the consecutive flares was calculated with an average spectrum of each flare individually and it is almost the same but decreasing in time ($\sim 2.2 \times 10^{-9}$ erg s^{-1} cm^{-2} (~ 0.3 Crab) -first flare, $\sim 2 \times 10^{-9}$ erg s^{-1} cm^{-2} (~ 0.3 Crab) -second flare, and $\sim 1.2 \times 10^{-9}$ erg s^{-1} cm^{-2} (~ 0.2 Crab) -third flare). An average $20 - 40$ keV flux of the whole flare was calculated from an average spectrum giving the value of $F_{20-40keV} = (6.5 \pm 0.5) \times 10^{-10}$ erg s^{-1} cm^{-2}. Pulsations with a period of ~360 seconds were clearly detected using the entire observation. During the 5 hours before

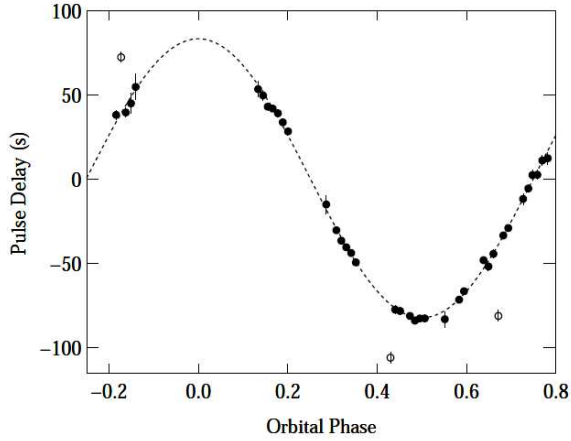

ORBITAL PARAMETERS OF XTE J1855−026

PARAMETER	ALL DATA		EDITED DATA	
	Eccentric	Circular	Eccentric	Circular
$P_{\rm pulse}$ (s).....	360.733 ± 0.006	360.734 ± 0.005	360.739 ± 0.002	360.741 ± 0.002
$\dot{P}_{\rm pulse}$ (s s$^{-1} \times 10^{-8}$).....	3.7 ± 12	2.1 ± 11	1.7 ± 4.4	1.5 ± 3.6
$a \sin i$ (lt-s).....	81.8 ± 4.2	82.4 ± 2.4	80.5 ± 1.4	82.8 ± 0.8
T0 (MJD−51400).....	Undefined	95.25 ± 0.02	91.4 ± 0.3	95.276 ± 0.007
e.....	0.0 ± 0.06	...	0.04 ± 0.02	...
ω (deg).....	Undefined	...	226 ± 15	...
χ^2_ν (dof)	11.5 (34)	10.8 (36)	1.0 (31)	1.06 (33)
Orbital period (days).....	6.0724 ± 0.0009	...	...	...
Mass function ($M_\odot$)	15.9 ± 2.5	16.3 ± 1.4	15.2 ± 0.8	16.5 ± 0.5

NOTES.—All parameters are 1 σ single-parameter confidence levels. Errors on individual pulse-timing measurements were scaled to make $\chi^2 = 1$ for the edited data set eccentric orbit fit. The edited data set excludes the points plotted as open circles in the figure that have large deviations from the best-fit curve. The orbital period is derived from the ASM light curve rather than the pulse timing. T0 corresponds to periastron passage for the eccentric orbit fits and the phase of mideclipse for the circular fits.

Figure 5.3: Fig. 5 and Table 1 of Corbet and Mukai [2002]. Pulse delay curve for XTE J1855-026 and table with orbital parameters obtained by Corbet and Mukai [2002]. The dashed line indicates the best-fit circular orbit.

the outburst and the following 2.5 hours, the $20-40$ keV flux was stable at ~ 30 mCrab [Watanabe et al., 2010].

- The source triggered BAT@Swift on 2011-09-18 at 10:07:28.3 UT (trigger 503434). The outburst lasted ~ 900 seconds with an intensity of ~ 230 mCrab in the $15-50$ keV band while the average monitor rate for that day was ~ 55 mCrab [Krimm et al., 2012].
- BAT@Swift detected an increase of the source intensity from its normal level of ~ 10 mCrab in the $15-50$ keV band on 2012-03-12 to ~ 50 mCrab on 2012-03-13 being the brightest single pointing a 768-second observation beginning 2012-03-13 00:22:48 UT with an intensity of ~ 175 mCrab [Krimm et al., 2012].

5.1 Observations

There is a series of high quality ISIS optical spectra for atmosphere model and spectral type determination (Table 5.1). There are a total of 39 optical spectra, 17 from IDS (Table 5.2), and 22 from FRODOSpec (Table 5.3), covering from 2003 to 2011 for radial velocity determinations. The ASM light curve is covering more than 15 years of observations, while the BAT light curve covers a total of 9 years (Table 5.4).

5.2 Data Analysis & Results

5.2.1 FASTWIND model fit

High quality spectra taken with the WHT (Table 5.1)[1] have been used to obtain a FASTWIND atmosphere model.

Spectra from 1 to 6 cover the same wavelength range, and have been taken almost at the same time, therefore it should be possible to obtain an average spectrum of this zone just by an average calculation. In spite of this, I have normalised every individual spectrum and calculated the relative velocities of the

[1] Table 5.1 is the same spectra used by [Negueruela et al., 2008a] to give a preliminary classification of the optical component

Table 5.1: Observation log of optical spectra for spectral classification of XTE J1855-026.

#	Date	MJD	Texp (s)	Instrument	$\Delta\lambda$ (Å)
1	17/08/2003 20:55:24	52868.87	1800.01	ISIS@WHT	3915–4800 (λ_C=4359)
2	17/08/2003 21:29:39	52868.89	1800.01	ISIS@WHT	3915–4800 (λ_C=4359)
3	17/08/2003 22:07:09	52868.92	1800.01	ISIS@WHT	3915–4800 (λ_C=4359)
4	17/08/2003 22:37:45	52868.94	1800.01	ISIS@WHT	3915–4800 (λ_C=4359)
5	17/08/2003 23:13:59	52868.97	1800.01	ISIS@WHT	3915–4800 (λ_C=4359)
6	17/08/2003 23:44:37	52868.99	1800.01	ISIS@WHT	3915–4800 (λ_C=4359)
7	18/08/2003 00:21:38	52869.01	1800.01	ISIS@WHT	4155–5040 (λ_C=4601)
8	18/08/2003 00:52:16	52869.04	1800.01	ISIS@WHT	4155–5040 (λ_C=4601)
9	18/08/2003 01:26:17	52869.06	1800.01	ISIS@WHT	5945–6840 (λ_C=6399)

Table 5.2: Observation log of IDS@INT optical data for radial velocities of XTE J1855-026.

#	Date	MJD	Texp (s)	Instrument
1	01/07/2003 22:54:08	52821.95	1672.567	IDS@INT
2	02/07/2003 02:13:42	52822.09	2000	IDS@INT
3	02/07/2003 22:41:36	52822.94	2400.01	IDS@INT
4	03/07/2003 02:30:11	52823.10	2000	IDS@INT
5	03/07/2003 22:59:03	52823.96	2400.01	IDS@INT
6	04/07/2003 03:17:51	52824.14	2000	IDS@INT
7	04/07/2003 22:35:13	52824.94	2400.01	IDS@INT
8	05/07/2003 03:45:35	52825.16	1800.1	IDS@INT
9	05/07/2003 22:15:29	52825.93	2400.01	IDS@INT
10	06/07/2003 02:58:19	52826.12	2400.01	IDS@INT
11	06/07/2003 23:21:17	52826.97	2400.01	IDS@INT
12	07/07/2003 03:16:43	52827.14	2400.01	IDS@INT
13	08/07/2003 22:49:22	52828.95	2500.01	IDS@INT
14	10/07/2003 00:00:21	52830.00	2400.01	IDS@INT
15	10/07/2003 23:44:09	52830.99	2400.01	IDS@INT
16	11/06/2009 00:11:24	54993.01	2000.01	IDS@INT
17	11/06/2009 23:43:20	54993.99	2000.01	IDS@INT

Table 5.3: Observation log of FRODOSpec@LT optical data for radial velocities of XTE J1855-026.

#	Date	MJD	Texp (s)	Instrument
1	09/04/2010 03:37:21	55295.15	2×1800	FRODOSpec@LT
2	11/04/2010 04:25:42	55297.18	2×1800	FRODOSpec@LT
3	23/04/2010 05:05:17	55309.21	2×1800	FRODOSpec@LT
4	26/04/2010 04:58:33	55312.21	2×1800	FRODOSpec@LT
5	08/05/2010 01:52:00	55324.09	2×1800	FRODOSpec@LT
6	15/05/2010 01:13:39	55331.05	2×1800	FRODOSpec@LT
7	16/05/2010 02:24:03	55332.10	1800	FRODOSpec@LT
8	17/05/2010 02:06:28	55333.09	2×1800	FRODOSpec@LT
9	18/05/2010 04:20:32	55334.18	2×1800	FRODOSpec@LT
10	19/05/2010 01:04:53	55335.04	2×1800	FRODOSpec@LT
11	20/05/2010 02:38:52	55336.11	2×1800	FRODOSpec@LT
12	21/05/2010 01:55:21	55337.08	2×1800	FRODOSpec@LT
13	23/05/2010 02:55:29	55339.12	2×1800	FRODOSpec@LT
14	25/05/2010 04:08:37	55341.17	2×1800	FRODOSpec@LT
15	26/05/2010 04:52:14	55342.20	2×1800	FRODOSpec@LT
16	19/06/2010 04:01:48	55366.18	2×1800	FRODOSpec@LT
17	23/06/2010 03:36:28	55370.15	2×1800	FRODOSpec@LT
18	08/07/2010 02:20:14	55385.10	2×1800	FRODOSpec@LT
19	15/07/2010 02:13:22	55392.09	2×1800	FRODOSpec@LT
20	12/05/2011 03:46:34	55693.16	3×1200	FRODOSpec@LT
21	28/05/2011 02:55:11	55709.12	3×1200	FRODOSpec@LT
22	30/05/2011 03:13:16	55711.13	2×1200	FRODOSpec@LT

Table 5.4: Observation log of X-ray data of XTE J1855-026.

Date	MJD	Data points	Instrument	Energy range
06/01/1996–13/10/2011	50088–55847	60304 (dwells)	ASM@RXTE	1.5–12.2 keV
06/01/1996–13/10/2011	50088–55847	4724 (daily)	ASM@RXTE	1.5–12.2 keV
14/02/2005–19/02/2014	53415–56707	2997	BAT@Swift	15–50 keV

Table 5.5: Relative velocities of spectra in Table 5.1. The first column represents the number of the spectrum from Table 5.1, the second column is the number of the reference spectrum against which the $V_{\rm rel}$ has been calculated, and the third column is the $V_{\rm rel}$.

#	# Ref	v_{rel} (km s^{-1})	#	# Ref	v_{rel} (km s^{-1})
1	1	0.00 ± 0.00	7	7	0.00 ± 0.00
2	1	1.33 ± 6.70	8	7	3.57 ± 11.63
3	1	7.41 ± 7.49			
4	1	2.25 ± 7.26			
5	1	6.64 ± 7.46			
6	1	1.85 ± 6.51			

6 spectra relative to the first spectrum of the data series, finding no significant velocity shifts (see Table 5.5). The same process has been done for spectra 7 and 8 with the same result -no significant relative velocities.

The weighted average of spectra from 1 to 6, and from 7 to 8 has been performed following the expresion:

$$\bar{S} = \frac{\sum_{i=1}^{n} S_i {}^{S}/_{N_i}}{\sum_{i=1}^{n} N} \tag{5.1}$$

where, $\bar{S}$ is the average spectrum, S_i is the individual spectrum, ${}^{S}/_{N_i}$ is the S/N of an individual spectrum, and N_i is the rms of an individual spectrum.

The parameters for this calculation have been obtained with the spectra before normalization, selecting zones without lines, calculating the average counts and the rms for that zone, and S/N as the average counts over the rms[2].

Once this weighted average has been calculated, the total spectrum covers from 3915Å to 6840Å with small gaps in between, but the important lines (such as H, Si or He lines) for the model atmosphere and the spectral classification are present and with good S/N.

[2] The average signal is ~ 800 counts, and the average rms is ~ 70.

Table 5.6: Stellar parameters derived from the spectroscopic analysis.

$v \sin i$ (km s^{-1})	120 ± 20
$\Theta_{\rm RT}$ (km s^{-1})	80 ± 40
$T_{\rm eff}$ (K)	25000 ± 800
$\log\ g$	2.69 ± 0.06
$\xi_{\rm t}$ (km s^{-1})	32.0 ± 2.9
$Y_{\rm He}$	0.20 ± 0.11
$\log\ Q$	-12.50 ± 0.10

Table 5.7: Chemical abundances of XTE J1855-026 in $\log\frac{N(X)}{N(H)}$+12 resulting from the FASTWIND spectroscopic analysis. Chemical abundances derived by Nieva and Przybilla [2012] for B-type stars in Solar neighbourhood, and the solar abundances from Asplund et al. [2009] are included for comparison.

Species	XTEJ 1855-026	B-type stars	Sun
Si	7.61 ± 0.21	7.50 ± 0.05	7.51 ± 0.03
Mg	7.80 ± 1.20	7.56 ± 0.05	7.60 ± 0.04
C	7.29 ± 0.16	8.33 ± 0.04	8.43 ± 0.05
N	8.08 ± 0.23	7.79 ± 0.04	7.83 ± 0.05
O	8.56 ± 0.24	8.76 ± 0.05	8.69 ± 0.05

The FASTWIND synthetic spectrum has been obtained as explained in Chapter 2, Sec. 2.2.2 [see Castro et al., 2012, for a detailed description]. An automatised χ^2 fitting of synthetic FASTWIND spectra including lines from H, He I-II, Si II-IV, Mg II, C II, N II-III, and O II to the global spectrum between 3900 and 5100 Å. This synthetic spectrum together with the WHT spectrum obtained as explained in the previous paragraphs is shown in Fig. 5.4 where line identifications are also provided.

The parameters from the best fit obtained for the atmosphere model are summarised in Table 5.6, while chemical abundances are shown in Table 5.7.

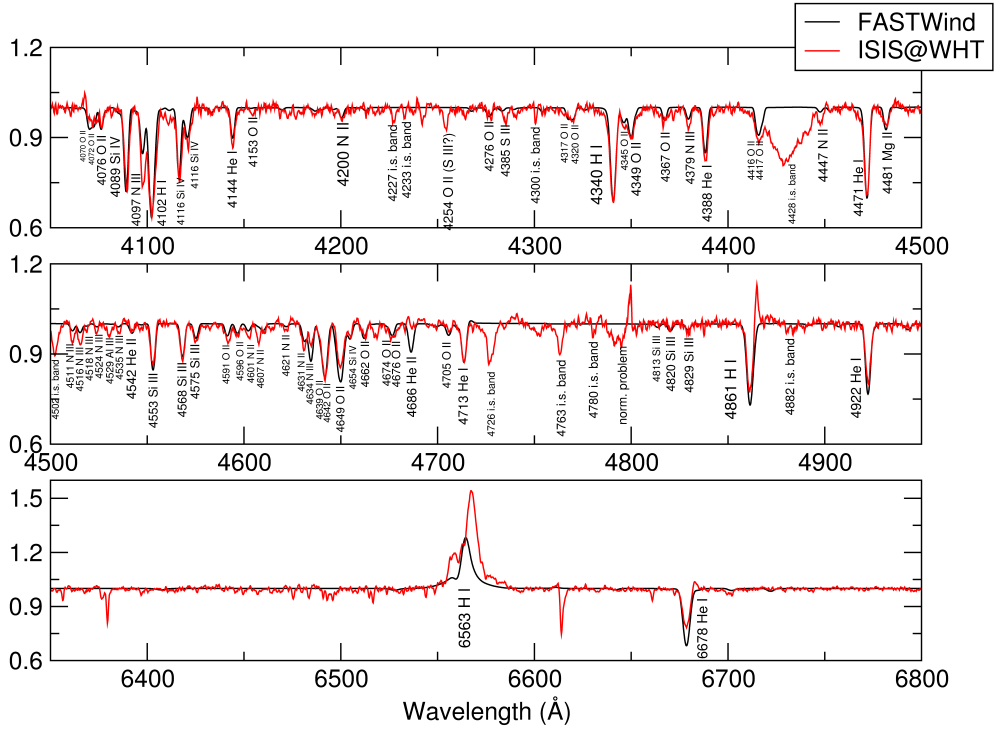

Figure 5.4: XTE J1855-026 spectrum together with the FASTWIND synthetic spectrum. Spectral line identifications are provided.

5.2.2 Radial velocities & Orbital solutions

Data from Tables 5.2 and 5.3 has been used to obtain radial velocity points through two different methods due to the different S/N of the two data sets. Fig. 5.5 shows an example of one spectrum of each data set for comparison.

IDS@INT data

The IDS spectra covers from $\sim 4000\,\text{Å}$ to $\sim 5800\,\text{Å}$, and have very low S/N (Fig. 5.5a). For the IDS spectra V_{rad} points have been calculated by cross-correlating the whole spectra, avoiding H lines. These cross-correlations have been performed with Tom Marsh's software *molly* (`http://deneb.astro.warwick.ac.uk/phsaap/software/molly/html/INDEX.html`), and the results are shown in the first three columns of Table 5.8.

A Lomb-Scargle periodogram of these values has been performed obtaining a value of 5.5444 ± 0.0035 days (see Fig. 5.6), not compatible with the $P_{\text{orb}} = 6.0724 \pm 0.0009$ days of Corbet and Mukai [2002]. This discrepancy could be due to the small coverage of the data set (it spans just one orbital period).

In spite of this fact, these points have been fitted with SBOP forcing the P_{orb} value (see Table 5.9 and Fig. 5.7a). This result shows an important eccentricity which is not compatible with the result of Corbet and Mukai [2002]. Therefore, setting the eccentricity value to obtain a circular solution, another orbital solution has been found (see Table 5.9 and Fig. 5.7b).

Comparing Figs. 5.7a and 5.7b, and the σ values (see Table 5.9) of both orbital solutions it is possible to conclude that both solutions are compatible within this data set. The circular solution may be favoured because its σ is slightly smaller.

The orbital phase and its uncertainty are calculated with the following equations:

$$\phi = 1 - \left[\frac{T_0 - HJD}{P_{ORB}} - INT\left(\frac{T_0 - HJD}{P_{ORB}} \right) \right] \tag{5.2}$$

$$\Delta\phi = \frac{\Delta T_0}{P_{ORB}} + \left(\frac{T - T_0}{P_{ORB}^2} \right) \Delta P_{ORB} \tag{5.3}$$

Table 5.8: Radial velocities of XTE J1855-026 obtained with IDS and FRODOSpec data.

IDS (Table 5.2)			FRODOSpec Table 5.3		
#	HJD	$V_{\rm rad}$ (km s^{-1})	#	HJD	$V_{\rm rad}$ (km s^{-1})
1	2822.47	15.3 ± 4.5	1	5295.67	-49.7 ± 3.5
2	2822.61	2.0 ± 3.9	2	5297.71	-27.9 ± 2.2
3	2823.46	-22.4 ± 4.2	3	5309.73	-22.7 ± 4.5
4	2823.62	-25.3 ± 3.8	4	5312.73	5.6 ± 2.5
5	2824.48	-13.1 ± 4.7	5	5324.60	3.3 ± 2.1
6	2824.65	-26.5 ± 7.0	6	5331.58	-25.0 ± 3.0
7	2825.46	-10.7 ± 6.6	7	5332.61	-66.7 ± 5.5
8	2825.67	-16.7 ± 7.7	8	5333.61	-39.5 ± 4.7
9	2826.45	9.4 ± 5.7	9	5334.71	-15.3 ± 3.6
10	2826.64	16.6 ± 5.9	10	5335.57	11.2 ± 2.9
11	2827.49	4.0 ± 4.2	11	5336.64	29.1 ± 2.7
12	2827.66	13.0 ± 3.9	12	5337.61	-47.6 ± 2.8
13	2829.47	-39.8 ± 4.7	13	5339.65	-5.9 ± 2.6
14	2830.52	-26.2 ± 3.6	14	5341.70	0.6 ± 4.7
15	2831.51	-16.9 ± 15.9	15	5342.73	7.5 ± 10.3
16	4993.52	-16.2 ± 6.5	16	5366.69	7.8 ± 2.6
17	4994.51	6.6 ± 4.3	17	5370.68	-26.4 ± 3.3
			18	5385.62	6.9 ± 3.2
			19	5392.62	-38.4 ± 3.5
			20	5693.68	-15.6 ± 5.7
			21	5709.65	-31.5 ± 3.5
			22	5711.65	0.3 ± 4.3

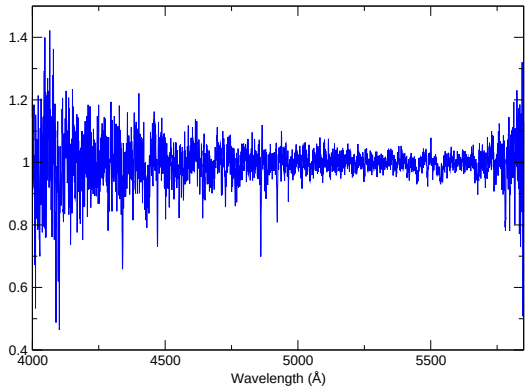

(a) XTE J1855-026 IDS spectrum taken the 8th of July 2003.

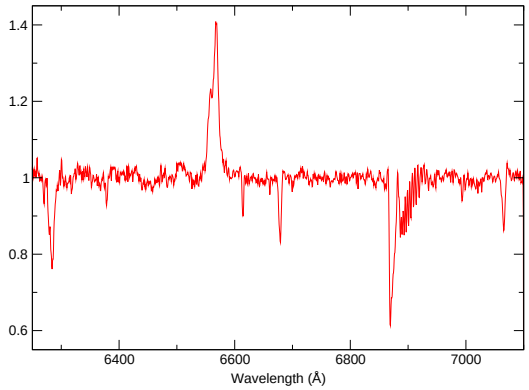

(b) XTE J1855-026 FRODOSpec spectrum taken the 15th of May 2010.

Figure 5.5: XTE J1855-026 IDS and FRODOSpec spectra. The S/N is clearly much better in the FRODOSpec spectrum than in the IDS one.

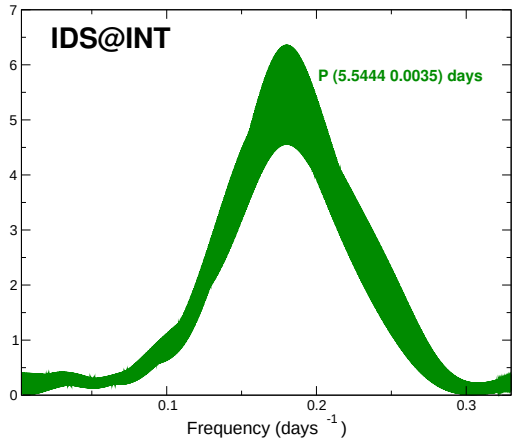

Figure 5.6: Lomb-Scargle periodogram of the radial velocity points of IDS data (left columns of Table 5.8) obtained with the PERIOD package within the *Starlink* environment.

The T_0 values are different for both solutions because the circular solution is referring this to the eclipse, while the eccentric solution is referring this value to the periastron passage. The value of the eclipse time given by this circular solution corresponds to phase 0.057 ± 0.055 (calculated with Eqs. 5.2 and 5.3) related to the eclipse time given by Corbet and Mukai [2002]. Therefore, both values are perfectly compatible with each other taking into account the upper and lower limits given for the eclipse ($\phi_{\rm eclipse} = [0.862 - 1.131]$).

An important parameter for the determination of the mass function is K, which is different in both fittings but compatible within the error bars.

FRODOSpec@LT data

Due to the incompatibility of the $P_{\rm orb}$ found in the IDS data with the Corbet and Mukai [2002] value, an application for more data was submitted. This extra data is the FRODOSpec data of Table 5.3.

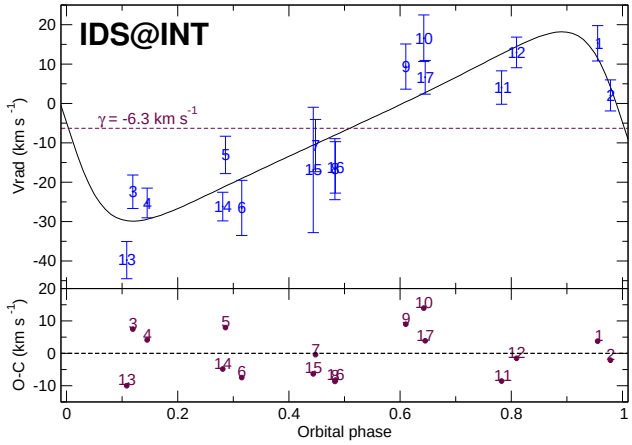

(a) XTE J1855-026 eccentric radial velocity curve (IDS).

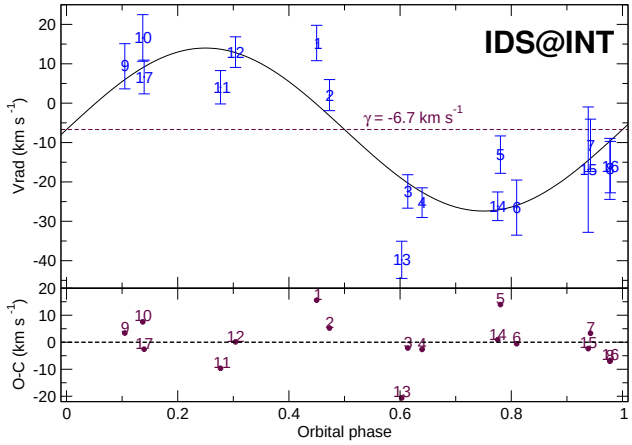

(b) XTE J1855-026 circular radial velocity curve (IDS).

Figure 5.7: XTE J1855-026 radial velocity fittings with IDS $V_{\rm rad}$ values assuming the $P_{\rm orb}$ = 6.0724 days of Corbet and Mukai [2002]. Fig. 5.7a shows an eccentric fit, while Fig. 5.7b shows a circular fit. In both figures the top panel represents the fit, and the bottom panel the residuals from the observed $V_{\rm rad}$ points to the fitted radial velocity curve. The parameters of this fitted curve are in Table 5.9.

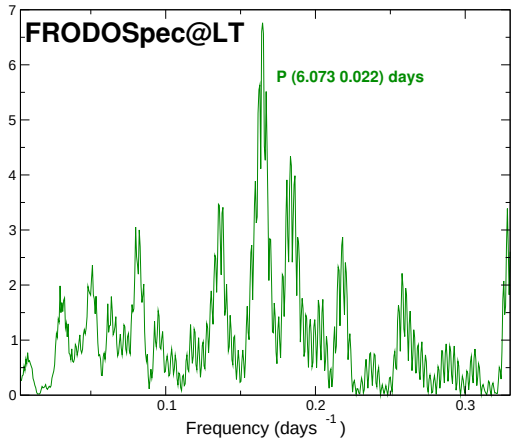

Figure 5.8: Lomb-Scargle periodogram of the radial velocity points of FRODOSpec data (right columns of Table 5.8) obtained with the PERIOD package within the *Starlink* environment.

The FRODOSpec spectra covers from ~ 6200 Å to ~ 7090 Å and have better S/N than the IDS data (Fig. 5.5b). For these spectra the regions around two $\mathrm{He\,I}$ lines ($\lambda 6678$Å and $\lambda 7065$Å) have been used for radial velocity determinations by a cross-correlation with the FASTWIND synthetic spectrum shown in Fig. 5.4 obtaining the values shown in the last columns of Table 5.8.

A Lomb-Scargle periodogram of the radial velocity values obtained with this data set has been performed with *Starlink* and it is shown in Fig. 5.8. This value of 6.073 ± 0.022 d, contrary to the value found within the IDS data set (Fig. 5.6), is perfectly compatible within errors with the $P_{\rm orb} = 6.0724 \pm 0.009$ days obtained by Corbet and Mukai [2002].

These points have been fitted with SBOP forcing the value of the orbital period to that of Corbet and Mukai [2002] (see Table 5.9 and Fig. 5.9a). Again, an important eccentricity, not compatible with a circular solution is found in this fit. So, setting the eccentricity value to obtain a circular solution, in the same way as it was done to IDS data, another orbital solution has been found (see Table 5.9 and Fig. 5.9b).

And again, comparing Figs. 5.9a and 5.9b and the σ values of Table 5.9 for both fittings, we could say that both solutions are compatible with the data set, but this time, favouring the eccentric solution.

The value of the eclipse time given by this circular solution corresponds to phase 0.16 ± 0.10 (calculated again with Eqs. 5.2 and 5.3) related to the eclipse time given by Corbet and Mukai [2002]. Therefore, both values are perfectly compatible with each other, and with the value obtained with the IDS data set (0.057 ± 0.055), taking into account the limits for the eclipse.

The K value is different in both fittings (eccentric and circular) but compatible within the error bars. Both values are compatible with the eccentric solution of the IDS data set, but not with the circular solution of the IDS data set.

A completely incompatible parameter between IDS and FRODOSpec data sets is the systemic velocity γ. This is the reason why both data sets appear separately. It seems that there is a shift of this value that might be due to the different wavelength ranges of both instruments or perhaps to an instrumental zero point.

FRODOSpec@LT and IDS data

In order to put together both data sets, the IDS values have been shifted in velocity. The average of the systemic velocity values for the circular and eccentric solution of the IDS data set is $\sim -6.5\,\mathrm{km\,s^{-1}}$, while the average γ value of the FRODOSpec orbital solutions is $\sim -16.3\,\mathrm{km\,s^{-1}}$ (see Table 5.9). Therefore, the IDS V_{rad} values have been shifted $-16.3 - (-6.5) = -9.8\,\mathrm{km\,s^{-1}}$ to make them match with the V_{rad} values of FRODOSpec.

The Lomb-Scargle periodogram of both data sets together results in a period of 6.0889 ± 0.0032 days (Fig. 5.10), compatible with the Corbet and Mukai [2002] value, and with the value obtained within the FRODOSpec data set.

This combined data set has been fitted with SBOP (Fig. 5.11a and Table 5.9) obtaining, for the third time, an eccentricity value not compatible with the circular orbital solution of Corbet and Mukai [2002]. Therefore, imposing again an $e = 0.0$, another solution has been obtained (Fig. 5.11b and Table 5.9).

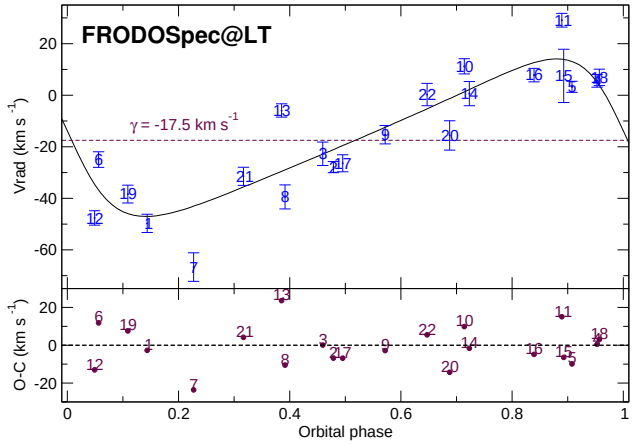

(a) XTE J1855-026 eccentric radial velocity curve (FRODOSpec).

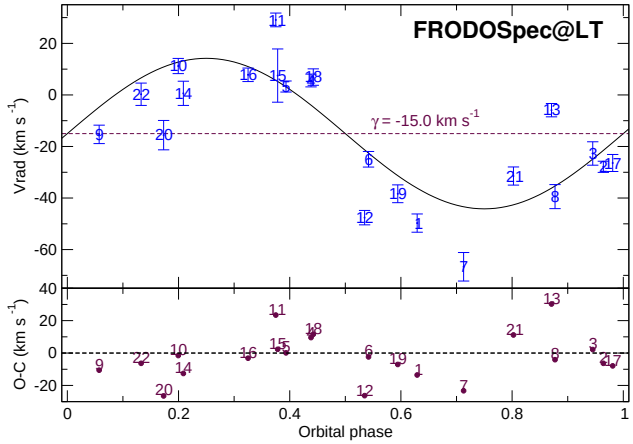

(b) XTE J1855-026 circular radial velocity curve (FRODOSpec).

Figure 5.9: XTE J1855-026 radial velocity fittings with FRODOSpec $V_{\rm rad}$ values assuming the $P_{\rm orb} = 6.0724$ days of Corbet and Mukai [2002]. Fig. 5.9a shows an eccentric fit, while Fig. 5.9b shows a circular fit. In both figures the top panel represents the fit, and the bottom panel the residuals from the observed $V_{\rm rad}$ points to the fitted radial velocity curve. The parameters of this fitted curve are in Table 5.9.

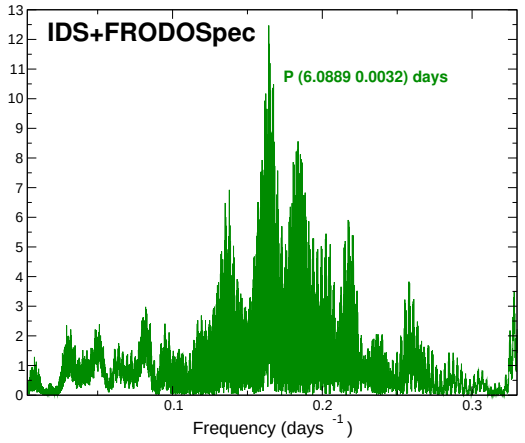

Figure 5.10: Lomb-Scargle periodogram of the radial velocity points of IDS and FRODOSpec data (Table 5.8) obtained with the PERIOD package within the *Starlink* environment.

Again, both solutions are compatible with the data set, this time favouring the eccentric one due to its smaller σ value.

In this case, the T_0 value for the circular fitting corresponds to $\phi = 0.938 \pm 0.035$ related to the eclipse predicted by Corbet and Mukai [2002], so it is perfectly compatible with this eclipse time within its upper and lower limits.

The K values are compatible with each other and compatible with the values from FRODOSpec data set fittings, as well as with the IDS value for the eccentric solution.

5.2.3 Hα and He lines

A search for any correlation of these lines with the orbital motion is performed in this Section making an attempt for an explanation of the eccentricity found in the orbital solutions (Sec. 5.2.2).

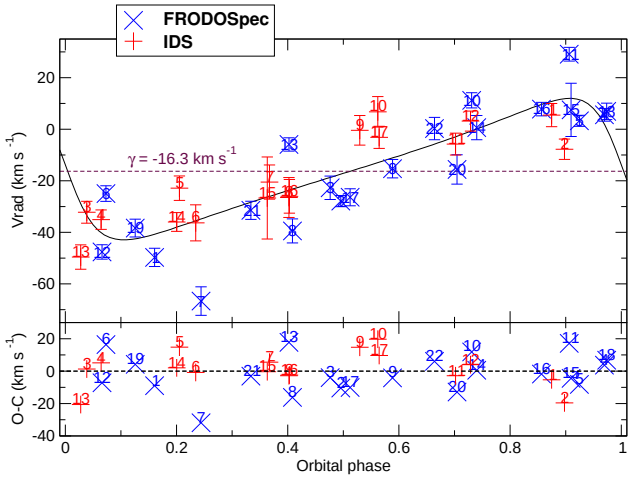

(a) XTE J1855-026 eccentric radial velocity curve (IDS+FRODOSpec).

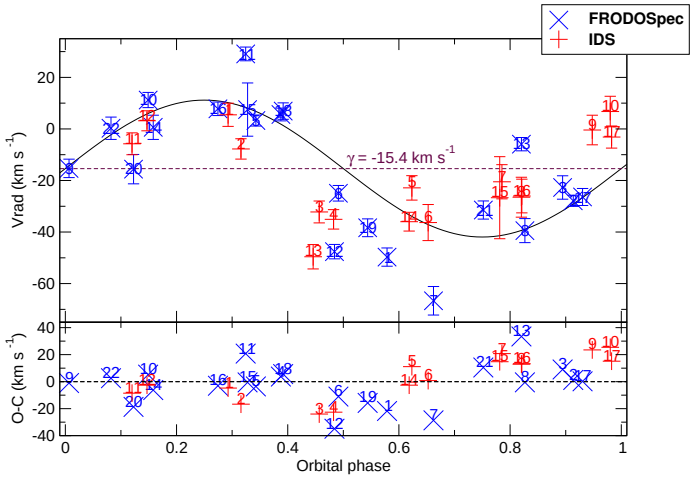

(b) XTE J1855-026 circular radial velocity curve (IDS+FRODOSpec).

Figure 5.11: XTE J1855-026 radial velocity fittings with IDS+FRODOSpec $V_{\rm rad}$ values assuming the $P_{\rm orb} = 6.0724$ days of Corbet and Mukai [2002]. Fig. 5.11a shows an eccentric fit, while Fig. 5.11b shows a circular fit. In both figures the top panel represents the fit, and the bottom panel the residuals from the observed $V_{\rm rad}$ points to the fitted radial velocity curve. The parameters of this fitted curve are in Table 5.9.

Table 5.9: Orbital parameters obtained by fitting the IDS and FRODOSpec radial velocity points (Table 5.8) using Lehmann-Filhes method implemented in SBOP on the left, and setting a circular solution on the right. All the fittings have been obtained forcing the period of 6.0724 days of Corbet and Mukai [2002].

IDS@INT

Eccentric solution	(Fig.5.7a)	Circular solution	(Fig. 5.7b)
T_0 (HJD)	2828.81 ± 0.34	T_0 (HJD)	2825.81±0.14
e	0.44±0.18	e	0.0
γ (km s^{-1})	-6.3±1.6	γ (km s^{-1})	-6.7±2.0
K_0 (km s^{-1})	24.0±4.9	K_0 (km s^{-1})	20.7±2.6
ω (degrees)	87±24		
σ	1.55	σ	1.49

FRODOSpec@LT

Eccentric solution	(Fig.5.9a)	Circular solution	(Fig. 5.9b)
T_0 (HJD)	5616.64 ± 0.30	T_0 (HJD)	5297.924±0.050
e	0.39±0.10	e	0.0
γ (km s^{-1})	-17.5±2.6	γ (km s^{-1})	-15.0±1.1
K_0 (km s^{-1})	30.6±3.9	K_0 (km s^{-1})	29.2±1.9
ω (degrees)	85±21		
σ	1.79	σ	2.35

IDS@INT+FRODOSpec@LT

Eccentric solution	(Fig.5.11a)	Circular solution	(Fig. 5.11b)
T_0 (HJD)	2841.45 ± 0.0.16	T_0 (HJD)	2626.375±0.046
e	0.50±0.08	e	0.0
γ (km s^{-1})	-16.3±1.9	γ (km s^{-1})	-15.4±1.0
K_0 (km s^{-1})	27.4±2.8	K_0 (km s^{-1})	26.6±1.6
ω (degrees)	86±14		
σ	1.39	σ	2.06

Note: $\sigma = |O-C|/\sqrt{\textit{number of data points}}$ is an indicator of the goodness of the fits for comparison.

Figs. 5.12b and 5.12a show $\mathrm{H}\alpha$ normalised lines ordered by time and by phase[3] (notice the colors correspond to the same date in both plots). The phase is the orbital phase calculated following Eq. 5.2 where,

- $T_0 = 51495.75$, mid-eclipse time from Corbet and Mukai [2002].
- $P_{\mathrm{orb}} = 6.0724$ days, orbital period from Corbet and Mukai [2002]

Apart from these plots, in order to look for any relation of $\mathrm{H}\alpha$ evolution with the orbital phase, all the spectra have been corrected of the radial velocity measurements (shown in Table 5.3) by the IRAF routine DOPCOR, and those spectra corresponding to $\phi = 0.00 \pm 0.10$, $\phi = 0.25 \pm 0.10$, $\phi = 0.50 \pm 0.10$, and $\phi = 0.75 \pm 0.10$ have been averaged and are shown in Fig. 5.13.

Moreover, the $\mathrm{H}\alpha$ EW has been calculated by an IRAF routine that subtracts the linear continuum and sums up the pixels. This measurement has been performed three times per line, therefore the final measurement is the average of these three, and the uncertainty is the statistical deviation. A Lomb-Scargle periodogram of these measurements has been performed with no result. Fig. 5.14 shows the evolution of this EW vs the orbital phase. This value is very variable in time in this system, but it seems to have no correlation with the orbital phase, although some of the EW measurements agree with the values of $EW = -6$Å and $EW = -5.5$Å found by Verrecchia et al. [2002].

The $\mathrm{He\ I}$ lines located at $\lambda = 6678$Å and $\lambda = 7065$Å might have *P-Cygni* profiles as noticed by Verrecchia et al. [2002]. The resolution of FRODOSpec spectra is not good enough to confirm this fact with a single spectrum. Therefore, all the spectra have been corrected of the radial velocity measurements (shown in Table 5.8) by the IRAF routine DOPCOR and averaged. The resulting profiles are shown in Fig. 5.15.

Both $\mathrm{He\ I}$ lines seem to have *P-Cygni* profiles. Therefore, in order to look for relations of the evolution of this profile with the orbital period, the averaged lines in four different phases are shown in Figs 5.16 and 5.17.

The EW of both lines have been calculated the same way as the $\mathrm{H}\alpha$ EW, and its evolution with the orbital phase is shown in Fig. 5.18. A Lomb-Scargle periodogram of these values have been performed with no significant result.

[3] The orbital phase has been calculated using Eq. 5.2 and these values for T_0 and P_{orb} during the whole section.

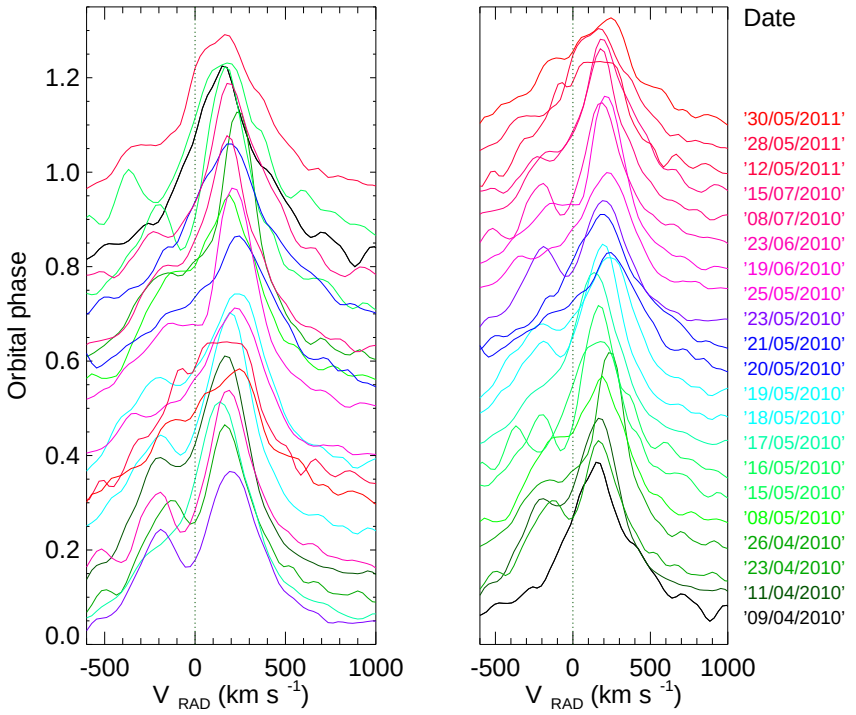

(a) Hα evolution with the orbital period.

(b) Hα evolution with time.

Figure 5.12: Hα normalised profile evolution with the orbital phase calculated following Eq. 5.2 on Fig. 5.12a, and with time on Fig. 5.12b. Notice that in both figures the colors correspond to the same date.

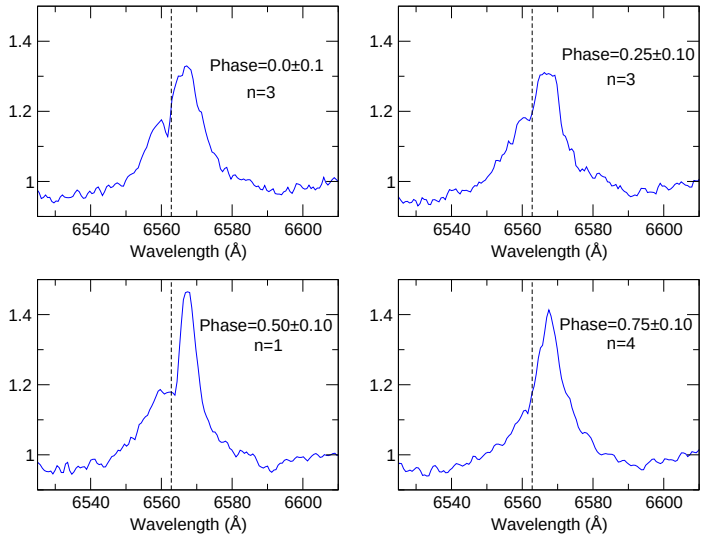

Figure 5.13: Hα averaged in four different orbital phases. The n number appearing in the plots is the number of spectra averaged for that orbital phase.

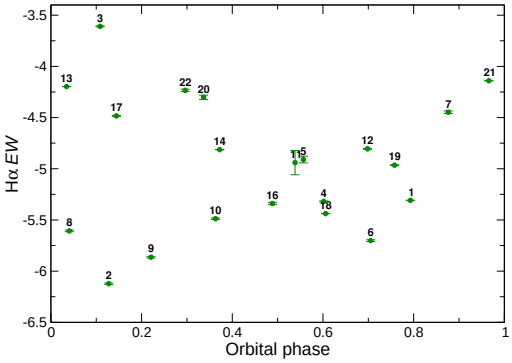

Figure 5.14: Hα EW vs the orbital phase. The numbers on top of each data point correspond to Table 5.3. Notice that some of the EW measurements agree with the values of $EW = -6$Å and $EW = -5.5$Å found by Verrecchia et al. [2002].

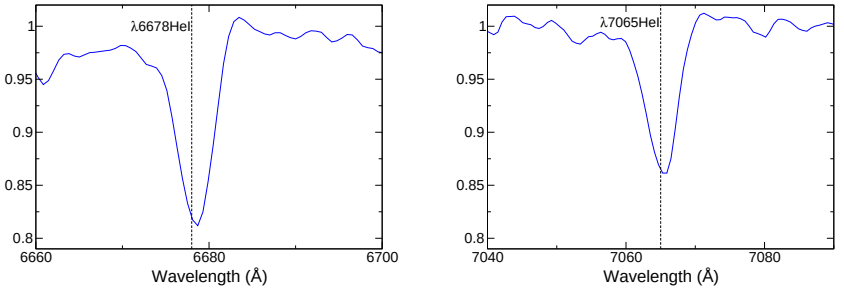

(a) Averaged He I line at λ6678Å.

(b) Averaged He I line at λ7065Å.

Figure 5.15: Averaged He I lines at λ6678Å and λ7065Å.

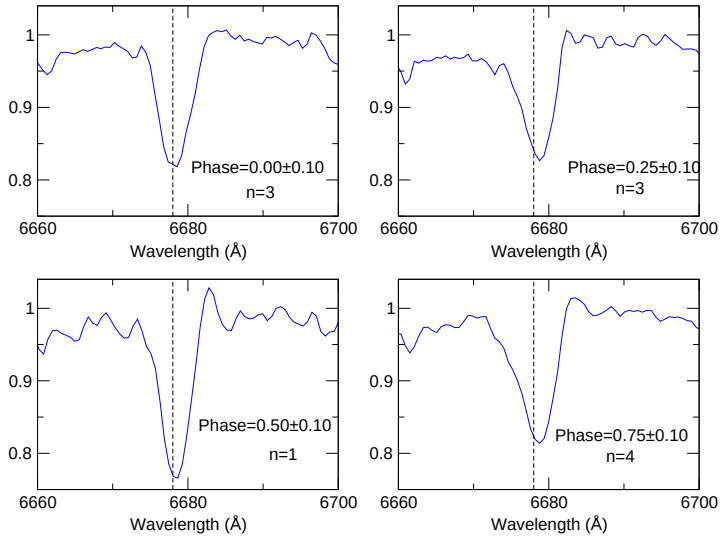

Figure 5.16: He Iλ6678Å averaged in four different orbital phases. The n number appearing in the plots in the number of spectra averaged for that orbital phase.

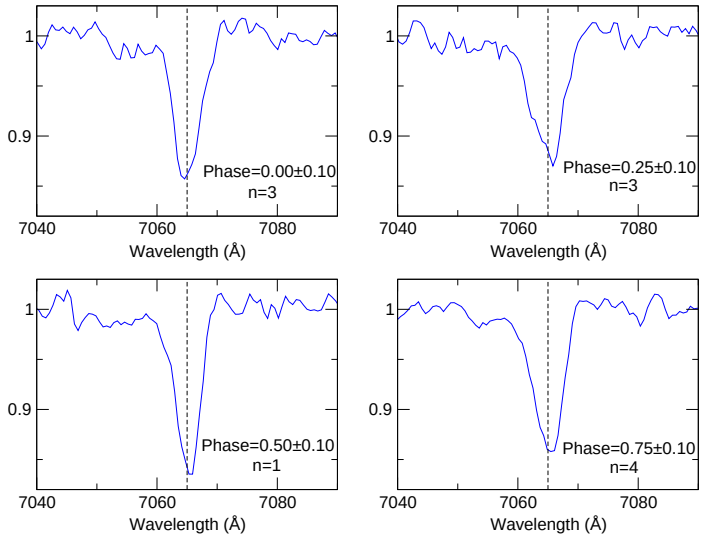

Figure 5.17: He Iλ7065Å averaged in four different orbital phases. The n number appearing in the plots in the number of spectra averaged for that orbital phase.

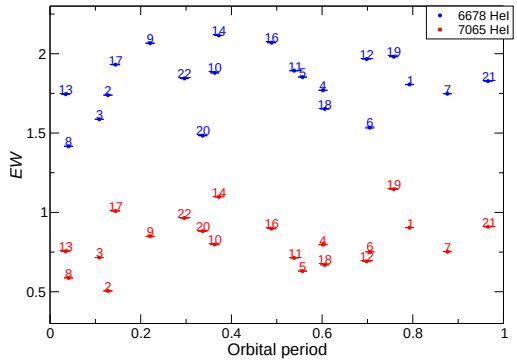

Figure 5.18: He I EW vs the orbital phase. Numbers on top of each data point correspond to Table 5.3.

5.2.4 X-ray light curves

The Lomb-Scargle periodograms of the 'dwell' ASM light curve and the BAT light curve (see Fig. 5.19) give periods of 6.0743 ± 0.0016 d and 6.0738 ± 0.0028 d respectively. These values are perfectly compatible with the Corbet and Mukai [2002] orbital period, and also with the period obtained from the radial velocity values from FRODOSpec spectra (Fig. 5.8).

Foldings of ASM 'one day averaged', and BAT light curves are shown in Fig 5.20. Two foldings have been performed for each light curve, one with the orbital period published in Corbet and Mukai [2002] (Fig. 5.20a) and other with the period obtained in the Lomb-Scargle periodogram (Fig. 5.20b) of the corresponding light curve. In all the foldings, the upper and lower limits of the eclipse, published by Corbet and Mukai [2002] (see Fig. 5.1), are pointed out by red vertical lines.

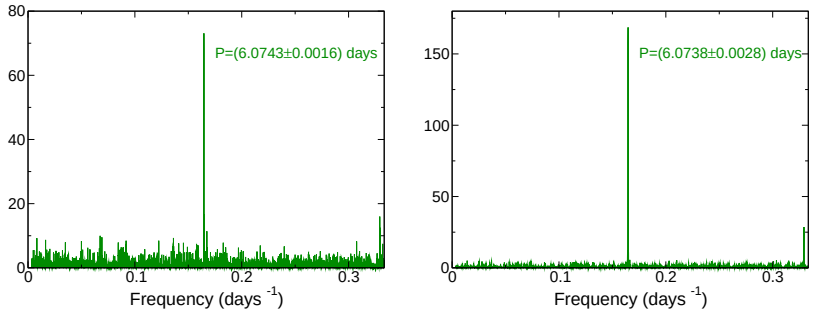

(a) Lomb-Scargle periodogram of ASM@RXTE light curve.

(b) Lomb-Scargle periodogram of BAT@Swift light curve.

Figure 5.19: Lomb Scargle periodograms of X-ray light curves. The periods obtained are perfectly compatible with Corbet and Mukai [2002] orbital period, and also with the period found in the Lomb Scargle periodogram of the radial velocity values of FRODOSpec spectra (Fig. 5.8).

5.3 Discussion

5.3.1 Orbital period

Although $P_{\rm orb}$ from Corbet and Mukai [2002] has been adopted for the orbital calculations and to observe variations along the orbit of the $\rm He\ I$ and $\rm H\alpha$ lines, several values for this parameter have been obtained during this work. These values are summarised in Table 5.10 and all of them are compatible with each other within error bars except the IDS $V_{\rm rad}$ value, and being the IDS+FRODOSpec $V_{\rm rad}$ value the more distant value to the others.

This source has an X-ray eclipse [Corbet and Mukai, 2002]. This eclipse is pointed out by red vertical lines in Figs. 5.1 and 5.20. The $P_{\rm orb}$ of ~ 6.073 days fits better with the eclipse time than the $P_{\rm orb} = 6.0724$ days of Corbet and Mukai [2002].

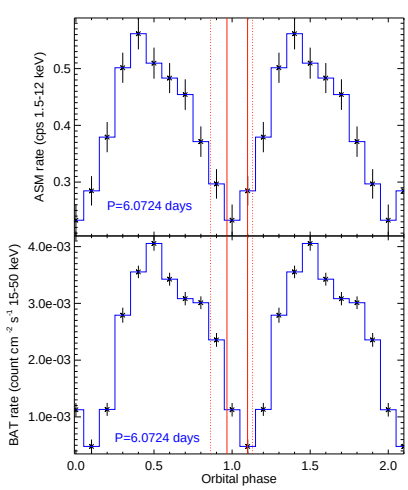

(a) Folding of ASM and BAT X-ray light curves over Corbet and Mukai [2002] orbital period.

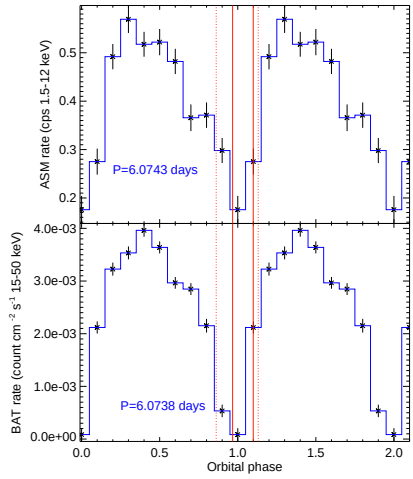

(b) Folding of ASM and BAT X-ray light curves over the periods obtained in the Lomb Scargle periodograms (see Fig. 5.19).

Figure 5.20: Average folded light curves in two energy ranges over the $P_{\rm orb}$ of Corbet and Mukai [2002] on Fig. 5.20a, and over the period found in the Lomb-Scargle of the corresponding X-ray light curves in Fig. 5.20b. An offset of 0.15 ASM cps has been introduced in the ASM foldings following Corbet and Mukai [2002] criteria. The red vertical lines indicate the lower and upper limits on the eclipse duration calculated by Corbet and Mukai [2002].

Table 5.10: Different values for the orbital period.

	$P_{\rm orb}$ (days)
Corbet and Mukai [2002]	6.0724 ± 0.0009
IDS $V_{\rm rad}$	5.5444 ± 0.0035
FRODOSpec $V_{\rm rad}$	6.073 ± 0.022
IDS+FRODOSpec $V_{\rm rad}$	6.0889 ± 0.0032
ASM light curve	6.0743 ± 0.0016
BAT light curve	6.0738 ± 0.0028

Table 5.11: Chemical abundances of XTE J1855-026 in $\log\frac{N(X)}{N(H)}$+12 resulting from the FASTWIND spectroscopic analysis and chemical abundances derived by Crowther et al. [2006] for B0.5 Ia in the Milky Way for comparison.

Species	XTEJ 1855-026	B0.5 Ia
C	7.29 ± 0.16	~ 7.9
N	8.08 ± 0.23	~ 8.3
O	8.56 ± 0.24	~ 8.5

5.3.2 Spectral classification

The main indicator of the spectral type is Si IV to Si III EW ratio [Walborn, 1971], which in this case indicate a spectral type of BN0.2 Ia. The "N" in the classification is because this kind of stars show strong C lines which are not present in this star. In spite of the EW ratio of these lines is used for $T_{\rm eff}$ calculations, the $T_{\rm eff}$ of XTE J1855-026 is too low for this spectral type. Indeed, Coleiro and Chaty [2013] assigned a $T_{\rm eff} = 28100$ K to this source based on Negueruela et al. [2008a] classification. But $T_{\rm eff}$ values for spectral classifications and other purposes are tabulated following different models being just indicative. Its $\log\ g$ clearly indicates that it is a supergiant star.

Related to the abundances, in Table 5.7 there are stellar abundances,derived by Nieva and Przybilla [2012], for B-type stars in the Solar neighbourhood for comparison. In addition, solar abundances from Asplund et al. [2009] are also shown in the same table. The N and O abundance (within errors) is compatible with the solar abundances and with B-type stars of the main-sequence, although the C abundance is too low.

Comparing the abundances of C, N and O of XTE J1855-025 with those derived by Crowther et al. [2006] for similar spectral type and luminosity stars (see Table 5.11), O and N abundances are in the average, while C is well below the average.

The rotation of the optical counterpart of XTE J1855-026 is also very high for a star with such a high luminosity, with typical rotational values of ~ 80 km s^{-1} [e.g., Crowther et al., 2006]. Indeed, the number of Galactic early-B super-

giants with projected rotational velocities above $80\,\mathrm{km\,s^{-1}}$ is marginal, most of them concentrate around $40{-}80\,\mathrm{km\,s^{-1}}$ [see Fig. 14 in Simón-Díaz and Herrero, 2014].

The high rotational velocity and its belonging to a binary system makes it different to an isolated standard star of this spectral type due to its different evolutionary path caused by interactions (mass transfer, tidal effects, etc.) with its companion.

A nominal distance can be calculated using the $B = 16.1$ value of Verrecchia et al. [2002] and the distance module. Making use of the Rieke and Lebofsky [1985] law ($A_\mathrm{B}/A_\mathrm{V} = 1.324$) and the absorption value $A_\mathrm{V} = 5.8{\pm}0.9$ of Coleiro and Chaty [2013]: $A_\mathrm{B} = A_\mathrm{V} \times 1.324 \Rightarrow A_\mathrm{B} = 7.7 \pm 1.2$. Therefore, the unabsorbed $B_0 = 8.4 \pm 1.2$ together with the $(B - V) = -0.206$ from the atmosphere model gives an estimation of $V_0 = 8.6 \pm 1.2$. The $M_\mathrm{V} = -6.4$ of the atmosphere model is in coincidence with the Crowther et al. [2006] values for the corresponding spectral type, consequently, using this value, the nominal distance is $\mathbf{d = 10^{+7}_{-4}\,kpc}$.

With this value of the distance and the atmosphere model parameters, approximate values for the radius ($\mathbf{R = 27^{+21}_{-10}\,R_\odot}$) and the mass ($\mathbf{M = 13^{+19}_{-7}\,M_\odot}$) have been calculated. This value of the radius is perfectly compatible with the minimum radius of $\sim 20\,\mathrm{R_\odot}$ calculated by Corbet and Mukai [2002] from the limits of the eclipse.

The complex $W43$ is a massive and concentrated molecular cloud located in the Galactic plane, probably one of the most extreme molecular complexes in the Milky way. It spands the range $l = 29.6°$ to $l = 31.4°$, and it is located at a distance $\sim 6\,\mathrm{kpc}$ [Nguyen Luong et al., 2011]. Therefore, the galactic longitude of $W43$ coincides with the galactic longitude of XTE J1855-026 [$l \sim 31°$; Cutri et al., 2003] and the minimum distance of XTE J1855-026 happens to meet the $W43$ distance. The latitude of $W43$ spans from $b = -0.5°$ to $b = 0.3°$ [Nguyen Luong et al., 2011], which means (through basic trigonometric relations), that it spans from $-52\,\mathrm{pc}$ below to $31\,\mathrm{pc}$ above the Galactic plane. The latitude of XTE J1855-026 is $b \sim -2°$ [Cutri et al., 2003]. Therefore, assuming the minimum distance of $6\,\mathrm{kpc}$ it would be at $\sim -210\,\mathrm{pc}$ away from the Galactic plane. Consequently, XTE J1855-026 would be $\sim 158\,\mathrm{pc}$ apart of $W43$ and perfectly visible at this distance and also at further away distances.

The maximum distance of XTE J1855-026 locates the source ~ 580 pc away from the Galactic plane. For the distance of ~ 10 kpc the source would be ~ 340 pc away from the Galactic plane, it is also a long distance, but not such as ~ 580 pc. This such a large distance from the Galactic plane might be explained with the system being ejected from a cluster outside the Galactic plane, or with a large 'recoil velocity' after que Supernovae explosion, or with a combination of both.

5.3.3 Orbital solution

Comparing the σ values of the whole set of fittings (Table 5.9), the smallest one corresponds to the eccentric solution taking into account both data sets, while the largest one is for the circular solution of FRODOSpec data. Therefore, there is something that is introducing eccentricity in the orbital solution, but this something should be related to the orbital motion as the Lomb-Scargle periodograms of the $V_{\rm rad}$ values of FRODOSpec data are giving values compatible with the orbital period determined by Corbet and Mukai [2002] and also with the values obtained with periodograms from both X-ray light curves (Table 5.10).

The K_0 value is important in the sense that it is the parameter determining the dynamical masses of the components of the binary system through the mass function. As there are several orbital solutions with different parameters (Table 5.9), there are dissimilar K_0 values. The only K_0 value compatible with the IDS circular solution is the K_0 value from the IDS eccentric solution. So, discarding this value, doing an weighted average of the rest of the K_0 values (where weights are $1/\Delta K$), and taking the uncertainty value as

$$\Delta K_0 = \frac{max(K_0 + \Delta K_0) - min(K_0 - \Delta K_0)}{2}, \tag{5.4}$$

the value obtained is $\mathbf{K_0 = 26.8 \pm 8.2\,km\,s^{-1}}$.

From the mass function value of Corbet and Mukai [2002] for the circular solution taking into account all the data points (see Fig. 5.3), it is possible to derive a $K_{\rm X}$ value:

$$\left.\begin{array}{l} K_{\rm X} = \frac{2\pi a_{\rm X} \sin i}{P_{\rm orb}} \\ f(M_0) = \frac{4\pi^2}{G} \frac{a_{\rm X}^3 \sin^3 i}{P_{\rm orb}^2} \end{array}\right\} \Rightarrow K_{\rm X} = \left(2\pi G \frac{f(M_0)}{P_{\rm orb}}\right)^{1/3}, \tag{5.5}$$

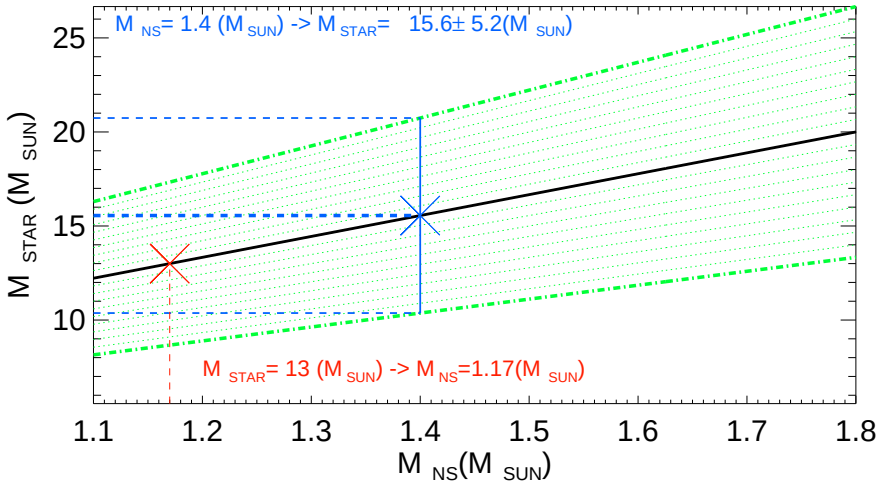

Figure 5.21: XTE J1855-026 range of masses permitted given the relation between the $K_{\rm X}$ value of Corbet and Mukai [2002] and the K_0 value obtained in this work (see Eq. 5.7). The value of the corresponding mass of the supergiant for the canonical value of $1.4\,{\rm M}_{\odot}$ of the neutron star is pointed out with a blue cross symbol. The value of the corresponding mass for the neutron star given the spectral mass value of the donor star is pointed out with a red cross symbol.

with the corresponding uncertainty:

$$\Delta K_{\rm X} = \frac{1}{3}\left(\frac{2\pi G}{P_{\rm orb} f\,(M_0)^2}\right)^{1/3} \Delta f\,(M_0) + \frac{1}{3}\left(\frac{2\pi G f\,(M_0)}{P_{\rm orb}^4}\right)^{1/3} \Delta P_{\rm orb}. \tag{5.6}$$

Introducing the corresponding values [$P_{\rm orb} = 6.0724 \pm 0.0009$ days and $f\,(M_0) = 16.4 \pm 1.4\,{\rm M}_{\odot}$; Corbet and Mukai, 2002] in the appropriate units in Eqs. 5.5 and 5.6, the value obtained is $\mathbf{K_X = 297 \pm 8\,km\,s^{-1}}$.

These K values follow the relation of Eq. 2.11 as explained in Sec. 2.2.4 of Chapter 2, therefore:

$$\left.\begin{array}{l} q = \frac{M_{\rm X}}{M_0} = \frac{K_0}{K_{\rm X}} \\ \Delta q = \frac{\Delta K_0}{K_{\rm X}} + \frac{K_0 \Delta K_{\rm X}}{K_{\rm X}^2} \end{array}\right\} \Rightarrow \mathbf{q = 0.090 \pm 0.030} \tag{5.7}$$

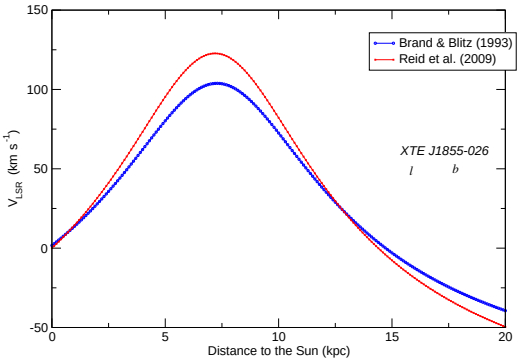

Figure 5.22: Radial velocity curve with respect to the LSR due to galactic rotation as function of distance, using the rotation curve of Brand and Blitz [1993] and Reid et al. [2009] in the direction of XTE J1855-026.

Fig. 5.21 shows the possible masses of both components of the binary system permitted by the obtained q value. The canonical value of $1.4\,M_\odot$ for the neutron star, corresponds to a value of $15.6 \pm 5.2\,M_\odot$ for the supergiant or donor star of the binary system. The spectroscopic mass of $\sim 13\,M_\odot$ corresponds to a value of $1.17\,M_\odot$ for the neutron star. The uncertainty in this value (the spectroscopic mass) is related to the uncertainty in the distance value. A value of $32\,M_\odot$ for the donor star corresponds to the upper limit in the distance. If the donor star had this mass value, it would imply a mass of $\sim 3\,M_\odot$ for the neutron star. This value of the mass of the neutron star is well above the limit of masses permitted by the Equation of State of dense nuclear matter [$\sim 2.4\,M_\odot$; see e.g., Sec. 1.2 of Chapter 1 or Lattimer, 2012]. The minimum distance sets a lower limit in the mass of the donor star of $6\,M_\odot$, implying a mass of $\sim 0.5\,M_\odot$ for the neutron star. This minimum value of the mass is well below the permitted limit [$\sim 1.2\,M_\odot$; see e.g., Sec. 1.2 of Chapter 1 or Lattimer, 2012]. In addition, the mass of the neutron star of $1.17\,M_\odot$ predicted by the relation of the semi-amplitudes of the radial velocity curves and the spectroscopic mass calculated with the distance and the atmosphere model, is in the lower limit of masses permitted for neutron stars. In view of this, we would set as the lower limit of the distance the value of

10 kpc, and an upper limit not reaching the 17 pc. These lower an upper limits would set the masses of the supergiant and the neutron star at $\sim 15\,M_\odot$ and $\sim 1.4\,M_\odot$ respectively. The radius of the donor star at such a distance would be $\sim 25\,R_\odot$, still compatible with the Corbet and Mukai [2002] value of $\sim 20\,R_\odot$.

There is an important discrepancy between systemic velocities found within the FRODOSpec and the IDS data sets (see Table 5.9). In spite of this difference, both data sets give negative values of this parameter. Fig. 5.22 shows the dependence of radial velocity with distance in the direction to XTE J1855-026 ($l = 31°.1$, $b = -02°.1$) according to two widely used rotation curves. The blue curve is computed assuming circular galactic rotation and adopting the rotation curve of Brand and Blitz [1993], while the red one follows the rotation curve of Reid et al. [2009]. Therefore, assuming a distance of ~ 10 kpc, the v_{LSR} would be $\sim 50\,km\,s^{-1}$ which is at least $\sim 60\,km\,s^{-1}$ away from the systemic velocity found within the data sets of this work. This could be interpreted as a large recoil velocity of the binary system after the Supernovae explosion during its formation. This large value might explain a distance of ~ 100 pc to the Galactic plane of XTE J1855-026, but not the corresponding distance of ~ 340 pc.

Moreover, for such a recoil velocity, the kick during the Supernovae explosion should have caused a large eccentricity in the binary system, which is not observed in the X-ray orbital solution of Corbet and Mukai [2002]. This absence of eccentricity might be due to the circularisation of the orbit through tidal forces. The orbital period of the system is smaller than ~ 8 days, and this kind of systems are expected to circularise [see Sec. 1.5.2 of Chapter 1, or e.g., Pfahl et al., 2002].

5.3.4 X-ray flux behaviour

Generally it is a persistent source except for the X-ray eclipses. But it has had some outbursts since it was discovered.

Scaling the X-ray flux value of Corbet et al. [1999] to the nominal distance of $d = 10^{+7}_{-4}$ kpc, the $L_{2-10\mathrm{keV}} = 1.3^{+2.5}_{-0.8} \times 10^{36}$ erg s^{-1}, which is the $\sim 10^{36}$ erg s^{-1} typical value of wind-fed SGXBs. Doing the same thing for the X-ray flare detected by Mereghetti et al. [2010], $L_{20-40\mathrm{keV}} = 2.4^{+4.5}_{-1.5} \times 10^{37}$ erg s^{-1}, but this value is not comparable with Corbet et al. [1999] value as the energy ranges are totally different.

Since the source is monitored by ASM in 1996, just three flares have been detected. Therefore, the average folded ASM and BAT light curves (Fig. 5.20) could give a realistic idea of the modulation of the X-ray flux as well as the average flux in both energy ranges.

If the count rates of the average foldings are roughly transformed into Crab units[4] the average flux values are $\bar{F}_{1.5-12\mathrm{keV}} \sim 3$ mCrab and $\bar{F}_{15-50\mathrm{keV}} \sim 11$ mCrab. Consequently, the X-ray source emits more in the hard ($15-50$ keV) X-ray range than in the soft ($1.5-12$ keV) one.

The amplitude of the ASM ($1.5-12$ keV) folding is of 5 mCrab, while the amplitude of BAT ($15-50$ keV) is of 16 mCrab. Taking into account the existence of an eclipse in the X-rays, the larger amplitude of BAT average folded light curve agrees with the idea of the source emitting more in the hard ($15-50$ keV) than in the soft ($1.5-12$ keV) energy range. Also notice, the amplitude of the ASM average folding is perfectly compatible with that published by Corbet and Mukai [2002].

The average flux of the BAT average folded light curve with a value of ~ 11 mCrab could be compared with the highest BAT flare detected by Krimm et al. [2012] that reached a value of ~ 230 mCrab. This increase of the flux is of a factor of ~ 20, therefore, it is below the flux range of the flares that defines the SFXTs [e.g., Walter and Zurita Heras, 2007].

The maximum value of the flux is reached at $\phi = 0.4$ (~ 2.4 days after the eclipse) in the ASM average folded light curve over the $P_{\mathrm{orb}} = 6.0724$ d of Corbet and Mukai [2002], and at $\phi = 0.3$ (~ 1.8 days after the eclipse) in the the folded over the period obtained in the periodogram of the light curve. In the case of BAT average folded light curve, the maximum occurs at $\phi = 0.5$ (~ 3 days after the eclipse) in the case of the Corbet and Mukai [2002] P_{orb} and at $\phi = 0.4$ (~ 2.4 days after the eclipse) in the average folding over the other period. Consequently, in both cases, the maximum occurs first in the soft band ($1.5-12$ keV) and, 0.1 phases after in the hard band ($15-50$ keV). The minimum flux occurs at $\phi = 0.0$ in all cases except for the BAT average folding over the Corbet and Mukai [2002] P_{orb} where it takes place at $\phi = 0.1$ (~ 0.6 days after

[4] Values for the transformation from ASM and BAT rates into Crabs can be found at `http://xte.mit.edu/ASM_lc.html` and `http://swift.gsfc.nasa.gov/results/transients/` respectively.

the predicted mid-time of the eclipse). This means that the new $P_{\rm orb}$ could fit better with eclipse times.

5.4 Conclusions

XTE J1855-026 is a HMXB which consists of a NS and a $\rm BN0.5\,Ia$ supergiant, typical of wind-fed SGXBs [see e.g., Coleiro and Chaty, 2013]. The overabundance of $\rm N$ and the high rotational velocity could be due to the binary evolution.

The X-ray luminosity would be $\sim 10^{36}$ erg s^{-1} for the distance of ~ 10 kpc, again typical of wind-fed SGXBs, but with brief excursions to higher X-ray luminosities not reaching amplitudes similar to that of SFXTs.

The orbital period of Corbet and Mukai [2002] is reinforced with the results of this work, although the eclipse is better observed in the average X-ray foldings with the ~ 6.3 days period obtained from FRODOSpec radial velocity values and X-ray light curves periodograms.

The large distance to the Galactic plane make this source different from the majority of HMXBs which are largely confined in a disc [see Sec. 1.5 of Chapter 1, or Coleiro and Chaty, 2013]. Such a long distance from the plane might be explained with the combination of an ejection of this source from a cluster outside the Galactic plane and a large recoil velocity (that is certainly observed). This large recoil velocity should imply an important eccentricity of the binary system due to the expected kick from the Supernovae explosion during its formation. In spite of this, the X-ray orbital solution is circular. However the circularisation of the binary system is possible due to its relatively short orbital period [see e.g., Pfahl et al., 2002].

The main issue is the discrepancy between the eccentricity found in the optical data and the X-ray orbital solution. There is something inducing eccentricity in the $V_{\rm rad}$ measurements of the optical data that is accompanying the orbital movement. It might be an extended mass loss causing the *P-Cygni* profiles as proposed for the first time by Verrecchia et al. [2002], but no modulation have been detected either in the $\rm H\alpha$ nor in $\rm He\ I$ lines analysis.

In spite of this discrepancy, the mass function seems to be well determined. The semi-amplitudes of the different orbital solutions are compatible with each other except for semi-amplitude of the circular solution of the IDS data set (see Table. 5.9). Combining the results of the atmosphere model and the orbital parameters, it is possible to consider a value of $\sim 15\,\mathrm{M}_{\odot}$ and $\sim 1.4\,\mathrm{M}_{\odot}$ for the supergiant star and the neutron star respectively.

More data are necessary to disentangle the origin of the eccentricity found in the optical orbital solution. Accurate photometry would give a better measurement of A_{V}, allowing a better determination of the distance, and consequently the X-ray luminosity or the radius of the donor star would be better defined. Additionally, high quality blue spectra, with Si lines well defined, would be useful to determine an accurate optical orbital solution to combine it with the NS orbital solution and have a complete picture of this binary system.

CHAPTER 6

Two Supergiant Fast X-ray Transients:

AX J1841.0-0535 & AX J1845.0-0433

The two sources discussed in this Chapter, AX J1841-0535 and AX J1845.0-0433, present the behaviour typical of the SFXTs, they are undetectable with INTEGRAL most of the time having fast X-ray transient activity (lasting less than a day) showing outbursts with complex structures characterised by several fast flares [e.g., Sguera et al., 2006, Negueruela et al., 2006b, Walter and Zurita Heras, 2007, Blay et al., 2012].

AX J1841-0535

AX J1841-0535 was firstly detected by Bamba and Koyama [1999] with ASCA during an X-ray outburst with a rise time of < 1000 seconds and highly variable X-ray flux. Further ASCA observations of the Scutum arm region performed by Bamba et al. [2001] detected the same source with highly variable X-ray flux and two extremely rapid flares (the fluxes increased by one order of magnitude within one hour) in the $2.0 - 10.0$ keV band, while in the $0.7 - 2.0$ keV band the fluxes were essentially constant.

Bamba et al. [2001] detected a period of 4.7394 ± 0.0008 seconds during the brightest flare, that was interpreted as the spin period of the pulsar. The quiescent level of the source during these observations was $F_{2.0-10.0\,\mathrm{keV}} \sim 2 \times 10^{-12}$ erg cm^{-2} s^{-1}, with the brightest flares reaching values of $F_{2.0-10.0\,\mathrm{keV}} \sim 10^{-10}$ erg cm^{-2} s^{-1}.

Since the X-ray luminosity was consistent with that of a "Type I outburst" of a Be/X-ray binary [Negueruela, 1998], and the erratic flux variability together with the coherent pulsations are characteristic of Be/X-ray binaries, Bamba et al. [2001] proposed that AX J1841-0535 would be either a member of this sub-class of X-ray pulsars, or could be part of a new sub-class of X-ray transients that were showing multiple flares with fast-rise of a few hours such as AX J1845.0-0433 [Yamauchi et al., 1995] or XTE J1739-302 [Smith et al., 1998].

Halpern et al. [2004] observed AX J1841-0535 with Chandra detecting a bright variable source at $RA = 18^h41^m0^s.54$ and $Dec = -05°35'46".8$ with $F_{0.5-10.0\,\mathrm{keV}} = 4.2 \times 10^{-12}\,\mathrm{erg\,cm^{-2}\,s^{-1}}$, perfectly compatible with Bamba et al. [2001] results. Halpern et al. [2004] selected an optical counterpart by positional coincidence from the digitized UK Schmidt plates and 2MASS at coordinates $RA = 18^h41^m0^s.43$ and $Dec = -05°35'35".46$, a reddened star that shows weak double-peaked Hα emission lines supporting the Be/X-ray binary hypothesis of Bamba et al. [2001].

Negueruela et al. [2006b] took better quality optical spectra of this source and suggested it to be a luminous B0-1 type rather than a Be star and classified the binary system as a Supergiant Fast X-ray Transient, that was a new sub-class of binary systems at that moment. This spectral classification and its SFXT nature was confirmed by Nespoli et al. [2008].

The spectral classification of the optical counterpart was refined by Negueruela et al. [2008b] as a B0.2 Ibp supergiant at a distance of ~ 4 kpc.

AX J1845.0-0433

AX J1845.0-0433 was discovered by Yamauchi et al. [1995] with ASCA as an X-ray transient source. During the initial ~ 9 hours the source was in a very faint quiescent state, and suddenly flared up in less than ~ 20 minutes. Subsequently the source was characterised by several other peaks lasting a few tens of minutes, until the end of the observation. Therefore, the X-ray flux showed flare-like activity, being stable in the quiescent state and highly variable during flares. The amplitude of these variations was more than 90% of the average flux in the $0.7 - 10$ keV band. The peak flux of the flare was $F_{0.7-10.0\,\mathrm{keV}} \sim 1 \times 10^{-9}\,\mathrm{erg\,cm^{-2}\,s^{-1}}$, while the average flux during the quiescent state was $F_{0.7-10.0\,\mathrm{keV}} \sim 3 \times 10^{-12}\,\mathrm{erg\,cm^{-2}\,s^{-1}}$.

In spite of the X-ray spectral analysis resembles those of the typical X-ray pulsars, no coherent pulsations were found in the range from 125 ms to 4096 seconds. This lack of a pulsation period could be explained by a shorter or longer spin period, or by an alignment of the magnetic dipole and the rotation axis [Yamauchi et al., 1995].

Coe et al. [1996] proposed an optical counterpart for AX J1845.0-0433 identifying the object as a $\mathrm{O9.5\,I}$ supergiant at a distance of ~ 3.6 kpc. Negueruela et al. [2006b] showed that the optical counterpart proposed by Coe et al. [1996] had strong $\mathrm{H}\alpha$ emission, with strength and shape variable, typical of a luminous supergiant in an interacting binary system.

Sguera et al. [2007a] reported two fast flares, one in April 2005 and other one in April 2006, with time-scales of a few tens of minutes of the source detected by INTEGRAL in the $20 - 40$ keV energy range with IBIS, and in the $3 - 10$ keV energy range with JEM-X. The first flare reached a peak flux of $F_{20-40\,\mathrm{keV}} \sim 4.5 \times 10^{-10}\,\mathrm{erg\,cm^{-2}\,s^{-1}}$, and $F_{3-10\,\mathrm{keV}} \sim 4.8 \times 10^{-10}\,\mathrm{erg\,cm^{-2}\,s^{-1}}$; while the second flare reached a peak flux of $F_{20-40\,\mathrm{keV}} \sim 6 \times 10^{-10}\,\mathrm{erg\,cm^{-2}\,s^{-1}}$. In both flares the source displayed a kind of pre and post flaring activity characterised by several other small flares having the same fast time-scale but a smaller peak flux [Sguera et al., 2007a].

Sguera et al. [2007a] also reported Swift observations where the fast flaring of the source was evident. AX J1845.0-0433 reached a peak flux of $F_{0.2-10\,\mathrm{keV}} \sim 2.3 \times 10^{-10}\,\mathrm{erg\,cm^{-2}\,s^{-1}}$ in November 2005. The source underwent a very fast flare in March 2006 reaching in only 4 minutes a peak flux of $F_{0.2-10\,\mathrm{keV}} \sim 1.3 \times 10^{-10}\,\mathrm{erg\,cm^{-2}\,s^{-1}}$. The source flux dropped again to a very low level after this flare with the same fast time-scale.

The Swift analysis of Sguera et al. [2007a] provided a very accurate position of the source at $RA = 18^h45^m01^s.9$ and $Dec = -04°33'57".6$. This position is at $4".7$ from the supergiant proposed by Coe et al. [1996] as it optical counterpart, confirming the supergiant nature of AX J1845.0-0433.

The fast flaring activity reported to that date made Sguera et al. [2007a] set AX J1845.0-0433 apart from classical SGXBs and classify it as a member of the "new" discovered class of Supergiant Fast X-ray Transients [e.g. Negueruela et al., 2006b, Sguera et al., 2006].

Negueruela et al. [2008b] refined the classification the optical counterpart reported by Coe et al. [1996] with a spectral type of $09\,\mathrm{Ia}$ and a distance of ~ 7 kpc. Scaling the previous fluxes to this distance:

- $L_{0.7-10.0\,\mathrm{keV}} \sim 6{\times}10^{36}\,\mathrm{erg\,s^{-1}}$ during the ASCA flare detected by Yamauchi et al. [1995].
- $L_{0.7-10.0\,\mathrm{keV}} \sim 2\times10^{34}\,\mathrm{erg\,s^{-1}}$ during the quiescent state before the previous flare detected with ASCA [Yamauchi et al., 1995].
- $L_{20-40\,\mathrm{keV}} \sim 2.6\times10^{36}\,\mathrm{erg\,s^{-1}}$ and $L_{3-10\,\mathrm{keV}} \sim 2.8\times10^{36}\,\mathrm{erg\,s^{-1}}$ during the first flare detected with INTEGRAL by [Sguera et al., 2007a].
- $L_{20-40\,\mathrm{keV}} \sim 3.5\times10^{36}\,\mathrm{erg\,s^{-1}}$ during the second flare detected with INTEGRAL by [Sguera et al., 2007a].
- $L_{0.2-10\,\mathrm{keV}} \sim 1.4\times10^{36}\,\mathrm{erg\,s^{-1}}$ during the first flare detected with Swift by [Sguera et al., 2007a].
- $L_{0.2-10\,\mathrm{keV}} \sim 7.6\times10^{35}\,\mathrm{erg\,s^{-1}}$ during the second flare detected with Swift by [Sguera et al., 2007a].

Zurita Heras and Walter [2009] finally confirmed the supergiant counterpart of AX J1845.0-0433 reported by Coe et al. [1996] with XMM-Newton astrometry. They observed quiescent luminosities of $L_{0.4-10\,\mathrm{keV}} \sim 5.3\times10^{35}\,\mathrm{erg\,s^{-1}}$ and $L_{20-100\,\mathrm{keV}} \sim 1\times10^{35}\,\mathrm{erg\,s^{-1}}$, while during the flares the average luminosities were $L_{0.4-10\,\mathrm{keV}} \sim 6.8\times10^{36}\,\mathrm{erg\,s^{-1}}$ and $L_{20-100\,\mathrm{keV}} \sim 1.7\times10^{36}\,\mathrm{erg\,s^{-1}}$, being the minimum luminosity $L_{0.4-10\,\mathrm{keV}} \sim 4.1\times10^{34}\,\mathrm{erg\,s^{-1}}$ (assuming a distance of ~ 7 kpc). Therefore, the source was considered as a persistent source in the soft $(0.4-10\,\mathrm{keV})$ energy range with variations of factors of as high as 50 on extremely short time-scales (few ks). The X-ray spectrum obtained in this work was again typical of wind-fed accreting pulsars. Zurita Heras and Walter [2009] proposed clumps of mass $M \sim 10^{22}$ g within the stellar wind of the supergiant companion to explain the persistent X-ray flux in the soft band in contrast with the flare characteristics (number, luminosity, duration, increase/decrease time).

Goossens et al. [2013] have recently found a periodicity of ~ 5.7 days in the IBIS/INTEGRAL $(18-60\,\mathrm{keV})$ light curve of this source that was interpreted as the orbital period of the binary system.

Table 6.1: Observation log of AX J1841.0-0535 (blue classification spectrum).

#	Date	MJD	Texp (s)	Instrument
1	04/04/2007 05:31:36.005	54194.23	900.1	ISIS@WHT
2	05/04/2007 05:27:20.017	54195.23	900.1	ISIS@WHT
3	06/04/2007 05:38:01.029	54196.23	900.1	ISIS@WHT
4	07/04/2007 05:57:20.457	54197.25	900.1	ISIS@WHT

6.1 Observations

Data for radial velocity determinations have mostly been obtained with FRODOSpec, therefore reduced with my pipeline (Chapter 3). AX J1841.0-0535 data set for radial velocities covers from 2007 to 2012 (Table. 6.2), while AX J1845.0-0433 covers from 2005 to 2012 (Table 6.4). In both data sets, apart from FRODOSpec spectra, there are also long-slit spectra from other instruments complementing the full data set. There are also blue spectra of AX J1841.0-0535 which is useful for a rough spectral clasification (Table 6.1). The X-ray available light curves cover, in both cases, about 15 years in ASM, and ~ 9 years in BAT (Tables 6.3 and 6.5).

6.2 Data Analysis & Results

6.2.1 Spectral classification of AX J1841.0-0535

The blue ISIS spectra of Table 6.1 have been cross-correlated against a TLUSTY synthetic spectrum. These cross-correlations have given a radial velocity value for each spectrum. The four spectra have been corrected of the corresponding radial velocity value with the DOPCOR task of IRAF. After this correction, all the spectra have been averaged in order to obtain the spectrum shown in Fig. 6.1.

Balmer lines of this spectrum are broader at "bluer" wavelengths, which is a peculiar feature of this source. With these data, we could just confirm the spectral classification of Negueruela et al. [2008b] as a $\mathrm{B0.2\,Ibp}$, with the 'p' meaning "peculiar". More data would be necessary to better classify this supergiant star.

Table 6.2: Observation log of AX J1841.0-0535 (radial velocity determinations).

#	Date	MJD	Texp (s)	Instrument
1	04/04/2007 05:31:34	54194.23	900.1	ISIS@WHT
2	05/04/2007 05:27:19	54195.23	900.1	ISIS@WHT
3	06/04/2007 05:37:55	54196.23	900.1	ISIS@WHT
4	07/04/2007 05:57:17	54197.25	900.1	ISIS@WHT
5	04/04/2011 03:58:44	55655.15	3×1200	FRODOSpec@LT
6	06/04/2011 03:39:36	55657.15	3×1200	FRODOSpec@LT
7	07/04/2011 03:35:09	55658.15	3×1200	FRODOSpec@LT
8	11/04/2011 03:31:10	55662.13	3×1200	FRODOSpec@LT
9	14/04/2011 04:12:34	55665.18	3×1200	FRODOSpec@LT
10	26/04/2011 02:24:12	55677.10	3×1200	FRODOSpec@LT
11	05/05/2011 03:25:11	55686.13	3×1200	FRODOSpec@LT
12	07/05/2011 02:01:54	55688.11	3×1200	FRODOSpec@LT
13	10/05/2011 03:35:07	55691.14	3×1200	FRODOSpec@LT
14	13/05/2011 03:18:35	55694.15	3×1200	FRODOSpec@LT
15	29/05/2011 02:41:41	55710.11	3×1200	FRODOSpec@LT
16	30/05/2011 01:47:49	55711.07	3×1200	FRODOSpec@LT
17	31/05/2011 00:52:23	55712.04	3×1200	FRODOSpec@LT
18	15/05/2012 02:59:19	56062.10	3×1200	FRODOSpec@LT
19	27/05/2012 03:32:47	56074.15	3×1200	FRODOSpec@LT
20	31/05/2012 03:13:26	56078.13	3×1200	FRODOSpec@LT
21	01/06/2012 03:34:27	56079.15	3×1200	FRODOSpec@LT
22	16/06/2012 02:50:22	56094.12	1200	FRODOSpec@LT
23	18/06/2012 03:27:49	56096.14	3×1200	FRODOSpec@LT
24	19/06/2012 00:50:09	56097.03	3×1200	FRODOSpec@LT

Table 6.3: Observation log of X-ray data of AX J1841.0-0535.

Date	MJD	Data points	Instrument	Energy range
06/01/1996–12/10/2011	50088–55847	70316 (dwell)	ASM@RXTE	$1.5 - 12.2$ keV
06/01/1996–12/10/2011	50088–55847	4629 (daily)	ASM@RXTE	$1.5 - 12.2$ keV
14/02/2005–15/01/2014	53415–56672	2965	BAT@Swift	$15 - 50$ keV

Table 6.4: Observation log of AX J1845.0-0433.

#	Date	MJD	Texp (s)	Instrument@Telescope
1	11/07/2005 20:28:24	53562.85	2000	Slit spectrograph@Skinakas 1.3m
2	12/07/2005 20:12:12	53563.84	2000	Slit spectrograph@Skinakas 1.3m
3	04/06/2006 01:28:37	53890.06	1200	ALFOSC@NOT
4	30/08/2008 20:46:36	54708.87	1500	ALFOSC@NOT
5	01/04/2011 04:38:42	55652.19	3×1200	FRODOSpec@LT
6	05/04/2011 03:46:12	55656.16	3×1200	FRODOSpec@LT
7	09/04/2011 03:27:39	55660.14	3×1200	FRODOSpec@LT
8	10/04/2011 03:40:45	55661.15	3×1200	FRODOSpec@LT
9	12/04/2011 04:04:31	55663.17	3×1200	FRODOSpec@LT
10	06/05/2011 03:01:25	55687.13	1200	FRODOSpec@LT
11	10/05/2011 02:24:14	55691.10	3×1200	FRODOSpec@LT
12	11/05/2011 03:18:55	55692.14	3×1200	FRODOSpec@LT
13	23/05/2011 00:43:24	55704.03	3×1200	FRODOSpec@LT
14	28/05/2011 01:34:56	55709.07	3×1200	FRODOSpec@LT
15	29/05/2011 00:48:17	55710.03	3×1200	FRODOSpec@LT
16	17/05/2012 02:18:32	56064.10	3×1200	FRODOSpec@LT
17	25/05/2012 03:37:46	56072.15	3×1200	FRODOSpec@LT
18	28/05/2012 02:38:30	56075.11	3×1200	FRODOSpec@LT
19	29/05/2012 01:36:18	56076.07	3×1200	FRODOSpec@LT
20	14/06/2012 02:05:18	56092.09	3×1200	FRODOSpec@LT
21	15/06/2012 01:44:07	56093.07	3×1200	FRODOSpec@LT
22	16/06/2012 00:18:51	56094.01	3×1200	FRODOSpec@LT
23	17/06/2012 00:07:29	56095.00	3×1200	FRODOSpec@LT
24	18/06/2012 02:09:18	56096.09	3×1200	FRODOSpec@LT
25	19/06/2012 03:03:30	56097.13	3×1200	FRODOSpec@LT

Table 6.5: Observation log of X-ray data of AX J1845.0-0433.

Date	MJD	Data points	Instrument	Energy range
08/01/1996–13/10/2011	50090–55847	47576 (dwell)	ASM@RXTE	$1.5 - 12.2$ keV
08/01/1996–13/10/2011	50090–55847	4452 (daily)	ASM@RXTE	$1.5 - 12.2$ keV
14/02/2005–13/01/2014	53415–56670	2958	BAT@Swift	$15 - 50$ keV

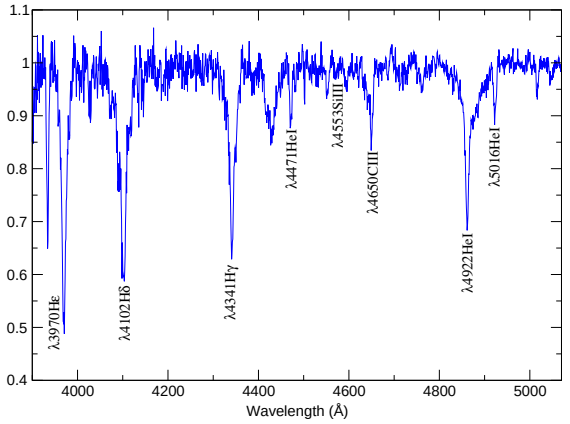

Figure 6.1: AX J1841.0-0535 blue spectrum. Median of four spectra obained with ISIS@WHT blue arm (see Table 6.1).

6.2.2 Radial velocity determinations

AX J1841.0-0535

He I lines in 6678 Å and 7065 Å have been used for the cross-correlations of FRODOSpec data of Table 6.2 against a TLUSTY synthetic spectrum, while the H Paschen series ($\lambda = 8467$ Å,$\lambda = 8545$ Å, $\lambda = 8598$ Å, $\lambda = 8750$ Å, $\lambda = 8862$ Å) and the He I line at 8778 Å has been used for ISIS data shown in the same Table. The results of these cross-correlations are shown in Table 6.6.

A Lomb-Scargle periodogram of the radial velocity values shown in Table 6.6 has been performed with *Starlink* resulting in a value of $P \sim 6.5$ days (Fig. 6.2). This value of the orbital period is an input for SBOP, that, after several iterations, calculates a more accurate orbital period value as well as the rest of the orbital parameters shown in Table 6.7 that corresponds to the radial velocity curve of Fig. 6.3.

AX J1845.0-0433

The radial velocity values shown in Table 6.8 have been obtained by cross-correlating the observed spectra (Table 6.4) against a FASTWIND synthetic spectrum provided by Dr. Artemio Herrero.

The lines used for the cross-correlations are He I at $\lambda = 65875$ Å, He I at $\lambda = 6678$ Å + He II at $\lambda = 6683$ Å and He I at $\lambda = 7065$ Å. In this case, a TLUSTY model was not enough for the cross-correlation because it is not able to reproduce the combination of the spectral lines He I at $\lambda = 6678$ Å + He II at $\lambda = 6683$ Å (see Fig. 6.4). The mass loss required to reproduce the observed features of the spectrum is $\log Q \sim -12.28$, perfectly compatible with the mass loss rates of IGR J00370+6122 [see Table 4.4 of Chapter 4, or González-Galán et al., 2014] or XTE J1855-026 (see Table 5.6 of Chapter 5). This FASTWIND synthetic spectrum just reproduces qualitatively the observed spectra.

A Lomb-Scargle periodogram of the radial velocity values has been performed with *Starlink* giving a value of $P \sim 4.7$ days (Fig. 6.5). This value of the orbital period is an input for SBOP, that, after several iterations, calculates a more accurate value for the orbital period as well as the rest of the orbital parameters.

Table 6.6: AX J1841.0-0535 $V_{\rm rad}$ values. The first column of this table is the number of the observation from Table 6.2. The second column is the phase of the observation, according to the orbital solution described in Table 6.7. Measurements have been sorted using this parameter. The third column is the radial velocity. The last column shows the residuals from the radial velocity curve calculated (see Fig. 6.3) and the observational points.

#	Phase	$V_{\rm rad}$ (km s^{-1})	O-C (km s^{-1})
10	0.0272	71.7 ± 5.0	0.12
7	0.0902	74.6 ± 6.2	−8.7
24	0.1038	90.0 ± 5.2	4.47
15	0.1433	90.8 ± 4.4	0.22
20	0.1748	83.1 ± 7.2	−10.36
9	0.1790	96.2 ± 4.7	2.51
1	0.1922	98.5 ± 5.6	3.98
13	0.2045	104.1 ± 5.2	9.03
16	0.2925	90.5 ± 5.0	−4.74
21	0.3320	87.6 ± 7.2	−6.02
2	0.3472	82.5 ± 8.2	−10.25
11	0.4286	102.0 ± 5.0	15.11
17	0.4415	85.4 ± 6.5	−0.28
3	0.5021	74.2 ± 7.2	−5.87
19	0.5570	67.4 ± 6.5	−7.04
5	0.6277	68.8 ± 5.5	1.96
22	0.6497	50.3 ± 8.0	−14.22
4	0.6571	75.8 ± 10.5	12.07
14	0.6677	73.8 ± 4.7	11.17
18	0.6936	66.2 ± 5.9	6.16
8	0.7097	46.3 ± 7.1	−12.26
12	0.7295	48.0 ± 9.8	−8.74
6	0.9357	59.2 ± 7.1	3.27
23	0.9658	59.8 ± 5.7	−0.46

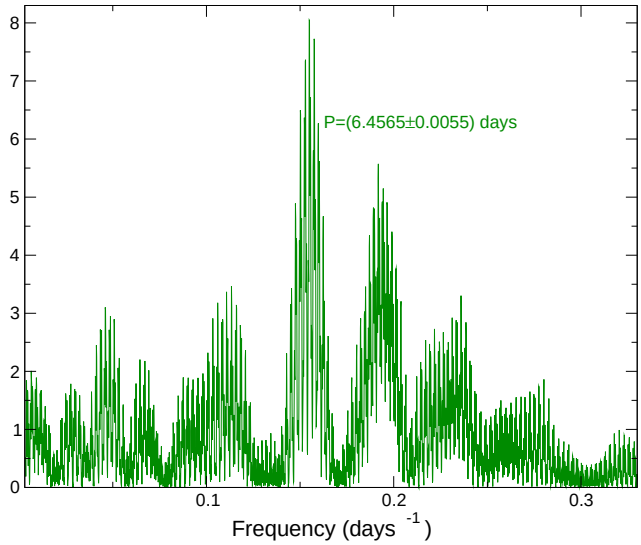

Figure 6.2: Lomb-Scargle periodogram of the radial velocity points of AX J1841.0-053 (Table 6.6) obtained with the PERIOD package within the *Starlink* environment.

Table 6.7: Orbital parameters of AX J1841.0-053 obtained by fitting the radial velocity points using Lehmann-Filhes method implemented in SBOP.

T_0 (HJD)	5883.9 ± 1.0
$P_{\rm orb}$ (days)	6.4530 ± 0.0016
e	0.16 ± 0.11
γ (km s^{-1})	74.4 ± 2.1
K_0 (km s^{-1})	22.6 ± 3.8
ω (degrees)	74.4 ± 2.1
$a_0 \sin i$ (km)	$(1.98 \pm 0.34)\ 10^6$
$f(M)$ ($M_\odot$)	0.0075 ± 0.0038

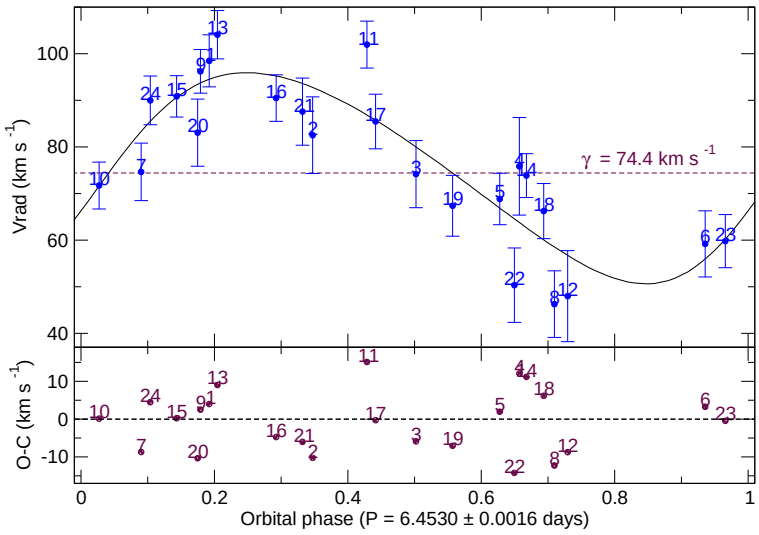

Figure 6.3: Radial velocity curve of AX J1841.0-0535. The number on top of each data point is the number of the observation from Table 6.2. *Top:* Fitted radial velocity curve and real data folded on the 6.4530 days period derived from a Lomb-Scargle analysis of the data. *Bottom:* Residuals from the observed radial velocity points to the fitted radial velocity curve.

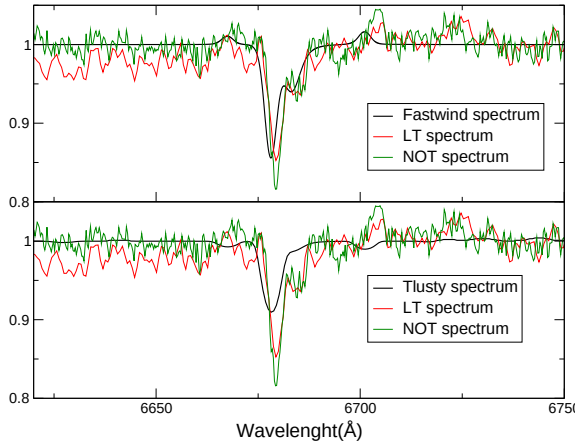

Figure 6.4: He I at $\lambda = 6678$ Å + He II at $\lambda = 6683$ Å lines of two of the observed spectra (numbers 3 and 17 of Table 6.4) of AX J1845.0-0433. The bottom panel shows the TLUSTY model that only is able to reproduce the He I $\lambda 6678$ Å line, while the top panel shows the FASTWIND model reproducing both lines.

Table 6.8: Radial velocities of AX J1845.0-0433 using FRODOSpec@LT data points on the left table, and all data points on the right one. The first column of both tables is the number of the observation from Table 6.4. The second column is the phase of the observation, according to the orbital solution described in Table 6.9. Measurements have been sorted using this parameter (orbital phase). The third column is the radial velocity. The last column shows the residuals from the radial velocity curve calculated (see Figs. 6.6) and the observational points.

FRODOSpec@LT				All data			
#	Phase	$V_{\rm RAD}$ (km s^{-1})	O-C (km s^{-1})	#	Phase	$V_{\rm RAD}$ (km s^{-1})	O-C (km s^{-1})
9	0.0544	44.7 ± 5.2	3.06	9	0.0288	44.7 ± 5.2	3.88
10	0.1047	29.0 ± 6.3	−11.93	10	0.0805	29.0 ± 6.3	−9.55
23	0.1399	40.2 ± 7.3	−2.32	23	0.1376	40.2 ± 7.3	−1.66
19	0.1452	42.1 ± 6.4	−0.76	12	0.1410	58.0 ± 5.7	15.82
12	0.1650	58.0 ± 5.7	13.73	19	0.1419	42.1 ± 6.4	−0.13
17	0.3192	53.8 ± 6.8	−2.48	2	0.2253	36.8 ± 3.5	−3.39
24	0.3687	57.7 ± 4.0	−1.94	17	0.3157	53.8 ± 6.8	−3.7
7	0.4161	60.1 ± 5.7	−2.56	24	0.3665	57.7 ± 4.0	−3.35
20	0.5243	68.3 ± 4.5	−0.18	7	0.3904	60.0 ± 5.7	−2.54
6	0.5751	71.7 ± 4.6	0.86	4	0.4771	73.7 ± 5.2	6.17
25	0.5875	76.2 ± 5.3	4.88	20	0.5219	68.3 ± 4.5	−1.37
16	0.6201	67.4 ± 6.1	−5.25	6	0.5492	71.7 ± 4.6	0.8
8	0.6290	72.4 ± 6.3	−0.58	25	0.5854	76.2 ± 5.3	3.91
13	0.6735	79.5 ± 4.9	5.19	8	0.6033	72.3 ± 6.3	−0.6
21	0.7322	80.2 ± 5.1	4.69	16	0.6162	67.3 ± 6.1	−6.03
14	0.7357	66.7 ± 5.4	−8.89	13	0.6502	79.5 ± 4.9	5.15
5	0.7390	76.8 ± 5.0	1.18	14	0.7126	66.7 ± 5.4	−8.9
22	0.9306	63.7 ± 4.4	0.37	5	0.7129	76.8 ± 5.0	1.2
15	0.9398	50.9 ± 4.9	−10.66	21	0.7298	80.2 ± 5.0	4.5
18	0.9433	59.1 ± 6.1	−1.83	1	0.9067	68.0 ± 6.2	2.63
11	0.9460	71.0 ± 4.5	10.63	15	0.9168	50.9 ± 4.9	−12.71
				11	0.9220	71.0 ± 4.5	8.31
				22	0.9283	63.7 ± 4.4	2.26
				3	0.9394	57.7 ± 3.6	−1.39
				18	0.9400	59.1 ± 6.1	0.07

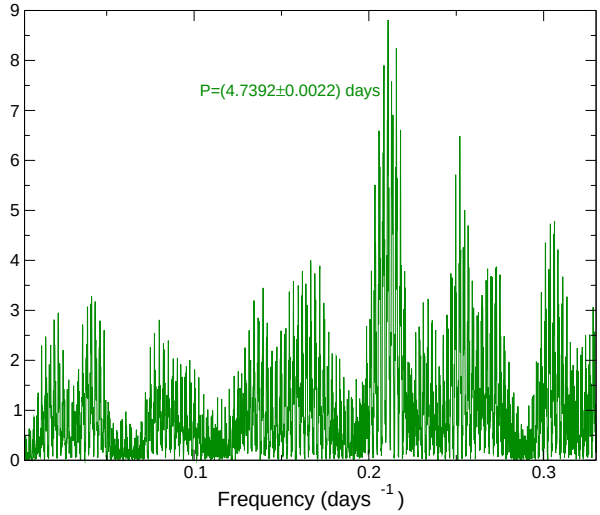

Figure 6.5: Lomb-Scargle periodogram of the radial velocity values of AX J1845.0-0433 (Table 6.8) obtained with the PERIOD package within the *Starlink* environment.

Table 6.9: Orbital parameters of AX J1845.0-0433 obtained by fitting the radial velocity points using Lehmann-Filhés method implemented in SBOP. On the left, the parameters obtained by fitting only FRODOSpec@LT data, and on the right, the parameters obtained fitting all the data points

FRODOSpec@LT		All data	
T_0 (HJD)	5691.88 ± 0.34	T_0 (HJD)	5691.99 ± 0.25
$P_{\rm orb}$ (days)	4.7410 ± 0.0019	$P_{\rm orb}$ (days)	4.73983 ± 0.00028
e	0.32 ± 0.16	e	0.34 ± 0.11
γ (km s^{-1})	61.1 ± 1.6	γ (km s^{-1})	61.0 ± 1.4
K_0 (km s^{-1})	17.5 ± 3.1	K_0 (km s^{-1})	18.0 ± 2.5
ω (degrees)	121 ± 32	ω (degrees)	128 ± 24
$a_0 \sin i$ (km)	$(1.08 \pm 0.20)\ 10^6$	$a_0 \sin i$ (km)	$(1.14 \pm 0.16)\ 10^6$
$f(M)$ ($M_\odot$)	0.0022 ± 0.0013	$f(M)$ ($M_\odot$)	0.0027 ± 0.0011

I have looked for an orbital solution just taking into account FRODOSpec@LT data finding the parameters shown on the left of Table 6.9 and the curve shown in Fig. 6.6a. To ensure this solution, I included some more data of the long-slit spectrograph at Skinakas 1.3 m telescope and ALFOSC@NOT finding the solution shown on the right of Table 6.9 that corresponds to the radial velocity curve of Fig. 6.6b, which is perfectly compatible with the FRODOSpec@LT solution, even more accurate and covering from 2005 to 2012.

6.2.3 Hα evolution

Balmer H lines, mainly Hα, are strongly affected by stellar winds [e.g., Klein and Castor, 1978, Leitherer, 1988, Puls et al., 1996, 2008]. Consequently, Figs, 6.7 and 6.8 would give an idea of the changes in the wind and mass loss along the orbit.

Hα appears in emission in both binary systems with no obvious correlation with the orbital period. Therefore, they would be mainly related to random changes in the wind of the supergiant.

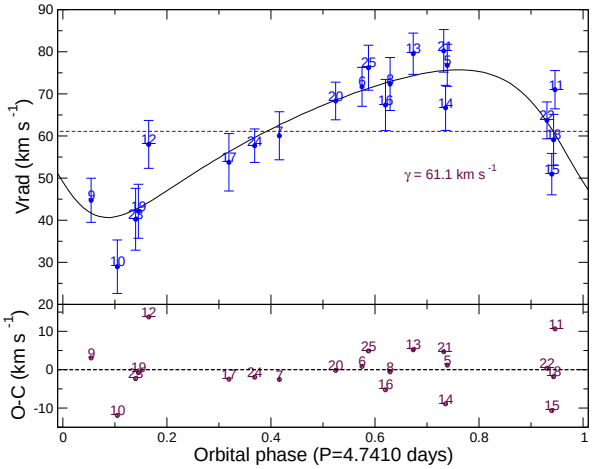

(a) Radial velocity curve of AX J1845.0-0433 obtained with FRODOSpec data.

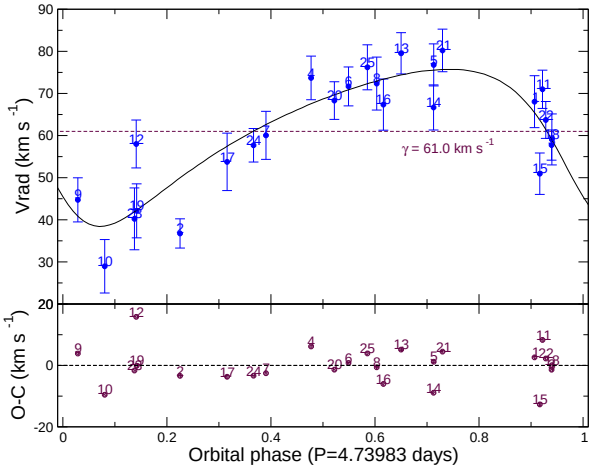

(b) Radial velocity curve of AX J1845.0-0433 obtained with all the data points.

Figure 6.6: Radial velocity curves of AX J1845.0-0433. The number on top of each data point is the number of the observation from Table 6.4. *Top panels:* Fitted radial velocity curve.*Bottom panels:* Residuals from the observed radial velocity points to the fitted radial velocity curve.

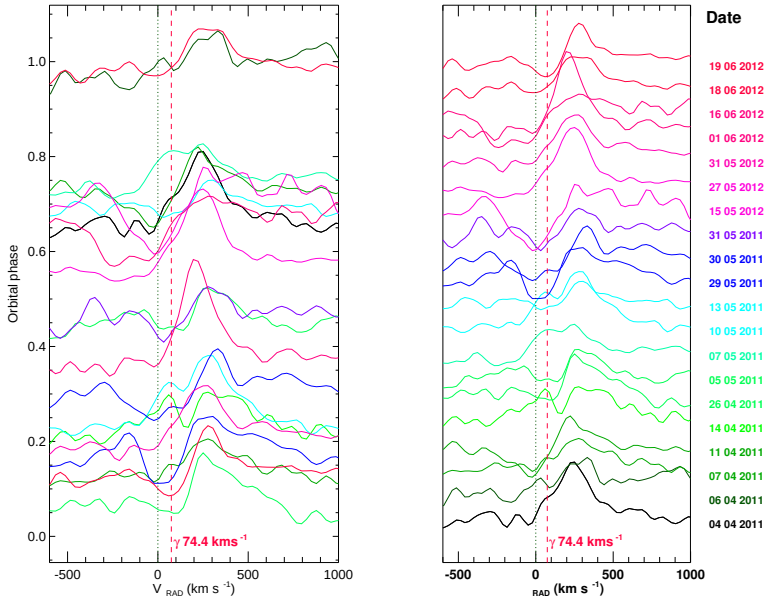

(a) Hα evolution with the orbital period.

(b) Hα evolution with time.

Figure 6.7: Hα normalised profile evolution with the orbital phase of AX J1841.0-0535 on Fig. 6.7a, and with time on Fig. 6.7b. Notice that in both figures the colors correspond to the same date.

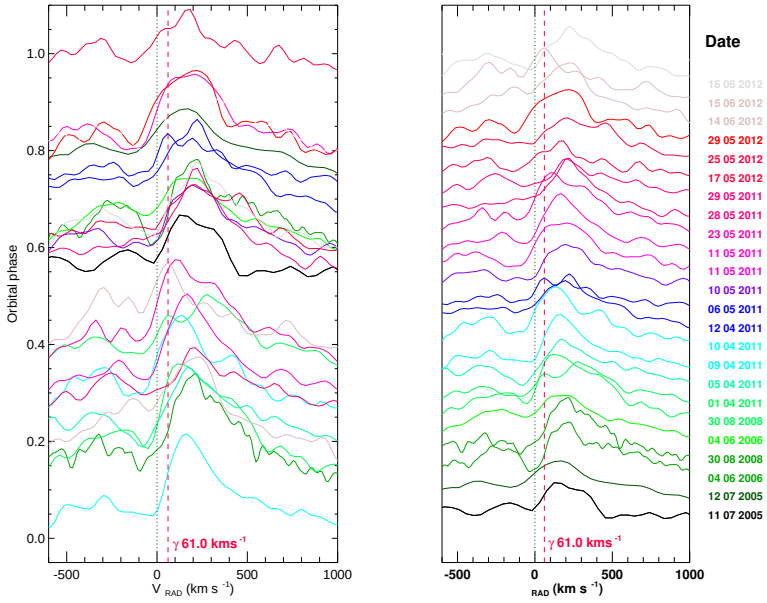

(a) $\mathrm{H}\alpha$ evolution with the orbital period.

(b) $\mathrm{H}\alpha$ evolution with time.

Figure 6.8: $\mathrm{H}\alpha$ normalised profile evolution with the orbital phase of AX J1845.0-0433 on Fig. 6.8a, and with time on Fig. 6.8b. Notice that in both figures the colors correspond to the same date.

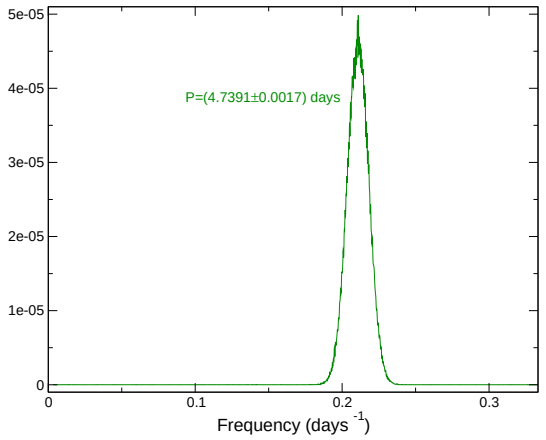

Figure 6.9: AX J1845.0-0433 clean periodogram of BAT@Swift data.

6.2.4 X-ray light curves

I have looked for periodicities within the available X-ray light curves of both sources (see Tables 6.3 and 6.5) between 3 and 300 days.

There is nothing significant either on none of the AX J1841.0-0535 data sets, nor in the ASM@RXTE light curve of AX J1845.0-0433. In spite of this, a period of 4.7391 ± 0.0017 days (see Fig. 6.9) has been detected in the BAT@Swift light curve that is perfectly compatible with the orbital period found with the $V_{\rm rad}$ data set (see Fig. 6.5 and Table 6.9).

Despite the lack of periodicity found in the AX J1841.0-0535 light curves, and in the ASM light curve of AX J1845.0-0433, averaged foldings over the orbital periods for both sources in both energy ranges have been performed and are shown in Figs 6.10 and 6.11.

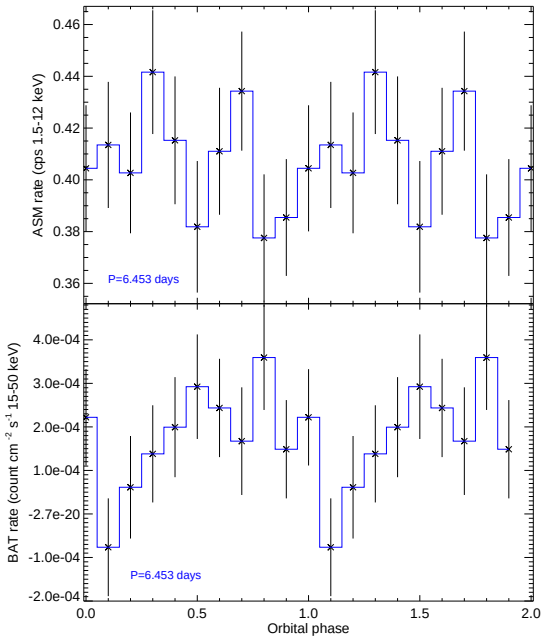

Figure 6.10: AX J1841.0-0535 averaged X-ray foldings. An offset of 0.15 ASM cps has been introduced in the ASM foldings following Corbet and Mukai [2002] criteria.

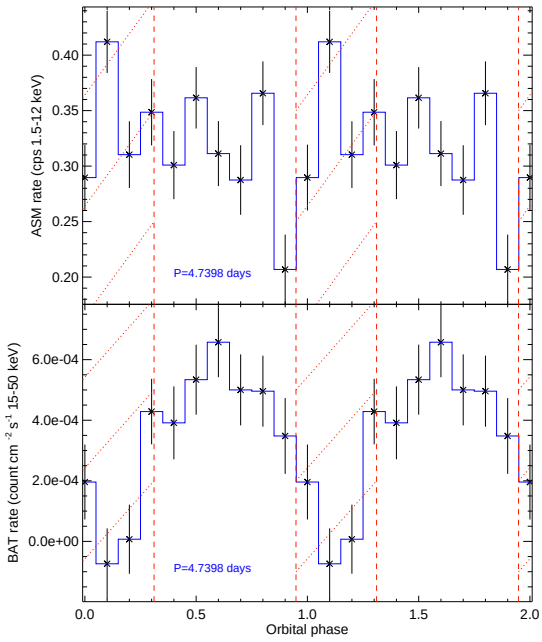

Figure 6.11: AX J1845.0-0433 averaged X-ray foldings. An offset of 0.15 ASM cps has been introduced in the ASM foldings following Corbet and Mukai [2002] criteria. Red vertical lines indicate the eclipse times predicted by SBOP.

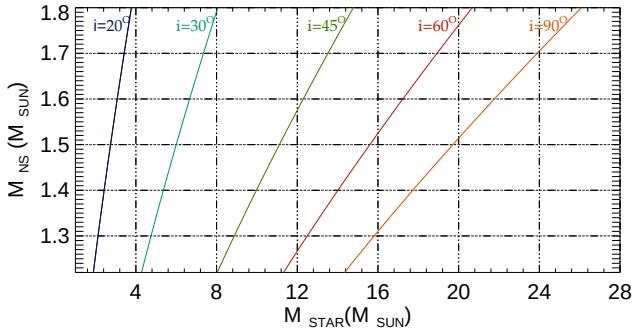

Figure 6.12: Relations between the supergiant mass and the neutron star mass of AX J1841.0-0535 from the mass function shown in Table 6.7. Lines for constant orbital inclination are constructed from the mass function and are labelled.

6.3 Discussion

Relations between masses of both components of a binary system depending on the orbital inclination can be obtained from the mass function (see Sec. 2.2.4 of Chapter 2). These relations are shown in Fig. 6.12 in the case of AX J1841.0-0535, and in Fig. 6.13 in the case of AX J1845.0-0433 (making use of the mass function of the orbital solution taking into account all the data points).

AX J1841.0-0535

To take a look about how much the uncertainty on the mass function affects to the calculation of the mass range permitted, Fig. 6.14 shows the possible range of masses for an inclination of $45°$ for AX J1841.0-0535. We have selected this inclination value due to the lack of X-ray periodicity (that discards an X-ray eclipse) found in both, the Lomb-Scargle periodograms and the X-ray foldings. In spite of the large uncertainties, Fig. 6.14 shows that either the mass value of the supergiant star should be low, or the value of the mass of the neutron star should be high compared to the canonical value of $\sim 1.4\,M_{\odot}$. This fact reinforces the idea of a "peculiar" supergiant star in this binary system.

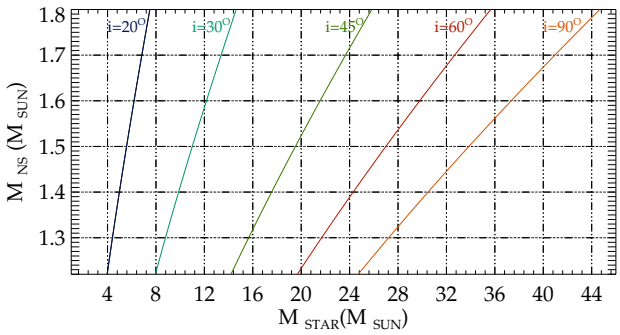

Figure 6.13: Relations between the supergiant mass and the neutron star mass of AX J1845.0-0433. Lines for constant orbital inclination are constructed from the mass function obtained with all the data points(see Table 6.9) and are labelled.

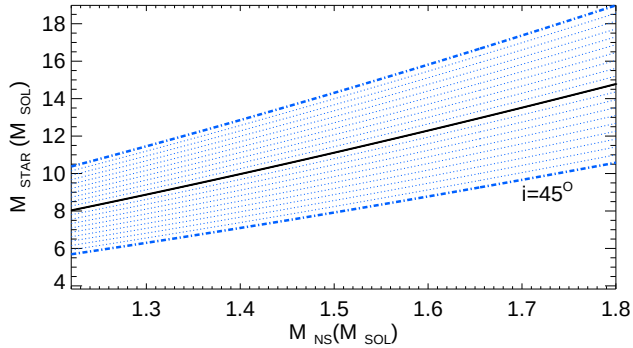

Figure 6.14: Relation between the supergiant mass and the neutron star mass for $i = 45°$ of AX J1841.0-0535. The shaded area represents the range of values allowed within a standard deviation for the value of $f(M)$ (see Table 6.7).

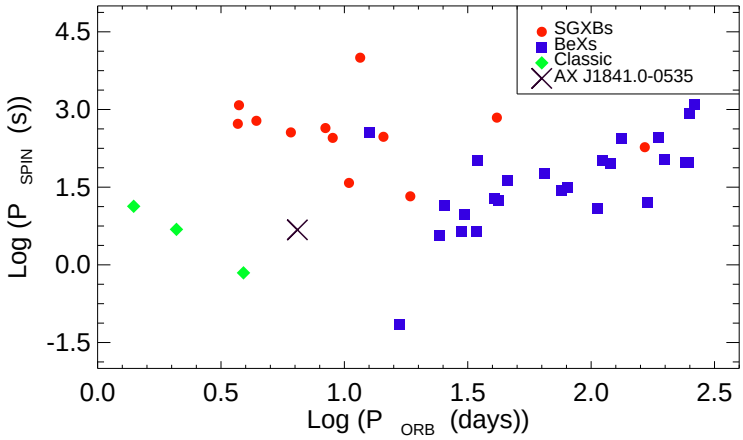

Figure 6.15: The $P_{\rm spin}/P_{\rm orb}$ (Corbet's) diagram for a large sample of HMXBs (see Fig. 1.9 of Chapter 1). The position of AX J1841.0-0535 is marked by a cross.

The double-peaked $\rm H\alpha$ emission detected by Halpern et al. [2004] is present in some of the spectra of this work (see Fig. 6.7). This line changes dramatically indicating a strong variability of the wind that does not seem to correlate with the orbital phase.

The lack of periodicity in the X-ray light curves of AX J1841.0-0535 might be due to the low eccentricity of its orbit ($e = 0.16 \pm 0.11$) which is perfectly compatible with a circular orbit. This low eccentricity is not the typical of a Be/X-ray binary [$e \gtrsim 0.3$; Reig, 2011]. The $P_{\rm orb} = 6.4530 \pm 0.0016$ d is too low compared to that of the typical Be/X-ray binary [$P_{\rm orb} \gtrsim 20$ d; Reig, 2011]. This fact, together with the spectral classification, would definitely discard the Be/X-ray binary nature proposed by Bamba et al. [2001].

The position of AX J1841.0-0535 in the Corbet diagram (see Fig. 6.15) does not locate the source in any of the established sub-groups. Its spin period is not typical of a wind-accreting system. Moreover, it has only been detected once. Some others published spin periods have been recently called into question [see e.g., Ducci et al., 2013, Drave et al., 2014].

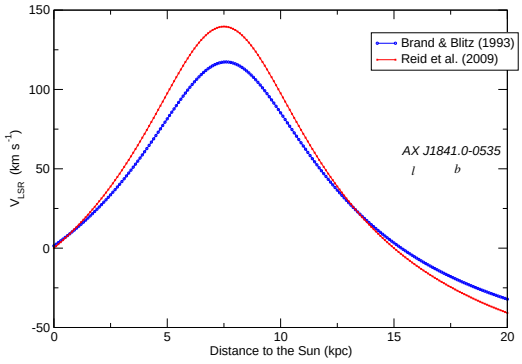

Figure 6.16: Radial velocity curve with respect to the LSR due to galactic rotation as function of distance, using the rotation curve of Brand and Blitz [1993] and Reid et al. [2009] in the direction of AX J1841.0-0535.

The X-ray fluxes reported by Bamba et al. [2001] could be scaled to the approximate distance of $\sim 4\,\mathrm{kpc}$ reported by Negueruela et al. [2008b] so that the quiescence value would be $L_{2.0-10.0\,\mathrm{keV}} \sim 4 \times 10^{33}\,\mathrm{erg\,s^{-1}}$, with the brightest flares reaching values of $L_{2.0-10.0\,\mathrm{keV}} \sim 2 \times 10^{35}\,\mathrm{erg\,s^{-1}}$. Consequently, the dynamical range of the X-ray luminosity covers perfectly the SFXTs dynamical range defined by Walter and Zurita Heras [2007]. However it is important to notice that this distance is just an approximation because of the peculiar optical spectrum that is really difficult to classify.

Fig. 6.16 shows the radial velocity with respect to the LSR due to the Galactic rotation in the direction of the source as a function of distance. The systemic velocity, with a value of $\gamma = 74.4 \pm 2.1\,\mathrm{km\,s^{-1}}$ is similar to the radial velocity of the Galaxy at the distance of $\sim 4\,\mathrm{kpc}$. Therefore, the kick induced by the Supernovae explosion, was not large in this case. This is consistent with the fact of the quasi-circular orbit.

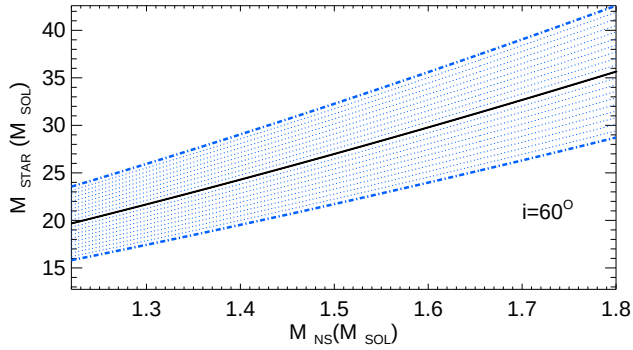

Figure 6.17: Relation between the supergiant mass and the neutron star mass for $i = 60°$ of AX J1845.0-0433. The shaded area represents the range of values allowed within a standard deviation for the value of $f(M)$ using all the data points (see Table 6.9).

AX J1845.0-0433

The eclipse time predicted by SBOP in the orbital solution coincides with the minimum of the X-ray folding of BAT light curve shown in Fig. 6.11. This fact reinforces the orbital period found in the radial velocity values data set, and also the orbital solution. The eccentricity of the orbit is $e = 0.34 \pm 0.11$, it is a considerable value but might be not high enough to explain the X-ray modulation of the BAT data by itself. Therefore, the existence of an eclipse cannot be discarded.

To take a look about how much the uncertainty on the mass function affects to the mass range permitted, Fig. 6.17 shows the possible range of masses for an inclination of $60°$ for AX J1845.0-0433. This inclination value has been adopted as an approximation due to the possibility of the existence of an eclipse in the X-ray light curve. Assuming such an inclination, a canonical value of $\sim 1.4\,M_\odot$ for the neutron star, corresponds to a value of $\sim 20\,M_\odot$ for the supergiant companion.

The strong $H\alpha$ emission observed by Negueruela et al. [2006b] is present in our spectra (Fig. 6.8). This emission is variable and does not seem to be correlated with the orbital period.

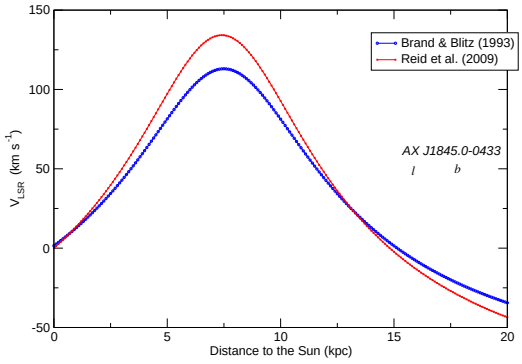

Figure 6.18: Radial velocity curve with respect to the LSR due to galactic rotation as function of distance, using the rotation curve of Brand and Blitz [1993] and Reid et al. [2009] in the direction of AX J1845.0-0433.

The periodicity found in the BAT X-ray light curve of AX J1845.0-0433 coincides with the one found in the radial velocity values, reinforcing this period as the orbital period of the binary system. Notice that Goossens et al. [2013] have recently found a ~ 5.7 days period in the IBIS light curve, which energy range ($18 - 60$ keV) is similar to that of BAT ($15 - 50$ keV). However, we are not able to reproduce that value.

The dynamical range of the X-ray luminosities is perfectly compatible with that defined by Walter and Zurita Heras [2007] for SFXTs. This fact together with the rapid X-ray flares definitely sets this source as a SFXT.

The systemic velocity, with value of $\gamma = 61.0 \pm 1.4\,\mathrm{km\,s^{-1}}$, is not compatible with the rotational velocity of the Galaxy at that distance (~ 7 kpc) in that direction ($v_{\mathrm{LSR}} \sim 100\,\mathrm{km\,s^{-1}}$; see Fig. 6.18). Therefore, in this case, there is a recoil velocity due to the Supernovae explosion, which is consistent with the eccentricity of the binary system.

6.4 Conclusions

Both sources show $\mathrm{H}\alpha$ variable emission not correlated with the orbital phase together with flaring variability in the X-ray flux similar to that of SFXTs. In addition, both of them harbour supergiant companions with similar spectral types. However, their eccentricity is completely different:

- $e \sim 0.16$ in AX J1841.0-0535, perfectly compatible with a circular orbit.
- $e \sim 0.34$ in AX J1845.0-0433, clearly eccentric.

This fact reinforces the idea that the eccentricity of the orbit of a wind-fed HMXB is not the unique factor that explains the X-ray behaviour of SFXTs.

CHAPTER 7

Conclusions & Future Work

Four wind-fed HMXBs have been characterised during this thesis. The main results of each of them are given in the corresponding chapters. In this Section I summarise the main global conclusions.

Related to the X-ray flux behaviour and, therefore, classification (see Fig. 1.8 of Chapter 1) IGR J00370+6122 is something intermediate between SFXTs and typical wind-fed SGXBs, while XTE J1855-026 is a typical SGXB and both, AX J1841.0-0535 and AX J1845.0-0433, are clearly SFXTs. Therefore, this sample should be good enough to deduce if any of the studied parameters during the thesis is able to explain the different X-ray flux detected behaviours.

IGR J00370+612 is the most eccentric HMXB with a supergiant donor known up to date. This source has a measurable recoil velocity which is perfectly compatible with this high eccentricity. Probably this system will not circularise due to its relatively high orbital period. The integrated X-ray flux of IGR J00370+612 seems to be persistent with a constant value below that of typical SGXBs. The eccentricity together with the possibility of an eclipse, could explain the X-ray flux overall variability shown in the averaged X-ray foldings. However, the X-ray flux is actually composed by continuous flares with lower intensities and lower amplitudes than that of SFXTs. Therefore, the classification of this HMXB within the established sub-classes is not plausible due to the infeasibility to fit its properties within any of these sub-classes.

XTE J1855-026 is also peculiar due to its large recoil velocity in combination with the low eccentricity detected in the X-ray pulse delay orbital solution. This

low eccentricity could be explained with the circularisation of the orbit, which is perfectly possible due to its relatively short orbital period. The distance of this source to the Galactic plane is also unusual, and might be explained as a combination of the large recoil velocity with the fact that this might have been ejected from a cluster not located in the Galactic plane. Despite the almost circular orbital solution found in the X-rays, which is perfectly compatible with the expected eccentricity of a persistent SGXB, we have found a measurable eccentricity in our optical orbital solution. This eccentricity might be associated to the mass loss reflected in the Hα and He I *P-Cygni* profiles. This kind of profiles causes a shift in the peak of the absorption lines, and might be interpreted as an extended mass loss from the supergiant to the neutron star. In spite of these shifts in the central peaks of the spectral lines, the orbital period found in the radial velocity points, is completely compatible with that of the X-ray orbital solution. Consequently, we were expecting variations of these profiles related to the orbital phase. The lack of correlation between *P-Cygni* profiles and orbital phase of our data, could be either explained with the non-existence of such a correlation, or with the need of a better quality spectra to detect it.

Both, AX J1841.0-0535 and AX J1845.0-0433, X-ray flux behaviour is the typical of SFXTs. Consequently, we were expecting similar orbital parameters or, at least, similar eccentricities. However, the eccentricity is perfectly compatible with a circular orbit in the case of AX J1841.0-0535, and has a significant value in the case of AX J1845.0-0433. Confirming the idea that eccentricity by itself cannot explain the X-ray flux behaviour.

In spite of their completely different X-ray flux behaviours, IGR J00370+612 and XTE J1855-026 are early-B supergiants, with similar masses, showing an excess of N in their atmospheres and high rotational values compared to those of isolated stars of the same spectral type. Both, the N over-abundance and the high rotational values, might be consequence of the binary evolution. The spectral classification of AX J1841.0-0535 and AX J1845.0-0433 is also similar, with a late-O supergiant and an early-B "peculiar" supergiant respectively. Basically this confirms the fact that typical optical counterparts for these kind of systems are mainly either late-O or early-B supergiants independently of their X-ray flux behaviour.

The highly variable winds of these HMXBs have been examined through the main wind indicator in the optical spectral range, i.e., Hα. All of the Hα profiles of the sources of study have emission features interpreted as a mass loss from

the supergiant star. Variations of this line do not seem to be correlated with the orbital phase in any of the targets of study. Consequently, these variations might be due mainly to intrinsic variations of the wind. However, their moderate mass values would correspond to lower mass loss rates than those detected. Presumably these high mass loss rates are due to the binary interaction, that is plausibly the responsible of the observed over-luminosity.

All these results together reinforce the idea of the existence of a continuum of properties in this kind of systems more than a strict classification into subclasses. In addition, they confirm there is not a unique simple factor determining the differences in the X-ray flux behaviour such as a higher eccentricity or wind clumpling, or even a combination of both. The plausible explanation to these differences could be a complex combination of factors plus a "gating" mechanism that mediates the accretion processes.

Blue spectra have metallic lines which are preferable to measure radial velocities. Therefore, as a future work we would like to obtain such spectra to better determine the orbits of XTE J1855-026, and the two SFXTs (AX J1841.0-0535 and AX J1845.0-0433). These blue spectra would also be useful to obtain a FASTWIND atmosphere model for AX J1841.0-0535 and AX J1845.0-0433 that will help to finally establish their spectral types and physical properties such as the $T_{\rm eff}$ or the $\log\ g$.

Red high quality spectral series will also help to be able to measure the variation of the *P-Cyni* profiles (in case of their existence) together with the $\mathrm{H}\alpha$ line profile variations. These measurements would finally disentangle whether or not there is a correlation between the wind variations reflected in these lines and the orbital phase.

We would also like to increase the sample of sources including, among others, the two peculiar SFXTs IGR J17544-2619 and XTE J1739-302. While XTE J1739-302 has a possible orbital period of ~ 50 days and showd orbital emission profiles that could be explained by the presence of a disc-like structure within the stellar wind of the supergiant companion; IGR J17544-2619 has a possible pulsation period of ~ 71 seconds, that combined with the ~ 5 days orbital period, locate the source close to the typical wind-fed SGXBs in the Corbet's diagram in spite of their different X-ray flux behaviour.

List of Figures

List of Tables

Bibliography

F. Aharonian, A. G. Akhperjanian, K.-M. Aye, A. R. Bazer-Bachi, M. Beilicke, W. Benbow, D. Berge, P. Berghaus, K. Bernlöhr, C. Boisson, O. Bolz, V. Borrel, I. Braun, F. Breitling, A. M. Brown, J. B. Gordo, P. M. Chadwick, L.-M. Chounet, R. Cornils, L. Costamante, B. Degrange, H. J. Dickinson, A. Djannati-Ataï, L. O. Drury, G. Dubus, D. Emmanoulopoulos, P. Espigat, F. Feinstein, P. Fleury, G. Fontaine, Y. Fuchs, S. Funk, Y. A. Gallant, B. Giebels, S. Gillessen, J. F. Glicenstein, P. Goret, C. Hadjichristidis, M. Hauser, G. Heinzelmann, G. Henri, G. Hermann, J. A. Hinton, W. Hofmann, M. Holleran, D. Horns, A. Jacholkowska, O. C. de Jager, B. Khélifi, N. Komin, A. Konopelko, I. J. Latham, R. Le Gallou, A. Lemière, M. Lemoine-Goumard, N. Leroy, T. Lohse, A. Marcowith, J.-M. Martin, O. Martineau-Huynh, C. Masterson, T. J. L. McComb, M. de Naurois, S. J. Nolan, A. Noutsos, K. J. Orford, J. L. Osborne, M. Ouchrif, M. Panter, G. Pelletier, S. Pita, G. Pühlhofer, M. Punch, B. C. Raubenheimer, M. Raue, J. Raux, S. M. Rayner, A. Reimer, O. Reimer, J. Ripken, L. Rob, L. Rolland, G. Rowell, V. Sahakian, L. Saugé, S. Schlenker, R. Schlickeiser, C. Schuster, U. Schwanke, M. Siewert, H. Sol, D. Spangler, R. Steenkamp, C. Stegmann, J.-P. Tavernet, R. Terrier, C. G. Théoret, M. Tluczykont, G. Vasileiadis, C. Venter, P. Vincent, H. J. Völk, and S. J. Wagner. Discovery of Very High Energy Gamma Rays Associated with an X-ray Binary. *Science*, 309:746–749, July 2005. doi: 10.1126/science.1113764.

M. Alpaslan. A quick guide to FXCOR. *ArXiv e-prints*, December 2009.

A. Ardeberg. *Some properties of the Nordic Optical Telescope*. 1989.

M. Asplund, N. Grevesse, A. J. Sauval, and P. Scott. The Chemical Composition of the Sun. *ARA&A*, 47:481–522, September 2009. doi: 10.1146/annurev.astro.46.060407.145222.

W. Baade and F. Zwicky. Cosmic Rays from Super-novae. *Proceedings of the National Academy of Science*, 20:259–263, May 1934. doi: 10.1073/pnas.20.5.259.

A. Bamba and K. Koyama. AX J1841.0-0535.8. *IAU Circ.*, 7324:4, December 1999.

A. Bamba, J. Yokogawa, M. Ueno, K. Koyama, and S. Yamauchi. Discovery of a Transient X-Ray Pulsar, AX J1841.0-0536, in the Scutum Arm Region with ASCA. *PASJ*, 53:1179–1183, December 2001. doi: 10.1093/pasj/53.6.1179.

R. M. Barnsley, R. J. Smith, and I. A. Steele. A fully automated data reduction pipeline for the FRODOSpec integral field spectrograph. *Astronomische Nachrichten*, 333:101–117, February 2012. doi: 10.1002/asna.201111634.

J. Barnstedt, R. Staubert, A. Santangelo, C. Ferrigno, D. Horns, D. Klochkov, P. Kretschmar, I. Kreykenbohm, A. Segreto, and J. Wilms. INTEGRAL observations of the variability of OAO 1657-415. *A&A*, 486:293–302, July 2008. doi: 10.1051/0004-6361:20078707.

S. D. Barthelmy, L. M. Barbier, J. R. Cummings, E. E. Fenimore, N. Gehrels, D. Hullinger, H. A. Krimm, C. B. Markwardt, D. M. Palmer, A. Parsons, G. Sato, M. Suzuki, T. Takahashi, M. Tashiro, and J. Tueller. The Burst Alert Telescope (BAT) on the SWIFT Midex Mission. *Space Sci. Rev.*, 120:143–164, October 2005. doi: 10.1007/s11214-005-5096-3.

O. Barziv, L. Kaper, M. H. Van Kerkwijk, J. H. Telting, and J. Van Paradijs. The mass of the neutron star in Vela X-1. *A&A*, 377:925–944, October 2001. doi: 10.1051/0004-6361:20011122.

T. W. Baumgarte, S. L. Shapiro, and M. Shibata. On the Maximum Mass of Differentially Rotating Neutron Stars. *ApJL*, 528:L29–L32, January 2000. doi: 10.1086/312425.

L. Binnendijk. *Properties of double stars; a survey of parallaxes and orbits.* 1960.

A. Blaauw. On the origin of the O- and B-type stars with high velocities (the "run-away" stars), and some related problems. *Bulletin of the Astronomical Institutes of the Netherlands*, 15:265, May 1961.

P. Blay, I. Negueruela, and V. Reglero. Supergiant Fast X-ray Transients: an INTEGRAL view . *MmSAI*, 83:251, 2012.

A. Bodaghee, J. A. Tomsick, J. Rodriguez, and J. B. James. Clustering between High-mass X-Ray Binaries and OB Associations in the Milky Way. *ApJ*, 744: 108, January 2012. doi: 10.1088/0004-637X/744/2/108.

E. Bozzo, M. Falanga, and L. Stella. Are There Magnetars in High-Mass X-Ray Binaries? The Case of Supergiant Fast X-Ray Transients. *ApJ*, 683: 1031–1044, August 2008. doi: 10.1086/589990.

J. Brand and L. Blitz. The Velocity Field of the Outer Galaxy. *A&A*, 275:67, August 1993.

I. Brott, S. E. de Mink, M. Cantiello, N. Langer, A. de Koter, C. J. Evans, I. Hunter, C. Trundle, and J. S. Vink. Rotating massive main-sequence stars. I. Grids of evolutionary models and isochrones. *A&A*, 530:A115, June 2011. doi: 10.1051/0004-6361/201016113.

Ş. Şahiner, S. Ç. Inam, and A. Baykal. A comprehensive study of RXTE and INTEGRAL observations of the X-ray pulsar 4U 1907+09. *MNRAS*, 421: 2079–2087, April 2012. doi: 10.1111/j.1365-2966.2012.20455.x.

S. Campana, L. Stella, G. L. Israel, A. Moretti, A. N. Parmar, and M. Orlandini. The Quiescent X-Ray Emission of Three Transient X-Ray Pulsars. *ApJ*, 580: 389–393, November 2002. doi: 10.1086/343074.

N. Castro, M. A. Urbaneja, A. Herrero, M. Garcia, S. Simón-Díaz, F. Bresolin, G. Pietrzyński, R.-P. Kudritzki, and W. Gieren. The ARAUCARIA project: Grid-based quantitative spectroscopic study of massive blue stars in NGC 55. *A&A*, 542:A79, June 2012. doi: 10.1051/0004-6361/201118253.

S. Chandrasekhar. The Maximum Mass of Ideal White Dwarfs. *ApJ*, 74:81, July 1931. doi: 10.1086/143324.

S. Chaty. Optical/infrared observations unveiling the formation, nature and evolution of High-Mass X-ray Binaries. *Advances in Space Research*, 52:2132–2142, December 2013. doi: 10.1016/j.asr.2013.09.010.

D. J. Clark, A. B. Hill, A. J. Bird, V. A. McBride, S. Scaringi, and A. J. Dean. Discovery of the orbital period in the supergiant fast X-ray transient IGR J17544-2619. *MNRAS*, 399:L113–L117, October 2009. doi: 10.1111/j.1745-3933.2009.00737.x.

D. J. Clark, V. Sguera, A. J. Bird, V. A. McBride, A. B. Hill, S. Scaringi, S. Drave, A. Bazzano, and A. J. Dean. The orbital period in the supergiant fast X-ray transient IGR J16465-4507. *MNRAS*, 406:L75–L79, July 2010. doi: 10.1111/j.1745-3933.2010.00885.x.

J. S. Clark, S. P. Goodwin, P. A. Crowther, L. Kaper, M. Fairbairn, N. Langer, and C. Brocksopp. Physical parameters of the high-mass X-ray binary <ASTROBJ>4U1700-37</ASTROBJ>. *A&A*, 392:909–920, September 2002. doi: 10.1051/0004-6361:20021184.

J. S. Clark, A. E. Tarasov, and E. A. Panko. Long term disc variability in the Be star <ASTROBJ>o Andromedae</ASTROBJ>. *A&A*, 403:239–246, May 2003. doi: 10.1051/0004-6361:20030248.

J. S. Clark, F. Najarro, I. Negueruela, B. W. Ritchie, M. A. Urbaneja, and I. D. Howarth. On the nature of the galactic early-B hypergiants. *A&A*, 541:A145, May 2012. doi: 10.1051/0004-6361/201117472.

M. J. Coe, J. Fabregat, I. Negueruela, P. Roche, and I. A. Steele. Discovery of the optical counterpart to the ASCA transient AX 1845.0-0433. *MNRAS*, 281:333–338, July 1996.

A. Coleiro and S. Chaty. Distribution of High-mass X-Ray Binaries in the Milky Way. *ApJ*, 764:185, February 2013. doi: 10.1088/0004-637X/764/2/185.

R. H. D. Corbet. Be/neutron star binaries - A relationship between orbital period and neutron star spin period. *A&A*, 141:91–93, December 1984.

R. H. D. Corbet. The three types of high-mass X-ray pulsator. *MNRAS*, 220: 1047–1056, June 1986.

R. H. D. Corbet and K. Mukai. The Orbit and Position of the X-Ray Pulsar XTE J1855-026: an Eclipsing Supergiant System. *ApJ*, 577:923–928, October 2002. doi: 10.1086/342244.

R. H. D. Corbet, F. E. Marshall, A. G. Peele, and T. Takeshima. RXTE PCA and ASM Observations of the X-ray Pulsar XTE J1855-026 - a Possible New High-Mass Supergiant System. In *American Astronomical Society Meeting Abstracts*, volume 30 of *Bulletin of the American Astronomical Society*, page 1313, December 1998.

R. H. D. Corbet, F. E. Marshall, A. G. Peele, and T. Takeshima. Rossi X-Ray Timing Explorer Observations of the X-Ray Pulsar XTE J1855-026: A Possible New Supergiant System. *ApJ*, 517:956–963, June 1999. doi: 10.1086/307235.

T. J.-L. Courvoisier, R. Walter, V. Beckmann, A. J. Dean, P. Dubath, R. Hudec, P. Kretschmar, S. Mereghetti, T. Montmerle, N. Mowlavi, S. Paltani, A. Preite Martinez, N. Produit, R. Staubert, A. W. Strong, J.-P. Swings, N. J. Westergaard, N. White, C. Winkler, and A. A. Zdziarski. The INTEGRAL Science Data Centre (ISDC). *A&A*, 411:L53–L57, November 2003. doi: 10.1051/0004-6361:20031172.

P. A. Crowther. Physical Properties of Wolf-Rayet Stars. *ARA&A*, 45:177–219, September 2007. doi: 10.1146/annurev.astro.45.051806.110615.

P. A. Crowther, D. J. Lennon, and N. R. Walborn. Physical parameters and wind properties of galactic early B supergiants. *A&A*, 446:279–293, January 2006. doi: 10.1051/0004-6361:20053685.

M. C. Cushing, J. D. Kirkpatrick, C. R. Gelino, R. L. Griffith, M. F. Skrutskie, A. Mainzer, K. A. Marsh, C. A. Beichman, A. J. Burgasser, L. A. Prato, R. A. Simcoe, M. S. Marley, D. Saumon, R. S. Freedman, P. R. Eisenhardt, and E. L. Wright. The Discovery of Y Dwarfs using Data from the Wide-field Infrared Survey Explorer (WISE). *ApJ*, 743:50, December 2011. doi: 10.1088/0004-637X/743/1/50.

R. M. Cutri, M. F. Skrutskie, S. van Dyk, C. A. Beichman, J. M. Carpenter, T. Chester, L. Cambresy, T. Evans, J. Fowler, J. Gizis, E. Howard, J. Huchra, T. Jarrett, E. L. Kopan, J. D. Kirkpatrick, R. M. Light, K. A. Marsh, H. McCallon, S. Schneider, R. Stiening, M. Sykes, M. Weinberg, W. A. Wheaton, S. Wheelock, and N. Zacarias. 2MASS All-Sky Catalog of Point Sources (Cutri+ 2003). *VizieR Online Data Catalog*, 2246:0, March 2003.

M. de Val-Borro, M. Karovska, and D. Sasselov. Numerical Simulations of Wind Accretion in Symbiotic Binaries. *ApJ*, 700:1148–1160, August 2009. doi: 10.1088/0004-637X/700/2/1148.

A. J. Dean, A. Bazzano, A. B. Hill, J. B. Stephen, L. Bassani, E. J. Barlow, A. J. Bird, F. Lebrun, V. Sguera, S. E. Shaw, P. Ubertini, R. Walter, and D. R. Willis. Global characteristics of the first IBIS/ISGRI catalogue sources: unveiling a murky episode of binary star evolution. *A&A*, 443:485–494, November 2005. doi: 10.1051/0004-6361:20053513.

P. R. den Hartog, L. M. Kuiper, R. H. D. Corbet, J. J. M. in't Zand, W. Hermsen, J. Vink, R. Remillard, and M. van der Klis. IGR J00370+6122 - A new high-mass X-ray binary. *The Astronomer's Telegram*, 281:1, May 2004.

P. R. den Hartog, W. Hermsen, L. Kuiper, J. Vink, J. J. M. in't Zand, and W. Collmar. INTEGRAL survey of the Cassiopeia region in hard X rays. *A&A*, 451: 587–602, May 2006. doi: 10.1051/0004-6361:20054711.

V. S. Dhillon, G. J. Privett, and K. P. Duffey. *PERIOD: A Time-Series Analysis Package. User Note 167.6 (User's Manual Starlink)* , December 2001.

V. Doroshenko, A. Santangelo, and V. Suleimanov. Witnessing the magnetospheric boundary at work in Vela X-1. *A&A*, 529:A52, May 2011. doi: 10.1051/0004-6361/201116482.

V. Doroshenko, A. Santangelo, L. Ducci, and D. Klochkov. Supergiant, fast, but not so transient 4U 1907+09. *A&A*, 548:A19, December 2012. doi: 10.1051/0004-6361/201220085.

S. P. Drave, A. J. Bird, L. Sidoli, V. Sguera, V. A. McBride, A. B. Hill, A. Bazzano, and M. E. Goossens. INTEGRAL and XMM-Newton observations of IGR J16418-4532: evidence of accretion regime transitions in a supergiant fast X-ray transient. *MNRAS*, 433:528–542, July 2013. doi: 10.1093/mnras/stt754.

S. P. Drave, A. J. Bird, L. Sidoli, V. Sguera, A. Bazzano, A. B. Hill, and M. E. Goossens. New insights on accretion in supergiant fast X-ray transients from XMM-Newton and INTEGRAL observations of IGR J17544-2619. *MNRAS*, 439:2175–2185, February 2014. doi: 10.1093/mnras/stu110.

L. M. Dray and C. A. Tout. On rejuvenation in massive binary systems. *MNRAS*, 376:61–70, March 2007. doi: 10.1111/j.1365-2966.2007.11431.x.

L. Ducci, L. Sidoli, and A. Paizis. INTEGRAL results on supergiant fast X-ray transients and accretion mechanism interpretation: ionization effect and formation of transient accretion discs. *MNRAS*, 408:1540–1550, November 2010. doi: 10.1111/j.1365-2966.2010.17216.x.

L. Ducci, V. Doroshenko, M. Sasaki, A. Santangelo, P. Esposito, P. Romano, and S. Vercellone. Spectral and temporal properties of the supergiant fast X-ray transient IGR J18483-0311 observed by INTEGRAL. *A&A*, 559:A135, November 2013. doi: 10.1051/0004-6361/201322299.

R. Edgar. A review of Bondi-Hoyle-Lyttleton accretion. *NewAR*, 48:843–859, September 2004. doi: 10.1016/j.newar.2004.06.001.

S. Ekström, C. Georgy, G. Meynet, J. Groh, and A. Granada. Red supergiants and stellar evolution. In P. Kervella, T. Le Bertre, and G. Perrin, editors, *EAS Publications Series*, volume 60 of *EAS Publications Series*, pages 31–41, May 2013. doi: 10.1051/eas/1360003.

M. Fich and L. Blitz. Optical H II regions in the outer galaxy. *ApJ*, 279:125–135, April 1984. doi: 10.1086/161872.

P. Filliatre and S. Chaty. The Optical/Near-Infrared Counterpart of the INTEGRAL Obscured Source IGR J16318-4848: An sgB[e] in a High-Mass X-Ray Binary? *ApJ*, 616:469–484, November 2004. doi: 10.1086/424869.

M. P. Fitzgerald. The Intrinsic Colours of Stars and Two-Colour Reddening Lines. *A&A*, 4:234, February 1970.

B. P. Flannery and E. P. J. van den Heuvel. On the origin of the binary pulsar PSR 1913 + 16. *A&A*, 39:61–67, February 1975.

S. Frandsen and B. Lindberg. FIES: A high resolution FIber fed Echelle Spectrograph for the NOT (poster). In H. Karttunen and V. Piirola, editors, *Astrophysics with the NOT*, page 71, 1999.

J. Frank, A. King, and D. J. Raine. *Accretion Power in Astrophysics: Third Edition*. January 2002.

C. D. Garmany and R. E. Stencel. Galactic OB associations in the northern Milky Way Galaxy. I - Longitudes 55 deg to 150 deg. *A&AS*, 94:211–244, August 1992.

N. Gehrels. The Swift Gamma-Ray Burst Mission. In V. Schoenfelder, G. Lichti, and C. Winkler, editors, *5th INTEGRAL Workshop on the INTEGRAL Universe*, volume 552 of *ESA Special Publication*, page 777, October 2004.

R. Giacconi, H. Gursky, F. R. Paolini, and B. B. Rossi. Evidence for x Rays From Sources Outside the Solar System. *Physical Review Letters*, 9:439–443, December 1962. doi: 10.1103/PhysRevLett.9.439.

M. Gilfanov, H.-J. Grimm, and R. Sunyaev. Statistical properties of the combined emission of a population of discrete sources: astrophysical implications. *MNRAS*, 351:1365–1378, July 2004. doi: 10.1111/j.1365-2966.2004.07874.x.

A. González-Galán, E. Kuulkers, P. Kretschmar, S. Larsson, K. Postnov, A. Kochetkova, and M. H. Finger. Spin period evolution of GX 1+4. *A&A*, 537:A66, January 2012. doi: 10.1051/0004-6361/201117893.

A. González-Galán, I. Negueruela, N. Castro, S. Simón-Díaz, J. Lorenzo, and F. Vilardell. Astrophysical parameters and orbital solution of the peculiar X-ray transient IGR J00370+6122. *ArXiv e-prints*, April 2014.

M. E. Goossens, A. J. Bird, S. P. Drave, A. Bazzano, A. B. Hill, V. A. McBride, V. Sguera, and L. Sidoli. Discovering a 5.72-d period in the supergiant fast X-ray transient AX J1845.0-0433. *MNRAS*, 434:2182–2187, September 2013. doi: 10.1093/mnras/stt1166.

H.-J. Grimm, M. Gilfanov, and R. Sunyaev. X-ray binaries in the Milky Way and other galaxies. *Chinese Journal of Astronomy and Astrophysics Supplement*, 3:257–269, December 2003.

E. D. Grundstrom, J. L. Blair, D. R. Gies, W. Huang, M. V. McSwain, D. Raghavan, R. L. Riddle, J. P. Subasavage, D. W. Wingert, A. M. Levine, and R. A. Remillard. Joint Hα and X-Ray Observations of Massive X-Ray Binaries. I. The B Supergiant System LS I +65 010 = 2S 0114+650. *ApJ*, 656:431–436, February 2007. doi: 10.1086/510508.

J. H. Grunhut, C. T. Bolton, and M. V. McSwain. Orbit and properties of the massive X-ray binary BD +60 73=IGR J00370+6122. *A&A*, 563:A1, March 2014. doi: 10.1051/0004-6361/201322738.

P. Haensel, A. Y. Potekhin, and D. G. Yakovlev, editors. *Neutron Stars 1 : Equation of State and Structure*, volume 326 of *Astrophysics and Space Science Library*, 2007.

J. P. Halpern, E. V. Gotthelf, D. J. Helfand, S. Gezari, and G. A. Wegner. Chandra and Optical Identification of AX J1841.0-0536. *The Astronomer's Telegram*, 289:1, June 2004.

U. Haug. UBV Observations of luminous stars in three Milky Way fields (Cassiopeia, Camelopardalis and Gemini). *A&AS*, 1:35, January 1970.

A. Heger and N. Langer. Presupernova Evolution of Rotating Massive Stars. II. Evolution of the Surface Properties. *ApJ*, 544:1016–1035, December 2000. doi: 10.1086/317239.

A. Herrero. Spectroscopic versus evolutionary masses. *Highlights of Astronomy*, 14:201–201, August 2007. doi: 10.1017/S1743921307010149.

A. Herrero, R. P. Kudritzki, J. M. Vilchez, D. Kunze, K. Butler, and S. Haser. Intrinsic parameters of galactic luminous OB stars. *A&A*, 261:209–234, July 1992.

J. W. T. Hessels, S. M. Ransom, I. H. Stairs, P. C. C. Freire, V. M. Kaspi, and F. Camilo. A Radio Pulsar Spinning at 716 Hz. *Science*, 311:1901–1904, March 2006. doi: 10.1126/science.1123430.

R. W. Hilditch. *An Introduction to Close Binary Stars*. May 2001.

W. A. Hiltner. Photometric, Polarization, and Spectrographic Observations of O and B Stars. *ApJS*, 2:389, October 1956. doi: 10.1086/190029.

W. A. Hiltner. *Astronomical techniques.* 1962.

J. H. Horne and S. L. Baliunas. A prescription for period analysis of unevenly sampled time series. *ApJ*, 302:757–763, March 1986. doi: 10.1086/164037.

R. M. Humphreys. Studies of luminous stars in nearby galaxies. I. Supergiants and O stars in the Milky Way. *ApJS*, 38:309–350, December 1978. doi: 10.1086/190559.

R. M. Humphreys and D. B. McElroy. The initial mass function for massive stars in the Galaxy and the Magellanic Clouds. *ApJ*, 284:565–577, September 1984. doi: 10.1086/162439.

A. F. Illarionov and R. A. Sunyaev. Why the Number of Galactic X-ray Stars Is so Small? *A&A*, 39:185, February 1975.

J. J. M. in 't Zand, A. Baykal, and T. E. Strohmayer. Recent X-Ray Measurements of the Accretion-powered Pulsar 4U 1907+09. *ApJ*, 496:386, March 1998. doi: 10.1086/305362.

J. J. M. in't Zand. Chandra observation of the fast X-ray transient IGR J17544-2619: evidence for a neutron star? *A&A*, 441:L1–L4, October 2005. doi: 10.1051/0004-6361:200500162.

J. J. M. in't Zand, L. Kuiper, P. R. den Hartog, W. Hermsen, and R. H. D. Corbet. A probable accretion-powered X-ray pulsar in IGR J00370+6122. *A&A*, 469: 1063–1068, July 2007. doi: 10.1051/0004-6361:20077189.

C. Jain, B. Paul, and A. Dutta. Discovery of a short orbital period in the Supergiant Fast X-ray Transient IGR J16479-4514. *MNRAS*, 397:L11–L15, July 2009. doi: 10.1111/j.1745-3933.2009.00668.x.

L. Kaper and A. W. Fullerton, editors. *Cyclical variability in stellar winds*, 1998.

L. Kaper, A. van der Meer, and F. Najarro. VLT/UVES spectroscopy of Wray 977, the hypergiant companion to the X-ray pulsar <ASTROBJ>GX301-2</ASTROBJ>. *A&A*, 457:595–610, October 2006. doi: 10.1051/0004-6361:20065393.

H. Karttunen, P. Krüger, H. Oja, M. Poutanen, and K. J. Donner, editors. *Fundamental Astronomy*, 2007.

J. D. Kirkpatrick. New Spectral Types L and T. *ARA&A*, 43:195–245, September 2005. doi: 10.1146/annurev.astro.42.053102.134017.

J. D. Kirkpatrick, I. N. Reid, J. Liebert, R. M. Cutri, B. Nelson, C. A. Beichman, C. C. Dahn, D. G. Monet, J. E. Gizis, and M. F. Skrutskie. Dwarfs Cooler than "M": The Definition of Spectral Type "L" Using Discoveries from the 2 Micron All-Sky Survey (2MASS). *ApJ*, 519:802–833, July 1999. doi: 10.1086/307414.

J. D. Kirkpatrick, C. R. Gelino, M. C. Cushing, G. N. Mace, R. L. Griffith, M. F. Skrutskie, K. A. Marsh, E. L. Wright, P. R. Eisenhardt, I. S. McLean, A. K. Mainzer, A. J. Burgasser, C. G. Tinney, S. Parker, and G. Salter. Further Defining Spectral Type "Y" and Exploring the Low-mass End of the Field Brown Dwarf Mass Function. *ApJ*, 753:156, July 2012. doi: 10.1088/0004-637X/753/2/156.

B. Kiziltan, A. Kottas, M. De Yoreo, and S. E. Thorsett. The Neutron Star Mass Distribution. *ApJ*, 778:66, November 2013. doi: 10.1088/0004-637X/778/1/66.

R. I. Klein and J. I. Castor. H and He II spectra of Of stars. *ApJ*, 220:902–923, March 1978. doi: 10.1086/155980.

K. Koyama, M. Kawada, H. Kunieda, Y. Tawara, and Y. Takeuchi. Is the 5-kpc Galactic arm a colony of X-ray pulsars? *Nature*, 343:148, January 1990. doi: 10.1038/343148a0.

H. A. Krimm, S. D. Barthelmy, W. Baumgartner, J. Cummings, E. Fenimore, N. Gehrels, C. B. Markwardt, D. Palmer, P. Romano, T. Sakamoto, G. Skinner, M. Stamatikos, J. Tueller, and T. Ukwatta. Swift/BAT reports a new outburst from the HMXB XTE J1855-026. *The Astronomer's Telegram*, 3964:1, March 2012.

H. A. Krimm, S. T. Holland, R. H. D. Corbet, A. B. Pearlman, P. Romano, J. A. Kennea, J. S. Bloom, S. D. Barthelmy, W. H. Baumgartner, J. R. Cummings, N. Gehrels, A. Y. Lien, C. B. Markwardt, D. M. Palmer, T. Sakamoto, M. Stamatikos, and T. N. Ukwatta. The Swift/BAT Hard X-ray Transient Monitor. *ArXiv e-prints*, September 2013.

R.-P. Kudritzki and J. Puls. Winds from Hot Stars. *ARA&A*, 38:613–666, 2000. doi: 10.1146/annurev.astro.38.1.613.

R.-P. Kudritzki, M. A. Urbaneja, F. Bresolin, N. Przybilla, W. Gieren, and G. Pietrzyński. Quantitative Spectroscopy of 24 A Supergiants in the Sculptor Galaxy NGC 300: Flux-weighted Gravity-Luminosity Relationship, Metallicity, and Metallicity Gradient. *ApJ*, 681:269–289, July 2008. doi: 10.1086/588647.

V. La Parola, G. Cusumano, P. Romano, A. Segreto, S. Vercellone, and G. Chincarini. Detection of an orbital period in the supergiant high-mass X-ray binary IGR J16465-4507 with Swift-BAT. *MNRAS*, 405:L66–L70, June 2010. doi: 10.1111/j.1745-3933.2010.00860.x.

N. Langer. Presupernova Evolution of Massive Single and Binary Stars. *ARA&A*, 50:107–164, September 2012. doi: 10.1146/annurev-astro-081811-125534.

T. Lanz and I. Hubeny. A Grid of Non-LTE Line-blanketed Model Atmospheres of O-Type Stars. *ApJS*, 146:417–441, June 2003. doi: 10.1086/374373.

T. Lanz and I. Hubeny. A Grid of NLTE Line-blanketed Model Atmospheres of Early B-Type Stars. *ApJS*, 169:83–104, March 2007. doi: 10.1086/511270.

S. Larsson. Parameter estimation in epoch folding analysis. *A&AS*, 117:197–201, May 1996.

J. M. Lattimer. Equation of state constraints from neutron stars. *Ap&SS*, 308:371–379, April 2007. doi: 10.1007/s10509-007-9381-3.

J. M. Lattimer. The Nuclear Equation of State and Neutron Star Masses. *Annual Review of Nuclear and Particle Science*, 62:485–515, November 2012. doi: 10.1146/annurev-nucl-102711-095018.

J. M. Lattimer and M. Prakash. Neutron Star Structure and the Equation of State. *ApJ*, 550:426–442, March 2001. doi: 10.1086/319702.

J. M. Lattimer and M. Prakash. The Physics of Neutron Stars. *Science*, 304: 536–542, April 2004. doi: 10.1126/science.1090720.

R. Lehmann-Filhés. Über die Bestimmung einer Doppelsternbahn aus spectroskopichen Messungen der im Visionsradius liegenden Geschwindigkeitscomponente. *Astronomische Nachrichten*, 136:17, July 1894. doi: 10.1002/asna.18941360202.

C. Leitherer. H-alpha as a tracer of mass loss from OB stars. *ApJ*, 326:356–367, March 1988. doi: 10.1086/166097.

A. M. Levine, H. Bradt, W. Cui, J. G. Jernigan, E. H. Morgan, R. Remillard, R. E. Shirey, and D. A. Smith. First Results from the All-Sky Monitor on the Rossi X-Ray Timing Explorer. *ApJL*, 469:L33, September 1996. doi: 10.1086/310260.

C. C. Lin, C. Yuan, and F. H. Shu. On the Spiral Structure of Disk Galaxies. III. Comparison with Observations. *ApJ*, 155:721, March 1969. doi: 10.1086/149907.

Q. Z. Liu, S. Chaty, and J. Z. Yan. Be/X-ray binaries as the progenitors of the supergiant fast X-ray transients IGR J18483-0311 and IGR J11215-5952. *MNRAS*, 415:3349–3353, August 2011. doi: 10.1111/j.1365-2966.2011.18949.x.

N. R. Lomb. Least-squares frequency analysis of unequally spaced data. *Ap&SS*, 39:447–462, February 1976. doi: 10.1007/BF00648343.

J. Lorenzo, I. Negueruela, N. Castro, A. J. Norton, F. Vilardell, and A. Herrero. Astrophysical parameters of the peculiar X-ray transient IGR J11215-5952. *A&A*, 562:A18, February 2014. doi: 10.1051/0004-6361/201321913.

A. Lutovinov, M. Revnivtsev, M. Gilfanov, P. Shtykovskiy, S. Molkov, and R. Sunyaev. INTEGRAL insight into the inner parts of the Galaxy. High mass X-ray binaries. *A&A*, 444:821–829, December 2005. doi: 10.1051/0004-6361:20042392.

M.-M. Mac Low, D. S. Balsara, J. Kim, and M. A. de Avillez. The Distribution of Pressures in a Supernova-driven Interstellar Medium. I. Magnetized Medium. *ApJ*, 626:864–876, June 2005. doi: 10.1086/430122.

A. Maeder. *Physics, Formation and Evolution of Rotating Stars*. 2009. doi: 10.1007/978-3-540-76949-1.

J. Maíz-Apellániz. CHORIZOS: A χ^2 Code for Parameterized Modeling and Characterization of Photometry and Spectrophotometry. *PASP*, 116:859–875, September 2004. doi: 10.1086/424021.

N. Markova and J. Puls. Bright OB stars in the Galaxy. IV. Stellar and wind parameters of early to late B supergiants. *A&A*, 478:823–842, February 2008. doi: 10.1051/0004-6361:20077919.

N. Markova, J. Puls, S. Scuderi, and H. Markov. Bright OB stars in the Galaxy. II. Wind variability in O supergiants as traced by Hα. *A&A*, 440:1133–1151, September 2005. doi: 10.1051/0004-6361:20041774.

N. Markova, J. Puls, S. Simón-Díaz, A. Herrero, H. Markov, and N. Langer. Spectroscopic and physical parameters of Galactic O-type stars. II. Observational constraints on projected rotational and extra broadening velocities as a function of fundamental parameters and stellar evolution. *A&A*, 562: A37, February 2014. doi: 10.1051/0004-6361/201322661.

F. Martins. UV, optical and near-IR diagnostics of massive stars. *Bulletin de la Societe Royale des Sciences de Liege*, 80:29–41, January 2011.

F. Martins, D. Schaerer, and D. J. Hillier. On the effective temperature scale of O stars. *A&A*, 382:999–1004, February 2002. doi: 10.1051/0004-6361:20011703.

P. Massey. *A User's Guide to CCD Reductions with IRAF*, February 1997.

P. Massey, F. Valdes, and J. Barnes. *A User's Guide to Reducing Slit Spectra with IRAF*, 1992.

M. V. McSwain. *The evolution of massive stars: The Be star and microquasar phenomena*. PhD thesis, Georgia State University, Georgia, USA, 2004.

S. Mereghetti, D. Götz, J. Borkowski, R. Walter, and H. Pedersen. The INTEGRAL Burst Alert System. *A&A*, 411:L291–L297, November 2003. doi: 10.1051/0004-6361:20031289.

S. Mereghetti, A. Paizis, D. Gotz, E. Bozzo, C. Ferrigno, M. Beck, and J. Borkowski. IBAS alert 5992 is not a GRB, but XTE J1855-026. *GRB Coordinates Network*, 10483:1, 2010.

E. J. A. Meurs and E. P. J. van den Heuvel. The number of evolved early-type close binaries in the Galaxy. *A&A*, 226:88–107, December 1989.

G. Meynet, C. Georgy, R. Hirschi, A. Maeder, P. Massey, N. Przybilla, and M.-F. Nieva. Red Supergiants, Luminous Blue Variables and Wolf-Rayet stars: the single massive star perspective. *Bulletin de la Societe Royale des Sciences de Liege*, 80:266–278, January 2011.

A. A. Michelson. The Echelon Spectroscope. *ApJ*, 8:37, June 1898. doi: 10.1086/140491.

I. F. Mirabel and L. F. Rodríguez. Sources of Relativistic Jets in the Galaxy. *ARA&A*, 37:409–443, 1999. doi: 10.1146/annurev.astro.37.1.409.

L. Morales-Rueda, D. Carter, I. A. Steele, P. A. Charles, and S. Worswick. The Liverpool Telescope Spectrograph: FRODOSpec. *Astronomische Nachrichten*, 325:215–215, March 2004. doi: 10.1002/asna.200310228.

T. Morel, S. V. Marchenko, A. K. Pati, K. Kuppuswamy, M. T. Carini, E. Wood, and R. Zimmerman. Large-scale wind structures in OB supergiants: a search for rotationally modulated Hα variability. *MNRAS*, 351:552–568, June 2004. doi: 10.1111/j.1365-2966.2004.07799.x.

W. W. Morgan and P. C. Keenan. Spectral Classification. *A&AA*, 11:29, 1973. doi: 10.1146/annurev.aa.11.090173.000333.

W. W. Morgan, A. D. Code, and A. E. Whitford. Studies in Galactic STRUCTURE.II.LUMINOSITY Classification for 1270 Blue Giant Stars. *ApJS*, 2:41, July 1955. doi: 10.1086/190016.

H. Nagaoka and T. Mishima. A Combination of a Concave Grating with a Lummer-Gehrcke Plate or an Echelon Grating for Examining Fine Structure of Spectral Lines. *ApJ*, 57:92, March 1923. doi: 10.1086/142732.

F. Nagase. Accretion-powered X-ray pulsars. *PASJ*, 41:1–79, 1989.

National Optical Astronomy Observatories. IRAF: Image Reduction and Analysis Facility, November 1999. Astrophysics Source Code Library.

I. Negueruela. On the nature of Be/X-ray binaries. *A&A*, 338:505–510, October 1998.

I. Negueruela. Stellar Wind Accretion in High-Mass X-Ray Binaries. In J. Martí, P. L. Luque-Escamilla, and J. A. Combi, editors, *High Energy Phenomena in Massive Stars*, volume 422 of *Astronomical Society of the Pacific Conference Series*, page 57, May 2010.

I. Negueruela and A. Marco. Stellar tracers of the Cygnus Arm. I. Spectroscopic study of bright photometric candidates. *A&A*, 406:119–130, July 2003. doi: 10.1051/0004-6361:20030605.

I. Negueruela, P. Reig, M. J. Coe, and J. Fabregat. Large-scale perturbations in the circumstellar envelopes of Be/X-ray binaries. *A&A*, 336:251–262, August 1998.

I. Negueruela, A. T. Okazaki, J. Fabregat, M. J. Coe, U. Munari, and T. Tomov. The Be/X-ray transient 4U 0115+63/V635 Cassiopeiae. II. Outburst mechanisms. *A&A*, 369:117–131, April 2001. doi: 10.1051/0004-6361:20010077.

I. Negueruela, D. M. Smith, T. E. Harrison, and J. M. Torrejón. The Optical Counterpart to the Peculiar X-Ray Transient XTE J1739-302. *ApJ*, 638:982–986, February 2006a. doi: 10.1086/498935.

I. Negueruela, D. M. Smith, P. Reig, S. Chaty, and J. M. Torrejón. Supergiant Fast X-ray Transients: A New Class of High Mass X-ray Binaries Unveiled by INTEGRAL. In A. Wilson, editor, *The X-ray Universe 2005*, volume 604 of *ESA Special Publication*, page 165, January 2006b.

I. Negueruela, J. Casares, F. Verrecchia, P. Blay, G. L. Israel, and S. Covino. XTE J1855-026 is a supergiant X-ray binary. *The Astronomer's Telegram*, 1876:1, December 2008a.

I. Negueruela, J. M. Torrejón, and P. Reig. Optical and Infrared characterisation of High Mass X-ray Binaries discovered by INTEGRAL. In *Proceedings of the 7th INTEGRAL Workshop*, 2008b.

I. Negueruela, J. M. Torrejón, P. Reig, M. Ribó, and D. M. Smith. Supergiant Fast X-ray Transients and Other Wind Accretors. In R. M. Bandyopadhyay, S. Wachter, D. Gelino, and C. R. Gelino, editors, *A Population Explosion: The Nature & Evolution of X-ray Binaries in Diverse Environments*, volume 1010 of *American Institute of Physics Conference Series*, pages 252–256, May 2008c. doi: 10.1063/1.2945052.

E. Nespoli, J. Fabregat, and R. E. Mennickent. Unveiling the nature of six HMXBs through IR spectroscopy. *A&A*, 486:911–917, August 2008. doi: 10.1051/0004-6361:200809645.

Q. Nguyen Luong, F. Motte, F. Schuller, N. Schneider, S. Bontemps, P. Schilke, K. M. Menten, F. Heitsch, F. Wyrowski, P. Carlhoff, L. Bronfman, and T. Henning. W43: the closest molecular complex of the Galactic bar? *A&A*, 529: A41, May 2011. doi: 10.1051/0004-6361/201016271.

M.-F. Nieva and N. Przybilla. Present-day cosmic abundances. A comprehensive study of nearby early B-type stars and implications for stellar and Galactic evolution and interstellar dust models. *A&A*, 539:A143, March 2012. doi: 10.1051/0004-6361/201118158.

P. North and J.-P. Zahn. Circularization in B-type eclipsing binariesin the Magellanic Clouds. *A&A*, 405:677–684, July 2003. doi: 10.1051/0004-6361: 20030571.

A. Nota and H. Lamers, editors. *Luminous Blue Variables: Massive Stars in Transition*, volume 120 of *Astronomical Society of the Pacific Conference Series*, 1997.

A. T. Okazaki. Long-term V/R variations of Be stars due to global one-armed oscillations of equatorial disks. *PASJ*, 43:75–94, February 1991.

A. T. Okazaki. Emission-Line Profiles from Be-Star Envelopes with m=1 Perturbation Patterns. *PASJ*, 48:305–315, April 1996. doi: 10.1093/pasj/48.2.305.

A. T. Okazaki and I. Negueruela. A natural explanation for periodic X-ray outbursts in Be/X-ray binaries. *A&A*, 377:161–174, October 2001. doi: 10.1051/0004-6361:20011083.

J. R. Oppenheimer and G. M. Volkoff. On Massive Neutron Cores. *Physical Review*, 55:374–381, February 1939. doi: 10.1103/PhysRev.55.374.

L. M. Oskinova, A. Feldmeier, and P. Kretschmar. Clumped stellar winds in supergiant high-mass X-ray binaries: X-ray variability and photoionization. *MNRAS*, 421:2820–2831, April 2012. doi: 10.1111/j.1365-2966.2012.20507.x.

D. A. Ostlie and B. W. Carroll. *An Introduction to Modern Stellar Astrophysics*. 1996.

B. Paczyński. Evolution of Close Binaries. V. The Evolution of Massive Binaries and the Formation of the Wolf-Rayet Stars. *Acta Astronomica*, 17:355, 1967.

Š. Parimucha and P. Škoda. Comparison of Selected Methods for Radial Velocity Measurements. In W. I. Hartkopf, P. Harmanec, and E. F. Guinan, editors, *IAU Symposium*, volume 240 of *IAU Symposium*, pages 486–489, August 2007. doi: 10.1017/S1743921307006412.

J. Petrovic, N. Langer, and K. A. van der Hucht. Constraining the mass transfer in massive binaries through progenitor evolution models of Wolf-Rayet+O binaries. *A&A*, 435:1013–1030, June 2005. doi: 10.1051/0004-6361:20042368.

E. Pfahl, S. Rappaport, P. Podsiadlowski, and H. Spruit. A New Class of High-Mass X-Ray Binaries: Implications for Core Collapse and Neutron Star Recoil. *ApJ*, 574:364–376, July 2002. doi: 10.1086/340794.

P. Podsiadlowski. The Structure and Evolution of Thorne-Zytkow Objects. In J. van Paradijs, E. P. J. van den Heuvel, and E. Kuulkers, editors, *Compact Stars in Binaries*, volume 165 of *IAU Symposium*, page 29, 1996.

P. Podsiadlowski, P. C. Joss, and J. J. L. Hsu. Presupernova evolution in massive interacting binaries. *ApJ*, 391:246–264, May 1992. doi: 10.1086/171341.

O. R. Pols. Case A evolution of massive close binaries: formation of contact systems and possible reversal of the supernova order. *A&A*, 290:119–128, October 1994.

J. M. Porter and T. Rivinius. Classical Be Stars. *PASP*, 115:1153–1170, October 2003. doi: 10.1086/378307.

A. Y. Potekhin. The physics of neutron stars. *Physics Uspekhi*, 53:1235–1256, December 2010. doi: 10.3367/UFNe.0180.201012c.1279.

W. H. Press and G. B. Rybicki. Fast algorithm for spectral analysis of unevenly sampled data. *ApJ*, 338:277–280, March 1989. doi: 10.1086/167197.

J. Puls, R.-P. Kudritzki, A. Herrero, A. W. A. Pauldrach, S. M. Haser, D. J. Lennon, R. Gabler, S. A. Voels, J. M. Vilchez, S. Wachter, and A. Feldmeier. O-star mass-loss and wind momentum rates in the Galaxy and the Magellanic Clouds Observations and theoretical predictions. *A&A*, 305:171, January 1996.

J. Puls, M. A. Urbaneja, R. Venero, T. Repolust, U. Springmann, A. Jokuthy, and M. R. Mokiem. Atmospheric NLTE-models for the spectroscopic analysis of blue stars with winds. II. Line-blanketed models. *A&A*, 435:669–698, May 2005. doi: 10.1051/0004-6361:20042365.

J. Puls, N. Markova, and S. Scuderi. Stellar winds from massive stars - What are the REAL mass-loss rates? *ArXiv Astrophysics e-prints*, July 2006.

J. Puls, J. S. Vink, and F. Najarro. Mass loss from hot massive stars. *A&ARv*, 16:209–325, December 2008. doi: 10.1007/s00159-008-0015-8.

H. Quaintrell, A. J. Norton, T. D. C. Ash, P. Roche, B. Willems, T. R. Bedding, I. K. Baldry, and R. P. Fender. The mass of the neutron star in Vela X-1 and tidally induced non-radial oscillations in GP Vel. *A&A*, 401:313–323, April 2003. doi: 10.1051/0004-6361:20030120.

F. Rahoui and S. Chaty. IGR J18483-0311: a new intermediate supergiant fast X-ray transient. *A&A*, 492:163–166, December 2008. doi: 10.1051/0004-6361:200810695.

R. A. Rampy, D. M. Smith, and I. Negueruela. IGR J17544-2619 in Depth With Suzaku: Direct Evidence for Clumpy Winds in a Supergiant Fast X-ray Transient. *ApJ*, 707:243–249, December 2009. doi: 10.1088/0004-637X/707/1/243.

G. Raskin, H. van Winckel, H. Hensberge, A. Jorissen, H. Lehmann, C. Waelkens, G. Avila, J.-P. de Cuyper, P. Degroote, R. Dubosson, L. Dumortier, Y. Frémat, U. Laux, B. Michaud, J. Morren, J. Perez Padilla, W. Pessemier, S. Prins, K. Smolders, S. van Eck, and J. Winkler. HERMES: a high-resolution fibre-fed spectrograph for the Mercator telescope. *A&A*, 526: A69, February 2011. doi: 10.1051/0004-6361/201015435.

M. L. Rawls, J. A. Orosz, J. E. McClintock, M. A. P. Torres, C. D. Bailyn, and M. M. Buxton. Refined Neutron Star Mass Determinations for Six Eclipsing X-Ray Pulsar Binaries. *ApJ*, 730:25, March 2011. doi: 10.1088/0004-637X/730/1/25.

P. S. Ray and D. Chakrabarty. The Orbit of the High-Mass X-Ray Binary Pulsar 1E 1145.1-6141. *ApJ*, 581:1293–1296, December 2002. doi: 10.1086/344300.

M. J. Reid, K. M. Menten, X. W. Zheng, A. Brunthaler, L. Moscadelli, Y. Xu, B. Zhang, M. Sato, M. Honma, T. Hirota, K. Hachisuka, Y. K. Choi, G. A. Moellenbrock, and A. Bartkiewicz. Trigonometric Parallaxes of Massive Star-Forming Regions. VI. Galactic Structure, Fundamental Parameters, and Non-circular Motions. *ApJ*, 700:137–148, July 2009. doi: 10.1088/0004-637X/700/1/137.

P. Reig. Be/X-ray binaries. *Ap&SS*, 332:1–29, March 2011. doi: 10.1007/s10509-010-0575-8.

P. Reig and P. Roche. Discovery of two new persistent Be/X-ray pulsar systems. *MNRAS*, 306:100–106, June 1999. doi: 10.1046/j.1365-8711.1999.02473.x.

P. Reig, I. Negueruela, G. Papamastorakis, A. Manousakis, and T. Kougentakis. Identification of the optical counterparts of high-mass X-ray binaries through optical photometry and spectroscopy. *A&A*, 440:637–646, September 2005. doi: 10.1051/0004-6361:20052684.

R. A. Remillard and A. M. Levine. The RXTE All Sky Monitor: First Year of Performance. In M. Matsuoka and N. Kawai, editors, *All-Sky X-Ray Observations in the Next Decade*, page 29, 1997.

T. Repolust, J. Puls, and A. Herrero. Stellar and wind parameters of Galactic O-stars. The influence of line-blocking/blanketing. *A&A*, 415:349–376, February 2004. doi: 10.1051/0004-6361:20034594.

A. P. Reynolds, R. W. Hilditch, S. A. Bell, and G. Hill. Optical spectroscopy of the massive X-ray binary SMC X-1/Sk 160. *MNRAS*, 261:337–345, March 1993.

G. H. Rieke and M. J. Lebofsky. The interstellar extinction law from 1 to 13 microns. *ApJ*, 288:618–621, January 1985. doi: 10.1086/162827.

M. S. Riquelme, J. M. Torrejón, and I. Negueruela. Circumstellar emission in Be/X-ray binaries of the Magellanic Clouds and the Milky Way. *A&A*, 539: A114, March 2012. doi: 10.1051/0004-6361/201117738.

D. H. Roberts, J. Lehar, and J. W. Dreher. Time Series Analysis with Clean - Part One - Derivation of a Spectrum. *AJ*, 93:968, April 1987. doi: 10.1086/114383.

Keith Robinson. The p cygni profile and friends. In *Spectroscopy: The Key to the Stars*, Patrick Moore's Practical Astronomy Series, pages 119–125. Springer New York, 2007. ISBN 978-0-387-36786-6. doi: 10.1007/978-0-387-68288-4_10. URL http://dx.doi.org/10.1007/978-0-387-68288-4_10.

P. Romano, L. Sidoli, V. Mangano, S. Mereghetti, and G. Cusumano. Swift/XRT observes the fifth outburst of the periodic supergiant fast X-ray transient IGR J11215-5952. *A&A*, 469:L5–L8, July 2007. doi: 10.1051/0004-6361:20077383.

P. Romano, S. Mereghetti, L. Sidoli, and P. A. Evans. Swift/XRT localisation of XTE J1855-026. *The Astronomer's Telegram*, 1875:1, December 2008.

P. Romano, L. Sidoli, L. Ducci, G. Cusumano, V. La Parola, C. Pagani, K. L. Page, J. A. Kennea, D. N. Burrows, N. Gehrels, V. Sguera, and A. Bazzano. Swift/XRT monitoring of the supergiant fast X-ray transient IGR J18483-0311 for an entire orbital period. *MNRAS*, 401:1564–1569, January 2010. doi: 10.1111/j.1365-2966.2009.15789.x.

M. C. Runacres and S. P. Owocki. The outer evolution of instability-generated structure in radiatively driven stellar winds. *A&A*, 381:1015–1025, January 2002. doi: 10.1051/0004-6361:20011526.

D. Russeil. Star-forming complexes and the spiral structure of our Galaxy. *A&A*, 397:133–146, January 2003. doi: 10.1051/0004-6361:20021504.

D. Russeil, C. Adami, and Y. M. Georgelin. Revised distances of Northern HII regions. *A&A*, 470:161–171, July 2007. doi: 10.1051/0004-6361:20066051.

H. N. Russell. An Improved Method of Calculating the Orbit of a Spectroscopic Binary. *ApJ*, 15:252, May 1902. doi: 10.1086/140914.

R. E. Rutledge. Optical Identification of 1RXS J003709.6+612131 with BD+60 73. *The Astronomer's Telegram*, 282:1, May 2004.

R. E. Rutledge, R. J. Brunner, T. A. Prince, and C. Lonsdale. XID: Cross-Association of ROSAT/Bright Source Catalog X-Ray Sources with USNO A-2 Optical Point Sources. *ApJS*, 131:335–353, November 2000. doi: 10.1086/317363.

A. E. Santolaya-Rey, J. Puls, and A. Herrero. Atmospheric NLTE-models for the spectroscopic analysis of luminous blue stars with winds. *A&A*, 323:488–512, July 1997.

J. D. Scargle. Studies in astronomical time series analysis. II - Statistical aspects of spectral analysis of unevenly spaced data. *ApJ*, 263:835–853, December 1982. doi: 10.1086/160554.

J. Schwab, P. Podsiadlowski, and S. Rappaport. Further Evidence for the Bimodal Distribution of Neutron-star Masses. *ApJ*, 719:722–727, August 2010. doi: 10.1088/0004-637X/719/1/722.

V. Sguera, A. Bazzano, A. J. Bird, A. J. Dean, P. Ubertini, E. J. Barlow, L. Bassani, D. J. Clark, A. B. Hill, A. Malizia, M. Molina, and J. B. Stephen. Unveiling Supergiant Fast X-Ray Transient Sources with INTEGRAL. *ApJ*, 646: 452–463, July 2006. doi: 10.1086/504827.

V. Sguera, A. J. Bird, A. J. Dean, A. Bazzano, P. Ubertini, R. Landi, A. Malizia, E. J. Barlow, D. J. Clark, A. B. Hill, and M. Molina. INTEGRAL and Swift observations of the supergiant fast X-ray transient AX J1845.0-0433 = IGR J18450-0435. *A&A*, 462:695–698, February 2007a. doi: 10.1051/0004-6361:20066210.

V. Sguera, A. B. Hill, A. J. Bird, A. J. Dean, A. Bazzano, P. Ubertini, N. Masetti, R. Landi, A. Malizia, D. J. Clark, and M. Molina. IGR J18483-0311: an accreting X-ray pulsar observed by INTEGRAL. *A&A*, 467:249–257, May 2007b. doi: 10.1051/0004-6361:20066762.

N. Shakura, K. Postnov, A. Kochetkova, and L. Hjalmarsdotter. Theory of quasi-spherical accretion in X-ray pulsars. *MNRAS*, 420:216–236, February 2012. doi: 10.1111/j.1365-2966.2011.20026.x.

N. Shakura, K. Postnov, and L. Hjalmarsdotter. On the nature of 'off' states in slowly rotating low-luminosity X-ray pulsars. *MNRAS*, 428:670–677, January 2013. doi: 10.1093/mnras/sts062.

N. I. Shakura, K. A. Postnov, A. Y. Kochetkova, and L. Hjalmarsdotter. Theory of wind accretion. In *European Physical Journal Web of Conferences*, volume 64 of *European Physical Journal Web of Conferences*, page 2001, January 2014. doi: 10.1051/epjconf/20136402001.

I. S. Shklovskii. The Nature of the X-Ray Source Sco X-1. *Astron. Zhur.*, 44: 930, 1967.

L. Sidoli. Supergiant Fast X-ray Transients: a review. In *Proceedings of "An INTEGRAL view of the high-energy sky (the first 10 years)" - 9th INTEGRAL Workshop and celebration of the 10th anniversary of the launch (INTEGRAL 2012). 15-19 October 2012. Bibliotheque Nationale de France, Paris, France. Published online at* http://pos.sissa.it/cgi-bin/reader/conf.cgi?confid=176*, id.11*, 2012.

L. Sidoli, P. Romano, S. Mereghetti, A. Paizis, S. Vercellone, V. Mangano, and D. Götz. An alternative hypothesis for the outburst mechanism in supergiant fast X-ray transients: the case of IGR J11215-5952. *A&A*, 476:1307–1315, December 2007. doi: 10.1051/0004-6361:20078137.

L. Sidoli, P. Romano, L. Ducci, A. Paizis, G. Cusumano, V. Mangano, H. A. Krimm, S. Vercellone, D. N. Burrows, J. A. Kennea, and N. Gehrels. Supergiant Fast X-ray Transients in outburst: new Swift observations of XTE J1739-302, IGR J17544-2619 and IGR J08408-4503. *MNRAS*, 397:1528–1538, August 2009. doi: 10.1111/j.1365-2966.2009.15049.x.

L. Sidoli, P. Esposito, V. Sguera, A. Bodaghee, J. A. Tomsick, K. Pottschmidt, J. Rodriguez, P. Romano, and J. Wilms. A Suzaku X-ray observation of one orbit of the supergiant fast X-ray transient IGR J16479-4514. *MNRAS*, 429: 2763–2771, March 2013. doi: 10.1093/mnras/sts559.

S. Simón-Díaz and A. Herrero. Fourier method of determining the rotational velocities in OB stars. *A&A*, 468:1063–1073, June 2007. doi: 10.1051/0004-6361:20066060.

S. Simón-Díaz and A. Herrero. The IACOB project. I. Rotational velocities in northern Galactic O- and early B-type stars revisited. The impact of other sources of line-broadening. *A&A*, 562:A135, February 2014. doi: 10.1051/0004-6361/201322758.

S. Simón-Díaz, A. Herrero, K. Uytterhoeven, N. Castro, C. Aerts, and J. Puls. Observational Evidence for a Correlation Between Macroturbulent Broadening and Line-profile Variations in OB Supergiants. *ApJ*, 720:L174–L178, September 2010. doi: 10.1088/2041-8205/720/2/L174.

M. F. Skrutskie, R. M. Cutri, R. Stiening, M. D. Weinberg, S. Schneider, J. M. Carpenter, C. Beichman, R. Capps, T. Chester, J. Elias, J. Huchra, J. Liebert, C. Lonsdale, D. G. Monet, S. Price, P. Seitzer, T. Jarrett, J. D. Kirkpatrick, J. E. Gizis, E. Howard, T. Evans, J. Fowler, L. Fullmer, R. Hurt, R. Light, E. L. Kopan, K. A. Marsh, H. L. McCallon, R. Tam, S. Van Dyk, and S. Wheelock. The Two Micron All Sky Survey (2MASS). *AJ*, 131:1163–1183, February 2006. doi: 10.1086/498708.

S. J. Smartt. Progenitors of Core-Collapse Supernovae. *ARA&A*, 47:63–106, September 2009. doi: 10.1146/annurev-astro-082708-101737.

D. M. Smith, D. Main, F. Marshall, J. Swank, W. A. Heindl, M. Leventhal, J. J. M. i. Zand, and J. Heise. XTE J1739-302: an Unusual New X-Ray Transient. *ApJL*, 501:L181–L184, July 1998. doi: 10.1086/311472.

D. M. Smith, C. B. Markwardt, J. H. Swank, and I. Negueruela. Fast X-ray transients towards the Galactic bulge with the Rossi X-ray Timing Explorer. *MNRAS*, 422:2661–2674, May 2012. doi: 10.1111/j.1365-2966.2012.20836.x.

I. A. Steele. The Liverpool telescope. *Astronomische Nachrichten*, 325:519–521, October 2004. doi: 10.1002/asna.200410271.

L. Stella, N. E. White, and R. Rosner. Intermittent stellar wind accretion and the long-term activity of Population I binary systems containing an X-ray pulsar. *ApJ*, 308:669–679, September 1986. doi: 10.1086/164538.

T. E. Sterne. Notes on Binary Stars. V. The Determination by Least-Squares of the Elements of Spectroscopic Binaries. *Proceedings of the National Academy of Science*, 27:175–181, March 1941. doi: 10.1073/pnas.27.3.175.

T. M. Tauris and E. P. J. van den Heuvel. *Formation and evolution of compact stellar X-ray sources*, pages 623–665. April 2006.

J. H. Telting, G. Avila, L. Buchhave, S. Frandsen, D. Gandolfi, B. Lindberg, H. C. Stempels, S. Prins, and NOT staff. FIES: The high-resolution Fiber-fed Echelle Spectrograph at the Nordic Optical Telescope. *Astronomische Nachrichten*, 335:41, January 2014. doi: 10.1002/asna.201312007.

T. W. J. Thompson, J. A. Tomsick, J. J. M. in 't Zand, R. E. Rothschild, and R. Walter. The Orbit of the Eclipsing X-Ray Pulsar EXO 1722-363. *ApJ*, 661: 447–457, May 2007. doi: 10.1086/513458.

K. S. Thorne and A. N. Zytkow. Red giants and supergiants with degenerate neutron cores. *ApJ*, 199:L19–L24, July 1975. doi: 10.1086/181839.

K. S. Thorne and A. N. Zytkow. Stars with degenerate neutron cores. I - Structure of equilibrium models. *ApJ*, 212:832–858, March 1977. doi: 10.1086/155109.

S. E. Thorsett and D. Chakrabarty. Neutron Star Mass Measurements. I. Radio Pulsars. *ApJ*, 512:288–299, February 1999. doi: 10.1086/306742.

F. X. Timmes, S. E. Woosley, and T. A. Weaver. The Neutron Star and Black Hole Initial Mass Function. *ApJ*, 457:834, February 1996. doi: 10.1086/176778.

R. C. Tolman. Static Solutions of Einstein's Field Equations for Spheres of Fluid. *Physical Review*, 55:364–373, February 1939. doi: 10.1103/PhysRev.55.364.

J. Tonry and M. Davis. A survey of galaxy redshifts. I - Data reduction techniques. *AJ*, 84:1511–1525, October 1979. doi: 10.1086/112569.

D. G. Turner. Association membership for the 20 day Cepheid RU Scuti. *ApJ*, 240:137–144, August 1980. doi: 10.1086/158216.

A. Tutukov and L. Yungelson. Evolution of close binaries and wolf-rayet stars. *Nauchnye Informatsii*, 27:58, 1973.

A. B. Underhill, editor. *The early type stars*, volume 6 of *Astrophysics and Space Science Library*, 1966.

M. A. Urbaneja. *B SUPERGIANTS IN THE MILKY WAY AND NEARBY GALAXIES : MODELS AND QUANTITATIVE SPECTROSCOPY*. PhD thesis, "Universidad de la Laguna", 2004.

E. van den Heuvel. INTEGRAL's contributions to the understandidng of the evolution of X-ray Binaries. In *Proceedings of "An INTEGRAL view of the high-energy sky (the first 10 years)" - 9th INTEGRAL Workshop and celebration of the 10th anniversary of the launch (INTEGRAL 2012). 15-19 October 2012. Bibliotheque Nationale de France, Paris, France. Published online at <A href="http://pos.sissa.it/cgi-bin/reader/conf.cgi?confid=176">http://pos.sissa.it/cgi-bin/reader/conf.cgi?confid=176</A>, id.9*, 2012.

E. P. J. van den Heuvel. Wolf-Rayet Systems and the Origin of Massive X-ray Binaries. *Nature Physical Science*, 242:71–72, April 1973. doi: 10.1038/physci242071a0.

E. P. J. van den Heuvel. Late Stages of Close Binary Systems. In P. Eggleton, S. Mitton, and J. Whelan, editors, *Structure and Evolution of Close Binary Systems*, volume 73 of *IAU Symposium*, page 35, 1976.

E. P. J. van den Heuvel. Double Neutron Stars: Evidence For Two Different Neutron-Star Formation Mechanisms. In T. di Salvo, G. L. Israel, L. Piersant, L. Burderi, G. Matt, A. Tornambe, and M. T. Menna, editors, *The Multicolored Landscape of Compact Objects and Their Explosive Origins*, volume 924 of *American Institute of Physics Conference Series*, pages 598–606, August 2007. doi: 10.1063/1.2774916.

E. P. J. van den Heuvel. The Formation and Evolution of Relativistic Binaries. In M. Colpi, P. Casella, V. Gorini, U. Moschella, and A. Possenti, editors, *Astrophysics and Space Science Library*, volume 359 of *Astrophysics and Space Science Library*, page 125, 2009. doi: 10.1007/978-1-4020-9264-0_4.

E. P. J. van den Heuvel and J. Heise. Centaurus X-3, Possible Reactivation of an Old Neutron Star by Mass Exchange in a Close Binary. *Nature Physical Science*, 239:67–69, October 1972. doi: 10.1038/physci239067a0.

E. P. J. van den Heuvel and S. Rappaport. X-ray observations of B-emission stars. In A. Slettebak and T. P. Snow, editors, *IAU Colloq. 92: Physics of Be Stars*, pages 291–307, 1987.

A. van der Meer, L. Kaper, M. H. van Kerkwijk, M. H. M. Heemskerk, and E. P. J. van den Heuvel. Determination of the mass of the neutron star in <ASTROBJ>SMC X-1</ASTROBJ>, <ASTROBJ>LMC X-4</ASTROBJ>, and <ASTROBJ>Cen X-3</ASTROBJ> with VLT/UVES. *A&A*, 473:523–538, October 2007. doi: 10.1051/0004-6361:20066025.

M. H. van Kerkwijk, P. A. Charles, T. R. Geballe, D. L. King, G. K. Miley, L. A. Molnar, E. P. J. van den Heuvel, M. van der Klis, and J. van Paradijs. Infrared helium emission lines from Cygnus X-3 suggesting a Wolf-Rayet star companion. *Nature*, 355:703–705, February 1992. doi: 10.1038/355703a0.

M. H. van Kerkwijk, R. P. Breton, and S. R. Kulkarni. Evidence for a Massive Neutron Star from a Radial-velocity Study of the Companion to the Black-widow Pulsar PSR B1957+20. *ApJ*, 728:95, February 2011. doi: 10.1088/0004-637X/728/2/95.

F. van Leeuwen. Validation of the new Hipparcos reduction. *A&A*, 474:653–664, November 2007. doi: 10.1051/0004-6361:20078357.

F. Verrecchia, I. Negueruela, S. Covino, and G. Israel. The optical counterpart to XTE J1855-026. *The Astronomer's Telegram*, 102:1, July 2002.

N. R. Walborn. Some Spectroscopic Characteristics of the OB Stars: an Investigation of the Space Distribution of Certain OB Stars and the Reference Frame of the Classification. *ApJS*, 23:257, August 1971. doi: 10.1086/190239.

R. Walter and J. Zurita Heras. Probing clumpy stellar winds with a neutron star. *A&A*, 476:335–340, December 2007. doi: 10.1051/0004-6361:20078353.

K. Watanabe, E. Bozzo, S. Mereghetti, and C. B. D. Gotz. INTEGRAL catches an exceptional bright outburst from the HMXB XTE J1855-026. *The Astronomer's Telegram*, 2482:1, March 2010.

L. B. F. M. Waters and M. H. van Kerkwijk. The relation between orbital and spin periods in massive X-ray binaries. *A&A*, 223:196–206, October 1989.

S. Wellstein and N. Langer. Implications of massive close binaries for black hole formation and supernovae. *A&A*, 350:148–162, October 1999.

S. Wellstein, N. Langer, and H. Braun. Formation of contact in massive close binaries. *A&A*, 369:939–959, April 2001. doi: 10.1051/0004-6361:20010151.

N. E. White, J. H. Swank, and S. S. Holt. Accretion powered X-ray pulsars. *ApJ*, 270:711–734, July 1983. doi: 10.1086/161162.

J. Wilsing. Über die Bestimmung von Bahnelementen enger Doppelsterne aus spectroskopischen Messungen der Geschwindigkeits Componenten. *Astronomische Nachrichten*, 134:89, November 1893. doi: 10.1002/asna.18941340602.

C. A. Wilson, M. H. Finger, and A. Camero-Arranz. Outbursts Large and Small from EXO 2030+375. *ApJ*, 678:1263–1272, May 2008. doi: 10.1086/587134.

C. J. E. Wolf and G. Rayet. *Comptes Rendus Hebdomadaires des Séanes de l'Acadèmié des Sciences*, 292:65, 1867.

R. H. Wolfe, Jr., H. G. Horak, and N. W. Storer. *The machine computation of spectroscopic binary elements*, page 251. 1967.

S. Yamauchi, T. Aoki, K. Hayashida, H. Kaneda, K. Koyama, M. Sugizaki, Y. Tanaka, H. Tomida, and Y. Tsuboi. New Transient X-Ray Source in the Scutum Region Discovered with ASCA. *PASJ*, 47:189–194, April 1995.

Y. B. Zel'dovich and I. D. Novikov. The Radiation of Gravity Waves by Bodies Moving in the Field of a Collapsing Star. *Soviet Physics Doklady*, 9:246, October 1964.

J. A. Zurita Heras and S. Chaty. Discovery of an eccentric 30 day period in the supergiant X-ray binary SAX J1818.6-1703 with INTEGRAL. *A&A*, 493: L1–L4, January 2009. doi: 10.1051/0004-6361:200811179.

J. A. Zurita Heras and R. Walter. INTEGRAL and XMM-Newton observations of AX J1845.0-0433. *A&A*, 494:1013–1019, February 2009. doi: 10.1051/0004-6361:200810219.